INFLUENCE OF EXTERNAL ENVIRONMENT AND ZEOLITE MATERIAL PROPERTIES ON EXTRAFRAMEWORK METAL STRUCTURES FOR PASSIVE ADSORPTION OF AUTOMOTIVE EXHAUST POLLUTANTS

by

Trevor Michael Lardinois

A Dissertation

Submitted to the Faculty of Purdue University

In Partial Fulfillment of the Requirements for the degree of

Doctor of Philosophy

Davidson School of Chemical Engineering

West Lafayette, Indiana

August 2021

THE PURDUE UNIVERSITY GRADUATE SCHOOL
STATEMENT OF COMMITTEE APPROVAL

Dr. Rajamani Gounder, Co-chair

Charles D. Davidson School of Chemical Engineering

Dr. Fabio H. Ribeiro, Co-chair

Charles D. Davidson School of Chemical Engineering

Dr. Jeffrey T. Miller

Charles D. Davidson School of Chemical Engineering

Dr. Andrew (Bean) Getsoian

Ford Motor Company

Approved by:

Dr. John Morgan

To my family - past, present, and future

ACKNOWLEDGMENTS

I would like to acknowledge the Davidson School of Chemical Engineering at Purdue University for the opportunity in the Ph.D. program. My advisors, Profs. Rajamani Gounder and Fabio Ribeiro, were excellent mentors, motivated me to strive for success in all aspects of my life, and provided abundant resources for research excellence. Additionally, I would like to acknowledge the major contributions of Prof. Jeffrey Miller and Dr. Andrew "Bean" Getsoian during my Ph.D. - their perspective and mentorship were instrumental for my growth as a Ph.D. researcher. Hidden from the publications and presentations, Yury Zvinevich was an outstanding instrumentation specialist, teaching me how to troubleshoot and prepare the most sophisticated equipment for high-quality data. Casey Jones and Laura Wilcox were great 'other workers at work' and friends, and I enjoyed the time we spent together in and outside of the lab. My last academic acknowledgement is for all the collaborators and members of Purdue Catalysis Center (PCC) for their fruitful discussions throughout the years.

None of this would be possible without the support and teachings from my parents, Kandy and Jesse, preaching the importance of a college education. I will forever be grateful for the support of my wife during my time at Purdue and all of the fun memories we made along the way, like welcoming our first son (Luca) to our family.

TABLE OF CONTENTS

LIST OF TABLES 9

LIST OF FIGURES 12

ABSTRACT 29

1 INTRODUCTION 31

2 STRUCTURAL INTERCONVERSION BETEWEEN AGGLOMERATED PALLADIUM DOMAINS AND MONONUCLEAR PD(II) CATIONS IN CHA ZEOLITES 34

2.1 Abstract 34

2.2 Introduction 35

2.3 Materials and methods 37

2.3.1 Synthesis of Pd-zeolites 37

2.3.2 Zeolite characterization 39

2.4 Results and discussion 43

2.4.1 Synthesis of Pd-CHA zeolites and origins of Pd agglomeration 43

2.4.2 Development of methods to quantify mononuclear Pd ions and PdO on Zeolite supports 49

2.4.3 Influence of zeolite framework Al arrangement on stabilizing mononuclear Pd^{2+} 58

2.4.4 Effects of the spatial distribution of agglomerated Pd on the conversion to mononuclear Pd^{2+} 65

2.5 Conclusions 69

2.6 Acknowledgements 72

2.7 Notes 73

2.8 Supporting information 73

2.8.1 Zeolite synthesis procedures 73

Hydroxide-mediated CHA synthesis 74

FAU-to-CHA interzeolite conversion . . . 76
Fluoride-mediated CHA and Beta syntheses . . . 76
2.8.2 Powder X-ray diffraction patters . . . 77
2.8.3 Ar and N_2 adsorption isotherms . . . 84
2.8.4 Co^{2+} titration of 2Al sites in 6-MR of CHA zeolites . . . 86
2.8.5 Diffuse-reflectance UV-visible spectra . . . 87
2.8.6 X-ray absorption spectroscopy (K- and L_3-edge) . . . 94
2.8.7 Temperature programmed desorption . . . 111
2.8.8 H_2 temperature programmed reduction . . . 116
2.8.9 NH_4^+ back-exchange of Pd-CHA samples . . . 122
2.8.10 Infrared spectroscopy . . . 124
2.8.11 O_2 chemisorption . . . 128
2.8.12 Transmission electron microscopy and energy-dispersive spectroscopy 129
2.8.13 X-ray photoelectron spectroscopy . . . 136

3 EFFECTS OF INITIAL PD NANOPARTICLE SIZE AND WATER PRESSURE ON THE FORMATION OF MONONUCLEAR PD(II) CATIONS IN CHA ZEOLITES DURING HIGH-TEMPERATURE AIR TREATMENT . . . 139
3.1 Abstract . . . 139
3.2 Introduction . . . 140
3.3 Methods . . . 142
3.3.1 Synthesis of Pd-CHA zeolites . . . 142
3.3.2 Pd-zeolite characterization . . . 145
3.3.3 Isothermal redispersion kinetics . . . 146
3.3.4 Details of DFT calculations . . . 147
3.3.5 Details of particle size dependent models . . . 148
3.3.6 Calculation of ab initio formation free energies and conversion of Pd nanoparticles to mononuclear Pd^{2+} . . . 149
3.3.7 Details of calculations of intermediate mobile species facilitating Pd redispersion . . . 150

3.4 Results and discussion . . . 151
3.4.1 Effects of initial Pd particle size and treatment conditions on the conversion of agglomerated Pd particles to exchanged Pd^{2+} ions . . . 151
3.4.2 Thermodynamics of Pd interconversion . . . 155
3.4.3 Quantifying apparent rates of Pd redispersion via Ostwald ripening . 165
3.5 Conclusions . . . 171
3.6 Acknowledgements . . . 173
3.7 Supporting Information . . . 173
3.7.1 Colloidal Pd nanoparticle synthesis and deposition . . . 173
3.7.2 Transmission electron microscopy and particle size distributions . . . 173
3.7.3 Thermal gravimetric analysis . . . 188
3.7.4 H_2 temperature programmed reduction . . . 190
3.7.5 Thermodynamic calculations . . . 207
3.7.6 Isothermal Pd structural interconversion rates . . . 215
3.7.7 O_2 chemisorption . . . 216

4 MICROPOROUS MATERIALS FOR THE STORAGE AND CONVERSION OF FORMALDEHYDE IN AUTOMOTIVE EXHAUST AFTERTREATMENT . . . 218
4.1 Abstract . . . 218
4.2 Introduction . . . 219
4.3 Methods . . . 220
4.3.1 Materials synthesis and characterization . . . 220
4.3.2 Formaldehyde adsorption and desorption tests . . . 220
4.4 Results and Discussion . . . 221
4.4.1 Formaldehyde storage over purely siliceous supports . . . 221
4.4.2 Influence of heteroatom identity and extraframework metals on formaldehyde storage and conversion . . . 226
4.5 Conclusions . . . 232
4.6 Acknowledgements . . . 232

REFERENCES . . . 233

A SYNTHESIS OF ENCAPSULATED PD SPECIES IN CHA ZEOLITES 257

B HYDROTHERMAL DEACTIVATION OF MONONUCLEAR CU STRUCTURES TO AGGLOMERATED PHASES IN CHA ZEOLITES FOR NH_3 SELECTIVE CATALYTIC REDUCTION OF NITROGEN OXIDES 264

C NO AND CO ADSORPTION SPECTROSCOPY OF Pd-ZEOLITES: DIFFUSE REFLECTANCE ULTRAVIOLET-VISIBLE AND PD L_3-EDGE X-RAY ABSORPTION 271

D Δ-EXAFS: NON-DESTRUCTIVE QUANTIFICATIONS OF METAL STRUCTURES IN ZEOLITES 280

E INFLUENCE OF ZEOLITE CRYSTALLITE SIZE ON THE REDISPERSION OF METALLIC PD NANOPARTICLES TO PD(II) SITES 283

VITA 288

LIST OF TABLES

2.1 Summary of identified Pd species in CHA zeolites with spectroscopic characterizations . . . 46

2.2 Summary of Pd-CHA and Pd-Beta sample characterizations, including Co^{2+} titration, Pd content, air treatment temperature before H_2 TPR quantification[a] 53

2.3 Summary of H_2 TPR and air treatment cycling experiments of Pd-CHA-12(24%)-3.3-298 . . . 66

2.4 Gel molar compositions used for hydroxide-mediated CHA zeolite syntheses . . 75

2.5 Gel molar compositions in the Al-containing, fluoride-mediated CHA syntheses . 77

2.6 Summary of Pd K-edge EXAFS fits using FEFF references. The fitted first-shell scattering pairs are denoted in parenthesis. See fits in Figures 2.24, 2.25, 2.26, and 2.27. . . . 95

2.7 Pd K-edge EXAFS fitting parameters for Pd-CHA-14(10%)-0.7-823 and Pd-CHA-5-1.2-923 after treatment in flowing 5 kPa H_2 at 473 K for 0.5 h. Samples were cooled in UHP He equipped with an in-line O_2 trap to decompose Pd^0-H and minimize oxidation of metallic Pd nanoparticles. Samples were fit to a theoretical (FEFF) Pd foil with a coordination number (CN) of 12 (see fits in Figures 2.28 and 2.29). The edge energy indicates the energy of the first inflection point in the normalized XANES spectra. . . . 96

2.8 NH_3, H_2, and N_2 TPD quantifications from Figures 2.37, 2.38, and 2.39 for a series of as-exchanged $[Pd(NH_3)_4]^{2+}$-CHA-12(24%) zeolites of varying Pd content (0–2.2 wt% Pd). . . . 115

2.9 A summary of TPR profile treatments in Figure 2.44 . . . 121

2.10 Effect of NH_4^+ back-exchange conditions with Pd-CHA-11-0.9-1023. . . . 122

2.11 Summary of H_2 TPR and NH_4^+ back-exchange with varied air treatments. . . . 123

2.12 Atomic surface (3-5 nm penetration depth and 400 m X-ray spot) composition percentages quantified with X-ray photoelectron spectroscopy for a Pd-CHA-12(24%)-1.5 sample after exchange, treatment in air to 773 K, and treatment in air to 1023 K. . . . 138

3.1 Characterization data on as-deposited Pd-CHA-X samples. Particle size distributions are in Figures 3.13, 3.14, and 3.15, SI . . . 152

3.2 HSE06-D3(BJ)vdw-calculated 0 K energies of formation (ΔE), and formation free energies of PdO_{bulk} (ΔG^{form}_{PdO}), and 3NN Z_2Pd ($\Delta G^{form}_{Z_2Pd}$) at 598 K, 20 kPa O_2, 0.014 kPa H_2O. . . . 156

3.3 Formation free energies of ion-exchanged Pd^{2+} ($\Delta G^{form}_{Z_{2Pd}}$, kJ mol^{-1}) for 2, 7, and 14 nm Pd particles at 598–873 K air treatment temperatures with 20 kPa O_2, 0.014 kPa H_2O. 158

3.4 Colloidal Pd nanoparticle solutions, Pd compositions measured by inductively coupled plasma, and amounts of compounds used for metal deposition to prepare Pd-CHA. 173

3.5 *Ex-situ* TEM characterization data for all samples after listed treatment conditions 174

3.6 H_2 TPR quantifications of the Pd-CHA-14 material treated in air to 673 K for 5 h and 1 h. 194

3.7 H_2 TPR quantifications of the Pd-CHA-7 material after treatment in flowing air with 6 kPa water for 1 and 18 h at 673 K 198

3.8 Quantifications of H_2 TPR characterization of the Pd-CHA-7 material after various treatments. H_2 TPR profiles are in Figure 3.30. 199

3.9 H_2 TPR quantifications of the H_2 TPR profiles in Figure 3.31 of the 2.2 wt% Pd-CHA (Si/Al = 12) sample. 199

3.10 GGA-PBE and HSE06-calculated 0 K energies of formation (ΔE) of PdO_{bulk}, 3NN and 2NN Z_2Pd, ZPd and ZPdOH. The formation free energies of PdO_{bulk} (ΔG^{form}_{PdO}), 3NN ($\Delta G^{form}_{3NN\,Z_2Pd}$), and 2NN Z2Pd ($\Delta G^{form}_{2NN\,Z_2Pd}$), ZPd ($\Delta G^{form}_{ZPd}$) and ZPdOH ($\Delta G^{form}_{ZPdOH}$) at 598 K, 20 kPa O_2, 0.014 kPa H_2O have been calculated using HSE06-D3(BJ)vdw energies. 208

3.11 Formation free energies (ΔG^{form}) of ion-exchanged Pd^{2+} at 3NN and 2NN 2Al sites, and Pd^+ and $[PdOH]^+$ exchanged at 1Al sites for 2, 7, and 14 nm Pd particles at air treatment temperature of 598 K with 20 kPa O_2, 0.014 kPa H_2O 211

3.12 O_2 chemisorption qualifications from Figure 3.44 217

4.1 A summary of the materials compositions and TPD quantifications. 'M' denotes the framework heteroatom or extraframework metal species (i.e., Al, Sn). Selectivity of desorbed products is defined as the molar sum carbon monoxide and dioxide divided by the total storage. 223

A.1 Synthesis mixtures using Pd-TEPA as the precursor to directly synthesize Pd-CHA. Syntheses A-C used 5 wt % Pd-TEPA with Pd:TEPA= 1 and syntheses D and E used 4.67 wt % Pd-TEPA with Pd:TEPA = 0.47. Typical total mixture masses were 5-15 grams. 257

A.2 Synthesis mixtures with 10 wt% $(NH_3)_4Pd(NO_3)_2$ as the precursor to directly synthesize Pd-CHA. Typical total mixture masses were 5–15 grams. 258

A.3 Characterization of Pd-CHA zeolites synthesized with Pd-TEPA from Table A.1. Ion-exchanged Pd^{2+} was quantified with NH_4^+ back-exchange experiments. . . . 260

A.4 Characterization of Pd-CHA zeolites synthesized with 10 wt % $(NH_3)_4Pd(NO_3)_2$ from Table A.2. Ion-exchanged Pd was quantified with NH_4^+ back-exchange experiments 260

B.1 A summary of Cu deposition procedures and estimation of Z2Cu and ZCuOH structures. 264

B.2 SCR rates, apparent activation energies, reactant orders, and extraframework Al (Al_{ex}, quantified with ^{27}Al MAS NMR) for three Cu-CHA zeolites with fixed Al density and Cu density but varying Cu speciation, before and after HTA. 265

E.1 A summary of the compositional space of CHA materials of varying average crystallite size. Co^{2+} titration values (normalized to total Al) were used to estimate the number of Al pairs in the 6-membered ring of CHA [22]. 284

LIST OF FIGURES

2.1 (a) In situ DRUV-Vis spectra during temperature programmed oxidation in air to 723 K (black to light red) of as-exchanged Pd-CHA-12(24%)-1.5-298, followed by cooling the sample to 293 K in flowing air (blue). (b) Reference spectra of a dehydrated and predominantly mononuclear Pd^{2+} CHA sample (Pd_{IE}-CHA; Pd-CHA-5-1.2-923 treated in air to 723 K air, spectra collected at 293 K in flowing air, green), a predominantly Pd nanoparticle-containing sample (Pd^0-CHA; Pd-CHA-5-1.2-923 under 5 kPa H_2 in balance N_2 at 473 K, gray), and a predominantly PdO-containing sample (PdO-Beta; Pd-Beta-Si-1.0-773, black) under ambient conditions. 47

2.2 Proposed changes to Pd structure and spatial distribution during air treatment of an as-exchanged Pd-CHA zeolite with anionic framework Al charges (orange circles) and deprotonated silanol groups (orange squares) 48

2.3 H_2 TPR profiles for dehydrated and hydrated Pd-CHA-15-2.3-1023. The samples were pretreated in flowing air to 1023 K (0.167 K s^{-1}) and held for 1 h. Hydrated sample had an intermittent exposure to 1–2 kPa H_2O in balance Ar at 303 K before TPR characterization. Regions for H_2 consumption features are denoted by labeled brackets. Pd-hydride decomposition marked with an asterisk (*). . . 52

2.4 Amount of mononuclear Pd^{2+} measured by H_2 TPR plotted against the amount of Pd exchanged by NH_4^+ in Beta (squares) and CHA (circles, black) under aqueous conditions (1 M NH_4NO_3) at 338 K for 1 day. Arrow denotes the same Pd-CHA sample after back-exchange using different conditions: 2 M NH_4NO_3, 363 K for 1 day (open circle) and 14 days (gray circle). 59

2.5 Values of $Pd(II)_{IE}/Pd_{tot}$ quantified with H_2 TPR as a function of air pretreatment temperature for Pd-CHA-12(18%)-3.9-298 (circles) and Pd-CHA-12(24%)-1.5-298 (squares; H_2 TPR profiles in Figures 2.42 and 2.43, SI); dashed line denotes the theoretical maximum amount of Pd_{IE}. 61

2.6 A comparison of mononuclear Pd^{2+} to total Pd normalized per total Al measured with H_2 TPR after treatment to 1023 K (0.167 K s^{-1}, 1 h) in flowing air (0.5 cm^3 s^{-1}) for a series of parent CHA samples with similar Al density (Si/Al = 9–15) but varied 6-MR paired Al content (percentage of Al in paired configuration in parentheses). Dashed line represents parity. (b) The amount of mononuclear Pd^{2+} (per total Al) measured with H_2 TPR for Pd-CHA (Pd/Al = 0.16–0.24) samples after treatment to 1023 K (0.167 K s^{-1}, 1 h) in flowing air (0.5 cm^3 s^{-1}) plotted against the percentage of Al in 6-MR paired configurations (per total Al). 63

2.7 O_2 chemisorption (313 K; mol O adsorbed per Pd_{tot}) cycling experiments of a Pd-CHA-12(24%)-2.2-298 sample. Sample was sequentially treated in O_2, followed by reduction H_2 at 573 K, and then O_2 adsorption at 313 K. The O_2 pretreatment temperatures were 773 K (Cycles 1-3, white), 1023 K (Cycles 4-6, light gray), and 773 K (Cycles 7-8, dark gray). 68

2.8 Ex situ XRD patterns of 8 independent zeolite syntheses of the same gel composition, before mixing these small batches to form one large batch of CHA-14(10%). Pattern (a) is for a reference Si-CHA material, previously air-treated to 853 K for 10 h to remove occluded organic content. Middle gray patterns (b-f) are of as-synthesized CHA-14(10%) samples. Top black patterns (g-i) are of washed (acetone, water) and air-treated (853 K, 10 h) Na-CHA-14(10%) samples. Patterns are offset vertically for clarity. Parentheses above peaks denote diffraction indices of CHA zeolites [95]. 78

2.9 Ex situ XRD patterns of parent CHA zeolites: (a) Si-CHA, (b) Na-CHA-5, (c) Na-CHA-11(7%), (d) Na-CHA-13(32%), (e) Na-CHA-12(18%), (f) Na-CHA-15(1.2%), (g) Na-CHA-9(28%), and (h) Na-CHA-14(1.0%). Patterns are offset vertically for clarity. Parentheses above peaks denote diffraction indices of CHA zeolites [95]. 79

2.10 Ex situ XRD patterns of (a) purely siliceous Beta (Beta-Si), (b) NH_4-Beta (CP814E, Zeolyst, Si/Al = 12.5), and (c) Pd-Beta-12.5-1.4-823. Patterns are offset vertically for clarity. 80

2.11 Ex situ XRD patterns of (a) PdO-CHA-Si-1.4-823, (b) Pd-CHA-14(10%)-0.7-823, and (c) NH_4-CHA-14(10%). Diffraction peaks locations and indices are listed for agglomerated PdO and Pd domains [96]. Patterns are offset vertically for clarity. See Figure 2.48 for STEM characterization of Pd particle sizes for Pd-CHA-14(10%)-0.7-823. 81

2.12 Ex situ XRD patterns of (a) Si-CHA and hydrothermally aged (b) Pd-CHA-30-1.0 and (c) Pd-CHA-5-1.2 after H_2 TPR characterization. Samples (b , c) were hydrothermally aged (1−2 kPa H_2O in balance air for 24 h at 1023 K, 0.5 cm^3 s^{-1}) similar to literature reports [41] in an attempt to maximize the amount of mononuclear Pd^{2+} before H_2 TPR characterization. After H_2 TPR analysis, samples were stored in vials under ambient atmosphere before ex situ XRD characterization. Patterns are offset vertically for clarity. 82

2.13 Ex situ XRD patterns of (a) reference Si-CHA, (b, from Figure 2.5 in main text) Pd-CHA-12(18%)-3.9-1023 and (c, from Table 2.3 in main text) Pd-CHA-12(24%)-3.3 after repeated H_2 TPR cycling experiments. Patterns are offset vertically for clarity. 83

2.14 Ar adsorption isotherm measured at 87 K on (a) H-CHA-14(10%) (0.21 cm^3 g^{-1}) and b) Pd-CHA-14(10%)-0.7-823 (0.23 cm^3 g^{-1}). Isotherm (a) is offset by 180 cm^3 g^{-1} at STP for clarity. 84

2.15 N_2 adsorption isotherm measured at 77 K on H-Beta-13 (0.22 cm^3 g^{-1}). 85

2.16 Co^{2+} ion-exchange isotherm of NH_4-CHA-12 using CoCl2 solutions of varying molarity. The amount of Co and Al were measured on solid samples after treatment in flowing air to 773 K. 86

2.17 DRUV-vis spectra measured under ambient conditions of three Co-CHA zeolites prepared via aqueous ion-exchange with 2 M CoCl2. Brackets denoting region where CoOx would appear (300–350 nm). Inset: d-d transition region of 390-590 nm for clarity. 87

2.18 (a, offset) DRUV-vis spectra measured under ambient conditions of the parent NH_4-CHA-12(24%) material (blue) and as-exchanged Pd-CHA-12(24%) samples of varied Pd content (0.35–2.2 wt%, light red to black) prepared via incipient wetness impregnation with $Pd(NH_3)_4(NO_3)_2$ solutions. (b) Transmission liquid-phase UV-vis spectra measured under ambient conditions of a diluted $Pd(NH_3)_4(NO_3)_2$ solution (black) and DRUV-vis spectra measured under ambient conditions of $Pd(NH_3)_4(NO_3)_2$ crystals (green). 88

2.19 (a) In situ DRUV-vis during TPD in He (30 K h^{-1} to 603 K) of as-exchanged Pd-CHA-12(24%)-1.5-298 and (b) after replacing the He stream with air (black to light red, spectrum collected every 20 min up to 80 min, arrow indicates the direction of increasing time). 90

2.20 (Black) DRUV-vis spectrum measured at 290 K of a dehydrated Pd-CHA-5-1.2-923 sample previously treated in flowing air (0.83 cm^3 s^{-1}) to 723 K (0.167 K s^{-1}, 0.5 h). (Gray) DRUV-vis spectrum measured at 290 K of a previously dehydrated Pd-CHA-5-1.2-923 sample after treatment in 1–2 kPa H_2O in balance air for at least 30 minutes. 91

2.21 (Black) DRUV-vis spectrum measured at 290 K of a PdO-Beta-Si-1.0-773 material treated in air to 473 K (0.167 K -1) for 0.5 h. (Gray) DRUV-vis spectrum measured under ambient conditions of the PdO-Beta-Si-1.0-773 material. 92

2.22 Transmission, liquid-phase UV-vis spectra measured under ambient conditions of NH_4^+ back-exchange solution after contacting with Pd-CHA-9(28%)-1.0-1023. . . 93

2.23 First-derivative Pd K-edge XANES analysis of reference Pd compounds: Pd foil (black), PdO (dark red, 98% purity, Sigma Aldrich), and K_2PdCl_6 (pink, 99% purity, Sigma Aldrich). Top black spectrum (offset + 200 units) is of the as-exchanged Pd-CHA-12(24%)-2.2-298 sample prepared via incipient wetness impregnation with $Pd(NH_3)_4(NO_3)_2$. Spectra were collected under ambient conditions. Dashed line indicates first inflection point (i.e., edge energy) of the Pd-CHA-12(24%)-2.2 sample at 24.353 keV. 97

2.24 (a) k^2-weighted $\chi(k)$ of the Pd K-edge EXAFS region for (gray) an as-exchanged Pd-CHA-12(24%)-2.2-298 collected under ambient conditions and (dashed black) the fit (Pd-N). (b) Real and imaginary Fourier transforms of the k^2-weighted EXAFS spectrum for (solid lines) an as-exchanged Pd-CHA-12(24%)-2.2-298 collected under ambient conditions and (dashed lines) fits (Pd-N). 98

2.25 (a) k^2-weighted χ(k) of the Pd K-edge EXAFS region for (gray) Pd-CHA-5-1.2-923 treated in flowing 1-2 kPa H_2O in balance air at ambient temperature and (dashed black) the fit (Pd-O). (b) Real and imaginary Fourier transforms of the k^2-weighted EXAFS spectrum for (solid lines) Pd-CHA-5-1.2-923 treated in flowing 1-2 kPa H_2O in balance air at ambient temperature and (dashed lines) fits (Pd-O). 99

2.26 (a) k^2-weighted χ(k) of the Pd K-edge EXAFS region for (gray) Pd-CHA-5-1.2-923 treated in air to 773 K then scanned at ambient temperature and (dashed black) the fit (Pd-O). (b) Real and imaginary Fourier transforms of the k^2-weighted EXAFS spectrum for (solid lines) Pd-CHA-5-1.2-923 treated in air to 773 K then scanned at ambient temperature and (dashed lines) fits (Pd-O). . . 100

2.27 (a) k^2-weighted χ(k) of the Pd K-edge EXAFS region for (gray) PdO-Beta-Si-1.0-773 treated in air to 773 K then scanned at ambient temperature and (dashed black) the fit (Pd-O). (b) Real and imaginary Fourier transforms of the k^2-weighted EXAFS spectrum for (solid lines) PdO-Beta-Si-1.0-773 treated in air to 773 K then scanned at ambient temperature and (dashed lines) fits (Pd-O). . 101

2.28 (a) k^2-weighted χ(k) of the Pd K-edge EXAFS region for (gray) Pd-CHA-14(10%)-0.7-823 treated in 5 kPa H_2 at 473 K, cooled in UHP He, then scanned at ambient temperature and (dashed black) the fit (Pd-Pd). (b) Real and imaginary Fourier transforms of the k^2-weighted EXAFS spectrum for (solid lines) Pd-CHA-14(10%)-0.7-823 treated in 5 kPa H_2 at 473 K, cooled in UHP He, then scanned at ambient temperature and (dashed lines) fits (Pd-Pd). 102

2.29 (a) k^2-weighted χ(k) of the Pd K-edge EXAFS region for (gray) Pd-CHA-5-1.2-923 treated in 5 kPa H_2 at 473 K, cooled in UHP He, then scanned at ambient temperature and (dashed black) the fit (Pd-Pd) (b) Real and imaginary Fourier transforms of the k^2-weighted EXAFS spectrum for (solid lines) Pd-CHA-5-1.2-923 treated in 5 kPa H_2 at 473 K, cooled in UHP He, then scanned at ambient temperature and (dashed lines) fits (Pd-Pd). 103

2.30 Ambient temperature Pd K-edge EXAFS of an as-exchanged Pd-CHA-12(24%)-2.2 sample prepared via incipient wetness impregnation with $Pd(NH_3)_4(NO_3)_2$. . 104

2.31 Ambient temperature Pd K-edge EXAFS of a predominantly mononuclear Pd-CHA-5-1.2-923 after treatment in flowing air to 1023 K for 0.5 h (gray) then exposure to 1–2 kPa H_2O in balance air at ambient temperatures for 0.5 h (dashed black). 105

2.32 Ambient temperature Pd K-edge (a) XANES and (b) EXAFS spectra of a PdO-Beta-Si-1.0-773 sample that was treated in flowing air (1.67 $cm^3\ s^{-1}$) to 1023 K (gray) for 0.5 h and subsequently treated in 1–2 kPa H_2O in balance air (1.67 $cm^3\ s^{-1}$) at ambient temperature for 0.5 h (dashed black). 106

2.33 Ambient temperature Pd K-edge XANES (a) and EXAFS (b) spectra of a PdO-CHA-Si-1.4-823 sample that was treated in flowing air (1.67 cm^3 s^{-1}) to 1023 K (gray) for 0.5 h and subsequently treated in 1–2 kPa H_2O in balance air (1.67 cm^3 s^{-1}) at ambient temperature for 0.5 h (dashed black). 107

2.34 First-derivative Pd K-edge XANES analysis of Pd materials at ambient temperature. Reference compounds were collected under ambient conditions: Pd foil (black), PdO (dark red, 98% purity, Sigma Aldrich), and K_2PdCl_6 (pink, 99% purity, Sigma Aldrich). (Offset +300 units for clarity) Pd-CHA-12(24%)-1.0-1023 treated in flowing air to 1023 K (black, divided by a factor of 10 for clarity) and treated in flowing 1−2 kPa H_2O in balance air at ambient temperature (green). (Offset +500 units for clarity) Pd-CHA-9-1.8-1023 treated in flowing air to 1023 K (black, divided by a factor of 7 for clarity) and treated in flowing 1–2 kPa H_2O in balance air at ambient temperature (blue). Dashed line represents an energy of 24.354 keV. 108

2.35 (a) First derivative analysis of Pd L_3-edge XANES for Pd reference compounds: metallic Pd nanoparticles (green dashed, treatment of Pd-CHA-5-1.4-923 in 5 kPa H_2 at 473 K), Pd(II) acetate (dotted red, 98%, Sigma Aldrich), Pd(II) hydroxide on carbon (red dashed, 20 wt%, Sigma Aldrich), agglomerated PdO domains on siliceous Beta (red line, Pd-Beta-Si-1.0-773), and Potassium hexachloropalladate(IV) (black, 99%, Sigma Aldrich). (b) First derivative analysis of L_3-edge XANES of a predominantly mononuclear sample, Pd-CHA-5-1.2-923. The sample was first scanned as-loaded in flowing He (solid black), then treated to 673 K in flowing 5 kPa O_2 in balance He (black dashed). The sample was cooled in flowing 5 kPa O_2 in He to 348 K (red dashed), then cooled to 298 K with 1−2 kPa H_2O (solid blue). 109

2.36 Ambient temperature Pd K-edge XANES (a) and EXAFS (b) region of Pd-CHA-14(10%)-0.7-823 (red) and Pd-CHA-5-1.2-923 (dashed black) after treatment in flowing 5 kPa H_2 to 473 K (gray) for 0.5 h. Samples were cooled in flowing UHP He with an in-line O_2 trap to decompose Pd-H species and mitigate reaction of metallic Pd with O_2. Reference spectra of Pd foil (solid black) and Pd(II) acetate (dashed blue) were collected under ambient atmosphere. 110

2.37 NH_3 desorption rates as a function of time and temperature for a series of as-exchanged $[Pd(NH_3)_4]^{2+}$-CHA-12(24%) zeolites of varying Pd content (0–2.2 wt% Pd). Arrow on top x-axis represents a temperature hold at 873 K. 112

2.38 H2 desorption rates as a function of time and temperature for a series of as-exchanged $[Pd(NH_3)_4]^{2+}$-CHA-12(24%) zeolites of varying Pd content (0–2.2 wt% Pd). Arrow on top x-axis represents a temperature hold at 873 K. 113

2.39 N_2 desorption rates as a function of time and temperature for a series of as-exchanged $[Pd(NH_3)_4]^{2+}$-12(24%) zeolites of varying Pd content (0–2.2 wt% Pd). Arrow on top x-axis represents a temperature hold at 873 K. 114

2.40 H_2 TPR profiles for (a, offset +1.5 units) PdO-CHA-Si-1.4 and (b) H-CHA-14(10%) after pretreatment in flowing air to 823 K (0.167 K s^{-1}, 0.5 cm^3 s^{-1}). H_2 consumption features are labeled for clarity. Asterisk (*) denotes Pd0-H decomposition. 116

2.41 H_2 TPR profile of an as-exchanged Pd-CHA-12(24%)-1.5-298 sample pretreated in flowing He (0.83 cm^3 s^{-1}) to 773 K (0.167 K s^{-1}, 1 h). 117

2.42 H_2 TPR profiles for a dehydrated Pd-CHA-12(24%)-1.5-298 material. The sample was first pretreated in flowing air (0.5 cm^3 s^{-1}) to 650 K (0.167 K s^{-1}) for 1 h before H_2 TPR characterization (bottom). The sample was subsequently cycled between increasing air pretreatments (750-1023 K) and H_2 TPR characterizations. Profiles are offset +4 units and listed with air pretreatment temperature and amounts of mononuclear Pd^{2+} cations (Pd_{IE}) per total Pd. 118

2.43 H_2 TPR profiles of a hydrated Pd-CHA-12(18%)-3.9-298 sample. The sample was first pretreated in flowing air (0.5 cm^3 s^{-1}) to 673 K (0.167 K s^{-1}) for 1 h before TPR characterization (bottom, black). The sample was subsequently cycled between increasing air pretreatments (673–1023 K, black to gray) and TPR characterizations. Profiles are offset +4 units and labeled with air pretreatment temperature and amounts of mononuclear Pd^{2+} ions (Pd_{IE}) per total Pd. 119

2.44 H_2 TPR profiles of hydrated Pd-CHA-12(24%)-3.3 reported in Table 2.3 of the main text and also summarized in Table 2.9. Black profiles (a-g) correspond to hydrated Pd-CHA-12(24%)-3.3 samples with different air pretreatment conditions (0.5 cm^3 s^{-1}, 0.167 K s^{-1}, 1 h, Table 2.9). Gray profiles correspond to reference TPR profiles of(h) predominantly hydrated, mononuclear Pd-CHA-5-1.2-923 and (i) PdO reference (PdO-CHA-Si-1.4-823). Profiles offset +10 units for clarity. 120

2.45 (a) OH stretching region of a parent H-CHA-15(1.2%) (black), Pd-CHA-15(1.2%)-1.2 (dark red), and Pd-CHA-15(1.2%)-2.3 (light red) treated ex situ in air to 1023 K. Samples were treated in situ in 20 kPa O_2 in balance He to 723 K before cooling to 473 K to collect spectra. The amount of mononuclear Pd^{2+} per Al (Pd(IE)/Al) measured by H_2 TPR after a 1023 K air treatment for each sample is listed in parentheses. (b) 3660 cm^{-1} region enlarged for clarity. 126

2.46 (a) OH stretching region of a parent H-CHA-12(24%) (black) and Pd-CHA-12(24%)-1.5 (red) treated ex situ in air to 1023 K. Samples were treated in situ in 20 kPa O_2 in balance He to 723 K before cooling to 473 K to collect spectra. The amount of mononuclear Pd^{2+} per Al (Pd(IE)/Al) measured by H_2 TPR after a 1023 K air treatment is listed in the parentheses. (b) 3660 cm^{-1} region enlarged for clarity. 127

2.47 O_2 chemisorption (313 K; mol O adsorbed per Pd_{tot}) cycling experiments of a Pd-CHA-12(24%)-2.2 sample. Sample was sequentially treated in O_2 (listed left to right: blue for 773 K, red for 1023 K, and green for subsequent 773 K treatment), followed by reduction H_2 at 573 K, and then O_2 adsorption at 313 K. Last measurement (yellow) is after treatment in H_2 to 1023 K. 128

2.48 Ex situ HAADF-STEM (left) and BF-STEM (right) images of a Pd-CHA-14(10%)-0.7-823 sample. 129

2.49 Ex situ HAADF-STEM (top panels) and EDS of Pd (green) and Si (red) at 1.25 Mx (bottom panels) of a Pd-CHA-12(24%)-1.5 sample treated in air to (a) 298 K, (b) 773 K, and (c) 1023 K. 130

2.50 Ex situ HAADF-STEM (top panels) and EDS of Pd (green) and Si (red) at 320 kx (bottom panels) of a Pd-CHA-12(24%)-1.5 sample treated in air to (a) 298 K, (b) 773 K, and (c) 1023 K. 130

2.51 Ex situ HAADF-STEM (top panels) and EDS of Pd (green) and Si (red) at 900 kx (bottom panels) of a Pd-CHA-12(24%)-1.5 sample treated in air to (a) 298 K, (b) 773 K, and (c) 1023 K. 131

2.52 EDS spots with quantifications (1.25 Mx) for an as-exchanged Pd-CHA-12(24%)-1.5 sample previously treated in air to 298 K. 132

2.53 EDS spots with quantifications (1.25 Mx) for a Pd-CHA-12(24%)-1.5 sample previously treated in air to 773 K. 133

2.54 EDS spots with quantifications (1.25 Mx) for a Pd-CHA-12(24%)-1.5 sample previously treated in air to 1023 K. 133

2.55 EDS spots with quantifications (900 kx) for an as-exchanged Pd-CHA-12(24%)-1.5 sample previously treated in air to 298 K. 134

2.56 EDS spots with quantifications (900 kx) for a Pd-CHA-12(24%)-1.5 sample previously treated in air to 773 K. 134

2.57 EDS spots with quantifications (900 kx) for a Pd-CHA-12(24%)-1.5 sample previously treated in air to 1023 K. 135

2.58 X-ray photoelectron spectra of Pd-CHA-12(24%)-1.5 samples. Bottom spectrum (black) is of the as-exchanged material, middle spectrum (red) is after treatment in air to 773 K, and top spectrum (blue) is after treatment in air to 1023 K. . . 136

2.59 X-ray photoelectron spectra (Pd 3d binding energy range) of Pd-CHA-12(24%)-1.5 samples. Bottom spectrum (black) is of the as-exchanged material, middle spectrum (red) is after treatment in air to 773 K, and top spectrum (blue) is after treatment in air to 1023 K. 137

3.1 Ex-situ TEM images of the as-deposited Pd-CHA-X materials. Pd-CHA-2 (left), Pd-CHA-7 (middle), Pd-CHA-14 (right). 152

3.2 (a) The amount of ion-exchanged Pd^{2+} (per total Pd) after treatment in flowing air (593–873 K) for Pd-CHA-2 (squares), Pd-CHA-7 (circles), and Pd-CHA-14 (triangles). (b) Total H_2 consumed (per total Pd) from (a). Dashed lines represent theoretical maximum amounts. H_2 TPR profiles reported in Figures 3.24, 3.25, and 3.26, SI. 155

3.3 Pd particle size-dependent thermodynamic phase diagram for the conversion of Pd particles to Z_2Pd in CHA (Si/Al =12, Pd/Al = 0.06) under (a) 20 kPa O_2, 0.014 kPa H_2O and (b) 20 kPa O_2, 6 kPa H_2O, based on HSE06-D3(BJ)vdw calculated energies. The fraction of Pd particles converted to Z_2Pd for 2 nm (squares), 7 nm (circles), and 14 nm (triangles) Pd particles at the experimental air treatment conditions for Pd-CHA-X samples are labeled. (c) Thermodynamic phase diagram for the conversion of 7 nm Pd particle to ion-exchanged Pd^{2+} cations on CHA (Si/Al =12, Pd/Al = 0.06) as a function of temperature and P_{H_2O}. The fraction of Pd particles converted to ion-exchanged Pd^{2+} cations at 20 kPa O_2, 0.014 kPa H_2O (squares), and 20 kPa O_2, 6 kPa H_2O (circles) at treatment temperatures of 598–1023 K are labeled. 160

3.4 (a) The amount of ion-exchanged Pd^{2+} and (b) total H_2 consumed normalized per total Pd as a function of treatment temperature in flowing air (squares), 6 kPa H_2O in balance air (circles), air (1 h) then adding 6 kPa H_2O (1h, diamond), and 6 kPa H_2O in balance air (1 h) then air (1 h, tringle) for the Pd-CHA-7 material. Dashed line represents theoretical maximum values. H_2 TPR profiles are reported in Figure 3.30, SI. 164

3.5 (a) The amount of ion-exchanged Pd^{2+} normalized per total Pd as a function of time during isothermal switching experiments for three different treatment temperatures (square: 673 K, triangle: 648 K, circle: 598 K) using a 2.2 wt% Pd-CHA material (Si/Al = 12) prepared via incipient wetness impregnation. (b) The total H_2 consumed normalized per total Pd from (a). Dashed line represents theoretical maximum amount. H_2 TPR profiles are in Figures 3.32, 3.33, 3.34, SI. 167

3.6 (a) The amount of ion-exchanged Pd^{2+} (normalized per ion-exchanged Pd^{2+} content after treatment for 1 h, and denoted as conversion) as a function of time during isothermal switching experiments (648 K) in air (circles), 2 kPa H_2O in balance air (squares), and air after treatment in air to 873 K (diamonds) using a 2.2 wt% Pd-CHA material (Si/Al = 12) prepared via incipient wetness impregnation. H_2 TPR profiles are in Figures 3.33, 3.35, and 3.36, SI. (b) H_2 consumed normalized to total Pd of materials in (a). 169

3.7 Ex-situ HAADF-STEM images (340 kx resolution) of the as-exchanged 2.2 wt% Pd-CHA sample synthesized via incipient wetness impregnation after treatment in flowing H_2 (5 kPa) at 673 K for 1 h. Histogram is reported in Figure 3.8 . . . 175

3.8 Histogram (normalized frequency), normal distribution (solid black line), and log-normal distribution (dashed black line) for the as-exchanged 2.2 wt% Pd-CHA material after treatment in flowing H_2 (5 kPa) at 673 K for 1 h. Histogram bins contain particles ± 0.5 nm from bin listing. The total number of particles imaged was 164, and the average particle size was 3.2 nm with a 98% confidence interval of 0.3 nm and standard deviation of 1.5 nm, assuming a normal distribution. The mean (average of ln(x)) of the log-normal distribution was 1.1 (corresponding to an average particle size of 2.9 nm) with a standard deviation (σ(ln(x)) of 0.5. . 176

3.9 Ex-situ TEM images (71 kx resolution) of the colloidal Pd nanoparticle solutions. (Far left) nominally 2 nm particles, (middle) nominally 7 nm particles, (right) nominally 14 nm particles. Histograms are reported in Figures 3.10, 3.11, 3.12. . 177

3.10 Histogram (normalized frequency) and normal distribution (black line) for the nominally 2 nm colloidal Pd nanoparticle solution. Histogram bins contain particles ± 0.2 nm from bin listing. The total number of particles imaged was 164, and the average particle size was 2.2 nm with a 98% confidence interval of 0.1 nm and standard deviation of 0.5 nm. 177

3.11 Histogram (normalized frequency) and normal distribution (black line) for the nominally 7 nm colloidal Pd nanoparticle solution. Histogram bins contain particles ± 0.3 nm from bin listing. The total number of particles imaged was 161, and the average particle size was 6.9 nm with a 98% confidence interval of 0.1 nm and standard deviation of 0.7 nm. 178

3.12 Histogram (normalized frequency) and normal distribution (black line)for the nominally 14 nm colloidal Pd nanoparticle solution. Histogram bins contain particles ± 1 nm from bin listing. The total number of particles imaged was 378, and the average particle size was 14 nm with a 98% confidence interval of 0.3 nm and standard deviation of 2.3 nm. 179

3.13 Histogram (normalized frequency) and normal distribution (black line) for the as-exchanged Pd-CHA-2 material. Histogram bins contain particles ± 0.2 nm from bin listing. The total number of particles imaged was 164, and the average particle size was 2.2 nm with a 98% confidence interval of 0.1 nm and standard deviation of 0.5 nm. 180

3.14 Histogram (normalized frequency) and normal distribution (black line) for the nominally 7 nm colloidal Pd nanoparticle solution. Histogram bins contain particles ± 0.3 nm from bin listing. The total number of particles imaged was 112, and the average particle size was 6.8 nm with a 98% confidence interval of 0.2 nm and standard deviation of 0.7 nm. 181

3.15 Histogram (normalized frequency) and normal distribution (black line) for the nominally 14 nm colloidal Pd nanoparticle solution. Histogram bins contain particles ± 1 nm from bin listing. The total number of particles imaged was 73, and the average particle size was 14.0 nm with a 98% confidence interval of 0.5 nm and standard deviation of 1.6 nm. 182

3.16 Ex-situ TEM images of the air-treated (548 K) Pd-CHA-X materials. Pd-CHA-2 (left), Pd-CHA-7 (middle), Pd-CHA-14 (right). Histograms are plotted in Figures 3.17, 3.18, and 3.19. 182

3.17 Histogram (normalized frequency) and normal distribution (black line) for the nominally 2 nm colloidal Pd nanoparticle solution after treatment in flowing air to 548 K (60 K h^{-1}) for 4 h. Histogram bins contain particles ± 0.2 nm from bin listing. The total number of particles imaged was 164, and the average particle size was 2.2 nm with a 98% confidence interval of 0.1 nm and standard deviation of 0.5 nm. 183

3.18 Histogram (normalized frequency) and normal distribution (black line) for the nominally 7 nm colloidal Pd nanoparticle solution after treatment in flowing air to 548 K (60 K h^{-1}) for 4 h. Histogram bins contain particles ± 0.3 nm from bin listing. The total number of particles imaged was 72, and the average particle size was 6.6 nm with a 98% confidence interval of 0.2 nm and standard deviation of 0.7 nm. 184

3.19 Histogram (normalized frequency) and normal distribution (black line) for the nominally 14 nm colloidal Pd nanoparticle solution after treatment in flowing air to 548 K (60 K h^{-1}) for 4 h. Histogram bins contain particles ± 1 nm from bin listing. The total number of particles imaged was 74, and the average particle size was 13.5 nm with a 98% confidence interval of 0.4 nm and standard deviation of 1.3 nm. 185

3.20 Ex-situ HAADF-STEM images (340 kx resolution for top panels and 470 kx resolution for bottom panels) of the as-exchanged Pd-CHA sample after treatment in flowing H_2 (5 kPa) at 673 K for 1 h, then air at 873 K for 1 h. Histogram is reported in Figure 3.21. 186

3.21 Histogram (normalized frequency), normal distribution (solid black line), and log-normal distribution (dashed black line) for the as-exchanged 2.2 wt% Pd-CHA material after treatment in flowing H_2 (5 kPa) at 673 K for 1 h, treatment in air to 873 K for 1 h, then treatment in flowing H_2 (5 kPa) to 573 K for 1 h. Histogram bins contain particles ± 0.3 nm from bin listing. The total number of particles imaged was 179, and the average particle size was 2.2 nm with a 98% confidence interval of 0.2 nm and standard deviation of 1.0 nm, assuming a normal distribution. The mean (average of ln(x)) of the log-normal distribution was 0.7 (corresponding to an average particle size of 2.1 nm) with a standard deviation (σ(ln(x)) of 0.4. 187

3.22 TGA weight loss derivative profiles (298 523 K, hold at 523 K) of as-deposited Pd-CHA-14 nm Pd-CHA (red), air-treated (548 K, 60 K h^{-1}, 4 h) monodisperse Pd-CHA materials (yellow for Pd-CHA-14, green for Pd-CHA-7, and black for Pd-CHA-2), and H-CHA support (blue). 188

3.23 TGA weight loss derivative profiles (298–1073 K) of as-deposited Pd-CHA-14 (red), air-treated (548 K, 60 K h^{-1}, 4 h) monodisperse Pd-CHA-X materials (yellow for Pd-CHA-14, green for Pd-CHA-7, and black for Pd-CHA-2), and H-CHA support (blue). Dotted line is for temperature (secondary y-axis). . . . 189

3.24 H_2 TPR profiles of the Pd-CHA-2 material after treatment in flowing (0.5 cm^3 s^{-1}) air to 598 K (black), 673 K (red, offset +5 units), and 773 K (blue, offset + 10 units) for 1 h. Quantifications are plotted in Figure 3.1, main text. Dashed gray lines for 598 K air treatment are for two Gaussian fits for agglomerated PdO particles (centered near 340 K) and ion-exchanged Pd^{2+} (centered near 390 K). Dashed red line is the sum of the two Gaussians. 191

3.25 H_2 TPR profiles of the Pd-CHA-7 material after treatment in flowing (0.5 cm^3 s^{-1}) air to 598 K (black), 673 K (red, offset +5 units), and 773 K (blue, offset + 10 units) for 1 h. Quantifications are plotted in Figure 3.1. 192

3.26 H_2 TPR profiles of the Pd-CHA-14 material after treatment in flowing (0.5 cm^3 s^{-1}) air to 673 K (black, 1 h), 673 K (red, offset +10 units, 5 h), 773 K (blue, offset + 20 units, 1 h), and 873 K (green, offset +30 units, 1 h). Quantifications are plotted in Figure 3.1. 193

3.27 (a) The amount of ion-exchanged Pd^{2+} and (b) total H_2 consumed normalized per total Pd as a function of treatment temperature in flowing air (squares), 6 kPa water in balance air (circles), and 10 kPa water in balance air (tringle) for the Pd-CHA-2 material. Dashed line represents theoretical maximums. See above for discussion of data. H_2 TPR profiles are found in Figure 3.28. 196

3.28 H_2 TPR profiles of the Pd-CHA-2 material after treatment in flowing air (with and without water) for 1 h. Profiles are offset by +5 unit increments and labeled for clarity. Quantifications are plotted in Figure 3.27. For profiles that required fitting, gray dashed lines are for Gaussian fits of agglomerated PdO domains and ion-exchanged Pd^{2+}, and the dotted black lines are for the sum of the respective Gaussian fits. 197

3.29 H_2 TPR profiles of the Pd-CHA-7 material after treatment in flowing air with 6 kPa water for 1 h (black) and 18 h (red, offset + 6 units) at 673 K. 198

3.30 H_2 TPR profiles of the Pd-CHA-7 material (reported in Figure 3.4 of the main text) after various treatments, which are listed next to profile. Profiles are offset +5 units for clarity. H_2 TPR quantifications are listed in Table 3.8. 200

3.31 H_2 TPR profiles of a 2.2 wt% Pd-CHA (Si/Al = 12) material after treatment in flowing air to 473 K for 2 h (black), 473 K for 5 h (blue, offset +5 units), and 473 K in air for 2 h, then 648 K in flowing He for 1 h (red, offset + 10 units). Bracket region denotes an integrated region attributed to agglomerated PdO domains for the +10 units offset profile. 201

3.32 H_2 TPR characterization of the 2.2 wt% Pd-CHA material after isothermal redispersion experiments at 673 K. Air exposure times are listed by profiles (offset +5 units for clarity). Gaussian peak deconvolutions were performed to determine agglomerated PdO more and ion-exchanged contents more accurately. Dotted gray lines are for PdO (lower temperature) and ion-exchanged Pd^{2+} (highest temperature) Gaussian deconvolutions, dotted red lines are the sum of the Gaussian fits, and the black lines are for the experimentally measured H_2 consumption rate. . 202

3.33 H_2 TPR characterization of the 2.2 wt% Pd-CHA material after isothermal redispersion experiments at 648 K. Air exposure times are listed by profiles (offset +5 units for clarity). Gaussian peak deconvolutions were performed to determine agglomerated PdO more and ion-exchanged contents more accurately. Dotted gray lines are for PdO (lower temperature) and ion-exchanged Pd^{2+} (highest temperature) Gaussian deconvolutions, dotted red lines are the sum of the Gaussian fits, and the black lines are for the experimentally measured H_2 consumption rate. . 203

3.34 H_2 TPR characterization of the 2.2 wt% Pd-CHA material after isothermal redispersion experiments at 598 K. Air exposure times are listed by profiles (offset +5 units for clarity). Gaussian peak deconvolutions were performed to determine agglomerated PdO more and ion-exchanged contents more accurately. Dotted gray lines are for PdO (lower temperatures) and ion-exchanged Pd^{2+} (highest temperature) Gaussian deconvolutions, dotted red lines are the sum of the Gaussian fits, and the black lines are for the experimentally measured H_2 consumption rate. For the 11.4 s trial, the entire profile was integrated to determine H_2 consumed per Pd, and the ion-exchanged Pd^{2+} content was estimated with a Gaussian. . . 204

3.35 H_2 TPR characterization of the 2.2 wt% Pd-CHA material after isothermal redispersion experiments in wetted (2 kPa H_2O) air at 648 K. Wetted air exposure times are listed by profiles (offset +5 units for clarity). Gaussian peak deconvolutions were performed to determine agglomerated PdO more and ion-exchanged contents more accurately. Dotted gray lines are for PdO (lower temperatures) and ion-exchanged Pd^{2+} (highest temperature) Gaussian deconvolutions, dotted red lines are the sum of the Gaussian fits, and the black lines are for the experimentally measured H_2 consumption rate. 205

3.36 H_2 TPR characterization of the 2.2 wt% Pd-CHA (treated in air to 873 K for 1 h before each redispersion sequence, particle size distribution in Figure 3.21, O_2 chemisorption dispersion measurements in Figure 3.44) material after isothermal redispersion experiments in air at 648 K. Wetted air exposure times are listed by profiles (offset +5 units for clarity). Gaussian peak deconvolutions were performed to determine agglomerated PdO more and ion-exchanged contents more accurately. Dotted gray lines are for PdO (lower temperatures) and ion-exchanged Pd^{2+} (highest temperature) Gaussian deconvolutions, dotted red lines are the sum of the Gaussian fits, and the black lines are for the experimentally measured H_2 consumption rate. 206

3.37 Thermodynamic bulk phase diagram based on HSE06-D3(BJ)vdw calculated energies at 0.014 kPa H_2O . . . 207

3.38 (a) Comparison of particle size-dependent thermodynamic models with DFT-computed energies of Pd nanoparticles. (b) Optimized structures of the Pd nanoparticles considered . . . 209

3.39 Particle size dependent thermodynamic phase diagram based on HSE06-D3(BJ)vdw calculated energies for conversion of Pd particle sizes ranging from 1.8 to 100 nm to exchanged cations at 2Al sites as (a) Pd^{2+} at 2NN 6-MR (3NN 6-MR Z_2Pd), and (b) 2NN 6-MR Z_2Pd, and at 1Al sites as (c) Pd^{+} (ZPd), and (d) $[PdOH]^{+}$ (ZPdOH). (e) Combined phase diagram of all the Pd-exchanged species at 1Al and 2Al sites shown in (a)-(d). Air treatment conditions of 0.014 kPa H_2O and 20 kPa O_2 are used. . . . 210

3.40 Size-dependent thermodynamic phase diagram for Pd/Al ratios of (a) 0.06, (b) 0.10, and (c) 0.16 based on HSE06-D3(BJ)vdw calculated energies at 20 kPa O_2, 0.014 kPa H_2O. . . . 212

3.41 Thermodynamic phase diagram for the conversion of (a) d_{Pd} = 2 nm, and (b) d_{Pd} = 14 nm to ion-exchanged Pd^{2+} cations on CHA (Si/Al =12, Pd/Al = 0.06) as a function of temperature and P_{H_2O}. The fraction of Pd particles converted to ion-exchanged Pd^{2+} cations at 20 kPa O_2, 0.014 kPa H_2O (squares), and 20 kPa O_2, 6 kPa H_2O (circles) at treatment temperatures of 598–1023 K are labeled. 213

3.42 Comparison of enthalpy and entropy contributions to the conversion of d_{Pd} = 7 nm to Z_2Pd based on HSE06-D3(BJ)vdw calculated energies at 20 kPa O_2, 6 kPa H_2O . . . 214

3.43 The amount of ion-exchanged Pd^{2+} normalized per total Pd as a function of time during isothermal switching experiments (648 K) in air (circles, triangle) or 2 kPa water in balance air (squares, diamond). The flowrates (in cm^3 s^{-1}) for each measurement are given in parentheses in the legend. . . . 215

3.44 O_2 chemisorption (313 K) experiment of a 2.2 wt% Pd-CHA material. The as-exchanged material was treated in flowing H_2 (103 kPa) to 673 K for 1 h before performing O_2 chemisorption characterization (no offset, circles). Following, the sample was treated in flowing O_2 (103 kPa) to 873 K for 1 h, cooled to ambient temperatures, treated in flowing H_2 to 573 K, then prepared for O_2 chemisorption (triangles, offset +0.12 mmol O_2 g^{-1}). Quantifications are reported in Table 3.12. 216

4.1 TPD profile of the Si-Beta-F material under flowing air after adsorption of formaldehyde. Black profile is for formaldehyde, red profile is for carbon monoxide, blue profile is for carbon dioxide, and dashed black line is for temperature (on the secondary y-axis) . . . 222

4.2 TPD profile of the dealuminated Si-Beta material under flowing air after adsorption of formaldehyde. Black profile is for formaldehyde, red profile is for carbon monoxide, blue profile is for carbon dioxide, and dashed black line is for temperature (on the secondary y-axis). 225

4.3 TPD profile of the Al-Beta material under flowing air after adsorption of formaldehyde. Black profile is for formaldehyde, red profile is for carbon monoxide, blue profile is for carbon dioxide, and dashed black line is for temperature (on the secondary y-axis). 227

4.4 TPD profile of the Sn-Beta-41 material under flowing air after adsorption of formaldehyde. Black profile is for formaldehyde, red profile is for carbon monoxide, blue profile is for carbon dioxide, and dashed black line is for temperature (on the secondary y-axis). 229

4.5 TPD profile of the Sn-Beta-109 material under flowing air after adsorption of formaldehyde. Black profile is for formaldehyde, red profile is for carbon monoxide, blue profile is for carbon dioxide, and dashed black line is for temperature (on the secondary y-axis). 230

4.6 TPD profile of the SnO_x-Si-Beta material under flowing air after adsorption of formaldehyde. Black profile is for formaldehyde, red profile is for carbon monoxide, blue profile is for carbon dioxide, and dashed black line is for temperature (on the secondary y-axis). 231

A.1 XRD patterns of zeolites synthesized with Pd-TEPA after treatment in flowing air to 853 K and cooling to ambient. Bottom XRD pattern is for a reference Si-CHA material. Samples A, B, C, D, E refer to the samples in Table A.1. . . . 258

A.2 XRD patterns of zeolites synthesized with $(NH_3)_4Pd(NO_3)_2$ after treatment in flowing air to 853 K. Bottom XRD pattern is for a reference Si-CHA material. Samples A, B, C, D, E refer to the samples in Table A.2. 259

A.3 Transmission UV-Vis spectra of Pd-containing solutions used for syntheses collected under ambient conditions. 261

A.4 Transmission UV-Vis spectra of Pd-TEPA solutions used for syntheses collected under ambient conditions after removal of Cl^- species with $Ag(NO_3)$. 262

B.1 The relative decrease in SCR rate of fresh and HTA Cu-CHA zeolite samples as a function of Cu speciation. 266

B.2 The SCR rate normalized to mass of catalyst measured after sequential treatments at 723 K in air then 500 ppm NO and 530 ppm NH3 at 523 K for 24 and 48 hours. White bars are for CuO and H-CHA zeolite (Si/Al = 15) mixture. Striped bars are for CuAl2O4 and H-CHA zeolite mixture. Gray bars are for Cu(85)-Z-HTA. The rates plotted for the HTA sample were divided by a factor of 10 for graphical comparison. 267

B.3 Ex-situ XRD (Cu Kα) pattern of an intimate mixture of γ-Al2O3 and CuO after treatment in air to 1023 K for 24 h. 269

B.4 The relative SCR rate of fresh and HTA Cu-CHA catalysts plotted as a function of the initial fraction of Al that is extraframework. The relative SCR rate was calculated by dividing the HTA SCR rate by the fresh SCR rate. Al_{ex} was quantified with ^{27}Al MAS NMR on the hydrated, parent H-form zeolite before Cu exchange. 269

B.5 Ex-situ XRD (Cu Kα) pattern of $CuAl_2O_4$ (bottom), Siliceous Beta (middle), and HTA (1223 K, 48 hours) Cu-Beta. 270

C.1 DRUV-Vis spectra of Pd-zeolites dehydrated in flowing (50 cm^3 min^{-1}) air at 723 K for 30 minutes. Spectra were collected at 290 K. The characterized fractions of ion-exchanged Pd^{2+} to total Pd are in parentheses in legend. Ligand to metal charge transfer (LMCT, red) bands are assigned to absorptions around 250 nm, PdO particles show absorption features around 320 nm (blue), and d-d transitions are around 440 nm (green). 271

C.2 DRUV-Vis spectra of H-CHA (Si/Al = 6) treated in flowing (50 cm^3 min^{-1}) air to 723 K, then exposed to 1000 ppm NO in balance air at 348 K. Once the spectra stabilized indicating the sample has equilibrated, NO flow was cut off and the sample was treated to higher temperatures in air. Spectra for samples treated to temperatures above 473 K were collected after cooling to 293 K. 272

C.3 DRUV-Vis spectra of Pd-CHA(1.0) treated in flowing (50 cm^3 min^{-1}) air to 723 K, then exposed to 1000 ppm NO in balance air at 323 K. Once the spectra stropped changing, NO flow was cut off and the sample was ramped to higher temperatures. Spectra for samples treated to temperatures above 473 K were collected after cooling to 293 K. 273

C.4 DRUV-Vis spectra of Pd-CHA(1.0) previously treated in flowing air to 923 K. The sample was first dehydrated at 723 K in flowing air (50 cm^3 min^{-1}) then exposed to 2000 ppm CO in balance air at 323 K. Once the spectra stropped changing, 1000 ppm NO flow was added. The sample was then purged in dry air at 323 K, then ramped to higher temperatures. Spectra for samples treated to temperatures above 473 K were collected after cooling to 293 K. 274

C.5 DRUV-Vis spectra of Pd-CHA(1.0) previously treated in flowing air to 923 K. The sample was first dehydrated at 723 K in flowing air (50 cm^3 min^{-1}, black) and treated in flowing UHP He (50 cm^3 min^{-1}) for 15 hours at 723 K. The sample was cooled down under He flow and scanned at 290 K (green). The flowing He stream was then sent though a water bubbler, resulting in ~3 kPa H_2O / He stream. The sample was ramped to 723 K and held in flowing, wet He for 20 hours. The sample was then cooled to 290 K and scanned (blue). 275

C.6 (a) Series of Pd standards characterized with Pd L_3-edge XANES. 4 scans were averaged. Pd metal / CHA (black) was prepared by reducing a 1.2 wt% Pd-CHA zeolite in 5 kPa H_2 at 473 K, PdO / Si-Beta (dark red) was prepared by depositing $Pd(NH_3)_4(NO_3)_2$ on purely siliceous beta zeolite and treating in flowing air to 823 K, $Pd(OH)_2$ (red) was scanned as-loaded, $Pd(Acetate)_2$ (light pink) was scanned as-loaded, and K_2PdCl_6 (blue) was scanned as-loaded. (b) The derivative of (a) was plotted to clearly identify edge energies of the different Pd standards. The black spectrum is a Pd^0 reference (3172.8 eV), red spectra are Pd^{2+} references (3174 eV), and blue is a Pd^{4+} reference (3176 eV). Shaded regions are peak maximums (edge energies) for the labeled Pd oxidation sate standard. 276

C.7 (a) Pd L_3-XANES spectra of dehydrated Pd-CHA (Si/Al = 4.5, 1.2 wt% Pd, predominantly ion-exchanged Pd^{2+}) (reds) at various temperatures (308 673 K) and rehydrated in wetted (1–3 kPa H_2O) air at 298 K (blue). Inset is for clarity when comparing white line intensity. (b) The derivative of (a) to clearly identify edge energies. Shaded regions on right are to show edge energy for a zeolite ligated (red) or water ligated (blue) ion-exchanged Pd^{2+} cation. 277

C.8 (a) Pd L_3-edge XANES of a Pd-CHA (Si/Al = 4.5, 1.2 wt% Pd, predominantly ion-exchanged Pd^{2+}) material dehydrated in flowing air to 673 K (blue), then cooled to 348 K in flowing air (black), treated in flowing 500 ppm NO in balance air air at 348 K (dark red), then treated in flowing air to 413 K (red), 473 K (light red), and 673 K (pink). Air refers to 5 kPa O_2 in balance He. (b) The derivative of (a) to better show edge energies. 278

C.9 (a) Pd L_3-edge XANES of a Pd-CHA (Si/Al = 4.5, 1.2 wt% Pd, predominantly ion-exchanged Pd^{2+}) material dehydrated in flowing air to 673 K, then cooled to 348 K in flowing air then rehydrated in wet (1–3 kPa H_2O) air (black), treated in flowing 500 ppm NO / wetted (1–3 kPa H_2O) air at 348 K (dark red), purged flowing wetted (1–3 kPa H_2O) air at 348 K (red), then treated to 413 K (light red) and 473 K (pink) in wetted (1–3 kPa H_2O) air. Air means 5 kPa O_2 in balance He. (b) The derivative of (a) to better show edge energies. 279

D.1 A hydrated, dehydrated (773 K, air, 0.5 h, offset +0.02 units), and Δ-EXAFS (offset + 0.05 units) spectra of a predominantly mononuclear Pd^{2+} Beta material. 281

D.2 A comparison of the integrated Δ-EXAFS (k^2-weighted) second-shell area to the amount of ion-exchanged Pd^{2+} (per total Pd) after treatment in flowing air to 1023 K for 0.5 h. 282

E.1 Ex-situ scanning electron microscopy images of three CHA materials of different crystallite size: (a) 10 μm, (b) 500 nm, and (c) nanosheets (<10 nm). Table E.1 summarizes the material compositions. 283

E.2 H_2 TPR profiles of Pd-CHA materials of varied crystallite size: (a) 10 μm, (b) 500 nm, (c) nanosheets. Quantifications are plotted in Figure E.3. 285

E.3 Quantifications of mononuclear Pd^{2+} content (per framework Al) from Figure E.2. Average crystallite sizes listed in legend. 286

E.4 A summary of H_2 TPR quantifications of mononuclear Pd^{2+} as a function of air treatment temperature for CHA zeolites of Si/Al = 9–14. The nanosheet materials were flake-like, evidenced SEM but not provided here. The other CHA materials were not characterized with SEM, but the Al precursors are given in legend following literature reported recipes. 287

ABSTRACT

Metal-zeolites are promising materials for passive adsorber technologies for the abatement of nitrogen oxides (NOx, x = 1,2) and aldehydes during low-temperature operation in automotive exhaust aftertreatment systems. The aqueous-phase exchange processes used commonly to prepare metal-zeolites typically require mononuclear, transition metal complexes to diffuse within intrazeolite pore networks with their solvation shells and replace extraframework cations of higher chemical potential. When metal complexes are larger than the zeolite pore-limiting diameter, this imposes intracrystalline transport restrictions; thus, complexes and agglomerates tend to preferentially deposit near the surfaces of crystallites, requiring post-synthetic treatments to disperse metal species more uniformly throughout zeolite crystallites via solid-state ion-exchange processes. Here, we address the influence of post-synthetic gas treatments and zeolite material properties on the structural interconversion and exchange of extraframework Pd in CHA zeolites with a focus on the thermodynamic, kinetic, and mechanistic factors that dictate the Pd site structures and spatial distributions that form.

Pd-amine complexes introduced via incipient wetness impregnation on CHA zeolites were found to preferentially site near crystallite surfaces. Post-synthetic treatments in flowing air results in Pd-amine decomposition and agglomeration to metallic Pd^0 and supersequent oxidation to PdO, before converting to mononuclear Pd^{2+} cations through an Ostwald ripening mechanism at high temperatures (>550 K). Progressively higher air treatment temperatures (up to 1023 K) were found to (1) thermodynamically favor the formation of mononuclear Pd^{2+} cations relative to agglomerated PdO particles, (2) increase the apparent rate of structural interconversion to mononuclear Pd^{2+}, and (3) facilitate longer-range mobility of molecular intermediates involved in Ostwald ripening processes that allow Pd cations to form deeper within zeolite crystallites to form more uniformly dispersed Pd-zeolite materials. Additionally, the controlled synthetic variation of the atomic arrangement of 1 or 2 Al sites in the 6-membered ring of CHA was used to show a thermodynamic preference to form mononuclear Pd^{2+} cations charge-compensated by 2 Al sites over $[PdOH]^+$ complexes at 1 Al site. Colloidal Pd nanoparticle syntheses and deposition methods were used to pre-

pare monodisperse Pd-CHA materials to isolate the effects of Pd particle size on structural interconversion to mononuclear Pd^{2+} under a range of external environments. Consistent with computational thermodynamic predictions, smaller Pd particle sizes favor structural interconversion to mononuclear Pd^{2+} under high-temperature air treatments (598–973 K), while adding H_2O to the air stream inhibits the thermodynamics but not the kinetics of mononuclear Pd^{2+} formation, demonstrating that water vapor in exhaust streams may be deleterious to the long-term stability of Pd-zeolite materials for passive NOx adsorption.

The influence of metal-zeolite material properties on the adsorption, desorption, and conversion of formaldehyde, a government-regulated automotive pollutant, under realistic conditions was investigated to identify beneficial material properties for this emerging application in mobile engine pollution abatement. A suite of Beta zeolite materials was synthesized with varied adsorption site identity (Brønsted acid, Lewis acid, silanol groups, and extraframework metal oxide) and bulk site densities. All materials stored formaldehyde and converted a large fraction of formaldehyde to more environmentally benign CO and CO_2, demonstrating the efficacy of silanol defects and zeolitic supports for the storage of formaldehyde. Sn-containing zeotypes, containing either Lewis acidic framework Sn sites or extraframework SnO_x particles, resulted in the greatest selectivity to CO and CO_2 formed during formaldehyde desorption, suggests that Sn species are a beneficial component in metal-zeolite formulations for the abatement of formaldehyde in automotive exhaust streams.

This work demonstrates how combining precise synthesis of metal-zeolites of varied bulk and atomic properties with site-specific characterization and titration methods enables systematically disentangling the influence of separate material properties (e.g., Pd particle size, zeolite framework Al arrangement, silanol density, heteroatom identify) and external environment on changes to metal structure, speciation, and oxidation state. This approach provides thermodynamic, kinetic, and mechanistic insights into the factors that influence metal restructuring under the practical conditions encountered in automotive exhaust aftertreatment applications and guidance for materials design and treatment strategies to form desired metal structures during synthesis and after regeneration protocols.

1. INTRODUCTION

Mobile engine exhaust aftertreatment systems are challenged to abate greater amounts of pollutants as government regulations continue to tighten. The highly transient conditions in automotive exhaust streams require the development of robust abatement technologies that convert pollutants to more environmentally benign products over a wide range of external conditions (i.e., temperatures and gas composition) and for the entire lifetime of the vehicle. Currently, the majority of government-regulated pollutants, specifically NOx (x = 1, 2) and formaldehyde, are released during engine cold-start when abatement technologies are below their optimal operating temperature (<473 K) window, motivating the development of passive adsorber technologies. Passive adsorbers function by storing pollutants at lower temperatures and then desorbing them at higher temperatures compatible with downstream abatement technologies, thereby buffering the effects of transient temperature fluctuations (300–1000 K) in exhaust systems. This dissertation focuses on synthesis-structure-function relationships of metal-exchanged zeolites for the passive adsorption of NO_x and formaldehyde.

Pd-exchanged CHA zeolites have emerged as promising materials for passive NOx adsorption (PNA) [1], where the purported Pd structures for NO_x adsorption are mononuclear Pd cations [2] charge-compensated by anionic zeolite framework charges formed by the isomorphous substitution of tetravalent Si with trivalent Al. Chabazite (CHA) is the most promising zeolite framework for Pd-based PNA materials because the CHA topology hosts mononuclear Pd cations, minimizes the effects of sulfur poisoning of mononuclear Pd cations, and shows better durability under hydrothermal aging conditions (1023 K, 10 kPa H_2O in balance air) than other common zeolite frameworks (e.g., Beta, MFI) [3]. However, the formation of undesirable agglomerated Pd structures caused by reduction with H_2 and CO under realistic exhaust conditions [4], [5] motivates further fundamental studies to understand the relationship among Pd structures, zeolite framework material properties, and external environment conditions. The fundamental learnings here are applied to the rational design of Pd-zeolites to improve their long-term stability and efficacy as passive NOx adsorbers.

Determining the identity and number of Pd structures stabilized on zeolites remains challenging because of the co-existence of many Pd structures, which vary in nuclearity (mono- and polynuclear) and formal oxidation state (zero to tetravalent). Under external environments composed of air from 300–1023 K, density functional theory (DFT) calculations predict that CHA zeolites can host both mononuclear Pd^{+} and Pd^{2+} cations, where the distribution of these structures depends on the local arrangement Al in the framework [6]. Additionally, IR band assignments of NO adsorbed on Pd-zeolites have been assigned to adsorption at mononuclear Pd^{+} (ca. 1810 cm^{-1}) and Pd^{2+} (ca. 1860 cm^{-1}), supporting the viability of both species being present after air treatments. However, the proposal of multiple valence states of mononuclear Pd contradict other literature reports that propose Pd is predominantly in the divalent state after high-temperature (700–1000 K) air treatments [7], [8]. Additionally, the co-existence of agglomerated Pd species as Pd^{0}, PdO, and PdO_2 along with mononuclear Pd cations further obfuscates the quantification of the Pd structures present [9]. Therefore, Chapter 2 focuses on how zeolite material properties (i.e., the arrangement of framework Al sites) influences the formation and structures of mononuclear Pd sites, by synthesizing CHA zeolites with varied numbers of 6-MR paired Al sites (i.e., 2 Al sites in the 6-memebered ring) and developing methods to characterize the identify and quantify all Pd species after high temperature (773–1023 K) air treatments.

Another complexity with Pd-zeolite materials is the structural interconversion between mononuclear and agglomerated Pd species, which can proceed in either direction depending on the external gas environment. For example, Pd species in Y zeolites agglomerate to predominantly metallic Pd particles under flowing 5 kPa H_2 (>573 K), but subsequent treatment in flowing air to elevated temperatures (>573 K) causes metallic Pd particles to redisperse to mononuclear Pd cations. However, treating Pd-CHA zeolites to high temperatures (1023 K) in air streams containing water (10 kPa) facilitates agglomerated PdO interconversion to mononuclear Pd cations, reportedly maximizing mononuclear Pd cation content [10]. Computational studies on γ-Al_2O identified that the Pd nanoparticle size influences the interconversion into mononuclear Pd cation sites, where smaller Pd particles favor conversion to mononuclear Pd sites hosted at defect Al_{III} sites through an Ostwald ripening mechanism, which was corroborated with experiments on a series of monodisperse

Pd/Al_2O_3 samples that showed smaller Pd particles convert in air to mononuclear Pd sites at lower temperatures [11]. However, there have been no clear studies with CHA zeolites linking the thermodynamics, kinetics, and mechanisms of Pd structural interconversion as a function of Pd particle size and external gas conditions. In Chapter 2, the reversibility between agglomerated and mononuclear Pd species as a function of air treatment temperature was investigated to understand the changes in Pd structure that occur to favor the formation of mononuclear Pd at high temperatures. Additionally, Chapter 3 addresses the effects of the initial Pd particle size on the structural interconversion by synthesizing a series of monodisperse Pd nanoparticles of varied size that were supported on CHA zeolites. These Pd-CHA materials were treated in flowing air with and without water, and the amounts and apparent rates of mononuclear Pd^{2+} formation were quantified and compared to theoretical estimates. Together, these findings provide fundamental thermodynamic and kinetic insights into Pd structural interconversion mechanisms in CHA zeolites.

Unlike PNA with Pd-zeolites, a technological breakthrough for the passive adsorption of aldehydes (specifically formaldehyde) remains unestablished. This shortcoming motivates an exploratory synthesis-structure-function relationship study to identify beneficial zeolite material properties for the storage and conversion of formaldehyde. Previous literature identified the efficacy of Lewis acid sites for the adsorption of aldehydes and ketones in aqueous media, suggesting these site types may operate under realistic automotive exhaust conditions containing water (e.g., 1–10 kPa H_2O) [12], [13]. Therefore, in Chapter 4, a range of Beta zeolite materials were synthesized with varied heteroatom identity (Brønsted and Lewis acid sites) and densities. These materials were tested for formaldehyde storage and conversion, and the total storage and selectivity of desorbed products to more environmentally benign products (CO and CO_2) were correlated to different site types, revealing promising material properties for passive formaldehyde adsorption and abatement.

2. STRUCTURAL INTERCONVERSION BETEWEEN AGGLOMERATED PALLADIUM DOMAINS AND MONONUCLEAR PD(II) CATIONS IN CHA ZEOLITES

2.1 Abstract

Palladium-exchanged zeolites are candidate materials for passive NO_x adsorption in automotive exhaust aftertreatment, where mononuclear Pd cations behave as precursors to the purported NO_x adsorption sites. Yet, the structures of zeolite lattice binding sites capable of stabilizing mononuclear Pd^{2+} ions, and the mechanisms that interconvert agglomerated PdO and Pd domains into mononuclear Pd^{2+} ions during Pd redispersion treatments, remain incompletely understood. Here, we use a suite of spectroscopic methods and quantitative site titration techniques to characterize mononuclear and agglomerated Pd species on zeolites with varying material properties and treatment history. Aqueous-phase methods to introduce Pd onto NH_4-form zeolites initially form mononuclear $[Pd(NH_3)_4]^{2+}$ complexes, but subsequent thermal treatments (573–723 K; air) lead to in situ formation of H_2 that first reduces Pd^{2+} to metallic Pd domains, which are then oxidized by air to PdO domains. Progressive treatment of Pd-zeolites in air to higher temperatures (723–1023 K) converts larger fractions of agglomerated PdO to mononuclear Pd^{2+}, as quantified by H_2 temperature programmed reduction, because higher temperature treatments facilitate Pd redispersion toward deeper locations within chabazite (CHA) crystallites, which is corroborated by complementary titrimetric and spectroscopic data. Pd-CHA zeolites synthesized with similar bulk Pd and framework Al content, but varying framework Al arrangement, provide evidence that six-membered rings (6-MR) hosting paired Al sites (Al–O–$(Si–O)_x$–Al, x = 1, 2) stabilize Pd^{2+} ions and that otherwise isolated Al sites can stabilize $[PdOH]^+$ species, identifiable by an IR OH stretch at 3660 cm^{-1}. These findings clarify the underlying chemical processes and gas environments that cause Pd agglomeration in zeolites and their subsequent redispersion to mononuclear Pd^{2+} ions, which prefer binding at 6-MR paired Al sites in CHA, and indi-

cate that higher temperature air treatments lead to more uniform Pd spatial distributions throughout zeolite crystallites.

2.2 Introduction

The speciation of metal ions, complexes, and particles on a given zeolite support depends on bulk (e.g., framework topology) and atomic-scale properties (e.g., arrangement of lattice Al sites) and often on the specific protocols and treatments used to introduce metals onto the zeolite. The size and connectivity of microporous voids introduce different shape-selective limitations on the diffusion of metal species within crystallites [14] and influence the sizes of encapsulated metal nanoparticles [15]–[17]. The speciation of exchanged metal cations and complexes also depends on the atomic arrangements of framework Al sites [18]–[21], which introduce localized anionic charges into siliceous zeolite lattices. For example, the structure of mononuclear Cu^{2+} cations has been shown to depend on the arrangement of Al sites within six-membered rings (6-MR) of chabazite (CHA) zeolites [22], as Cu^{2+} cations prefer exchange at 6-MR paired Al sites (two Al per 6-MR; Al—O—$(Si—O)_x$—Al, x = 1, 2), while $[CuOH]^+$ prefer exchange at 6-MR isolated Al sites (one Al per 6-MR) [20], [23]. Identifying the framework Al arrangements that stabilize mononuclear metal cations becomes more challenging when agglomerated particles also form after relevant synthesis and treatment protocols, as is common for Pd- and Pt-exchanged zeolites [5], [11], [24], [25]. Furthermore, for applications in diesel NO_x (x = 1, 2) aftertreatment, metal-exchanged zeolites must be stable under a wide range of transient operating conditions, motivating methods to characterize and quantify metal structures that can improve mechanistic understanding of how such structures interconvert with changes in temperature and gas environment. Strategies to augment selective catalytic reduction (SCR)-based NO_x abatement, particularly at low temperatures (<473 K) wherein Cu-zeolite SCR catalysts tend to become ineffective in practice, have considered implementing Pd-zeolites as materials for passive NO_x adsorption (PNA) followed by subsequent NO_x desorption at temperatures compatible with catalytic conversion via SCR [1], [3].

Mononuclear Pd ions charge-compensating anionic framework Al charges are the proposed PNA precursor sites [2], [3], [26], but the structures of desired Pd binding sites among different possible cationic species remain incompletely understood. Various Pd species are reported to be present on zeolites under different gas conditions, including agglomerated clusters (metallic Pd [27], [28], PdO [29], PdO_2 [9]) and mononuclear cations (Pd^+ , Pd^{2+}, Pd^{3+}) [6], [8], [30]–[33]. Even when solely considering Pd-zeolites treated in air (600–1023 K), various mononuclear Pd sites have been proposed by CO IR spectra (2050—2250 cm^{-1} peaks assigned to Pd^{2+}, $[PdOH]^+$, Pd^+) [26], [29], [34]–[36] and by in situ X-ray absorption spectroscopy (XAS, majority four-coordinate Pd^{2+} in Pd-MFI) [37]. Density functional theory (DFT) calculations by Mandal et al. indicate that a divalent Pd^{2+} cation charge-compensated by a 6-MR paired Al site in CHA (denoted as Z_2Pd, where Z represents an anionic framework charge introduced by Al substitution) is the most thermodynamically stable mononuclear Pd^{2+} species, consistent with their experimental Pd-CHA samples that did not show the OH IR stretches near 3660 cm^{-1} expected for a monovalent $[PdOH]^+$ complex (denoted as ZPdOH) [38]. These findings appear consistent with the larger amounts of mononuclear Pd ions (higher Pd^{2+}/Al ratios) reported to form on zeolites of higher bulk Al density (lower Si/Al ratios) [37], [39], [40], which on average should contain larger amounts of proximal Al sites. Additionally, the Rietveld refinement of X-ray diffraction (XRD) patterns of dehydrated Pd-exchanged Y zeolites showed mononuclear Pd cations predominantly located in the plane of the 6-MR, likely as Z_2Pd sites. Although substantial evidence can be found in prior work for the formation of Z_2Pd sites in Pd-exchanged zeolites, there is relatively scant experimental evidence for ZPdOH sites, which in part may reflect the lack of synthetic or treatment methods to emphasize this mononuclear Pd^{2+} site motif.

Additionally, the mechanistic details by which mononuclear Pd^{2+} ions form at various zeolite binding sites during PdO redispersion at high temperatures are imprecisely known. Agglomerated PdO domains are reported to convert to mononuclear Pd^{2+} ions after hydrothermal aging (1023 K, 10 kPa H_2O in air) [41] or elevated temperature (>500 K in air) treatments of Pd-zeolites [42], with the extent of Pd redispersion reported to depend on bulk Pd and Al densities [11], [37], Pd particle size [11], and treatment temperature [43], [44]; yet, a unified mechanistic description for these redispersion phenomena is lacking. Goodman et

al. calculated the change in Gibbs free energy upon ejection of a $Pd(OH)_2$ molecule from a PdO particle and its subsequent adsorption on an Al_{III} defect on a γ-Al_2O_3 support to estimate the Boltzmann-averaged distribution of mononuclear Pd^{2+} formed (1048 K in dilute O_2) as a function of Pd content [11]. This mean-field model rationalized the experimental observation that decreasing the total Pd content relative to the Al_{III} defect sites on γ-Al_2O_3 led to increased fractions of mononuclear Pd. In the case of Pt on alumina, Simonsen et al. observed using transmission electron microscopy (TEM) that Pt particles of similar size either became larger or smaller during redispersion treatments (923 K in air), suggesting that Ostwald ripening processes that exchange atoms among particles depend on their local environment and relative proximity in a manner that cannot be fully described by a mean-field model [45].

Here, we investigate the influence of zeolite material properties on the structures and amounts of Pd species formed under various treatment conditions by preparing and interrogating a suite of Pd-exchanged CHA samples with varied Pd and framework 6-MR paired Al content. In situ diffuse reflectance UV−vis (DRUV−vis) spectroscopy was used to monitor the transformation of mononuclear $[Pd(NH_3)_4]^{2+}$ complexes to mononuclear Pd^{2+} sites and agglomerated Pd domains during high temperature treatments in air. The numbers of mononuclear Pd^{2+} ions and agglomerated PdO domains were quantified with H_2 temperature programmed reduction (TPR) to understand the influence of air treatment conditions and zeolite material properties on the formation of mononuclear Pd^{2+} sites. Cyclic treatments to agglomerate and redisperse Pd structures reveal that both reversible and irreversible structural changes occur, wherein PdO domains interconvert to mononuclear Pd^{2+} sites via an Ostwald ripening mechanism.

2.3 Materials and methods

2.3.1 Synthesis of Pd-zeolites

A Beta zeolite (Si/Al = 13) sample was obtained from Zeolyst International (CP814E). One CHA zeolite sample (Si/Al = 12) was provided by BASF Corporation. All other CHA and Beta zeolites were hydrothermally synthesized following previously reported procedures

[20], [23], [46]–[49] (detailed procedures in Section 2.8.1, Supporting Information (SI)). In general, zeolite synthesis solutions were homogenized in perfluoroalkoxy alkane (PFA) containers (Savillex Corporation) with magnetic Teflon stir bars. The solutions were transferred to Teflon-lined, stainless steel autoclaves (Parr Instruments), sealed under autogenous pressure, and placed in a forced convection oven controlled to 413−433 K for at least 6 days. Synthesis solutions were recovered via centrifugation, and the solids were washed (30 mL (g solid)$^{-1}$ per wash) with alternating cycles of deionized water (18.2 MΩ cm) and acetone (>99.5 wt%, Sigma-Aldrich), finishing a seventh wash with deionized water. Solids (0.2−2.0 g) were stored in a static drying oven at 373 K for >12 h before treating in flowing dry air (1.67 cm^3 s^{-1}, Air Zero, Indiana Oxygen) to 853 K (0.0167 K s^{-1}) to remove occluded organic content via combustion.

Zeolites were converted to their NH_4-forms by contacting with 1 M of NH_4NO_3 (99.9 wt% purity NH_4NO_3, Sigma-Aldrich) in PFA containers with a magnetic Teflon stir bar at a ratio of 150 g of solution (g solid)$^{-1}$ under ambient conditions for >24 h. NH_4-form zeolites were recovered by centrifugation, washed with deionized water (30 mL (g solid)$^{-1}$ per wash) until the pH of the supernatant was constant, treated in a static drying oven at 373 K for >12 h, and then stored under an ambient atmosphere in capped borosilicate scintillation vials.

Pd-exchanged samples were prepared via incipient wetness impregnation. First, deionized water was added dropwise to NH_4- form zeolites while stirring with a plastic spatula until saturation of the total pore volume, evidenced by transformation from an agglomerated powder-like substance to a shear-thickening slurry. Assuming the same mass saturation point as pure water, aqueous $Pd(NH_3)_4(NO_3)_2$ (10 wt%, Sigma-Aldrich) solutions were appropriately diluted with deionized water and added dropwise to NH_4-form zeolites while stirring to achieve targeted Pd loadings. As-exchanged Pd-zeolite samples were left under ambient conditions overnight before storing in capped borosilicate scintillation vials

2.3.2 Zeolite characterization

Zeolite framework topologies were characterized by powder XRD using a Rigaku SmartLab X-ray diffractometer (Cu Kα radiation source, XRD patterns in Section 2.8.2, SI). Samples (ca. 0.01 g) were pressed onto a low-dead-volume sample holder (Rigaku). XRD patterns were collected over a range of 4—40° 2θ with a 0.01° step size and a scan rate of 0.0167° s^{-1}. Diffractograms were compared to known references to identify the dominant crystalline phases.

The micropore volumes of CHA (Ar, 87 K) and Beta (N_2, 77 K) zeolites were determined via physisorption using a Micromeritics ASAP 2020 surface area and porosity analyzer. H-form and Pd-H-form zeolites were evacuated under dynamic vacuum (5 μHg), heated first (0.167 K $^{-1}$) to 393 K for 2 h, and then heated to 623 K for 9 h before adsorption measurements. Volumetric uptakes of adsorbates between 0.10 and 0.20 P/P_0 were linearly extrapolated to zero relative pressure to estimate the micropore volume. Micropore volumes were additionally estimated by finding the minimum of the semilogarithmic plot of $\partial(\text{Vads})/\partial(\ln(P/P_0))$ versus $\ln(P/P_0)$, which were within 10% of the linearly extrapolated estimate. Micropore volumes of all samples were within reported literature ranges for predominantly crystalline CHA and Beta zeolites (Section 2.8.3, SI).

The number of 6-MR paired Al sites in CHA samples was quantified by Co^{2+} titration [20], [22]. NH_4-form zeolites were contacted with 2 M of $CoCl_2$ (98 wt%, Sigma-Aldrich) in PFA containers with a magnetic Teflon stir bar at a ratio of 150 g of solution (g solid)$^{-1}$ for >24 h to achieve saturation (Co^{2+} ion-exchange isotherm in Section 2.8.4, SI). Co-exchanged zeolites were recovered via centrifugation, washed with water (30 mL (g solid)$^{-1}$ per wash) four times, and dried in a static oven at 373 K before treatment in flowing air to 773 K (0.0167 K s^{-1}) for 4 h. Co-form zeolites were characterized by DRUV—vis spectroscopy and did not contain features for Co_xO_y species (300—350 nm; Figure 2.17, SI) [50], [51], demonstrating that this Co-exchange procedure results in predominantly mononuclear Co^{2+} ions.

Elemental compositions were characterized by atomic absorption spectroscopy (AAS) using a PerkinElmer model AAnalyst 300 or inductively coupled plasma optical emission

spectrometry (ICP-OES) using a Thermo Scientific iCAP 7000 Plus Series ICP-OES. Samples (0.02−0.05 g) were digested with 2.5 g of hydrofluoric (HF) acid (48 wt%, Alfa Aesar) for at least 2 days before diluting with 50 g of deionized water at an ambient temperature. [Caution: use appropriate personal protective equipment, ventilation, and engineering controls when working with HF.] Samples analyzed by ICP analysis were further acidified with 2.5 g of HNO3 (70 wt%, Sigma-Aldrich) before analysis. Elemental compositions of Co, Pd, and Al were determined from calibration curves generated by elemental analysis standard solutions. The Si/Al ratios of the solids were estimated by subtracting the contribution of extraframework cations and assuming a molar composition of $Si_{1-x}O_2Al_x$.

DRUV−vis spectra were collected with a Varian Cary 5000 UV−vis−NIR spectrophotometer equipped with a Harrick Scientific Praying Mantis diffuse reflectance accessory. Baseline spectra were collected using poly(tetrafluoroethylene) (200 μm, Sigma-Aldrich). Samples were pelletized, sieved (180−250 μm), and lightly pressed using a glass microscope slide to achieve a flat surface of uniform height. Spectra were collected over a range of 190–1200 nm with a scan rate of 5 nm s^{-1}.

XAS was performed at the Advanced Photon Source at Argonne National Laboratory. Pd L_3-edge spectra were collected in fluorescence mode at sector 9-BM. Samples (0.1–0.2 g) were pressed into self-supporting wafers and placed on temperature-controlled resistive heater elements inside an in situ cube cell sealed with Kapton windows [52], [53]. Four spectra were collected over a range of 2973−3310 eV (resolution of 5 eV for 2973−3158 eV, 0.2 eV for 3158−3204 eV, and 1.5 eV for 3204−3310 eV) and averaged. Derivative spectra were calculated with a noise-robust seven-point stencil equation (details in Section 2.8.6, SI). Pd K-edge spectra were collected in transmission mode at sector 10-BM. Samples (0.05−0.10 g) were pressed into cylindrical holders as self-supporting wafers and placed in Kaptonsealed quartz tubes. Samples were treated in a separate furnace equipped with a gas flow manifold, cooled to an ambient temperature, and then sealed and transferred to the beamline for measurement. Energies for Pd K- and L_3-edge experiments were calibrated using the first inflection point (i.e., edge energy) of the X-ray absorption nearedge structure (XANES) of a Pd foil. Fitting details for the extended X-ray absorption fine structure (EXAFS) spectra are provided in Section 2.8.6 of the SI.

Temperature programmed desorption (TPD) experiments were performed with a Micromeritics AutoChem II 2920 Chemisorption Analyzer. Samples (0.02−0.05 g) were supported between two quartz wool plugs in a quartz U-shaped reactor, and a clam-shell furnace was used to control the temperature of a thermocouple touching the top quartz bed. Species that were adsorbed on the sample were desorbed under flowing (0.833 cm^3 s^{-1}) He (ultra high purity (UHP), 99.999%, Indiana Oxygen) to 873 K (0.167 K s^{-1}), and the products were quantified with a residual gas analyzer (MKS Cirrus 3).

H_2 TPR experiments were performed with a Micromeritics AutoChem II 2920 Chemisorption Analyzer equipped with an internal thermal conductivity detector (TCD) for H_2 consumption quantification. An isopropanol slurry (cooled to 184 K with liquid N_2) was placed in-line before the TCD to trap any condensable gases (e.g., H_2O). Mixtures of varying H_2 partial pressures (0.5−5 kPa) in balance Ar were used to generate a response factor, which quantified the theoretical H_2 consumption upon reduction of a reference Ag_2O material to within 10%. Samples (0.04−0.10 g) were supported between two plugs of quartz wool in a quartz U-tube reactor, and a clam-shell furnace controlled the temperature measured by a thermocouple above the sample bed. For H_2 TPR of dehydrated zeolites, samples were treated in flowing air (0.50 cm^3 s^{-1}, Air Zero, Indiana Oxygen) to a range of temperatures (573-1023 K, 0.167 K s^{-1}) for 1 h, cooled to 373 K before switching to flowing (0.50 cm^3 s^{-1}) Ar (UHP, 99.999%, Indiana Oxygen), and then cooled further to 203 K using a Micromeritics CryoCooler II accessory. For H_2 TPR of hydrated zeolite samples, H_2 TPR was performed after similar treatments as above, but instead of cooling directly from 373 K to 203 K in Ar, an intermediate step was used to hold the sample at 303 K under flowing (0.50 cm^3 s^{-1}) 1−2 kPa H_2O in balance Ar (UHP, 99.999%, Indiana Oxygen) for at least 0.5 h. After the temperature stabilized at 203 K, a flowing stream of 5 kPa H_2 in balance Ar (certified mixture, Indiana Oxygen) was sent over the sample (0.167 cm^3 s^{-1}) until a stable TCD baseline was achieved, and then the sample was treated to 573 K (0.167 K s^{-1}) and held for 0.5 h.

NH_4^+ back-exchange procedures were adapted from Lee et al. [26] and are similar to other Na^+ back-exchange procedures [35], [54], [55]. Pd-exchanged samples (0.05−0.08 g) were mixed with 25−50 g of 1 M NH_4NO_3 (99.9 wt% NH_4NO_3, Sigma-Aldrich) in PFA containers with a magnetic Teflon stir bar for 24 h at 338 K, unless stated elsewise. The solution was

removed from heated oil baths to cool to an ambient temperature before recovering solids via centrifugation, and the Pd content in the decanted and filtered (0.2 μm) supernatant was quantified with AAS.

IR spectra were collected with a Nicolet 6700 Fourier transform infrared (FTIR) spectrometer equipped with a mercury cadmium telluride (MCT) detector. Samples (0.03−0.05 g) were pressed into self-supporting wafers, placed in a custom-built FTIR cell described elsewhere [56], treated in 20 kPa O_2 (UHP, 99.98%, Indiana Oxygen) in balance He (UHP, 99.999%, Indiana Oxygen) to 723 K (0.083 K s^{-1}) for 1 h, and then cooled to 473 K. Spectra were collected as the average of 500 scans over a range of 400−4000 cm^{-1} with a resolution of 2 cm^{-1}. An empty cell spectrum collected under identical conditions was subtracted from all spectra before baseline-correcting and normalizing to T−O−T vibrations (2100 and 1750 cm^{-1}).

O_2 chemisorption experiments were performed with a Micromeritics ASAP 2020 Plus Chemisorption unit. Samples (0.4−0.5 g, pelleted and sieved to 180−250 μm) were supported between two plugs of quartz wool and flushed in flowing He (UHP, 99.999%, Indiana Oxygen) before degassing under vacuum (<3 μmHg) for 1 h at 373 K. Samples were leak-tested after the first degas and before chemisorption measurements and consistently had leak rates of <60 μmHg h^{-1}, which is below the <600 μmHg h^{-1} recommended by Micromeritics for chemisorption measurements. Samples were treated in flowing O_2 (UHP, 99.98%, Matheson) to 773 or 1023 K (0.167 K s^{-1}) for 1 h, evacuated at 313 K for 1 h, treated in H_2 (UHP, 99.999%, Praxair) to 573 K (0.167 K s^{-1}) for 1 h, evacuated at 573 K for 1 h, cooled to 313 K for a leak test, and then evacuated for 0.3 h at 313 K before collecting two O_2 adsorption isotherms (313 K, 2−42 kPa) with an evacuation step in between to remove physisorbed O_2. The isotherms were linearly extrapolated to zero partial pressure, and the difference in intercepts was used to quantify the amount of O_2 adsorbed per Pd. A stoichiometry of one O per surface Pd was assumed to quantify the Pd dispersion [57].

Scanning transmission electron microscopy (STEM) analysis was performed at the Oak Ridge National Laboratory. The morphology and elemental distribution of Pd-exchanged samples were analyzed on an FEI F200X Talos operating at 200 kV equipped with an extreme field emission gun electron source, a high-angle annular dark-field (HAADF) detector, and a

Super-X energy-dispersive X-ray spectroscopy (EDS) system with four silicon-drift detectors (Bruker XFlash 6 series with detector size 120 mm^2) with a solid angle of 0.9 sr for chemical analysis. To avoid and minimize any potential electron beam damage during imaging and spectroscopy analysis, the current of the electron beam was controlled to 0.490 nA. Samples for TEM analysis were prepared by a drop-cast method, wherein samples were dispersed in isopropanol via sonication and then deposited onto lacey carbon-coated copper grids (SPI Supplies, part no. Z3820C). Part of the microscopy experiments were also conducted on an aberration-corrected JEOL JEM-ARM200CF TEM/STEM operated at 200 kV with a unique cold field emission gun, a next-generation Cs corrector (ASCOR) that compensates for higher-order aberrations, and a Gatan 965 GIF Quantum electron energy loss spectroscopy (EELS) imaging filter with dual electron energy loss spectroscopy capabilities.

X-ray photoelectron spectroscopy (XPS) was performed using a Thermo Scientific K-Alpha XPS instrument equipped with a monochromatic Al K photon source, a hemispherical electron energy analyzer, and a 128-channel detector. Wide-energy-range survey spectra were acquired using a pass energy of 200 eV to determine all elements present. Core level spectra were also acquired for detailed analysis of elemental bonding using a pass energy of 50 eV. Samples were prepared for analysis by dispersing onto doublesided tape fixed to clean glass slides. Samples were introduced into the analysis chamber through a vacuum-pumped load lock. The base pressure in the analysis chamber is ca. 5×10^{-10} mbar, but was at 2×10^{-7} mbar during measurement of the mounted sample due to using a charge compensation system that uses both low-energy electrons and low-energy Ar ions to prevent sample charging. Data were collected and analyzed using Avantage version 4.61 software.

2.4 Results and discussion

2.4.1 Synthesis of Pd-CHA zeolites and origins of Pd agglomeration

All samples are referred to as F-CHA-A(X%)-B-C, where "F" denotes the cation or metal form (e.g., NH_4, Na, H, Pd, PdO, $[Pd(NH_3)_4]^{2+}$, Co), "A" denotes the solid Si/Al ratio (or "Si" for purely siliceous materials), "B" denotes the Pd wt%, and "C" denotes the highest air temperature treatment (in Kelvin) that the sample was exposed to before characterization.

Some parent zeolite materials have the same Si/Al ratio; these are differentiated by the percentage of Al in 6-MR configurations (determined by Co^{2+} titration) using the "(X%)" portion of the sample code. Extraframework, mononuclear Pd cations of arbitrary structure and oxidation state will be referred to as Pd_{IE}. Powder XRD patterns (Section 2.8.2, SI) for all zeolites in their as-made forms were consistent with the intended framework topology and were collected after the most severe treatments of Pd-form zeolites (i.e., 1023 K in air with and without 1−2 kPa H_2O) to assess their effects on long-range structural degradation. Additionally, XRD was not able to identify diffraction peaks for agglomerated Pd or PdO domains (Figure 2.11, SI) because these particles were smaller (<3 nm) than detection limits (Figure 2.48, SI) [58]. Micropore volumes of H-form and Pd-H-zeolites determined from Ar or N_2 adsorption isotherms (Section 2.8.3, SI) were also consistent with the respective topology.

DRUV−vis and XAS were used to characterize the initial structure of Pd before treatments that attempt to convert them to Pd_{IE}. As-exchanged Pd-CHA-12(24%)-1.5-298, chosen as a representative sample, showed two DRUV−vis absorption bands; the positions of their maxima are listed in Table 2.1 and plotted in Figure 2.1 (spectra for other as-exchanged Pd-zeolite samples in Figure 2.18, SI). The absorption band at 300 nm is assigned to Pd^{2+} d−d transitions, consistent with those in aqueous $[Pd(NH_3)_4]^{2+}$ complexes [59]–[61] (Figure 2.18, SI). The other band centered at 220 nm is in the range of ligand-to-metal charge-transfer (LMCT) in aqueous $[Pd(H_2O)_{4-n}Cl_n]^{(2-n)+}$ complexes [62], suggesting that this band reflects LMCT from the N atom in ligated NH_3 to Pd^{2+}. Additionally, the as-exchanged Pd-CHA-12(24%)-2.1-298 sample under an ambient atmosphere showed a Pd K-edge XANES edge energy of 24.353 keV, which is similar to a PdO standard (Figure 2.23, SI) and $[Pd(NH_3)_4]^{2+}$ complexes [63], indicating that the majority of Pd is divalent. First-shell coordination fits for Pd−N bonds using a FEFF-simulated $[Pd(NH_3)_4]^{2+}$ structure gave a coordination number of 4.0 ± 0.4 (Table 2.6, SI), and the k^2-weighted Fourier transform magnitude EXAFS spectra did not show a second-shell Pd−Pd scatter (Figure 2.30, SI) [64]. Additionally, the $Pd(NH_3)_4(NO_3)_2$ solution was dropped onto a microscope slide under ambient conditions, and the water was evaporated; the resultant crystals showed DRUV−vis spectra (Figure 2.18, SI) similar to the reference $[Pd(NH_3)_4]^{2+}$ solution, demonstrating that $Pd(NH_3)_4(NO_3)_2$ crystals could also be present on the as-exchanged Pd-CHA samples. Ex situ STEM characteri-

zation of an as-exchanged Pd-CHA sample showed evidence of Pd agglomerates, consistent with the possible formation of $Pd(NH_3)_4(NO_3)_2$ crystals during synthesis (Figures 2.49, 2.50, 2.51, SI). Taken together, these characterization data reflect the predominant presence of mononuclear Pd^{2+} in the form of $[Pd(NH_3)_4]^{2+}$ charge-compensated by deprotonated silanol groups [65], nitrate anions, or framework Al sites on as-exchanged Pd-CHA samples prepared by incipient wetness impregnation of $Pd(NH_3)_4(NO_3)_2$, as depicted in Figure 2.2.

Table 2.1. Summary of identified Pd species in CHA zeolites with spectroscopic characterizations

Pd speciation	Temperature	Charge-transfer band maximum / nm	d-d transition maximum / nm	EXAFS first-shell coordination number[a]
$[Pd(NH_3)_4]^{2+}$	ambient	220	300	4.0 ± 0.4 (Pd-N)
$[Pd(H_2O)_4]^{2+}/[Pd(H_2O)_3(OH)]^{+}$	ambient	275[b]	390[b]	4.1 ± 0.4 (Pd-O)
$[Pd(O_{zeo})_4]^{2+}/[Pd(O_{zeo})_3(OH)]^{+}$	ambient	240	465	3.5 ± 0.4 (Pd-O)
$[Pd(O_{zeo})_4]^{2+}/[Pd(O_{zeo})_3(OH)]^{+}$	723 K	260	500	–
agglomerated PdO domains	ambient	325	–	4.1 ± 0.4 (Pd-O)
metallic Pd domains	473 K	325	–	–

[a]Details of EXAFS first-shell fitting can be found in Section 2.8.6 and Table 2.23 in the SI.
[b]DRUV−vis spectra of hydrated, mononuclear Pd^{2+} cations reported in Figure 2.20 in the SI.

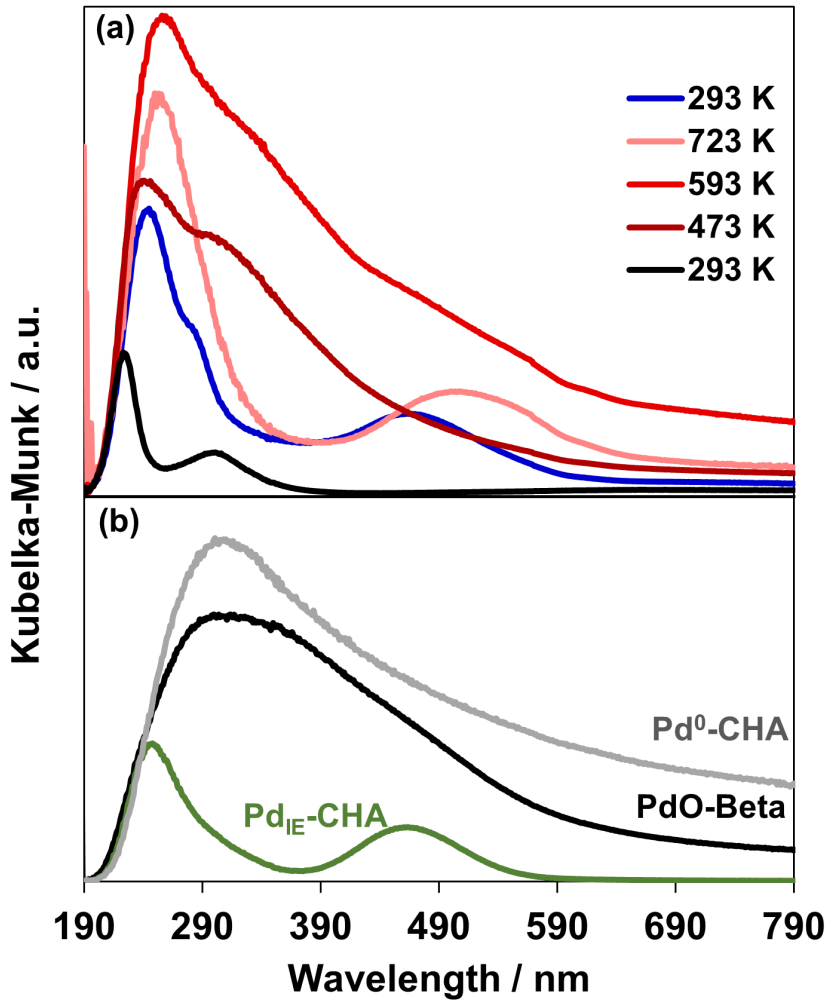

Figure 2.1. (a) In situ DRUV-Vis spectra during temperature programmed oxidation in air to 723 K (black to light red) of as-exchanged Pd-CHA-12(24%)-1.5-298, followed by cooling the sample to 293 K in flowing air (blue). (b) Reference spectra of a dehydrated and predominantly mononuclear Pd^{2+} CHA sample (Pd_{IE}-CHA; Pd-CHA-5-1.2-923 treated in air to 723 K air, spectra collected at 293 K in flowing air, green), a predominantly Pd nanoparticle-containing sample (Pd^0-CHA; Pd-CHA-5-1.2-923 under 5 kPa H_2 in balance N_2 at 473 K, gray), and a predominantly PdO-containing sample (PdO-Beta; Pd-Beta-Si-1.0-773, black) under ambient conditions.

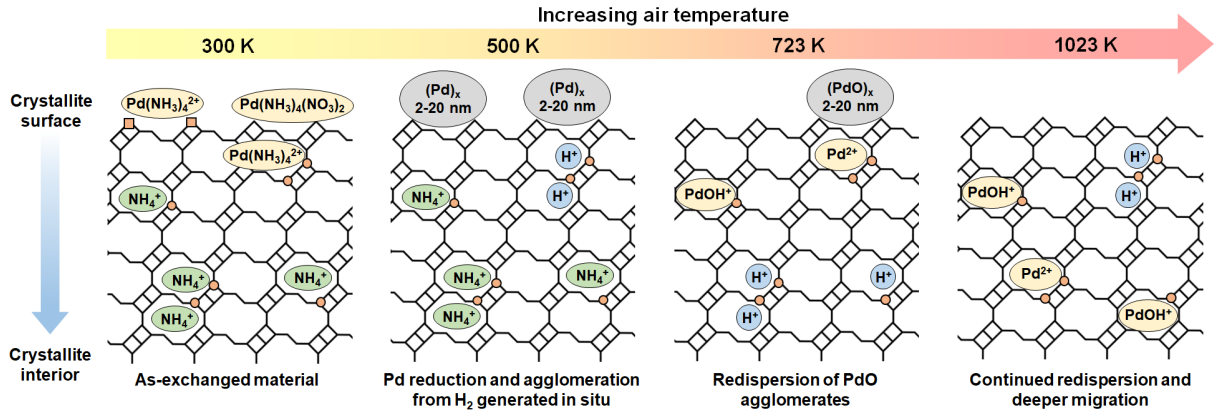

Figure 2.2. Proposed changes to Pd structure and spatial distribution during air treatment of an as-exchanged Pd-CHA zeolite with anionic framework Al charges (orange circles) and deprotonated silanol groups (orange squares)

An as-exchanged Pd-CHA-12(24%)-1.5-298 sample was treated in flowing air to 723 K while simultaneously collecting DRUV−vis spectra to monitor the transformation of $[Pd(NH_3)_4]^{2+}$ to mononuclear Pd sites (Figure 2.1a). Upon treatment to 473 K, the N−Pd LMCT band increased in intensity, and the d−d transition band for $[Pd(NH_3)_4]^{2+}$ started to broaden. Once the temperature reached 593 K, the charge-transfer region was more intense and red-shifted to 260 nm, while the d−d transition band for $[Pd(NH_3)_4]^{2+}$ was unidentifiable. Reference DRUV−vis spectra of PdO domains supported on purely siliceous Beta under ambient conditions (PdO-Beta) and metallic Pd nanoparticles supported on CHA (Pd^0-CHA) under 5 kPa H_2 in 473 K (Figure 2.1b) showed a single broad band with a maximum near 325 nm. The similarities between these reference spectra and that of the air-treated (473−593 K) as-exchanged Pd-CHA-12(24%)-1.5-298 sample suggest that $[Pd(NH_3)_4]^{2+}$ complexes have converted into Pd agglomerates. DRUV−vis (Figure 2.19, SI) and TPD (Section 2.8.7, SI) data suggest that as-exchanged $[Pd(NH_3)_4]^{2+}$-CHA underwent Pd reduction and agglomeration because of the H_2 formed in situ ca. 500 K (evidence for reduction of Pd with H_2 in Section 2.4.2.1, vide infra), contrary to prior proposals of Pd autoreduction followed by agglomeration in Y zeolites during thermal treatments in air [43], [66]. Additionally, $Pd(NH_3)_4(NO_3)_2$ crystals are reported to melt at 480 K and decompose to Pd agglomerates ca. 500 K [67]. Progressive heating to 723 K in air led to a decrease in

intensity of the 325 nm band and a concomitant increase in intensity of the 500 nm band, which is assigned to d−d transitions of mononuclear Pd^{2+} ligated by zeolite framework oxygen [61], [64], [68], indicating that agglomerated Pd domains progressively converted to mononuclear Pd^{2+} [61]. After the 723 K treatment, the sample was cooled in flowing air to ambient temperature (293 K) before collecting a spectrum that showed three absorption bands centered at 240, 290, and 465 nm, which are, respectively, assigned to charge transfer from zeolitic oxygen to mononuclear Pd^{2+}, absorption from agglomerated or multinuclear Pd species (Pd or PdO), and d−d transitions for mononuclear Pd^{2+} cations bound to the zeolite lattice. Taken together, these in situ DRUV−vis spectra indicate that treatment in air converts mononuclear $[Pd(NH_3)_4]^{2+}$ complexes into agglomerated Pd species en route to forming mononuclear Pd^{2+} sites [69]. Other studies have used different Pd precursors (e.g., $Pd(NO_3)_2$) and also observed Pd agglomeration en route to forming mononuclear Pd^{2+} cations after high temperature air treatments [10], suggesting that Pd agglomeration and redispersion occur irrespective of the choice of Pd precursor used in aqueous-phase methods to prepare Pd-CHA.

In summary, the in situ DRUV−vis data in air provide evidence that mononuclear Pd^{2+} ions in Pd-CHA zeolites predominantly form via solid-state transformation of agglomerated Pd domains, as depicted in Figure 2.2. With increasing temperature, $[Pd(NH_3)_4]^{2+}$ complexes first reduce and agglomerate to form metallic Pd domains caused by reduction with H_2 formed in situ (ca. 500 K). In air, metallic Pd domains then oxidize to PdO (>500 K) [57], which can convert to mononuclear Pd^{2+} at higher temperatures (>600 K). These spectroscopic observations motivate the development of methods to quantify the relative amounts of PdO and exchanged Pd^{2+} ion to clarify the mechanism and the influence of zeolite material properties on this process, as discussed next.

2.4.2 Development of methods to quantify mononuclear Pd ions and PdO on Zeolite supports

Section 2.4.2.1. H_2 TPR of Dehydrated and Hydrated Pd-Zeolites

H_2 TPR has been previously used to characterize the amounts and identities of Pd species exchanged on zeolites [70]. For example, H_2 TPR profiles of air-treated Pd-Y zeolites

contained two discernible reduction features with maximum H_2 consumption rates centered near 273 and 440 K. Homeyer and Sachtler deduced the reduction feature centered near 273 K reflected agglomerated PdO, evidenced by water production and by using a treatment (i.e., 5 kPa H_2 to 623 K, followed by 103 kPa O_2 at 373 K) that purposefully generated PdO domains in Pd-Y [27]. These authors proposed the higher temperature reduction feature centered near 440 K reflected mononuclear Pd^{2+} cations, evidenced by the absence of water production upon reduction and the use of a treatment sequence (i.e., 103 kPa O_2 to 773 K) that generated predominantly mononuclear Pd^{2+} in Pd-Y, likely as Z_2Pd sites [27]. Therefore, H_2 TPR represents a straightforward method to quantify the amounts of agglomerated PdO and mononuclear Pd^{2+} species, assuming equimolar H_2 consumption per Pd.

Figure 2.3 shows a representative H_2 TPR profile of a dehydrated Pd-CHA-15-2.3-298 sample treated in flowing air to 1023 K. The feature at the lowest temperature is attributed to the desorption of Ar (210—260 K) that is physisorbed within microporous void spaces, which gives rise to an apparent H_2 consumption feature measured by TCD, as noted previously [29] and confirmed by its appearance in the H_2 TPR profile of a H-CHA sample (Figure 2.40, SI). A sharp reduction feature near 260—310 K reflects the reduction of agglomerated PdO [29] and was the only observable feature during H_2 TPR of a sample purposefully synthesized to contain only PdO (PdO-CHA-Si-1.4-823; Figure 2.40, SI). H_2 consumption features at higher temperatures (>310 K) reflect mononuclear Pd^{2+} sites that are charge-compensated by framework Al [29]. The sharp H_2 production feature at 320 K reflects decomposition of a palladium-hydride phase that forms via reduction of PdO to metallic Pd domains and their subsequent reaction with H_2 (Figures 2.40 and 2.41, SI) [29], [71]. Reports for H_2 TPR profiles of dehydrated Pd-Y zeolites show two distinct features for agglomerated PdO and mononuclear Pd^{2+} sites; in contrast, the Pd-CHA zeolites studied here showed broader reduction features for mononuclear Pd^{2+} sites that partially overlap with the PdO reduction feature, precluding accurate quantification of these two site types.

This broad H_2 consumption feature for mononuclear Pd^{2+} was also observed for a dehydrated Pd-MOR sample, but exposure to a 1 kPa H_2O stream in balance inert at 284 K prior to performing H_2 TPR measurements altered the peak reduction temperature and sharpened this reduction feature, suggesting that hydration of Pd-zeolites before TPR characterization

could assist in resolving peaks for distinct reduction events [72]. Using mass spectrometry, Lee et al. observed the onset of H_2 reduction of hydrated, mononuclear Pd^{2+} sites coincided with the desorption of water, concluding that adsorbed water inhibited the reduction of Pd^{2+} cations [73]. Therefore, we used a similar H_2 TPR procedure for Pdexchanged zeolites by hydrating mononuclear Pd^{2+} sites in a flowing wet inert stream (1−2 kPa H_2O in balance Ar at 303 K) after high temperature air treatments; full hydration is evidenced by DRUV−vis d−d transition bands that shift from 460 nm for d−d transitions of dehydrated Pd^{2+} cations to 400 nm for d−d transitions of $[Pd(H_2O)_4]^{2+}$ in aqueous solution (Figure 2.20, SI; Table 2.1) [59], [60], [62], and EXAFS spectra that do not show second-shell Pd−Pd or Pd−Al/Si scatter (Figure 2.31, SI) for a sample containing predominantly mononuclear Pd^{2+} cations [2]. Additionally, a PdO reference material (PdO-Beta-Si-1.0-773 and PdO-CHA-Si-1.4-773) did not show observable structural changes by DRUV−vis or XAS when hydrated or dehydrated (Figures 2.21, 2.32, and 2.33, SI). Thus, water exposure at 303 K prior to a H_2 TPR characterization does not influence the relative amounts of PdO or mononuclear Pd^{2+} but changes the coordination of mononuclear Pd^{2+} ions and their solvation away from zeolite framework oxygen [38].

A comparison of H_2 TPR profiles for a dehydrated and hydrated Pd-CHA-15-2.3-1023 sample is shown in Figure 2.3. Profiles for both the dehydrated and hydrated forms of Pdzeolites contain similar temperatures for Ar desorption (<260 K), PdO reduction (290−320 K), and Pd-hydride decomposition (320 K), but the reduction feature for mononuclear Pd^{2+} on the hydrated sample is sharper and appears at higher temperatures (350−410 K). The total H_2 consumption (per Pd) for both the dehydrated and hydrated Pd-CHA-15-2.3-1023 samples were 0.97 and 0.96, yet the estimated fractions of mononuclear Pd^{2+} per total Pd were 0.34 and 0.49, respectively. Attempts to deconvolute overlapping features in the TPR profile of the dehydrated Pd-CHA-15-2.3-1023 sample underestimated the amount of mononuclear Pd^{2+} because part of its reduction feature is hidden beneath the tail of the PdO reduction feature, demonstrating the advantage of hydrating Pd-CHA zeolites prior to H_2 TPR to enable more accurate quantification of mononuclear Pd^{2+} content. Additionally, the broad reduction feature for dehydrated, mononuclear Pd^{2+} reflects a certain degree of site heterogeneity (e.g., in Pd or framework Al structure or configuration) that becomes homogenized

upon hydration of mononuclear Pd^{2+} ion to coordinate them within a more uniform ligand environment. Hydrating Pd-zeolites prior to H_2 TPR also attenuated the apparent H_2 reduction feature caused by Ar desorption because some physisorbed Ar was replaced by water, assisting in resolving the Ar desorption and PdO reduction features. A summary of all Pd speciation and parent material characterization used in this study can be found in Table 2.2.

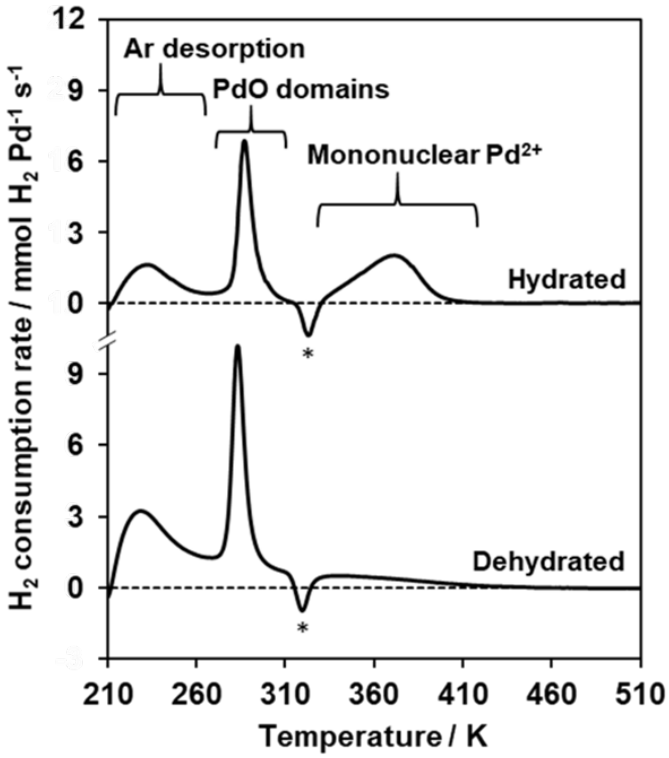

Figure 2.3. H_2 TPR profiles for dehydrated and hydrated Pd-CHA-15-2.3-1023. The samples were pretreated in flowing air to 1023 K (0.167 K s^{-1}) and held for 1 h. Hydrated sample had an intermittent exposure to 1–2 kPa H_2O in balance Ar at 303 K before TPR characterization. Regions for H_2 consumption features are denoted by labeled brackets. Pd-hydride decomposition marked with an asterisk (*).

Table 2.2. Summary of Pd-CHA and Pd-Beta sample characterizations, including Co^{2+} titration, Pd content, air treatment temperature before H_2 TPR quantification[a]

Sample name	Co/Al[b]	Pd_{tot}/Al[c]	Air treatment / K[d]	H_2/Pd_{tot} [e]	Pd_{IE}/Pd_{tot} [f]
Pd-CHA-14(10%)-0.68-823	0.05	0.058	473	1.03	0.30
Pd-CHA-14(10%)-0.68-823	0.05	0.058	823	1.08	0.71
Pd-CHA-14(10%)-0.68-823	0.05	0.058	1023	1.07	0.74
Pd-CHA-14(10%)-1.3-823	0.05	0.11	1023	0.94	0.87
Pd-CHA-14(10%)-2.2-823	0.05	0.19	1023	1.07	0.64
Pd-CHA-12(24%)-0.35-923	0.12	0.025	1023	1.05	1.05
Pd-CHA-12(24%)-1.0-923	0.12	0.074	1023	1.04	1.00
Pd-CHA-12(24%)-1.5-923	0.12	0.11	1023	0.99	0.95
Pd-CHA-12(24%)-2.2-923	0.12	0.16	1023	1.03	0.93
Pd-CHA-12(24%)-3.3-923	0.12	0.24	1023	1.03	0.67
Pd-CHA-12(24%)-3.3-923[g]	0.12	0.24	1023	1.03	0.66
Pd-CHA-9-1.0	0.14	0.053	1023	1.04	1.02
Pd-CHA-9-1.8	0.14	0.097	1023	0.96	0.87
Pd-CHA-9-3.2	0.14	0.17	1023	0.96	0.80
Pd-CHA-15-0.72	0.006	0.064	1023	0.98	0.71

continued on next page

Table 2.2. *continued*

Sample name	Co/Al[b]	Pd_{tot}/Al[c]	Air treatment / K[d]	H_2/Pd_{tot} [e]	Pd_{IE}/Pd_{tot} [f]
Pd-CHA-15-1.2	0.006	0.11	1023	0.94	0.53
Pd-CHA-15-2.3	0.006	0.19	1023	0.97	0.34
Pd-CHA-15-2.3[g]	0.006	0.19	1023	0.96	0.49
Pd-CHA-14(1.0%)-2.7	0.005	0.24	1023	0.73	0.34
Pd-CHA-12(18%)-0.92-923	0.09	0.069	823	0.96	1.00
Pd-CHA-12(18%)-0.92-923[g]	0.09	0.069	850	0.97	1.00
Pd-CHA-12(18%)-3.9-923	0.09	0.29	1023	0.99	0.59
Pd-CHA-11-3.5	0.035	0.24	1023	0.99	0.55
Pd-CHA-11-3.5[g]	0.035	0.24	1023	0.79	0.64
Pd-CHA-13-4.2	0.16	0.33	1023	1.02	0.41
Pd-CHA-13-4.2[g]	0.16	0.33	1023	0.80	0.76
Pd-CHA-30-0.95	0.00	0.17	1023	0.99	0.55
Pd-CHA-Si-1.4-823[g]	–	–	823	0.84	0.00
Pd-Beta-Si-0.6-823	–	–	823	1.04	0.00
Pd-Beta-Si-1.0-823	–	–	823	0.93	0.00
Pd-Beta-13-1.36-823	0.20	0.09	823	0.91	0.75

continued on next page

Table 2.2. *continued*

Sample name	Co/Al[b]	Pd_{tot}/Al[c]	Air treatment / K[d]	H_2/Pd_{tot} [e]	Pd_{IE}/Pd_{tot} [f]
Pd-Beta-13-0.6-823	0.20	0.04	823	1.02	0.78
Pd-Beta-13-0.13-823	0.20	0.009	823	0.99	0.67

[a]Samples are grouped according to common parent zeolite supports.

[b]Quantified using Co^{2+} titration (Section 2.8.4, SI).

[c]Calculated by taking the molar ratio of Pd and Al contents.

[d]Air treatment temperature before H_2 TPR characterization.

[e]Total molar consumption of H_2 for Pd species quantified by H_2 TPR divided by the total molar Pd content.

[f]Molar ratio of exchanged, mononuclear Pd^{2+} (estimated by H_2 TPR) to the total Pd content.

[g]Samples were treated in 1-2 kPa H_2O in balance Ar at 303 K before TPR characterization

The predominant forms of mononuclear Pd^{2+} sites are still debated in the literature because characterizations are performed under a wide range of measurement and treatment conditions, resulting in unknown and variable Pd structures. The H_2 consumption (per Pd) for the majority of hydrated or dehydrated samples after treatment in flowing air (>600 K) in this study was approximately unity (Table 2.2), consistent with the predominant presence of Pd^{2+} [7]. This conclusion is consistent with in situ K- and L_3-edge XANES edge energies reflecting square-planar, oxygen-ligated Pd^{2+} species (Figures 2.34 and 2.35, SI), and d−d transition band locations of DRUV−vis spectra (Figure 2.1). Therefore, the proposed H_2 reduction reactions for divalent Pd species are

$$Z_2Pd(II) + H_2 \leftrightarrow Z_2H_2 + Pd(0) \tag{2.1}$$

$$Z[Pd(II)OH] + H_2 \leftrightarrow ZH + H_2O + Pd(0) \tag{2.2}$$

$$(Pd(II)O)_n + H_2 \leftrightarrow (Pd(II)O)_{n-1} + H_2O + Pd(0) \tag{2.3}$$

Equations 2.1 and 2.2 represent the reduction of mononuclear Pd^{2+} structures proposed previously [34], [38], and Equation 2.3 represents the reduction of agglomerated PdO domains. Homeyer and Sachtler provided indirect evidence for the presence of Z_2Pd in Y zeolites by showing an absence of water formation upon reduction; thus, it is possible that similar 6-MR structures in CHA frameworks could host a Z_2Pd species. IR features upon CO adsorption have been assigned to $[PdOH]^+$ but remain debated as they have also been attributed to Pd^+ [36]. Mei et al. propose that $[Pd{-}O{-}Pd]^{2+}$ species may also form in Pd-zeolites [74], which should result in equimolar H_2 consumption per Pd, but dimeric Pd species were excluded from the proposed reduction reactions because they were not observed in the Pd-CHA-5-1.2-923 sample by EXAFS at ambient conditions (predominance of mononuclear sites reflected in the negligible second-shell scattering in Figure 2.31, SI). In summary, hydration of Pd-exchanged zeolites before H_2 TPR characterization allows for more accurate

quantification of mononuclear and agglomerated Pd species but does not enable resolving distinct mononuclear Pd^{2+} site types.

Section 2.4.2.2. NH_4^+ back-exchange of Pd-exchanged zeolites

Contacting ion-exchanged zeolites in one form (e.g., Pd-form) with aqueous solutions containing other cationic species (e.g., Na^+ , NH_4^+) under conditions that result in stoichiometric completion of cation-exchange reactions (i.e., NH_4^+ backexchange of Pd-form zeolites) enable quantifying the number of ion-exchanged species initially present on the sample via elemental analysis of the equilibrated solution phase [55]. Ogura et al. contacted NaCl solutions with Pd-exchanged MFI and amorphous SiO_2 after air treatment to 773 K, and the supernatant solution of the Pd-MFI mixture contained measurable quantities of Pd, whereas the supernatant of predominantly PdO on silica did not [35]. Further, Ogura et al. observed parity between the amount of Na^+-exchangeable Pd^{2+} and the amount of NO stored (1000 ppm NO in balance He at 323 K, evacuated for 0.5 h, NO stored quantified with TPD) for a series of Pd-exchanged MFI zeolites, concluding that Na^+ selectively exchanges mononuclear Pd^{2+} sites that stoichiometrically bind NO. Additionally, NH_4^+ back-exchange has been proposed to exchange an unknown amount of mononuclear Pd^{2+} sites in Pd-zeolites [9], as inferred by resulting decreases in NO_x storage (per g) [26]. Therefore, both Na^+ and NH_4^+ are reported to exchange mononuclear Pd^{2+}, but the effectiveness of both methods has been inferred indirectly by NO adsorption experiments that assume an equimolar NO/Pd stoichiometry, which conflicts with IR data reporting features at 1886 and 1845 cm^{-1} for dinitrosyl species adsorbed on mononuclear Pd^{2+} sites [75]–[77].

Thus, we characterized air-treated Pd-exchanged zeolites by H_2 TPR to directly quantify mononuclear Pd^{2+} sites and compared these values to the number of NH_4^+-exchangeable Pd^{2+} ions on these samples, and the data are summarized in Figure 2.4. Parity was observed for Pd-Beta zeolites of varying Pd composition. Transmission UV−vis spectra of the supernatant NH_4^+-containing exchange solutions, separated from the solids after the exchange experiment was performed, showed a single absorption band consistent with d−d transitions for $[Pd(H_2O)_x(NH_3)_{4-x}]^{2+}$ (x $\leq$1) (Figure 2.22, SI), demonstrating that the predominant species in solution was mononuclear Pd^{2+}. A model PdO-Beta-Si-1.0-823 material containing predominantly agglomerated PdO domains showed negligible amounts of NH_4^+-exchangeable

Pd^{2+} (0.02 Pd^{2+}/Pd_{tot}), confirming that the NH_4^+ back-exchange protocol used here does not detect PdO. These data provide evidence that both H_2 TPR and NH_4^+ back-exchange can quantify the amount of mononuclear Pd^{2+} in Beta zeolites.

In sharp contrast, Pd-exchanged CHA zeolites did not show parity (Figure 2.4) between the amount of NH_4^+-exchangeable Pd^{2+} and the amount of mononuclear Pd^{2+} measured with H_2 TPR. The amount of NH_4^+-exchangeable Pd^{2+} was consistently lower than that quantified by H_2 TPR, indicating that the NH_4^+-exchange conditions used did not allow equilibration of Pd-CHA samples with NH_4^+-exchange solutions, likely because of barriers to transport solvated Pd^{2+} cations out of small-pore CHA zeolite frameworks into the extra-zeolitic solution phase. Further evidence for this hypothesis was obtained by increasing the concentration of NH_4NO_3 from 1 to 2 M and the exchange temperature from 338 to 363 K for a Pd-CHA-11-0.9-1023 zeolite containing predominantly mononuclear Pd^{2+} sites (Pd_{IE}/Pd_{tot} = 1.0, 85 μmol g^{-1} of mononuclear Pd^{2+}) as measured by H_2 TPR, which resulted in an increase of the back-exchangeable Pd^{2+} content from 5 μmol g^{-1} (Pd_{IE}/Pd_{tot} = 0.06) to 13 μmol g^{-1} (Pd_{IE}/Pd_{tot} = 0.15; Table ??, SI). We note that the increase in back-exchangeable Pd^{2+} at higher NH_4^+-exchange temperatures may also, in part, reflect higher rates of reversible framework hydrolysis that facilitate Pd^{2+} cation diffusion within crystallites [78], [79]. Additionally, increasing the exchange time from 1 to 14 days at 363 K in 2 M NH_4NO_3 increased the amount to 55 μmol NH_4^+-exchangeable Pd^{2+} g^{-1} (Pd_{IE}/Pd_{tot} = 0.65; Table ??, SI), but still did not fully exchange all of the mononuclear Pd^{2+} ions present, highlighting the transport limitations of hydrated Pd^{2+} complexes in CHA zeolites under aqueous exchange conditions at 363 K.

2.4.3 Influence of zeolite framework Al arrangement on stabilizing mononuclear Pd^{2+}

The effects of air treatment temperature on PdO conversion to mononuclear Pd^{2+} sites were first investigated to determine appropriate treatment conditions that maximize the formation of mononuclear Pd^{2+}, to allow studying how zeolite samples with varied material properties influenced the number of such sites that could form. Recent reports showed that hydrothermal treatments (1023 K, 1-10 kPa H_2O in balance air) of Pd-exchanged zeolites

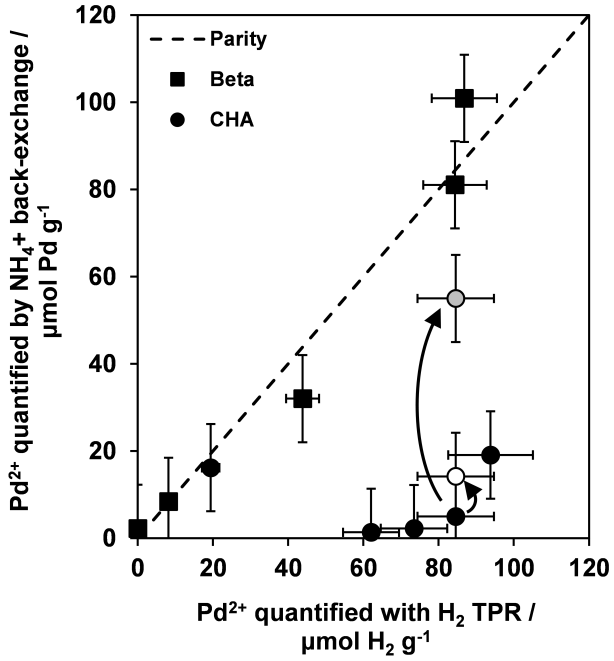

Figure 2.4. Amount of mononuclear Pd^{2+} measured by H_2 TPR plotted against the amount of Pd exchanged by NH_4^+ in Beta (squares) and CHA (circles, black) under aqueous conditions (1 M NH_4NO_3) at 338 K for 1 day. Arrow denotes the same Pd-CHA sample after back-exchange using different conditions: 2 M NH_4NO_3, 363 K for 1 day (open circle) and 14 days (gray circle).

appear to maximize the formation of mononuclear Pd^{2+} sites [10], potentially by favoring the formation of a mobile Pd species that reacts with Brønsted acid sites in zeolites [55], which resemble proposals for PdO redispersion via $Pd(OH)_2$ species on γ-Al_2O_3 [11]. The drawback of using hydrothermal conditions (1023 K, 1–2 kPa H_2O balance air, 24 h) is the potential to hydrolyze framework Al–O bonds [80], [81] leading to zeolite dealumination [82]–[84] and structural collapse [85], which occurred for a high-Al content Pd-CHA-5-1.2-923 sample as evidenced by the loss of crystalline order by XRD (Figure 2.12, SI). Therefore, using hydrothermal conditions to maximize the amount of mononuclear Pd^{2+} may be inadequate for comparing samples and studying the reversibility of redispersion treatments, given that the extent of dealumination and structural collapse likely varies with the bulk and atomic-scale properties of each zeolite sample.

To minimize these structural changes, Pd-zeolites were treated in flowing air to study the influence of temperature on the conversion of agglomerated PdO to mononuclear Pd^{2+}. Asexchanged Pd-CHA-12(24%)-1.5-298 and Pd-CHA-12(18%)- 3.9-298 zeolites containing different Pd contents, but similar framework Al arrangements and densities, were exposed to systematically increasing air treatment temperatures (650−1023 K), with intervening H_2 TPR characterization to quantify the fraction of Pd present as mononuclear Pd^{2+} (Figure 2.5). Treatment to 650 K in flowing air formed some fraction of agglomerated PdO on both samples, corroborating DRUV−vis data that showed that the treatment of mononuclear $[Pd(NH_3)_4]^{2+}$ in air (>400 K) causes Pd agglomeration, but that progressive heating to >600 K in air increased the extent to which PdO converted to mononuclear Pd^{2+} (Figure 2.1). After the H_2 TPR experiment, only metallic Pd is present, consistent with in situ DRUV−vis and XAS under similar conditions (≥473 K, 5 kPa H_2 in balance inert; Figures 2.1, 2.28, 2.29, and 2.36 and Table 2.7); thus, the Pd is metallic prior to the subsequent air treatment. The fraction of agglomerated Pd that converted to mononuclear Pd^{2+} increased systematically with air treatment temperature, evidenced by the decrease in the H_2 consumption upon reduction of agglomerated PdO particles (310 K) and the commensurate increase in H_2 consumption upon reduction of mononuclear Pd^{2+} (370 K). The 1023 K air treatment resulted in almost complete transformation to mononuclear Pd^{2+} for both samples, corroborating reports by Khivantsev et al. on a Pd-CHA-6-1.0-923 sample that showed that non-hydrothermal conditions can convert the majority of PdO to mononuclear Pd^{2+} [2]. XRD characterization of the sample repeatedly cycled between air treatments to 1023 K and H_2 TPR did not show evidence of structural collapse (Figure 2.13, SI), indicating that repeated air treatments to 1023 K do not cause significant structural damage to the zeolite framework. Thus, an air treatment at 1023 K was chosen as a protocol to maximize the formation of mononuclear Pd^{2+} when assessing the influence of zeolite material properties on the conversion of agglomerated PdO domains to mononuclear Pd^{2+}.

The amount of mononuclear Pd^{2+} formed on a Pd-zeolite material is reported to depend on several zeolite material properties such as hydrophobicity [2], bulk Al density [37], and Al arrangement [26], [38], but comparing data among different studies is difficult because samples are often synthesized and treated differently prior to characterization. Here, a series

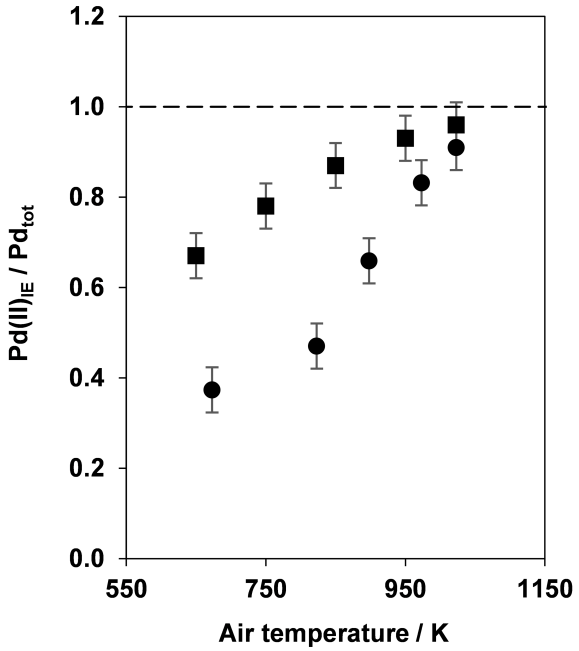

Figure 2.5. Values of $Pd(II)_{IE}/Pd_{tot}$ quantified with H_2 TPR as a function of air pretreatment temperature for Pd-CHA-12(18%)-3.9-298 (circles) and Pd-CHA-12(24%)-1.5-298 (squares; H_2 TPR profiles in Figures 2.42 and 2.43, SI); dashed line denotes the theoretical maximum amount of Pd_{IE}.

of CHA zeolites was synthesized with similar bulk Al density (Si/Al = 9-15) but varied 6-MR paired Al site content [20], [22] (0–28% Al in pairs, Co^{2+}/Al = 0.00–0.14; Table 2.2), and Pd was deposited using incipient wetness impregnation (Pd_{tot}/Al = 0.03–0.25). Pd-CHA samples were treated in flowing air to 1023 K and then characterized with H_2 TPR (Figure 2.6a). At low Pd content (Pd_{tot}/Al < 0.06), the majority of Pd was mononuclear for all samples. PdO domains began forming as Pd contents increased (Pd_{tot}/Al > 0.06), while the amounts of mononuclear Pd^{2+} continued to increase as a function of Pd content. Yet, the Pd_{tot}/Al ratio corresponding to the onset of PdO formation and the amount of cationic Pd formed in intermediate Pd composition ranges (Pd_{tot}/Al = 0.17–0.24) varied with the parent zeolite material studied. Given the similar Pd deposition and treatment procedure, this provides evidence that the bulk Al content (Si/Al) alone cannot be used to quantitatively predict the formation of cationic Pd^{2+} sites, suggesting that the framework Al arrangement in CHA also influences the formation of Pd^{2+} cations.

Previous DFT calculations report that 8-MR structures in zeolites are too large to stabilize certain bare divalent transition metal cations (Co^{2+}, Cu^{2+}, Pd^{2+}) [22], [23], [38], [86] in a square-planar configuration, suggesting that 6-MR paired Al sites (i.e., Co^{2+}-titratable) or nominally isolated Al sites serve as the preferred binding sites for mononuclear Pd^{2+}. Given that the majority of Pd is divalent and mononuclear, we hypothesize two possible mononuclear Pd^{2+} structures of Z_2Pd and ZPdOH, analogous to Z_2Cu and $Z[CuOH]^+$ in Cu-CHA [23]. Figure 2.6 compares the amount of mononuclear Pd^{2+} (per Al) after air treatment to 1023 K as a function of the number of 6-MR paired Al sites (per Al) for Pd-CHA zeolites ($Pd_{tot}/Al = 0.16–0.24$, which correspond to samples that contain a reservoir of PdO) with similar bulk Al density. CHA samples without any 6-MR paired Al sites (i.e., parent materials with $Co^{2+}/Al < 0.01$) stabilized 0.08 mononuclear Pd^{2+} per Al, suggesting that nominally isolated Al sites can stabilize mononuclear Pd^{2+}, proposed to be ZPdOH. IR spectra of H- and Pd-CHA-15(1.2%) samples collected at 473 K in flowing air showed the appearance of an OH stretching feature at 3660 cm^{-1} when Pd was present (Figure 2.45, SI), consistent with DFT-predicted IR stretching frequencies for Pd–OH (ca. 3660 cm^{-1}) potentially stabilized in the 8-MR of CHA [38]. We note, however, that OH groups associated with partial or extraframework Al also appear at 3660 cm^{-1} [87] and such species might form upon high temperature air treatments as was observed on the H-form. Previous attempts to identify as ZPdOH were unsuccessful, likely due to the composition of the Pd-CHA materials tested [38], which contained lower amounts of mononuclear Pd^{2+} than the estimated number of 6-MR paired Al sites on the sample assuming a random Al distribution obeying Löwenstein's rule ($Pd_{tot}/Al = 0.056$, Co^{2+}/Al 0.10 for Si/Al = 15) [23], given that cation siting energies suggest that Z_2Pd is more stable than ZPdOH. Consistent with this interpretation, a Pd-CHA-12(24%)-1.5-1023 material with $Pd_{IE}/Al = 0.10$ did not show an IR peak at 3660 cm^{-1} (Figure 2.46, SI), suggesting that the majority of mononuclear Pd^{2+} is in the form of Z_2Pd. Indeed, CHA zeolites containing larger amounts of 6-MR paired Al sites as quantified by Co^{2+} titration (Figure 2.6b) systematically stabilized larger amounts of mononuclear Pd^{2+}, consistent with thermodynamic calculations that Z_2Pd sites at 6-MR are more stable than ZPdOH after high temperature air treatments.

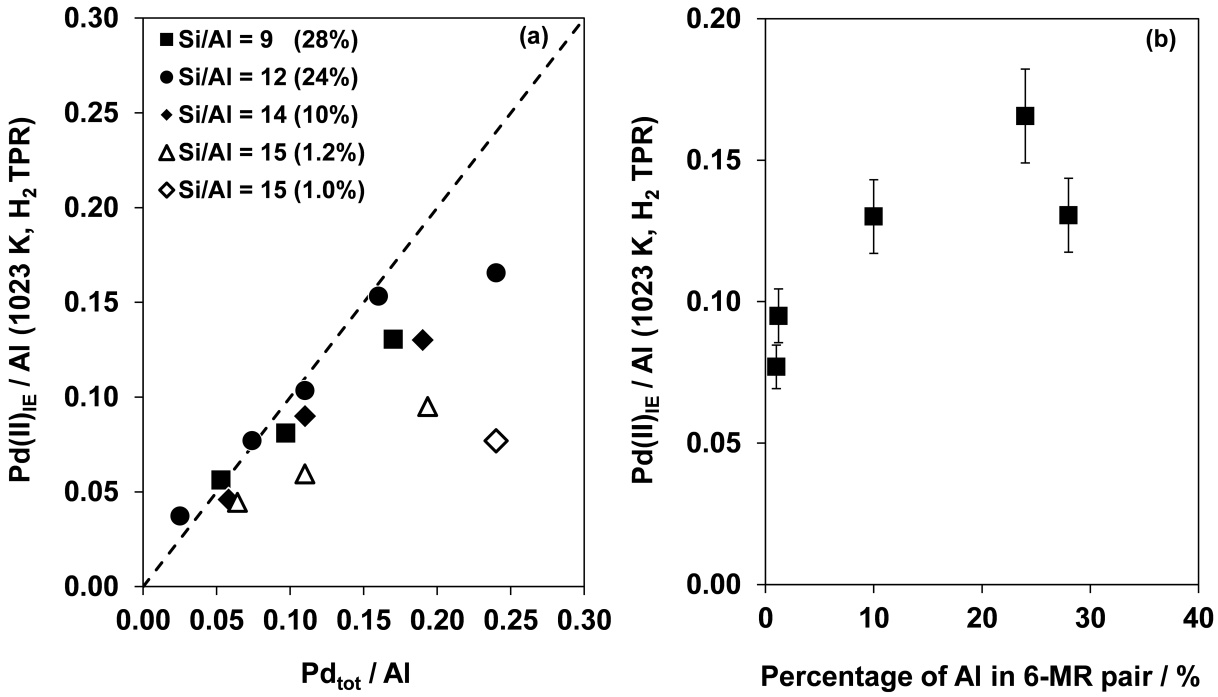

Figure 2.6. A comparison of mononuclear Pd^{2+} to total Pd normalized per total Al measured with H_2 TPR after treatment to 1023 K (0.167 K s^{-1}, 1 h) in flowing air (0.5 cm^3 s^{-1}) for a series of parent CHA samples with similar Al density (Si/Al = 9–15) but varied 6-MR paired Al content (percentage of Al in paired configuration in parentheses). Dashed line represents parity. (b) The amount of mononuclear Pd^{2+} (per total Al) measured with H_2 TPR for Pd-CHA (Pd/Al = 0.16–0.24) samples after treatment to 1023 K (0.167 K s^{-1}, 1 h) in flowing air (0.5 cm^3 s^{-1}) plotted against the percentage of Al in 6-MR paired configurations (per total Al).

Although mononuclear Pd^{2+} cations appear to exchange at both 6-MR paired or isolated Al sites, it remains unclear why PdO domains form before complete exchange of all available Brønsted acid sites. We surmise this is a consequence of the competition between solid-state exchange and Ostwald ripening processes [11], [25], as depicted in Equations 2.4, 2.5, 2.6, 2.7, 2.8, and 2.9.

$$(Pd(II)O)_x + (Pd(II)O)_y \leftrightarrow (Pd(II)O)_{x-1} + (Pd(II)O)_{y+1} \tag{2.4}$$

$$(Pd(II)O)_x + H_2O \leftrightarrow (Pd(II)O)_{x-1} + Pd(II)(OH)_2 \tag{2.5}$$

$$(Pd(II)O)_x + Z_2H_2 \leftrightarrow Z_2Pd(II) + H_2O + (Pd(II)O)_{x-1} \tag{2.6}$$

$$(Pd(II)O)_x + ZH \leftrightarrow Z[Pd(II)OH] + (Pd(II)O)_{x-1} \tag{2.7}$$

$$Pd(II)(OH)_2 + Z_2H_2 + Z_2Pd(II) + 2\ H_2O \tag{2.8}$$

$$Pd(II)(OH)_2 + ZH \leftrightarrow Z[Pd(II)OH] + H_2O \tag{2.9}$$

Equation 2.4 depicts an Ostwald ripening process, wherein two PdO particles exchange a PdO equivalent. Equation 2.5 is a hypothesized reaction to form a mobile Pd species wherein water reacts with a PdO surface to liberate a neutral, mobile $Pd(OH)_2$ species [11]. Equations 2.6, 2.7, 2.8, and 2.9 are proposed surface reactions of two types of mobile Pd species (i.e., $(PdO)_x$ and $Pd(OH)_2$) with two different Al arrangements, identified earlier as potential zeolite lattice binding sites. The surface reactions of mobile Pd species with Brønsted acid sites [55] would require invoking PdO decomposition to mobile Pd species that traverse zeolite crystallites. Reports from Moliner et al. observed intercrystallite transport of mobile Pd and Pt species from silica to zeolite supports, but the factors that influence the amounts of mobilized Pd species and their diffusion distances remain unclear [25]. Given that high Pd content zeolite samples ($Pd_{tot}/Al > 0.16$; Figure 2.6a) contain detectable amounts of agglomerated PdO, despite the availability of Brønsted acid sites that should have formed mononuclear Pd^{2+} ions (via Equations 2.6, 2.7, 2.8, and 2.9), the mobile Pd species formed from PdO particles are also able to attach to existing PdO particles (via Equations 2.4 and 2.5), indicating that the relative spatial distributions of PdO particles and available Brønsted acid sites influence the extent of Pd redispersion into mononuclear Pd^{2+} sites.

2.4.4 Effects of the spatial distribution of agglomerated Pd on the conversion to mononuclear Pd^{2+}

The interconversion of agglomerated Pd domains to mononuclear Pd^{2+} was investigated on a representative Pd-CHA-12(24%)-3.3-298 sample by treatment in sequential cycles of different air treatment temperatures and H_2 TPR characterization (Table 2.3; profiles in Figure 2.44, SI). The sample was first treated in flowing air to 773 K, and the amount of mononuclear Pd^{2+} per Al was characterized to be 0.11 (cycle 1). After H_2 TPR characterization (573 K, 5 kPa H_2 in Ar), the majority of Pd is agglomerated and metallic, which serves as the initial state of Pd before treatment in the next air cycle. The reduced sample was then treated again in air to 673 K (cycle 2), and the amount of mononuclear Pd^{2+} was within error of that formed after cycle 1, suggesting that this amount of mononuclear Pd^{2+} can be reversibly generated in air at a lower temperature. To ensure that repeated air treatments do not systematically influence the amount of mononuclear Pd^{2+} formed, cycles 3 and 4 were performed at a constant temperature of 773 K, and the amount of mononuclear Pd^{2+} per Al was again within error of cycle 1, further demonstrating the reversible interconversion of agglomerated, metallic Pd to mononuclear Pd^{2+}. We also note that 1−2 kPa H_2O was added to the air stream during cycle 4 to determine if water increases the amount of mononuclear Pd^{2+} as suggested in literature reports,14,84 but water introduction did not affect the amount of mononuclear Pd^{2+} formed at 773 K.

The sample was next treated to 1023 K in flowing air and characterized to contain 0.16 mononuclear Pd^{2+} per Al (cycle 5), consistent with earlier observations (Figure 2.5) that increasing the air treatment temperature increased the extent of PdO conversion to mononuclear Pd^{2+}. Cycle 6 used an air treatment temperature of 773 K, and the amount of mononuclear Pd^{2+} per Al was 0.15, which is within error of the value after cycle 5 but outside of measurement error after cycles 1−4. This observation suggests that Pd-CHA zeolites retain memory of their exposure to the highest air treatment temperature after additional redispersion cycles. A final air treatment to 1023 K (cycle 7) yielded identical amounts of mononuclear Pd^{2+} as after cycles 5 and 6, further corroborating that consecutive air treatments to the same temperature do not increase the amount of mononuclear Pd^{2+}.

Table 2.3. Summary of H_2 TPR and air treatment cycling experiments of Pd-CHA-12(24%)-3.3-298

Cycle	Air temperature / K[a]	H_2/Pd_{tot} [b]	PdO/Pd_{tot} [c]	$Pd(II)_{IE}/Pd_{tot}$ [d]	$Pd(II)_{IE}/Al$[e]
1	773	0.97	0.52	0.45	0.11
2	673	0.94	0.54	0.45	0.10
3	773	0.99	0.50	0.49	0.12
4	773[f]	0.96	0.50	0.47	0.11
5	1023	1.01	0.35	0.66	0.16
6	773	0.99	0.36	0.63	0.15
7	1023	1.03	0.37	0.66	0.16

[a]Air treatment temperature (600 K h^{-1}, hold 1 h) before H_2 TPR characterization.
[b]Molar hydrogen consumption normalized to Pd content.
[c]Amount of agglomerated PdO determined from H_2 TPR analysis normalized by the total Pd content.
[d]Amount of mononuclear Pd^{2+} quantified with H_2 TPR normalized by the total Pd content.
[e]Amount of mononuclear Pd^{2+} normalized to the total Al content.
[f]Sample was treated in 1–2 kPa H_2O in balance air.

The observed hysteresis in the mononuclear Pd^{2+} content as a function of air treatment temperature demonstrates that the interconversion between metallic Pd domains and dispersed Pd^{2+} ions after air treatments is not a fully reversible phenomenon. The first air treatment to 773 K (cycle 1) generated an initial distribution of mononuclear Pd^{2+} and agglomerated PdO domains, with the majority of Pd likely located near crystallite surfaces given the diffusion restriction of $[Pd(NH_3)_4]^{2+}$ complexes in CHA zeolites under aqueous conditions. After the subsequent H_2 TPR characterization, all divalent Pd species were reduced with H_2 and agglomerated (via Brownian motion [88]) with other reduced Pd species to form aggregates located within or external to each crystallite. Cycles 2–4 resulted in forming similar amounts of mononuclear Pd^{2+} and agglomerated PdO domains, suggesting that samples initially contained similar metallic Pd particle sizes and spatial distribution before treatment in flowing air. Cycle 5 (1023 K) resulted in higher amounts of mononuclear Pd^{2+}, indicating that the metallic Pd particle sizes and spatial distributions formed after H_2 TPR were different from those after cycles 1–4, likely because more mononuclear Pd^{2+} sites formed deeper within zeolite crystallites. The change in spatial distribution was evident after performing cycle 6, where the lower air treatment temperature of 773 K still resulted in 0.15 mononuclear Pd^{2+} per Al, which was higher than the values of 0.11 formed after cycles 1–4. If metallic Pd domains preferentially formed at extracrystalline surfaces after H_2 TPR, then cycle 6 should have resulted in the same amount of cationic Pd after an air treatment to 773 K, as observed in cycles 1–4. This suggests that the single exposure to the higher temperature air treatment at 1023 K treatment resulted in more homogeneous dispersion of Pd throughout zeolite crystallites; thus, subsequent H_2 reduction treatments yielded smaller average Pd particle sizes because a larger fraction of Pd particles were located within crystalline microporous voids.

Changes to the size and spatial distribution of metallic Pd particles between extracrystalline and intraporous locations after H_2 TPR were assessed quantitatively by Pd dispersion measurements via O_2 titration. A Pd-CHA-12(24%)-2.2-298 material was treated under similar conditions as the H_2 TPR and air cycling experiment (Figure 2.7); exposure to three consecutive cycles of treatment to 773 K (0.83 K s^{-1}, 1 h) in 103 kPa O_2 and then treatment to 573 K (0.83 K s^{-1}, 1 h) in 103 kPa H_2 resulted in a reversible measurement of the Pd

dispersion of 35 ± 2%. The sample was exposed to three more consecutive cycles, but at a higher temperature O_2 treatment of 1023 K, which resulted in a larger Pd dispersion of 55 ± 1% corresponding to a smaller average Pd particle size. Finally, two more cycles were performed with an O_2 treatment temperature of 773 K, and the Pd dispersion was the same (55 ± 1%) as that after the earlier O_2 treatment to 1023 K. These chemisorption data provide corroborating evidence of an irreversible change in Pd particle size after the air treatment to 1023 K. This irreversible change in Pd particle size persists even after Pd-CHA samples are exposed to an intervening reduction treatment in H_2 to 573 K; however, when samples are instead treated in a flowing H_2 to 1023 K, the resulting Pd dispersion was 3% because these more aggressive reduction conditions formed large Pd particles on external crystallite surfaces (Figure 2.47, SI).

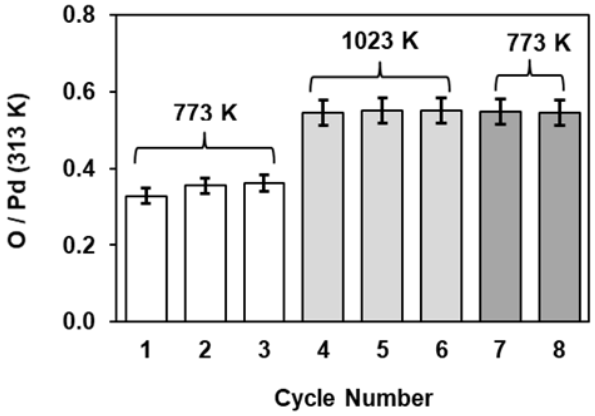

Figure 2.7. O_2 chemisorption (313 K; mol O adsorbed per Pd_{tot}) cycling experiments of a Pd-CHA-12(24%)-2.2-298 sample. Sample was sequentially treated in O_2, followed by reduction H_2 at 573 K, and then O_2 adsorption at 313 K. The O_2 pretreatment temperatures were 773 K (Cycles 1-3, white), 1023 K (Cycles 4-6, light gray), and 773 K (Cycles 7-8, dark gray).

Along with H_2 TPR and O_2 chemisorption characterization data, the change in Pd spatial distribution within crystallites was also investigated with a diffusion-limited NH_4^+ backexchange experiment. Two Pd-CHA zeolite samples were treated in air to either 823 or 1023 K and then characterized with H_2 TPR and NH_4^+ back-exchange (Table 2.11, SI). On a Pd-CHA sample predominantly containing mononuclear Pd^{2+} sites (Pd-CHA-11-0.9-823; Pd_{IE}/Pd_{tot} = 1.0, 85 μmol cationic Pd^{2+} g^{-1} by H_2 TPR), increasing the air treatment temperature from

823 to 1023 K resulted in a lower amount of NH_4^+ backexchangeable Pd^{2+} (14 compared to 5 μmol NH_4^+ backexchangeable Pd g^{-1}). On a Pd-CHA material (Pd-CHA12(24%)-2.2-823) containing some amount of PdO after air treatments to both 823 K (PdO/Pd_{tot} = 0.42) and 1023 K (PdO/Pd_{tot} = 0.10), a larger amount of back-exchangeable Pd^{2+} was present after the 823 K than after the 1023 K treatment (32 compared to 18 μmol cationic Pd^{2+} g^{-1}), despite the fact that the total mononuclear Pd^{2+} content was higher after the 1023 K treatment (190 μmol cationic Pd^{2+} g^{-1}) than after the 823 K treatment (120 μmol cationic Pd^{2+} g^{-1}). Thus, both samples contained lower amounts of NH_4^+-exchangeable Pd^{2+} after an air treatment to 1023 K than that at 823 K. Given the diffusion-limited nature of NH_4^+-back-exchange of Pd-CHA, mononuclear Pd^{2+} sites located near extracrystalline surfaces are more likely to be exchanged with NH_4^+. Therefore, the treatment of as-exchanged Pd-CHA materials in air (823 K) would cause Pd to agglomerate and then redisperse, with mobile Pd species preferentially exchanging at framework Al sites nearest to extracrystalline surfaces but more uniformly throughout CHA crystallites when treated to higher temperatures (1023 K). XPS (3—5 nm penetration depth) characterizations corroborated this proposal by showing a quantitative decrease in measurable Pd contents with increasing air temperatures (Section 2.8.13, SI). Altogether, these data indicate that high temperature air treatments (1023 K) shift the spatial distribution of Pd further into the interior of zeolite crystallites, causing a higher fraction of Pd cations to reversibly form from agglomerated Pd domains upon a subsequent air treatment at lower temperatures, as depicted in Figure 2.2.

2.5 Conclusions

A suite of quantitative and qualitative characterization techniques was used to study the influence of treatment conditions and zeolite material properties on the interconversion between agglomerated Pd domains and mononuclear Pd^{2+} species in CHA zeolites, which have received consideration for passive NO_x adsorption (PNA) applications in low-temperature automotive NO_x abatement. In situ DRUV—vis and Pd K-edge EXAFS spectra showed that as-exchanged Pd-CHA zeolites contain predominantly mononuclear $[Pd(NH_3)_4]^{2+}$ complexes and that subsequent treatment in flowing air resulted in agglomeration to metallic

Pd domains (593 K), followed by oxidation to agglomerated PdO domains and redispersion into mononuclear Pd^{2+} cations at higher temperatures (>723 K). Thermal treatments of as-exchanged $[Pd(NH_3)_4]^{2+}$-CHA revealed in situ generation of H_2, likely from decomposition of adsorbed ammonia species, as a pathway for the initial agglomeration of Pd species to metallic domains, suggesting that strategies to remove ammonia from Pd-zeolites prior to thermal treatments may suppress reduction and agglomeration to metallic Pd domains. Progressive treatment in flowing air to 723 K caused aggregated Pd domains to oxidize to PdO prior to forming Pd^{2+} sites, revealing that solid-state exchange processes are a dominant pathway by which mononuclear Pd^{2+} ions form in Pd-CHA zeolites during high temperature air treatments.

The relevance of solid-state Pd exchange and aggregation processes motivated the development of methods to accurately quantify and characterize the structures of aggregated and mononuclear Pd species in CHA zeolites after exposure to various treatments. In the case of H_2 TPR, hydration of mononuclear Pd^{2+} ions in Pd-zeolites (1−2 kPa H_2O, 303 K) delayed the onset temperature of Pd^{2+} reduction until H_2O desorption occurred (ca. 350 K), allowing better resolution and thus more accurate quantification of this reduction feature from that for PdO reduction. The number of mononuclear Pd^{2+} ions measured by H_2 TPR was similar to that measured by NH_4^+ back-exchange for large-pore Pd-Beta zeolites, yet was significantly higher than measured by NH_4^+ back-exchange for small-pore Pd-CHA zeolites, revealing the restricted transport of hydrated Pd^{2+} complexes in the CHA framework topology under the conditions studied. The structures of mononuclear Pd^{2+} ions were identified by systematically varying the fraction of paired framework Al sites (i.e., two Al sites in a 6-MR) in CHA zeolites of similar bulk Al density (Si/Al = 9–15). CHA zeolites that contained majority 6-MR isolated Al sites formed ZPdOH species, as suggested previously by theory and observed experimentally by an IR OH stretching feature at 3660 cm^{-1} [38]. At similar bulk Pd contents (Pd_{tot}/Al = 0.17–0.24), the amount of mononuclear Pd^{2+} sites formed on Pd-CHA samples systematically increased with their paired Al content, consistent with prior DFT calculations that suggest that Z_2Pd sites are more thermodynamically stable than ZPdOH sites [38].

Increasing the air treatment temperature (650–1023 K) systematically increased the amount of Pd^{2+} ion sites that were formed, a consequence of redistributing Pd species to regions located further in the interior of zeolite crystallites that contained higher numbers of Brønsted acid sites relative to PdO. Thus, the fraction of mononuclear Pd^{2+} ions that reversibly formed on a Pd-CHA sample were higher after air treatments to 1023 K than to 773 K and were preserved after a single exposure to 1023 K even with subsequent H_2 reduction and air treatment at a lower temperature of 773 K. These observations are consistent with literature proposals that higher NO_x storage (per total Pd) under PNA conditions can be achieved after Pd-zeolites are treated in air to higher temperatures (i.e., 1023 K) [10], [14], [44], [89]. Additionally, oxidation treatments of Pd-CHA at higher temperatures (1023 K relative to 773 K) facilitated Pd dispersion deeper inside CHA crystallites, resulting in the formation of smaller metallic Pd particles after a subsequent reduction treatment in H_2 at 573 K because intracrystalline void spaces limit the sizes of confined Pd particles relative to those that form at unconfined extracrystalline surfaces. These findings are consistent with the lower amounts of diffusion-limited NH_4^+ back-exchangeable Pd^{2+} ions quantified in Pd-CHA after air treatment to 1023 K and with XPS data that revealed Pd depletion from crystallite surfaces.

We conclude that synthetic and treatment methods that more uniformly distribute Pd species throughout zeolite crystallites result in Pd-zeolites that contain higher amounts of mononuclear Pd^{2+} ions, which are the purported NO_x storage sites for low-temperature PNA applications. The more homogeneous Pd spatial distribution in CHA zeolites formed after high-temperature air treatments (e.g., 1023 K) allows regeneration in air at lower temperatures (e.g., 773 K) to redisperse the agglomerated Pd domains that form after exposure to mild reducing conditions (e.g., 573 K in H_2) but not those that form after exposure to more aggressive reducing conditions (e.g., 1023 K in H_2). These findings highlight important considerations for reactions catalyzed by metal-zeolites in general given the well-documented effects of metal spatial distribution on rates, selectivity, and stability [90], [91] and for NO_x adsorption by Pd-zeolites specifically given the deactivation mechanism involving Pd sintering in the presence of reductants (e.g., H_2, CO) [5]. Improved mechanistic understanding of how agglomerated domains and mononuclear sites interconvert in metal-zeolites and how

they depend on zeolite material properties (e.g., hydrophobicity [2], framework Al density and arrangement, crystallite size) promises to provide new strategies in material design to facilitate metal redispersion into ion sites upon regeneration treatments. Specifically, synthesis methods that preferentially segregate framework Al near extracrystalline surfaces and arrange them locally in proximal configurations will result in minimizing distances between aggregated Pd domains and the preferred lattice binding sites for Pd^{2+} ions, thereby generating zeolite supports that can increase the amount of mononuclear Pd^{2+} ions that form after regeneration treatments. These findings highlight the dominant role of solid-state ion-exchange processes in the redispersion of agglomerated metal and metal oxide domains into mononuclear ion sites and the dependence of such processes on bulk and atomic-scale properties of the zeolite support, in contrast to solution-phase exchange and deposition processes performed under conditions that enable facile transport and unrestricted access of solvated metal precursors to the interior of zeolite crystallites.

2.6 Acknowledgements

The authors acknowledge the financial support from the Department of Energy, Energy Efficiency and Renewable Energy (DE-EE0008213). The authors thank the technical support of 9-BM and 10-BM staff at the Advanced Photon Source in Argonne National Lab during XAS characterization. The use of the Advanced Photon Source is supported by the U.S. Department of Energy, Office of Science, and Office of Basic Energy Sciences, under Contract no. DE-AC02-06CH11357. MRCAT operations and beamlines are supported by the Department of Energy and the MRCAT member institutions. The authors thank all members of our collaborative research team from the University of Kentucky, the University of California Berkeley, Ford Motor Company, the Oak Ridge National Laboratory, and BASF for helpful technical discussions. The authors additionally thank Casey B. Jones (Purdue) for his critical review of this manuscript and Brian Bayer (Purdue) for assistance with CHA zeolite synthesis. The authors also thank Sachem, Inc. for providing the organic structure-directing agent used to synthesize CHA zeolites. Microscopy research was supported by both the Center for Nanophase Materials Sciences (CNMS), which is sponsored by the Scientific

User Facilities Division, Office of Basic Energy Sciences, U.S. Department of Energy and the Department of Energy, Office of Nuclear Energy, Fuel Cycle R&D Program, and the Nuclear Science User Facilities (using instrumentation FEI Talos F200X S/TEM). The authors also thank Shawn K. Reeves for assistance with TEM sample preparation. This manuscript has been authored by UTBattelle, LLC, under contract DE-AC05-00OR22725 with the U.S. Department of Energy (DOE). The U.S. government retains and the publisher, by accepting the article for publication, acknowledges that the U.S. government retains a nonexclusive, paid-up, irrevocable, worldwide license to publish or reproduce the published form of this manuscript, or allow others to do so, for U.S. government purposes. DOE will provide public access to these results of federally sponsored research in accordance with the DOE Public Access Plan (http://energy.gov/downloads/doe-public-access-plan).

2.7 Notes

While this article is believed to contain correct information, Ford Motor Company (Ford) does not expressly or impliedly warrant, nor assume any responsibility, for the accuracy, completeness, or usefulness of any information, apparatus, product, or process disclosed, nor represent that its use would not infringe the rights of third parties. Reference to any commercial product or process does not constitute its endorsement. This article does not provide financial, safety, medical, consumer product, or public policy advice or recommendation. Readers should independently replicate all experiments, calculations, and results. The views and opinions expressed are of the authors and do not necessarily reflect those of Ford. This disclaimer may not be removed, altered, superseded or modified without prior Ford permission. The authors declare no competing financial interest.

2.8 Supporting information

2.8.1 Zeolite synthesis procedures

The broad material compositional space studied here required using different zeolite synthesis procedures. Samples synthesized using similar procedures (i.e., hydroxide mediated, fluoride mediated, and zeolite interconversion) are grouped together and differentiated

by the final Si/Al of the solid material as characterized by elemental analysis (atomic absorption spectroscopy (AAS) or inductively coupled plasma-optical emission spectroscopy (ICP-OES)) and the number of 6-MR paired Al sites measured by Co^{2+} titration (Section 2.8.4) [22].

All samples are referred to as F-CHA-A(X%)-B-C where F denotes the dominant cation or metal form (e.g., NH_4, Na, H, Pd, PdO, $[Pd(NH_3)_4]^{2+}$, Co), A denotes the solid Si/Al ratio (or 'Si' for purely siliceous materials), B denotes the Pd wt%, and C denotes the highest air temperature treatment (in K) that the sample was exposed to before characterization. Some parent zeolite materials have the same Si/Al ratio, so they will be differentiated by the percentage of Al in 6-MR configurations (determined by Co^{2+} titration) using the '(X)' portion of the sample code.

Hydroxide-mediated CHA synthesis

CHA zeolites synthesized in hydroxide media followed the report of Di Iorio and Gounder [20]. Trimethyladamantylammonium hydroxide (TMAdaOH, 25 wt%, Sachem) and deionized water (18.2 MΩ cm) were homogenized in a perfluoroalkoxy alkane (PFA) container (Savillex Corporation) with a magnetic Teflon stir bar under ambient conditions for 0.25 h. Next, the Al source, either $Al(OH)_3$ (98 wt%, SPI Pharma) or aluminium isopropoxide ($Al(i\text{-}pro)_3$, 98 wt%, Sigma-Aldrich), and NaOH pellets (98 wt%, Alfa Aesar) were mixed until completely dissolved. Finally, Ludox HS-40 (40 wt%, Sigma Aldrich) was added and homogenized for 2 hours. The molar water ratio in Table 2.4 includes the water content from TMAdaOH and Ludox HS-40 solutions. The mixtures were loaded into Teflon-lined metal autoclaves, sealed under autogenous pressure, and rotated in a forced convection oven at 433 K for at least 6 days.

Table 2.4. Gel molar compositions used for hydroxide-mediated CHA zeolite syntheses

Sample characterization		**Molar ratios in synthesis gel**					
Si/Al	Co/Al	SiO_2	$Al(OH)_3$	Al(i-pro)$_3$	TMAdaOH	Na	H_2O
15	0.006	1.0	0.067	0.00	0.50	0.00	44
11	0.035	1.0	0.067	0.00	0.50	0.00	44
14	0.05	1.0	0.067	0.00	0.25	0.25	44
13	0.16	1.0	0.067	0.00	0.25	0.25	44
12	0.09	1.0	0.00	0.067	0.25	0.25	44
9	0.14	1.0	0.00	0.067	0.25	0.25	44

FAU-to-CHA interzeolite conversion

The CHA-5 sample was synthesized following previously reported methods [23], [46], [47], [92]. The final synthesis gel molar ratio was 1 SiO_2/ 0.066 Al/ 0.20 TMAdaOH/ 0.34 Na/ 26 H_2O. First, sodium silicate (Sigma Aldrich), NaOH (98 wt%, Alfa Aesar) and deionized water were mixed in a PFA container with a magnetic stir bar under ambient conditions for 0.25 h. Next, a FAU sample sourced from Zeolyst (CBV100, NH_4-form) was added and mixed for 0.25 h before adding TMAdaOH (25 wt%, Sachem). The total mixture was homogenized for an additional 2 h under ambient conditions, then sealed in Teflon-line metal autoclaves. The vessels were rotated in a forced convection oven at 433 K for 11 days.

Fluoride-mediated CHA and Beta syntheses

Two Al-CHA zeolites were synthesized in fluoride media following literature reports [48], [49]. Under ambient conditions, Al_2O_3 (99.5 wt%, Alfa Aesar) and TMAdaOH (25 wt%, Sachem) were stirred in a PFA container with a magnetic Teflon stir bar for 0.25 h. Next, tetraethylorthosilicate (TEOS, 98 wt%, Sigma-Aldrich) was added, and the solution was homogenized in a sealed vessel for 2 h. Then, ethanol (200 proof, Koptec) was added to the solution, and the mixture was left uncapped until all ethanol evaporated. Additional deionized water was added so that the desired water-to-silica molar ratio in the final mixture would be achieved upon aqueous HF addition. Finally, HF acid (48 wt%, Sigma-Aldrich) was added dropwise with intermittent stirring using a Teflon stir rod. [Caution: working with concentrated HF acid is extremely dangerous; stringent safety procedures, personal protective equipment, and engineering controls should be in place.] The mixtures were loaded into Teflon-lined, stainless steel autoclaves, sealed under autogenous pressured, and rotated in a forced convection oven for at least 6 days at 433 K.

The purely siliceous CHA zeolite was synthesized by reproducing the procedure used by Di Iorio and Gounder [20]. The final synthesis solution molar ratio was 1 SiO_2/ 0.5 TMAda/ 0.5 HF/ 3 H_2O. TEOS (98 wt%, Sigma-Aldrich) and TMAdaOH (25 wt%, Sachem) were mixed in an open PFA container under ambient conditions with a magnetic Teflon stir bar until the hydrolysis of TEOS to form ethanol was complete. After evaporation of ethanol

Table 2.5. Gel molar compositions in the Al-containing, fluoride-mediated CHA syntheses

Sample characterization		**Molar ratios in synthesis gel**				
Si/Al	Co/Al	SiO_2	Al	TMAdaOH	HF	H_2O
14	0.005	1.0	0.050	0.50	0.50	3
30	0.000	1.0	0.017	0.50	0.50	3

and water, deionized water was added to achieve the target molar ratio, accounting for water in HF addition step. Next, HF acid (48 wt%, Sigma-Aldrich) was added dropwise while intermittently mixing with a Teflon stir rod. The mixture was left open to evaporate remaining HF for 0.5 h before sealing in Teflon-lined steel autoclaves. The autoclaves were rotated in forced convection ovens controlled to 423 K for 40 h.

The purely siliceous Beta zeolite was synthesized similar to the procedure of Camblor et al [93]. The final synthesis solution molar ratio was 1 SiO_2/ 0.54 TEAOH/ 0.54 HF/ 7.25 H_2O. First, tetraethylammonium hydroxide (TEAOH, 40 wt%, Sigma Aldrich) and TEOS (98 wt%, Sigma-Aldrich) were homogenized with a magnetic Teflon stir bar in an open PFA container without a lid to evaporate ethanol produced from the hydrolysis of TEOS. After the hydrolysis was complete, deionized water was added to reach the target molar ratio, accounting for water added during HF step. HF (48 wt%, Sigma-Aldrich) was added dropwise while stirring with a Teflon stir rod. The HF-containing synthesis was left open to evaporate residual HF for 0.5 h before sealing in Teflon-line metal autoclaves. The synthesis mixture was rotated in a forced convection oven controlled to 413 K for 6 days.

2.8.2 Powder X-ray diffraction patters

Ex situ powder X-ray diffraction (XRD) patterns were collected with a Rigaku Smart-Lab X-ray diffractometer using a Cu Kα radiation source (λ = 0.154 nm). XRD patterns were compared to both known reference materials and simulated patterns reported by the International Zeolite Association [94].

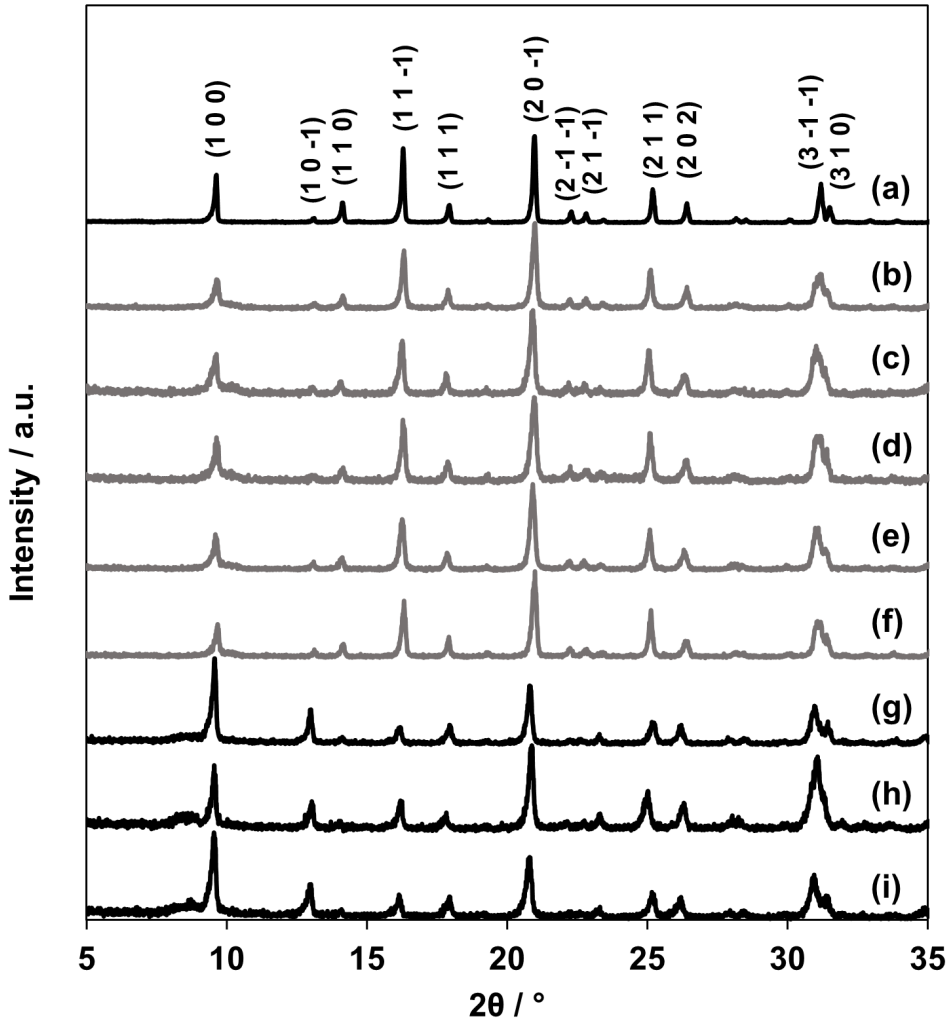

Figure 2.8. Ex situ XRD patterns of 8 independent zeolite syntheses of the same gel composition, before mixing these small batches to form one large batch of CHA-14(10%). Pattern (a) is for a reference Si-CHA material, previously air-treated to 853 K for 10 h to remove occluded organic content. Middle gray patterns (b-f) are of as-synthesized CHA-14(10%) samples. Top black patterns (g-i) are of washed (acetone, water) and air-treated (853 K, 10 h) Na-CHA-14(10%) samples. Patterns are offset vertically for clarity. Parentheses above peaks denote diffraction indices of CHA zeolites [95].

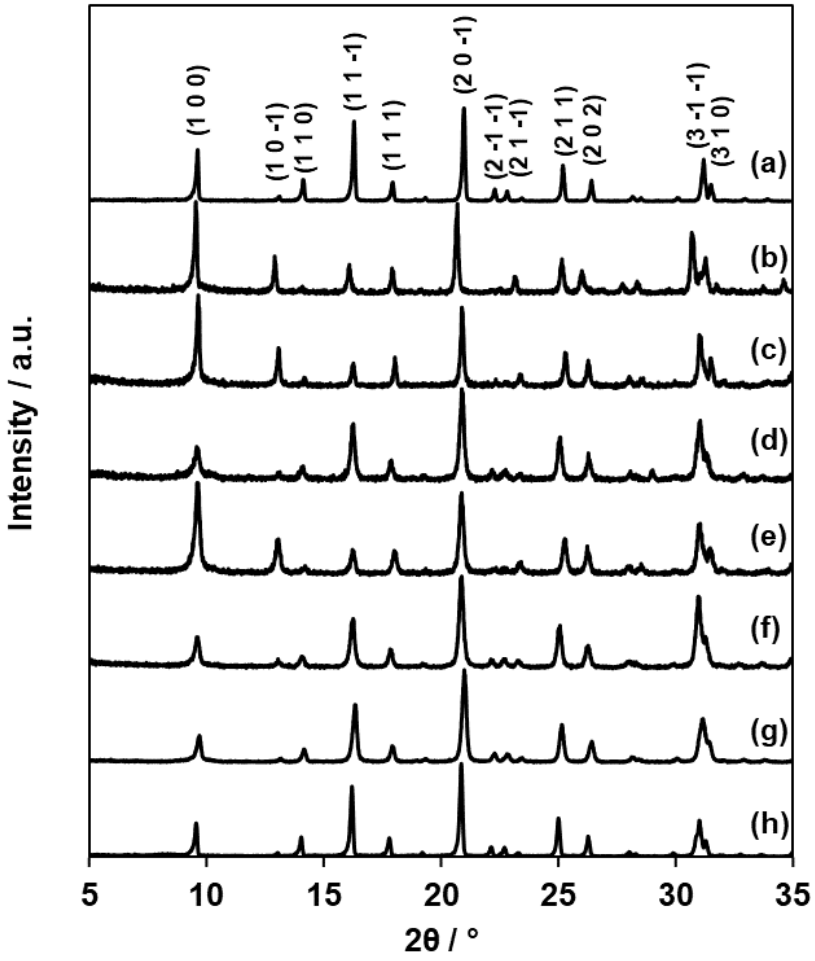

Figure 2.9. Ex situ XRD patterns of parent CHA zeolites: (a) Si-CHA, (b) Na-CHA-5, (c) Na-CHA-11(7%), (d) Na-CHA-13(32%), (e) Na-CHA-12(18%), (f) Na-CHA-15(1.2%), (g) Na-CHA-9(28%), and (h) Na-CHA-14(1.0%). Patterns are offset vertically for clarity. Parentheses above peaks denote diffraction indices of CHA zeolites [95].

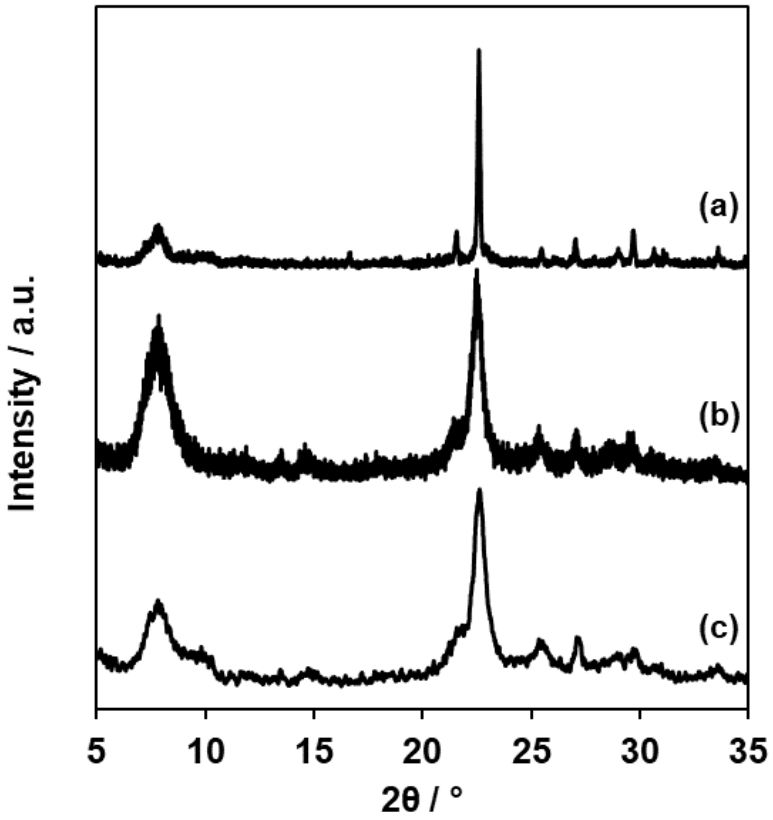

Figure 2.10. Ex situ XRD patterns of (a) purely siliceous Beta (Beta-Si), (b) NH_4-Beta (CP814E, Zeolyst, Si/Al = 12.5), and (c) Pd-Beta-12.5-1.4-823. Patterns are offset vertically for clarity.

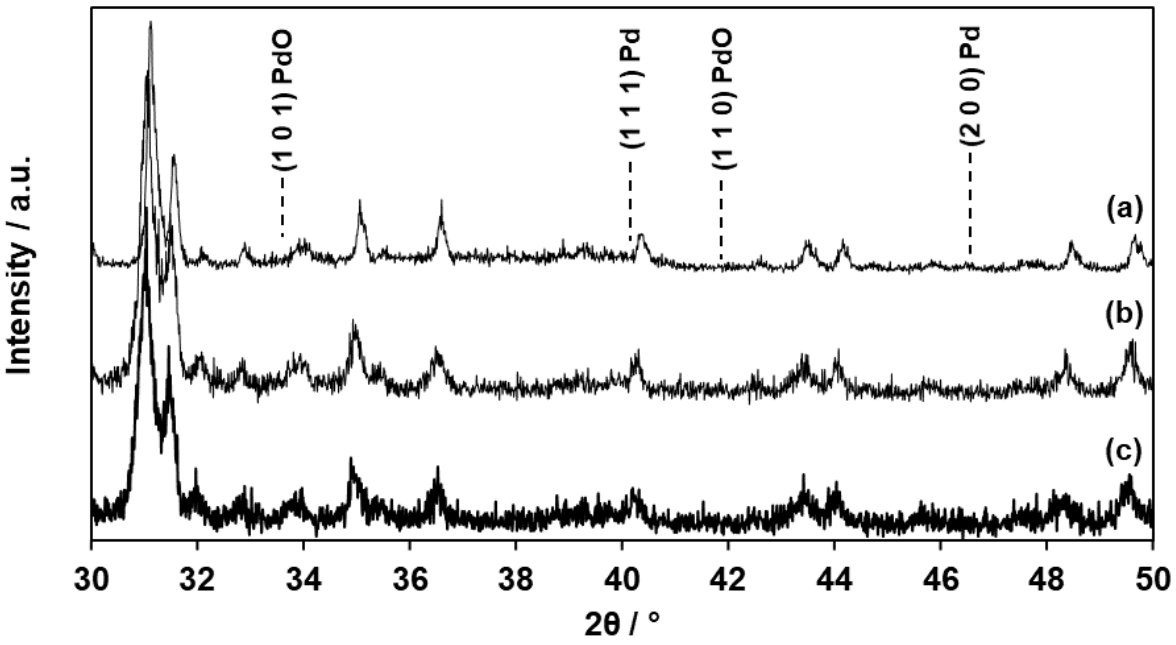

Figure 2.11. Ex situ XRD patterns of (a) PdO-CHA-Si-1.4-823, (b) Pd-CHA-14(10%)-0.7-823, and (c) NH_4-CHA-14(10%). Diffraction peaks locations and indices are listed for agglomerated PdO and Pd domains [96]. Patterns are offset vertically for clarity. See Figure 2.48 for STEM characterization of Pd particle sizes for Pd-CHA-14(10%)-0.7-823.

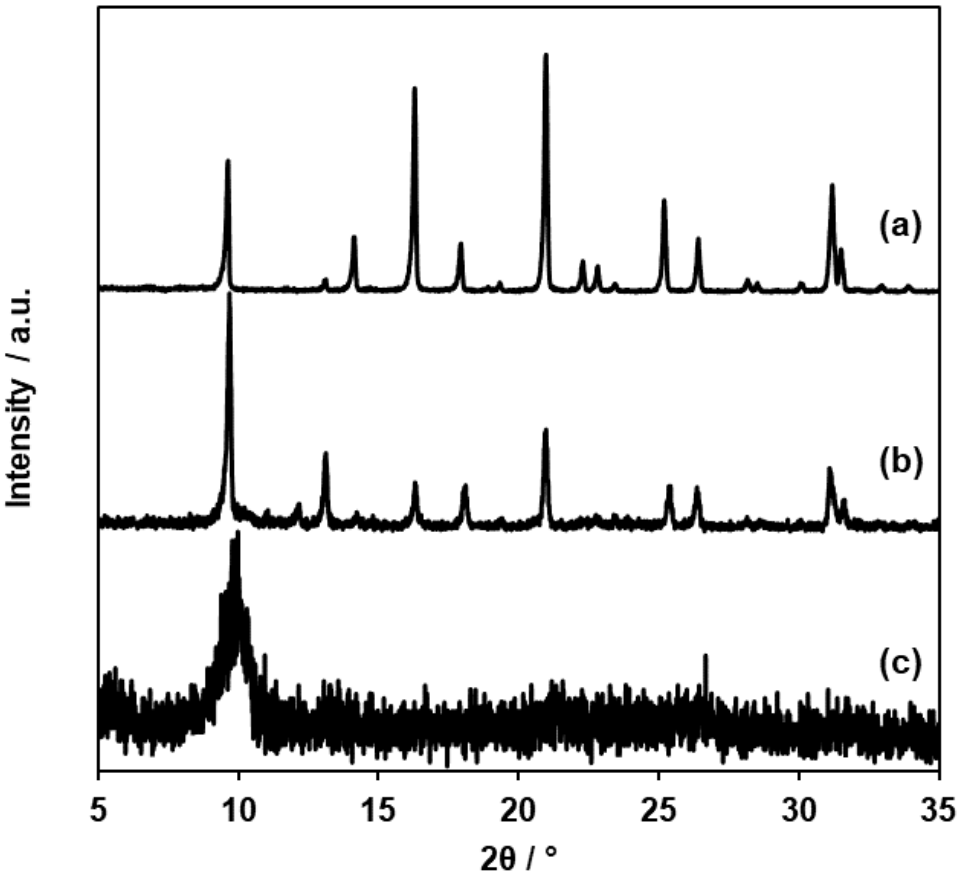

Figure 2.12. Ex situ XRD patterns of (a) Si-CHA and hydrothermally aged (b) Pd-CHA-30-1.0 and (c) Pd-CHA-5-1.2 after H_2 TPR characterization. Samples (b , c) were hydrothermally aged (1−2 kPa H_2O in balance air for 24 h at 1023 K, 0.5 cm^3 s^{-1}) similar to literature reports [41] in an attempt to maximize the amount of mononuclear Pd^{2+} before H_2 TPR characterization. After H_2 TPR analysis, samples were stored in vials under ambient atmosphere before ex situ XRD characterization. Patterns are offset vertically for clarity.

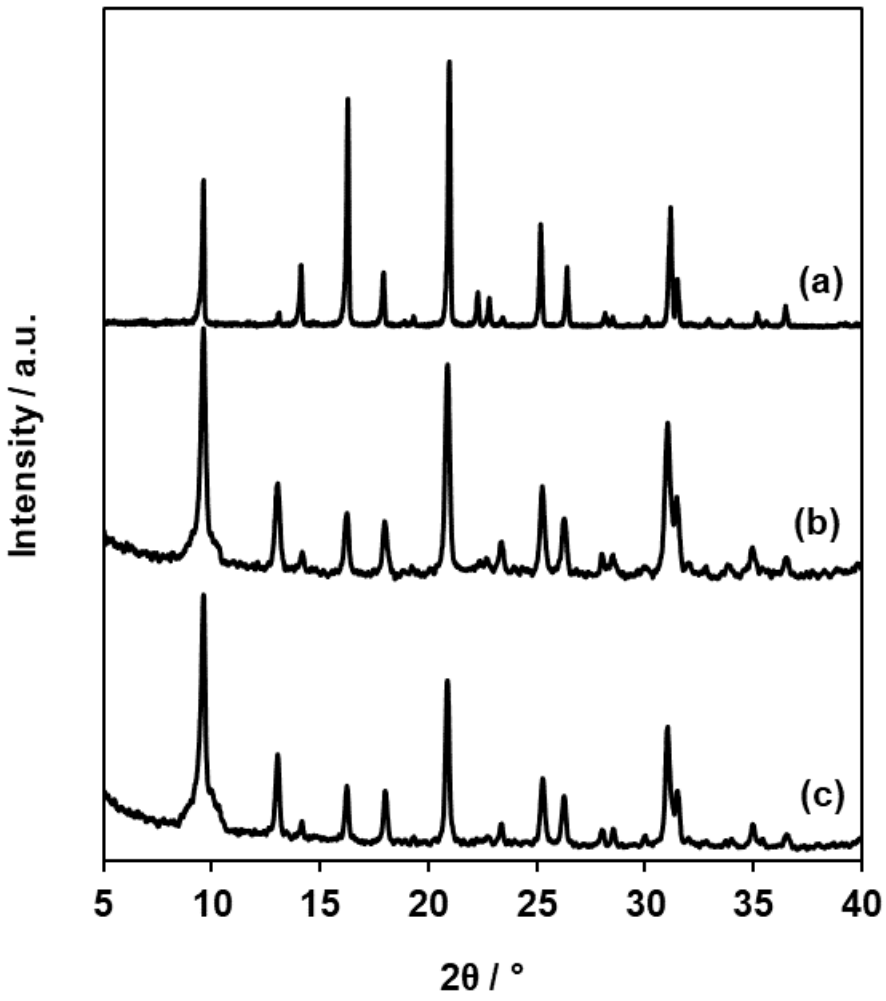

Figure 2.13. Ex situ XRD patterns of (a) reference Si-CHA, (b, from Figure 2.5 in main text) Pd-CHA-12(18%)-3.9-1023 and (c, from Table 2.3 in main text) Pd-CHA-12(24%)-3.3 after repeated H_2 TPR cycling experiments. Patterns are offset vertically for clarity.

2.8.3 Ar and N_2 adsorption isotherms

N_2 (77 K) and Ar (87 K) adsorption isotherms were measured with a Micromeritics ASAP 2020 Surface Area and Porosity Analyzer. Micropore volumes were calculated by converting the gas quantity adsorbed at standard temperature and pressure (STP, 273 K and 1 atm) to liquid volumes using the density of the respective gases at their condensation temperature. Micropore volumes were calculated by fitting a linear regression over the beginning range of mesopore filling (P/P_0 = 0.15–0.25) and estimating the quantity adsorbed at zero relative pressure.

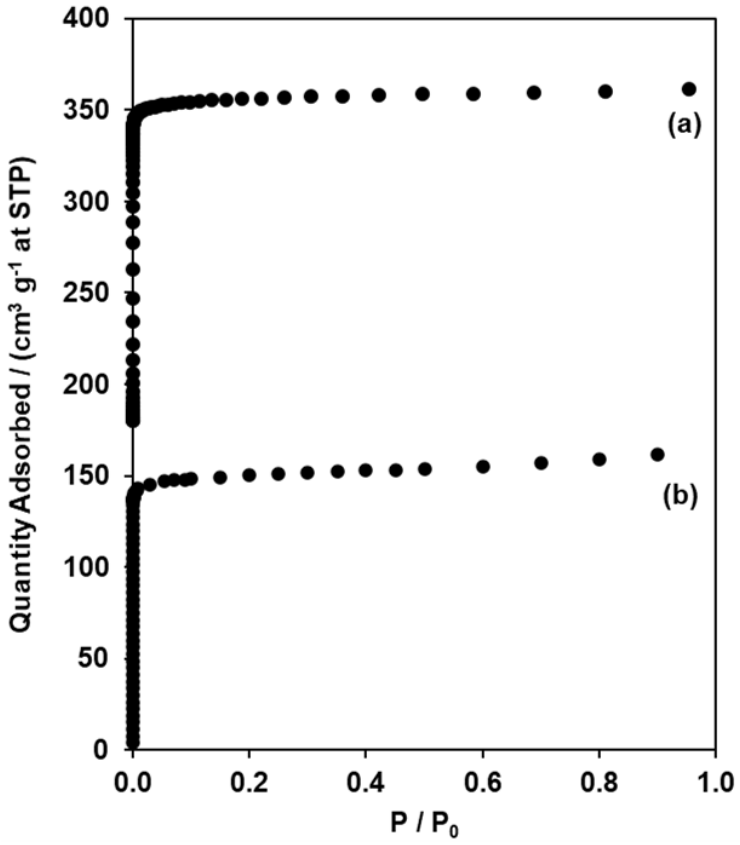

Figure 2.14. Ar adsorption isotherm measured at 87 K on (a) H-CHA-14(10%) (0.21 cm^3 g^{-1}) and b) Pd-CHA-14(10%)-0.7-823 (0.23 cm^3 g^{-1}). Isotherm (a) is offset by 180 cm^3 g^{-1} at STP for clarity.

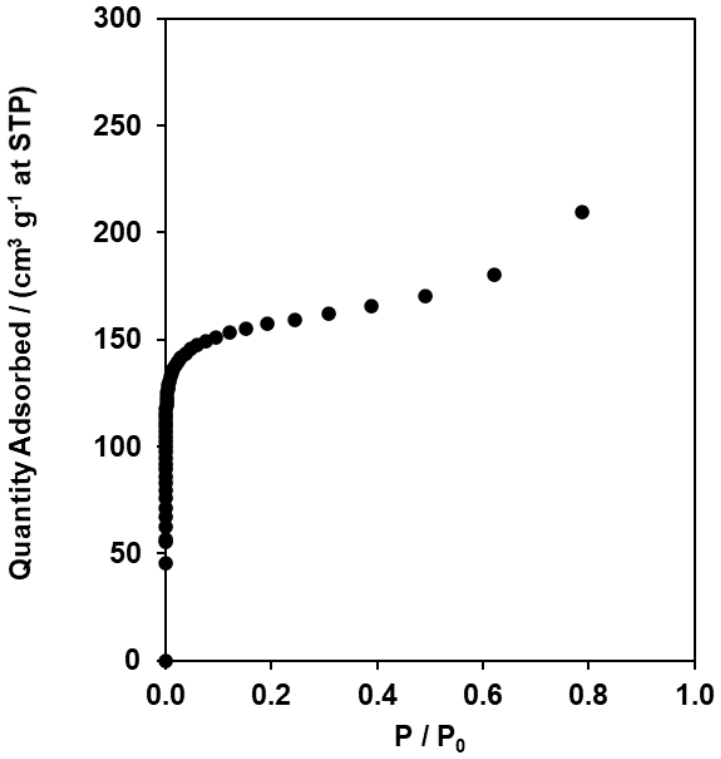

Figure 2.15. N_2 adsorption isotherm measured at 77 K on H-Beta-13 (0.22 cm^3 g^{-1}).

2.8.4 Co^{2+} titration of 2Al sites in 6-MR of CHA zeolites

The number of two Al sites in the 6-membered ring (6-MR) of CHA was quantified with aqueous-phase Co^{2+} titration [20], [23]. An aqueous ion-exchange isotherm was measured to identify exchange conditions that result in Co^{2+} saturation (Figure 2.16). A NH_4-CHA-12 zeolite was mixed with CoCl2 solutions of increasing molarity at a ratio of 150 gsolution (g solid)$^{-1}$ for >24 h under ambient conditions. Solids were recovered by centrifugation, washed with deionized water four times (30 mL (g solid)$^{-1}$ per wash), then dried in a static oven at 373 K for >12 h. Dried samples were treated in flowing air to 773 K (0.0167 K s^{-1}) for 4 h, and a portion of this sample was then digested for elemental analysis. From Figure 2.16, Co^{2+} saturation was achieved using a 2 M CoCl2 solution which was used for all other zeolites in this study.

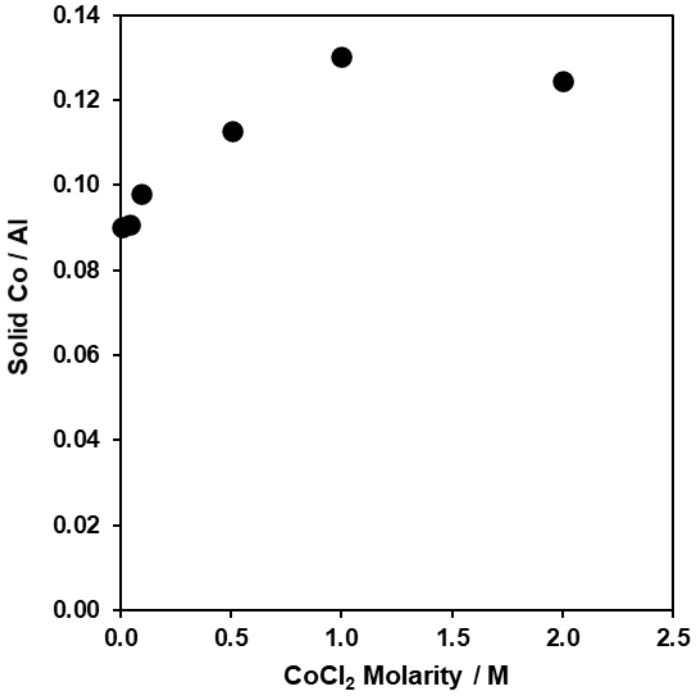

Figure 2.16. Co^{2+} ion-exchange isotherm of NH_4-CHA-12 using CoCl2 solutions of varying molarity. The amount of Co and Al were measured on solid samples after treatment in flowing air to 773 K.

2.8.5 Diffuse-reflectance UV-visible spectra

UV-vis spectra were collected with a Varian Cary 5000 UV-vis-NIR Spectrophotometer typically between 190 to 1200 nm with a scan rate of 5 nm s^{-1}. Liquid-phase transmission UV-vis spectra were collected under ambient conditions in plastic cuvettes. Diffuse reflectance UV-vis (DRUV-vis) measurements of pelleted and sieved (180–250 μm) powdered samples were collected with a Harrick Scientific Praying mantis diffuse reflectance accessory. An ambient scan of polytetrafluoroethylene (PTFE, 200 μm, Sigma Aldrich) was used as the purely reflective baseline for DRUV-vis spectra, and a plastic cuvette cell filled with deionized water was the baseline for transmission measurements. Arbitrary absorbances for DRUV-vis spectra were calculated with Kubelka-Munk theory using $F(R) = (1\text{-}R)^2/(2R)$, where $R = [\%R(\lambda)\text{sample}] / [\%R(\lambda)\text{PTFE}]$.

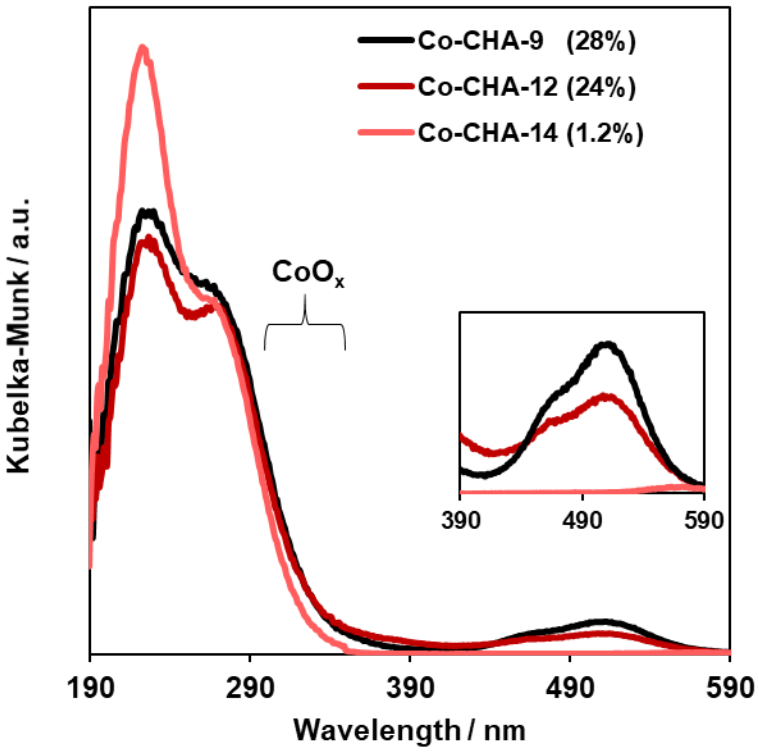

Figure 2.17. DRUV-vis spectra measured under ambient conditions of three Co-CHA zeolites prepared via aqueous ion-exchange with 2 M CoCl2. Brackets denoting region where CoOx would appear (300–350 nm). Inset: d-d transition region of 390-590 nm for clarity.

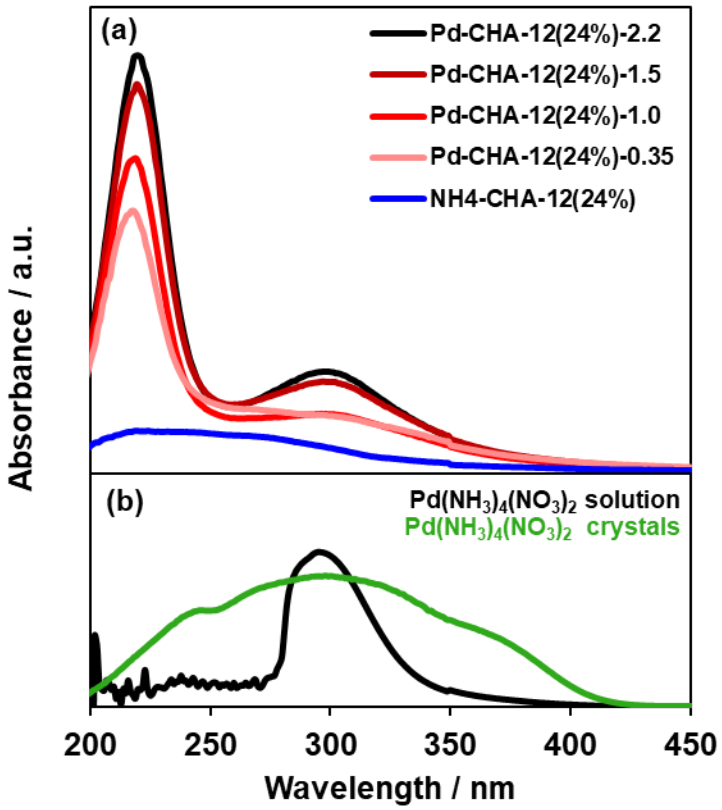

Figure 2.18. (a, offset) DRUV-vis spectra measured under ambient conditions of the parent NH_4-CHA-12(24%) material (blue) and as-exchanged Pd-CHA-12(24%) samples of varied Pd content (0.35–2.2 wt%, light red to black) prepared via incipient wetness impregnation with $Pd(NH_3)_4(NO_3)_2$ solutions. (b) Transmission liquid-phase UV-vis spectra measured under ambient conditions of a diluted $Pd(NH_3)_4(NO_3)_2$ solution (black) and DRUV-vis spectra measured under ambient conditions of $Pd(NH_3)_4(NO_3)_2$ crystals (green).

The hypothesis that Pd reduction and agglomeration resulted from in situ H_2 formation was further corroborated by in situ DRUV-vis (Figure 2.19) of an as-exchanged $[Pd(NH_3)_4]^{2+}$-CHA-12(24%)-1.5-298 sample treated under conditions similar to the He TPD protocol (Section 2.8.7, SI). The first spectrum collected at 288 K (Figure 2.19a) showed two absorption bands centered at 220 and 300 nm, consistent with the presence of $[Pd(NH_3)_4]^{2+}$ complexes. DRUV-vis spectra were collected as a function of temperature until the maximum operating temperature of the in situ cell was reached (603 K, flowing He). The bands for N-Pd LMCT (220 nm) and $[Pd(NH_3)_4]^{2+}$ d-d transitions (300 nm) began to increase in absorbance by 488 K, suggesting the ligand environments around Pd sites were changing. By 568 K, spectral bands assignable to LMCT or d-d transitions had fully disappeared, and a broad band with a maximum centered around 300 nm appeared. As the temperature increased to 603 K, the total absorbance continued to increase throughout the 250–700 nm range. The spectrum collected after treatment in flowing He to 603 K was similar to that of agglomerated Pd or PdO domains (reference materials in Figure 2.1b), consistent with $[Pd(NH_3)_4]^{2+}$ reduction and agglomeration to metallic Pd domains under the inert atmosphere of He TPD [63], [97]. Further evidence for this proposal was obtained by H_2 TPR of an as-exchanged Pd-CHA-12(24%)-1.5-298 sample after treatment in flowing He to 773 K (0.833 $cm^3\ s^{-1}$, 0.167 K s^{-1}, 1 h), which did not show any features for Pd reduction (see Section 2.4.2.1., main text) but did show a H_2 production feature caused by decomposition of a palladium-hydride phase (Figure 2.41, SI). Thus, treatment of as-exchanged $[Pd(NH_3)_4]^{2+}$-CHA zeolites in flowing He (>600 K) causes the reduction of mononuclear Pd^{2+} and subsequent agglomeration to metallic Pd particles.

Starting from the metallic Pd state at 603 K, the He stream was replaced with air while simultaneously collecting DRUV-vis spectra (Figure 2.19b). After switching from He to air, the in situ cell temperature increased from 603 K to a higher temperature of 723 K, a consequence of the instrument design. After 20 minutes of air exposure, the DRUV-vis spectrum showed absorbances of lower overall intensity and a small band in the range of d-d transitions (ca. 500 nm) for mononuclear Pd^{2+} ligated to the zeolite lattice, suggesting that metallic Pd domains were oxidizing to PdO and that some fraction of these PdO domains converted to mononuclear Pd^{2+}. With increasing time (20–80 minutes) under flowing air,

the d-d transition band centered at 500 nm and a LMCT band centered at 260 nm became more readily apparent, similar to the spectrum of Pd-CHA-12(24%)-1.5-298 treated in air to 723 K (Figure 2.1, main text). The changes observed in DRUV-vis spectra upon replacement of He with air at elevated temperatures (>603 K) indicates that metallic Pd particles can convert to mononuclear Pd^{2+} through a solid-state ion-exchange process.

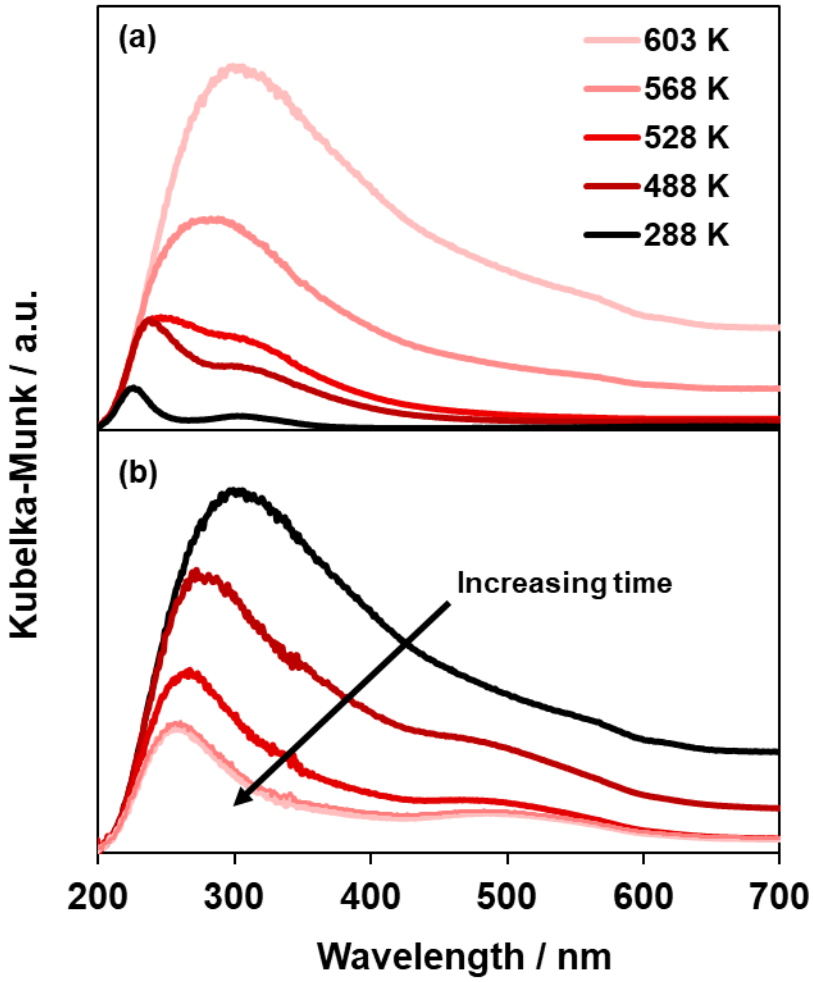

Figure 2.19. (a) In situ DRUV-vis during TPD in He (30 K h^{-1} to 603 K) of as-exchanged Pd-CHA-12(24%)-1.5-298 and (b) after replacing the He stream with air (black to light red, spectrum collected every 20 min up to 80 min, arrow indicates the direction of increasing time).

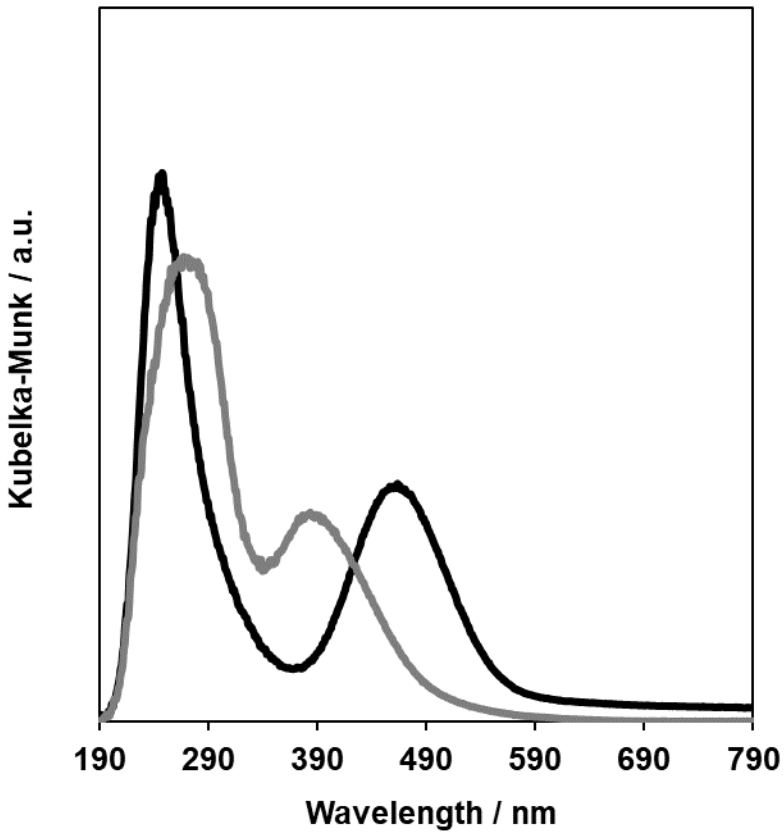

Figure 2.20. (Black) DRUV-vis spectrum measured at 290 K of a dehydrated Pd-CHA-5-1.2-923 sample previously treated in flowing air (0.83 cm^3 s^{-1}) to 723 K (0.167 K s^{-1}, 0.5 h). (Gray) DRUV-vis spectrum measured at 290 K of a previously dehydrated Pd-CHA-5-1.2-923 sample after treatment in 1–2 kPa H_2O in balance air for at least 30 minutes.

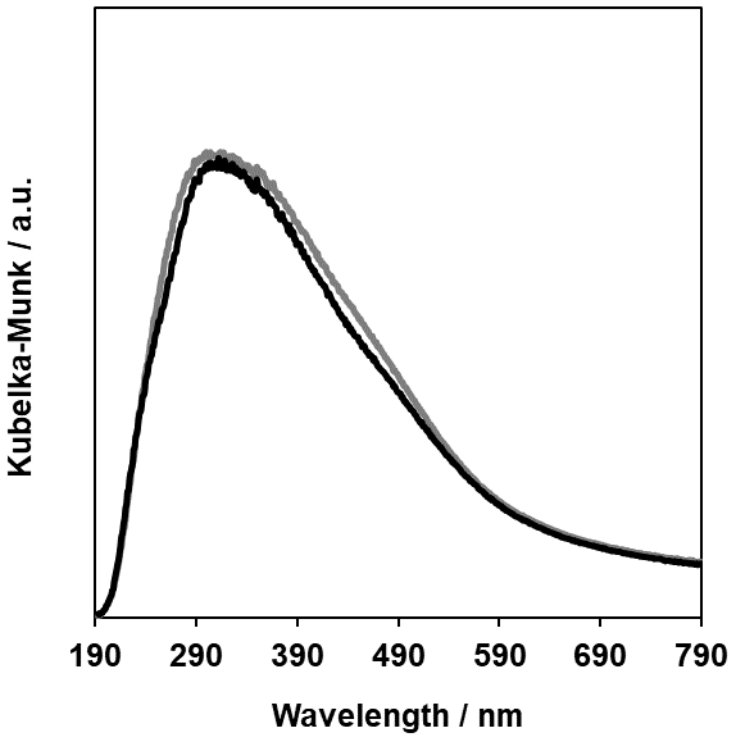

Figure 2.21. (Black) DRUV-vis spectrum measured at 290 K of a PdO-Beta-Si-1.0-773 material treated in air to 473 K (0.167 K -1) for 0.5 h. (Gray) DRUV-vis spectrum measured under ambient conditions of the PdO-Beta-Si-1.0-773 material.

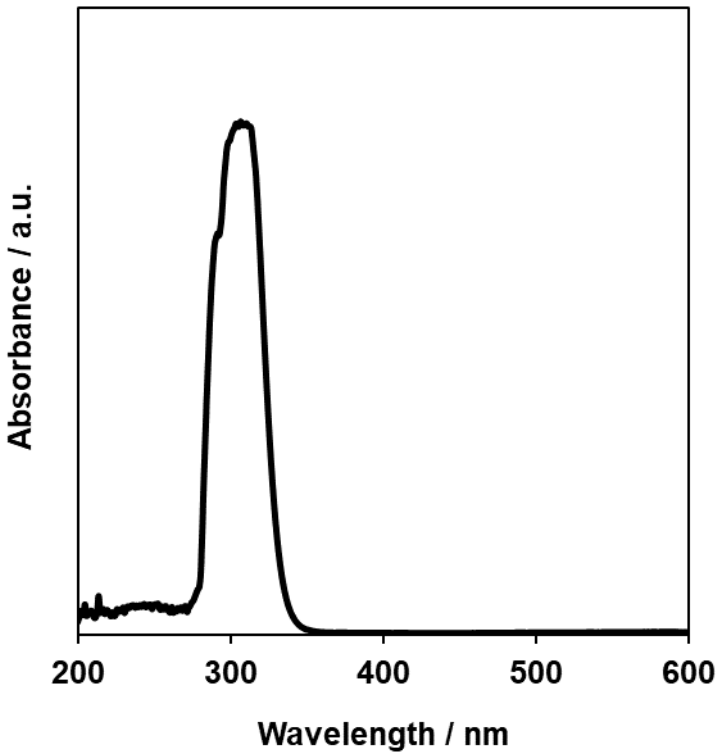

Figure 2.22. Transmission, liquid-phase UV-vis spectra measured under ambient conditions of NH_4^+ back-exchange solution after contacting with Pd-CHA-9(28%)-1.0-1023.

2.8.6 X-ray absorption spectroscopy (K- and L_3-edge)

Pd K- and L_3-edge experiments were performed at the Advanced Photon Source in Argonne National Laboratory at sectors 10-BM and 9-BM, respectively. For transmission Pd K-edge, samples were pressed inside six-shooters and loaded into Kapton sealed quartz tubes with valve openings for gas treatments. Pd L_3-edge fluorescence experiments were performed using an in situ cell sealed with Kapton windows. Pd samples were pressed into self-supporting wafers held by a metal fixture that was placed inside the in situ cell. Unless noted elsewise, X-ray absorption near edge spectra (XANES) are normalized, and extended X-ray absorption fine spectra (EXAFS) contain the k^2-weighted Fourier transform (FT) magnitude as a function of the non-phase corrected distance. Pd L_3-edge derivative data was smoothed using a noise-robust 7-point stencil (Equation 2.10) [98].

$$y_0(x_0) = [5(y_1 - y_{-1}) + 4(y_2 - y_{-2}) + (y_3 - y_{-3})]/(32h) \tag{2.10}$$

where h = x_1 - x_0 is the sampling interval.

Pd K-edge EXAFS spectra were analyzed using WinXAS 3.1. EXAFS spectra were k^2-weighted before Fourier transformation (k = 2.5–11 Å) into R-space. After isolating the first-shell in R space (k = 1.2–1.85 Å), the Debye-Waller factor, σ^2, was optimized in k^2-weighted k-space. The coordination numbers and bond distances were optimized using a least-squares fit in R-space, while holding σ^2 constant at its previously optimized value. FEFF simulations were used to fit the data, where experimentally determined Pd-X distances from crystallographic studies were used for FEFF scattering pair bond distances [99], [100]. The reduction factors, S_0^2, were determined by fitting a simulation of a single Pd-X (X = Pd, N, O) contribution.

Table 2.6. Summary of Pd K-edge EXAFS fits using FEFF references. The fitted first-shell scattering pairs are denoted in parenthesis. See fits in Figures 2.24, 2.25, 2.26, and 2.27.

Sample	E_{edge} / keV	Coordination number	R / Å	σ^2	E_0 / eV
Pd-CHA-12(24%)-2.2-298 (Pd-N)	24.353	4.1 ± 0.4	2.05 ± 0.01	0.001	3.78 ± 0.02
Pd-CHA-5-1.2-923 (Hydrated, Pd-O)[a]	24.352	4.1 ± 0.4	2.01 ± 0.01	0.001	2.61 ± 0.02
Pd-CHA-5-1.2-923 (Dehydrated, Pd-O)[b]	24.352	3.5 ± 0.4	2.03 ± 0.01	0.001	1.08 ± 0.02
PdO-Beta-Si-1.0-773 (Pd-O)	24.352	4.1 ± 0.4	2.00 ± 0.01	0.001	1.92 ± 0.06

[a]Sample was treated in flowing 1–2 kPa H_2O in balance air at ambient temperature for 0.5 h.
[b]bSample was treated in flowing air at 823 K for 0.5 h.

Table 2.7. Pd K-edge EXAFS fitting parameters for Pd-CHA-14(10%)-0.7-823 and Pd-CHA-5-1.2-923 after treatment in flowing 5 kPa H_2 at 473 K for 0.5 h. Samples were cooled in UHP He equipped with an in-line O_2 trap to decompose Pd^0-H and minimize oxidation of metallic Pd nanoparticles. Samples were fit to a theoretical (FEFF) Pd foil with a coordination number (CN) of 12 (see fits in Figures 2.28 and 2.29). The edge energy indicates the energy of the first inflection point in the normalized XANES spectra.

Sample name	Pd-Pd distance / Å	Pd-Pd CN	σ^2	Edge energy / eV	ΔE_0 / eV
Pd-CHA-14(10%)-0.7-823	2.72 ± 0.01	7.1 ± 0.5	0.004	24.3501	2.2
Pd-CHA-5-1.2-923	2.71 ± 0.01	5.4 ± 0.5	0.004	24.3501	2.1

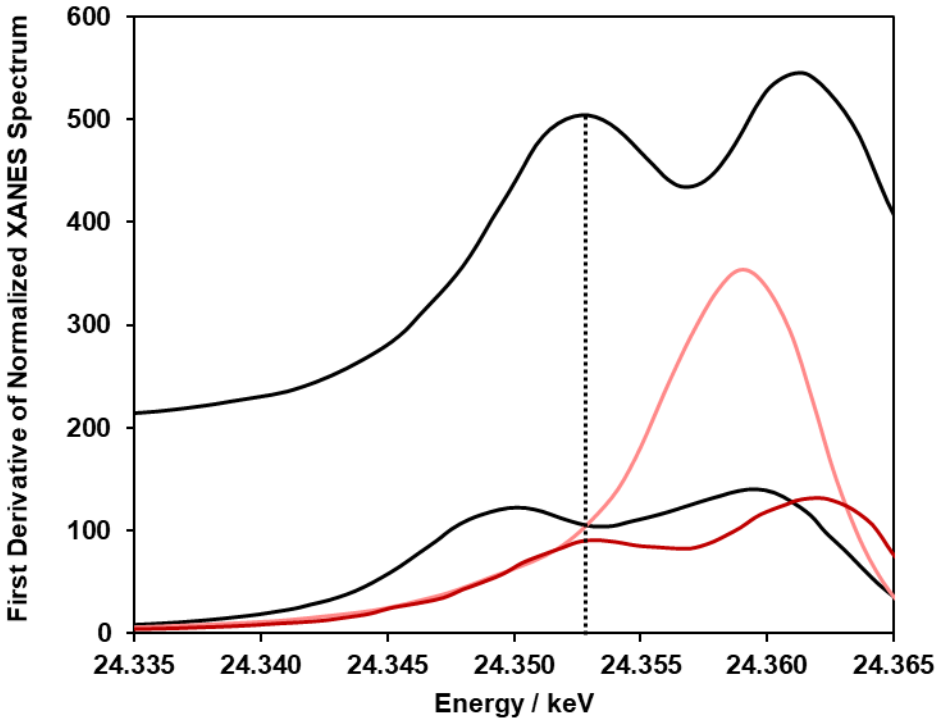

Figure 2.23. First-derivative Pd K-edge XANES analysis of reference Pd compounds: Pd foil (black), PdO (dark red, 98% purity, Sigma Aldrich), and K_2PdCl_6 (pink, 99% purity, Sigma Aldrich). Top black spectrum (offset + 200 units) is of the as-exchanged Pd-CHA-12(24%)-2.2-298 sample prepared via incipient wetness impregnation with $Pd(NH_3)_4(NO_3)_2$. Spectra were collected under ambient conditions. Dashed line indicates first inflection point (i.e., edge energy) of the Pd-CHA-12(24%)-2.2 sample at 24.353 keV.

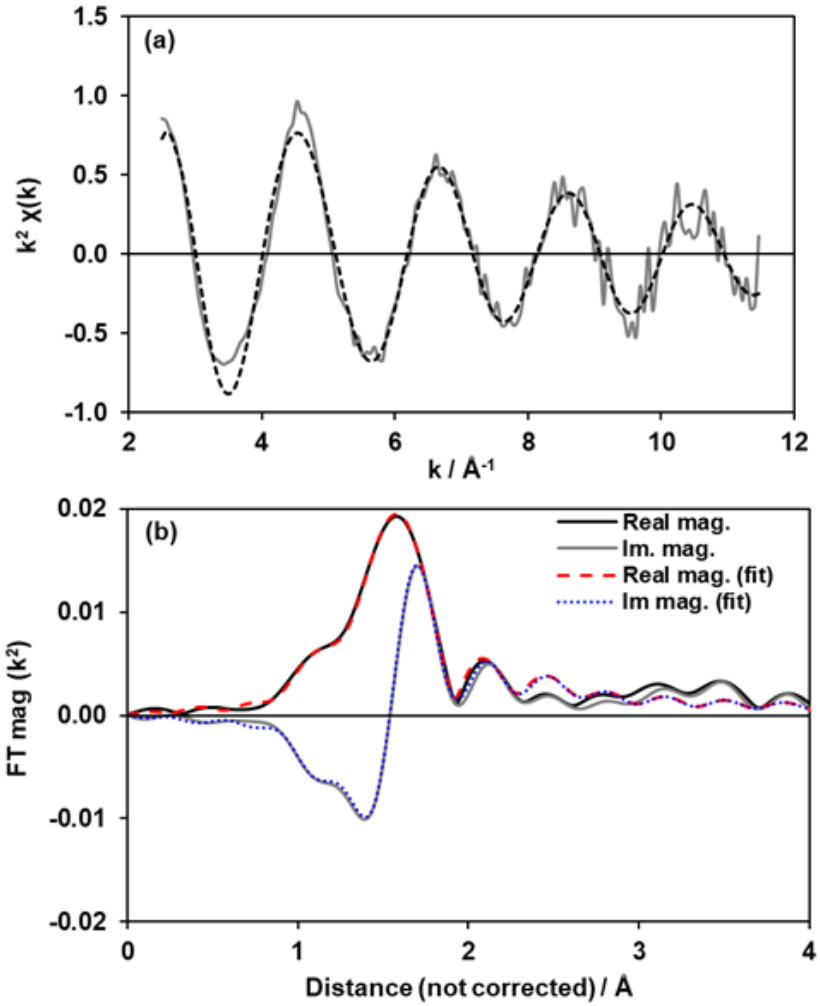

Figure 2.24. (a) k^2-weighted χ(k) of the Pd K-edge EXAFS region for (gray) an as-exchanged Pd-CHA-12(24%)-2.2-298 collected under ambient conditions and (dashed black) the fit (Pd-N). (b) Real and imaginary Fourier transforms of the k^2-weighted EXAFS spectrum for (solid lines) an as-exchanged Pd-CHA-12(24%)-2.2-298 collected under ambient conditions and (dashed lines) fits (Pd-N).

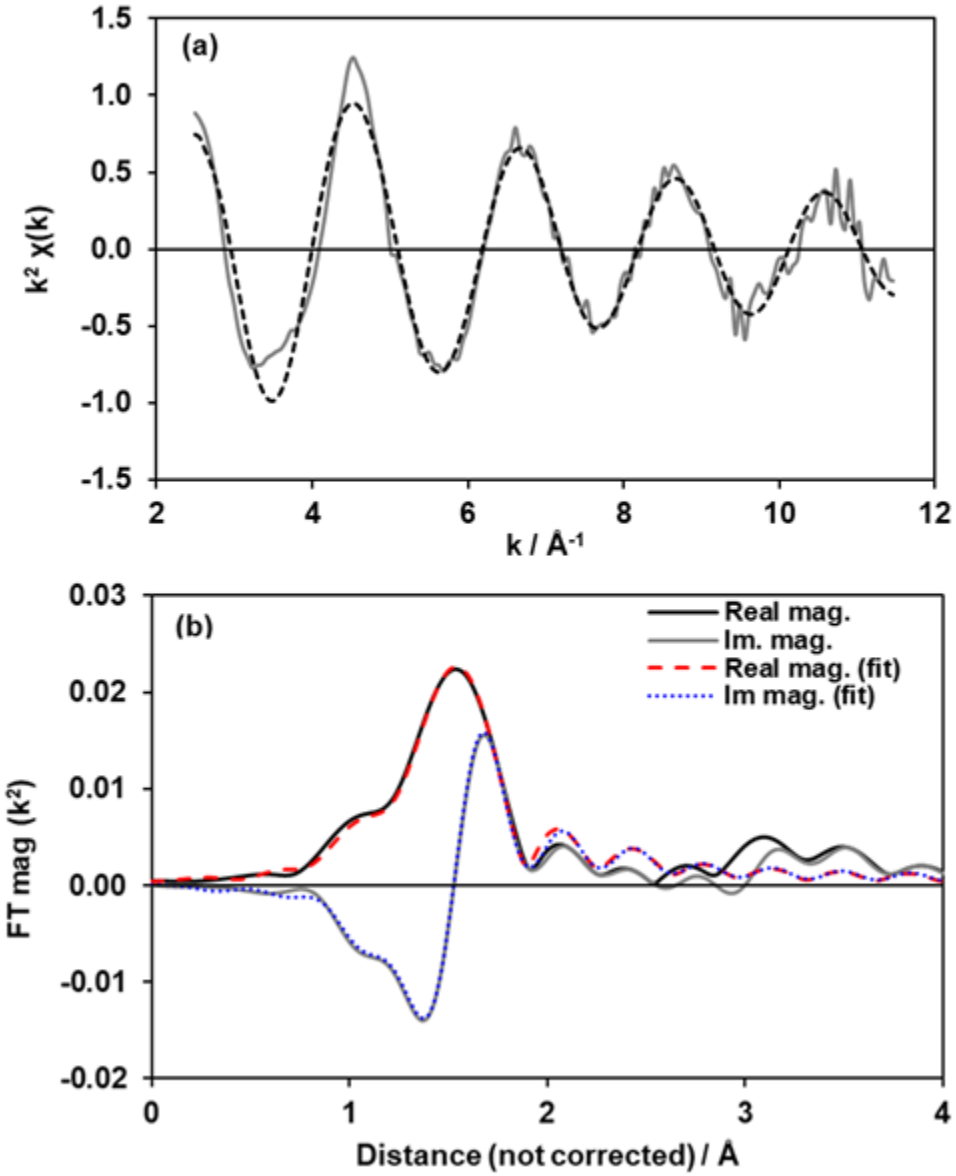

Figure 2.25. (a) k^2-weighted χ(k) of the Pd K-edge EXAFS region for (gray) Pd-CHA-5-1.2-923 treated in flowing 1-2 kPa H_2O in balance air at ambient temperature and (dashed black) the fit (Pd-O). (b) Real and imaginary Fourier transforms of the k^2-weighted EXAFS spectrum for (solid lines) Pd-CHA-5-1.2-923 treated in flowing 1-2 kPa H_2O in balance air at ambient temperature and (dashed lines) fits (Pd-O).

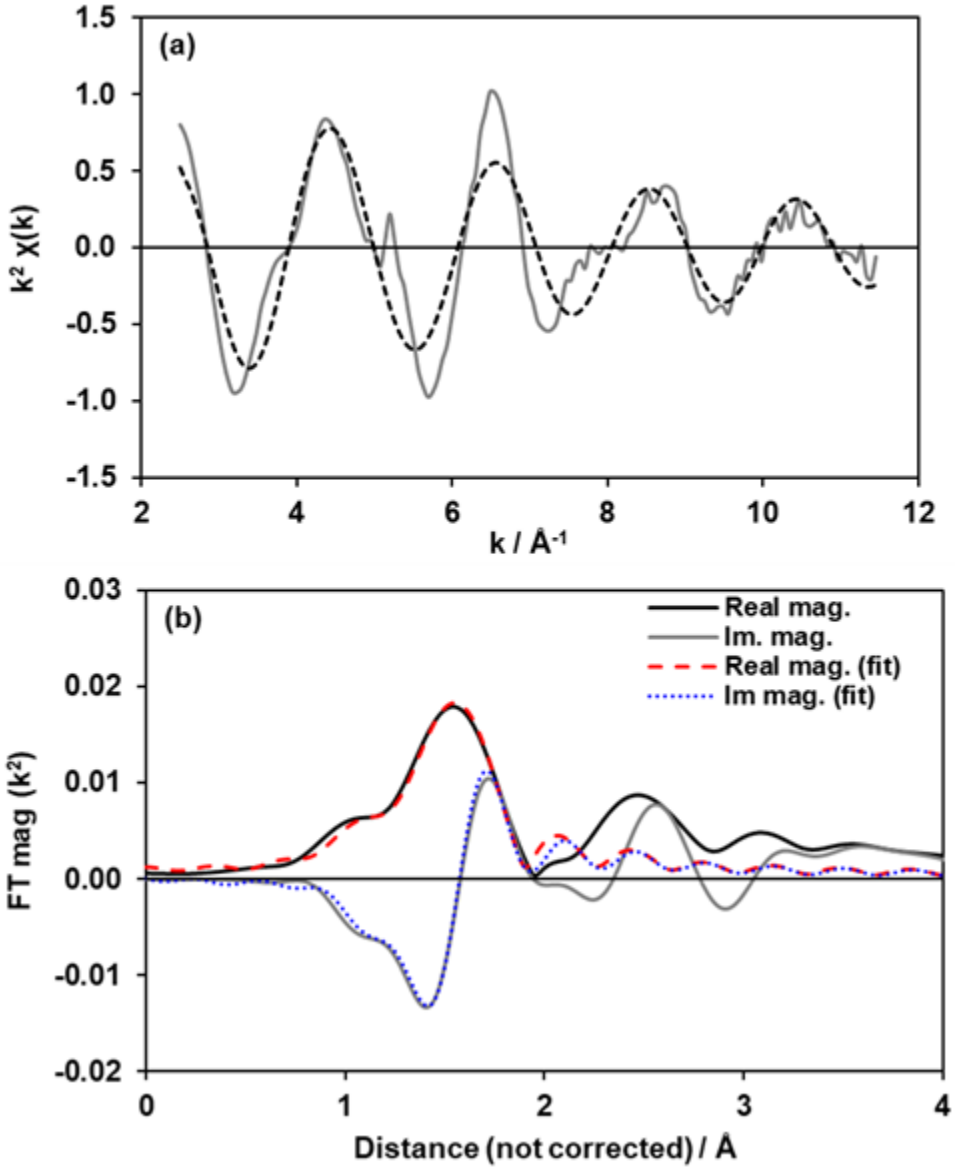

Figure 2.26. (a) k^2-weighted χ(k) of the Pd K-edge EXAFS region for (gray) Pd-CHA-5-1.2-923 treated in air to 773 K then scanned at ambient temperature and (dashed black) the fit (Pd-O). (b) Real and imaginary Fourier transforms of the k^2-weighted EXAFS spectrum for (solid lines) Pd-CHA-5-1.2-923 treated in air to 773 K then scanned at ambient temperature and (dashed lines) fits (Pd-O).

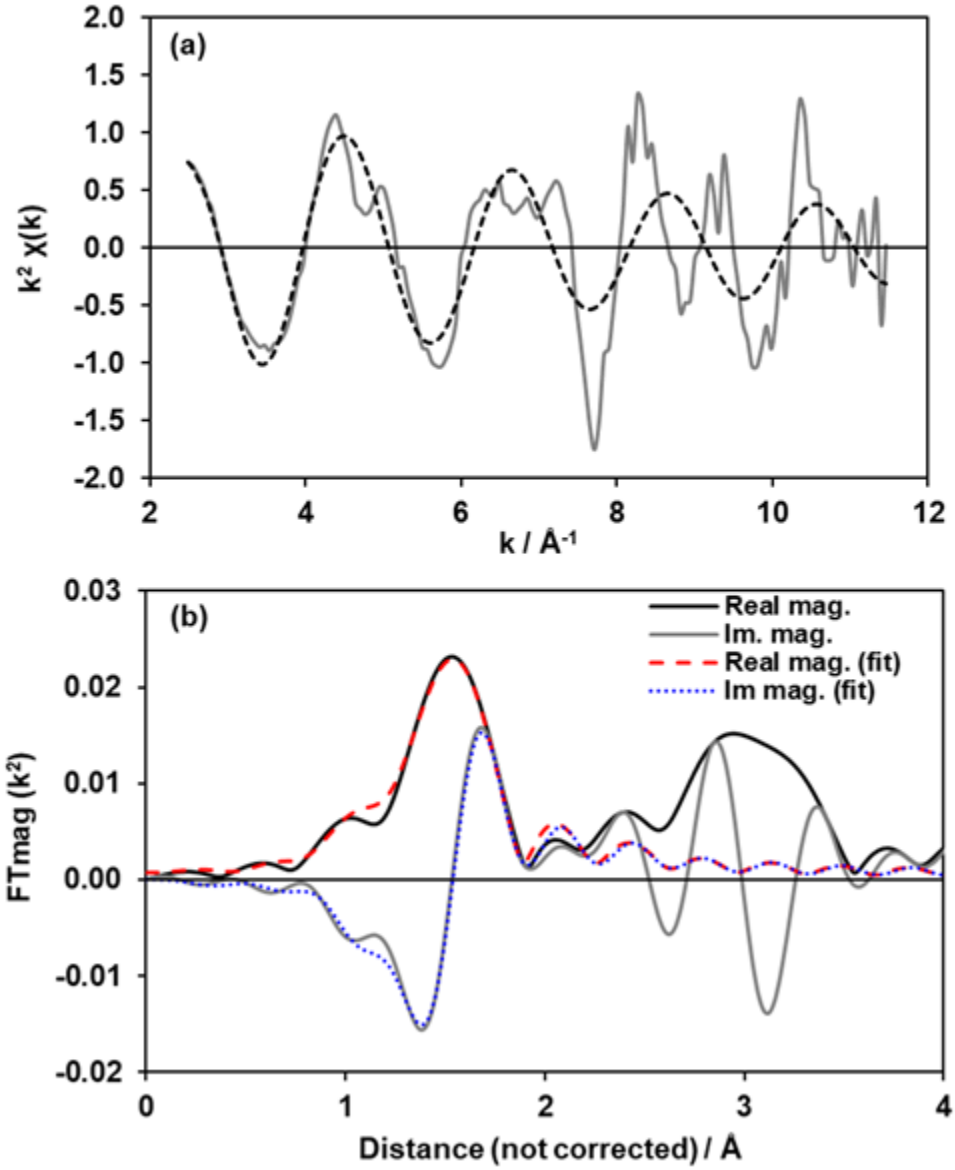

Figure 2.27. (a) k^2-weighted χ(k) of the Pd K-edge EXAFS region for (gray) PdO-Beta-Si-1.0-773 treated in air to 773 K then scanned at ambient temperature and (dashed black) the fit (Pd-O). (b) Real and imaginary Fourier transforms of the k^2-weighted EXAFS spectrum for (solid lines) PdO-Beta-Si-1.0-773 treated in air to 773 K then scanned at ambient temperature and (dashed lines) fits (Pd-O).

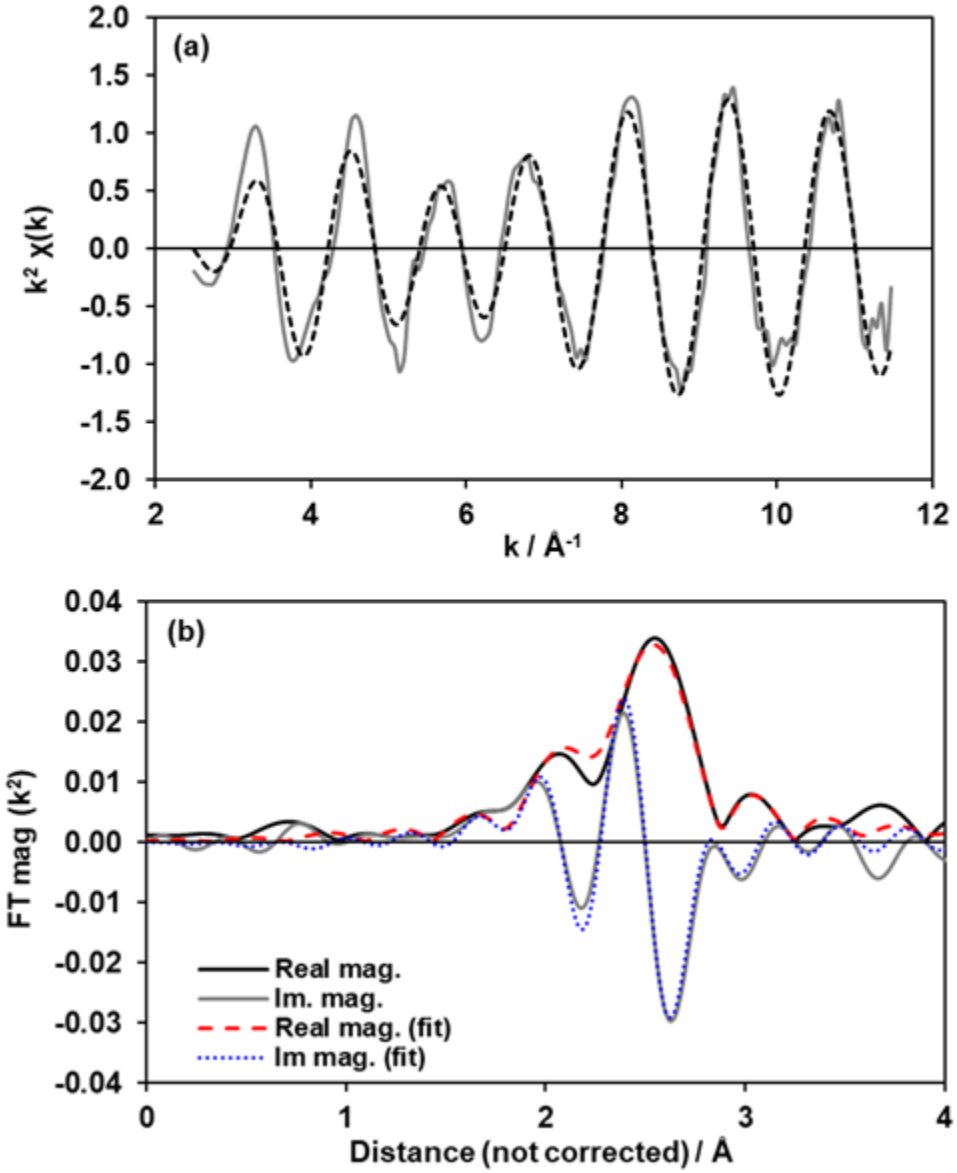

Figure 2.28. (a) k^2-weighted χ(k) of the Pd K-edge EXAFS region for (gray) Pd-CHA-14(10%)-0.7-823 treated in 5 kPa H_2 at 473 K, cooled in UHP He, then scanned at ambient temperature and (dashed black) the fit (Pd-Pd). (b) Real and imaginary Fourier transforms of the k^2-weighted EXAFS spectrum for (solid lines) Pd-CHA-14(10%)-0.7-823 treated in 5 kPa H_2 at 473 K, cooled in UHP He, then scanned at ambient temperature and (dashed lines) fits (Pd-Pd). .

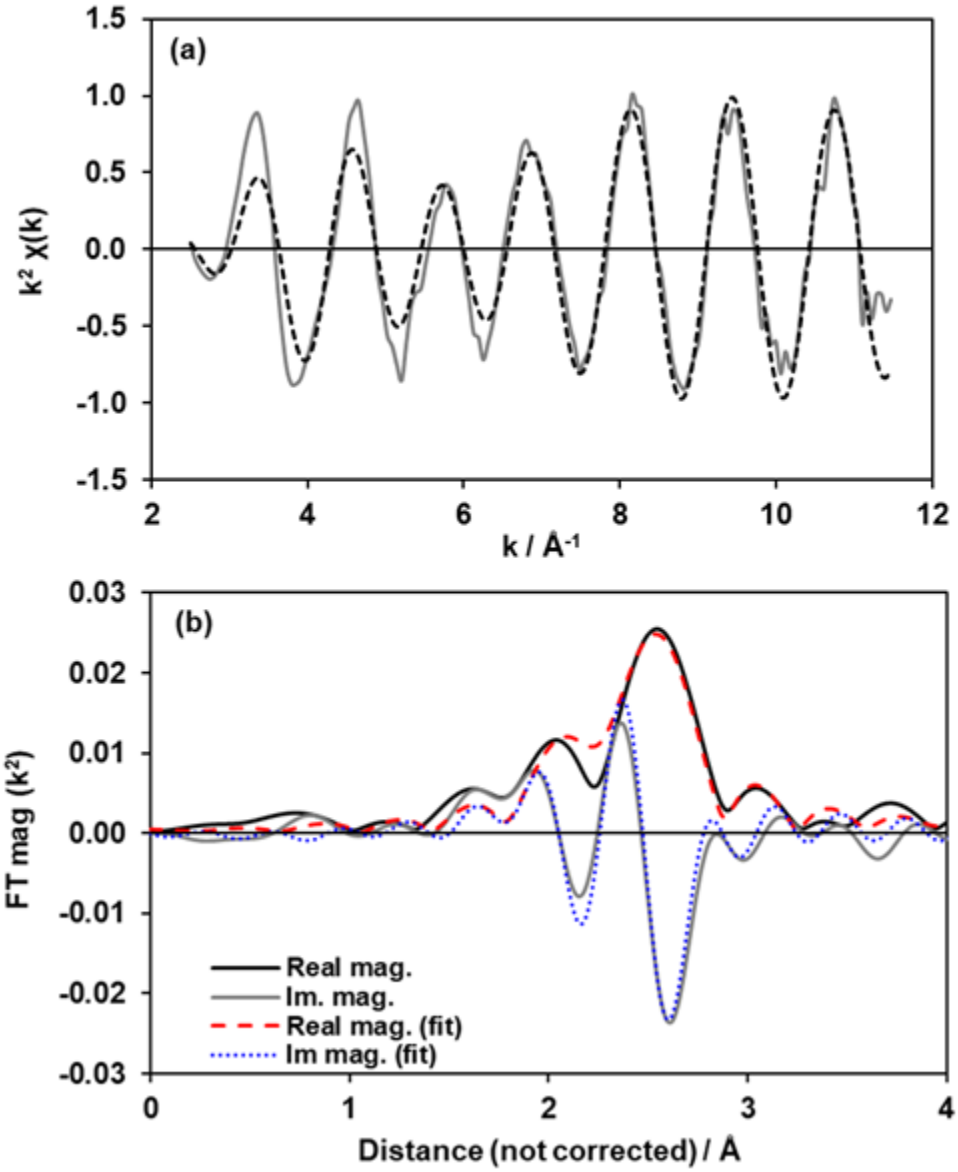

Figure 2.29. (a) k^2-weighted χ(k) of the Pd K-edge EXAFS region for (gray) Pd-CHA-5-1.2-923 treated in 5 kPa H_2 at 473 K, cooled in UHP He, then scanned at ambient temperature and (dashed black) the fit (Pd-Pd) (b) Real and imaginary Fourier transforms of the k^2-weighted EXAFS spectrum for (solid lines) Pd-CHA-5-1.2-923 treated in 5 kPa H_2 at 473 K, cooled in UHP He, then scanned at ambient temperature and (dashed lines) fits (Pd-Pd).

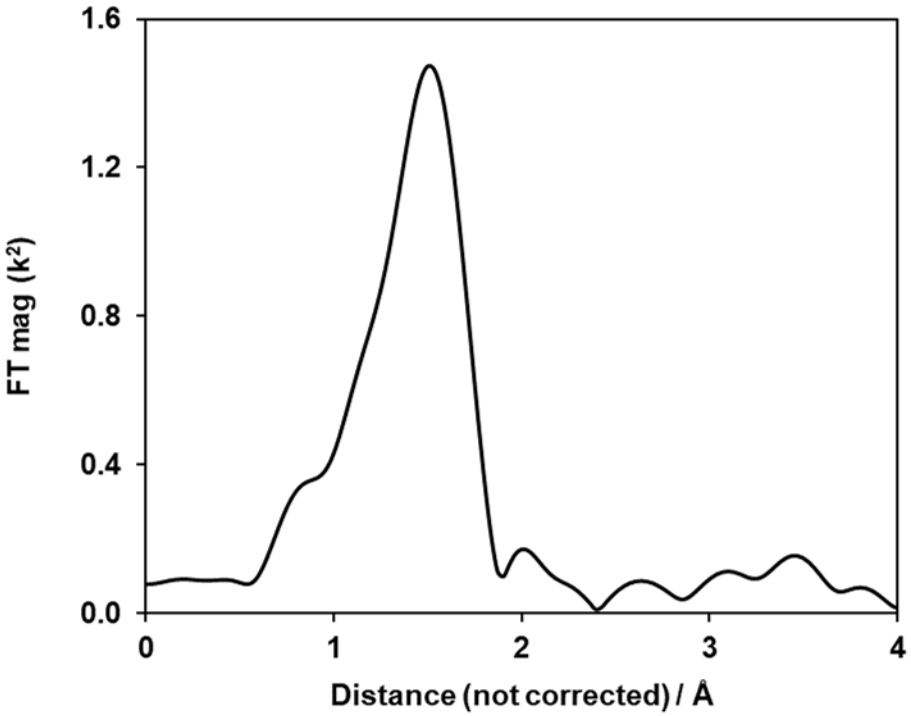

Figure 2.30. Ambient temperature Pd K-edge EXAFS of an as-exchanged Pd-CHA-12(24%)-2.2 sample prepared via incipient wetness impregnation with $Pd(NH_3)_4(NO_3)_2$.

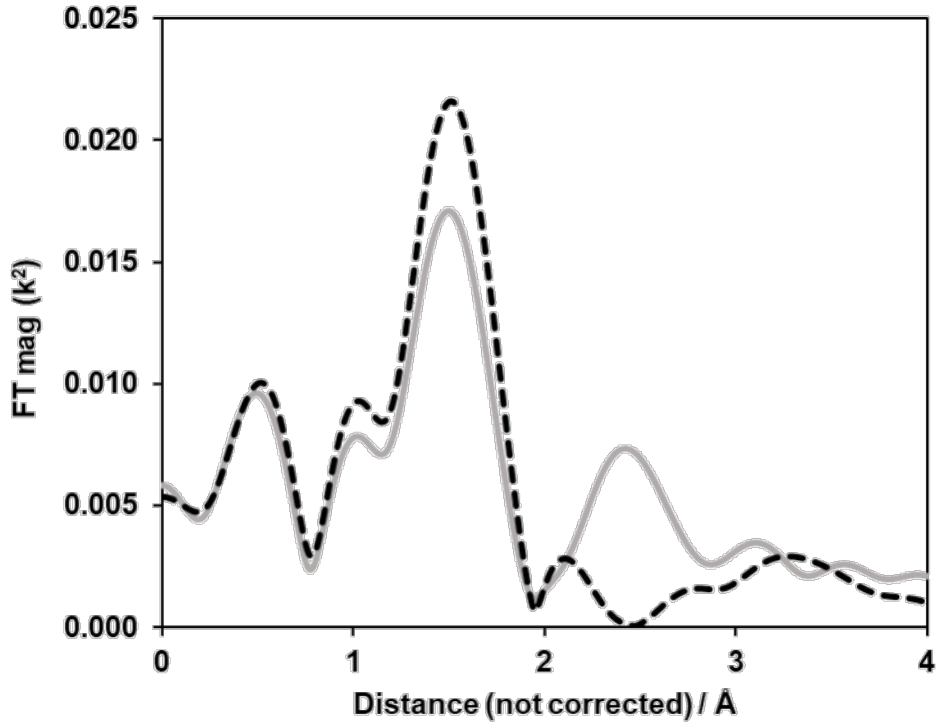

Figure 2.31. Ambient temperature Pd K-edge EXAFS of a predominantly mononuclear Pd-CHA-5-1.2-923 after treatment in flowing air to 1023 K for 0.5 h (gray) then exposure to 1−2 kPa H_2O in balance air at ambient temperatures for 0.5 h (dashed black).

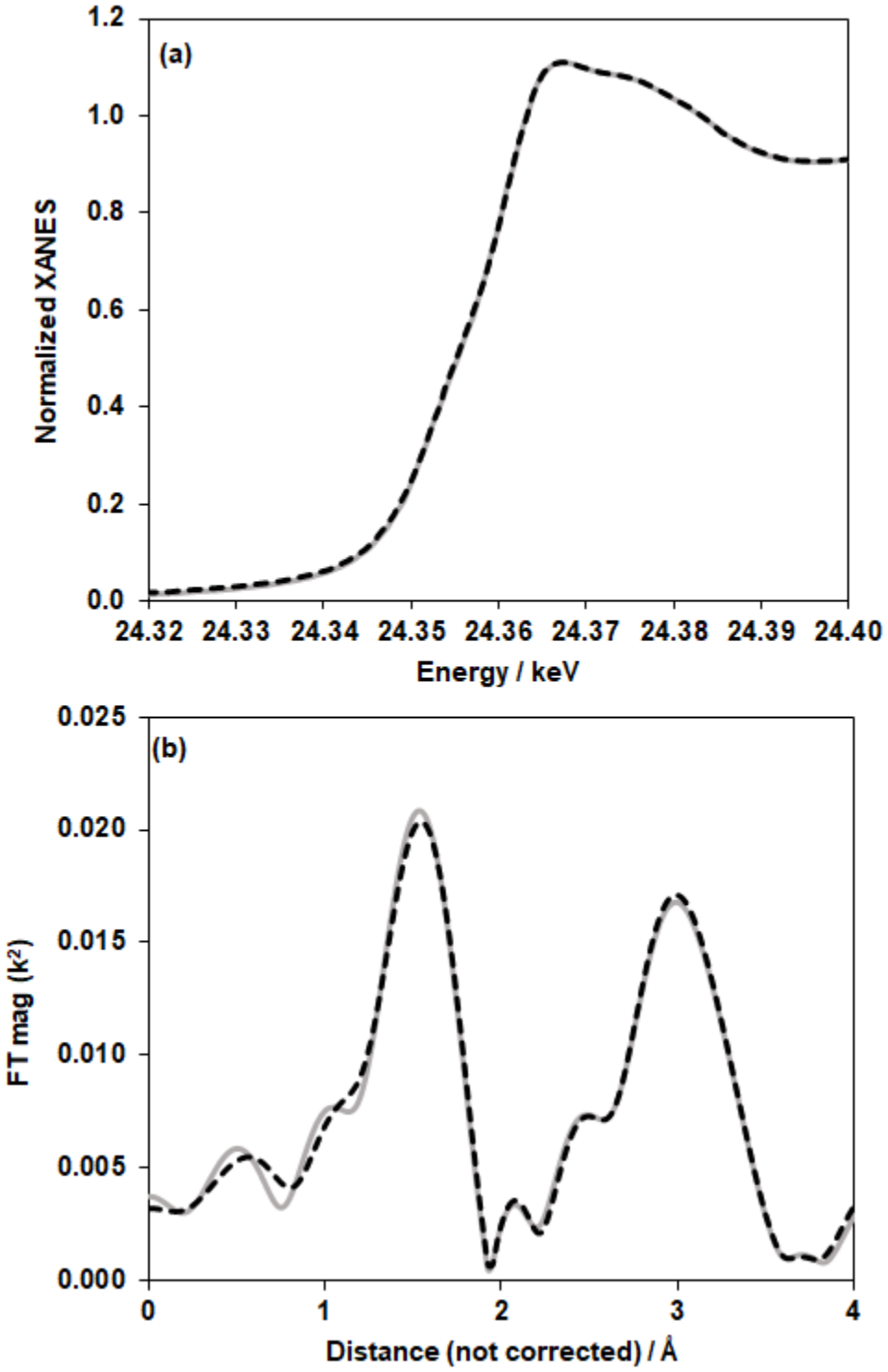

Figure 2.32. Ambient temperature Pd K-edge (a) XANES and (b) EXAFS spectra of a PdO-Beta-Si-1.0-773 sample that was treated in flowing air (1.67 $cm^3\ s^{-1}$) to 1023 K (gray) for 0.5 h and subsequently treated in 1–2 kPa H_2O in balance air (1.67 $cm^3\ s^{-1}$) at ambient temperature for 0.5 h (dashed black).

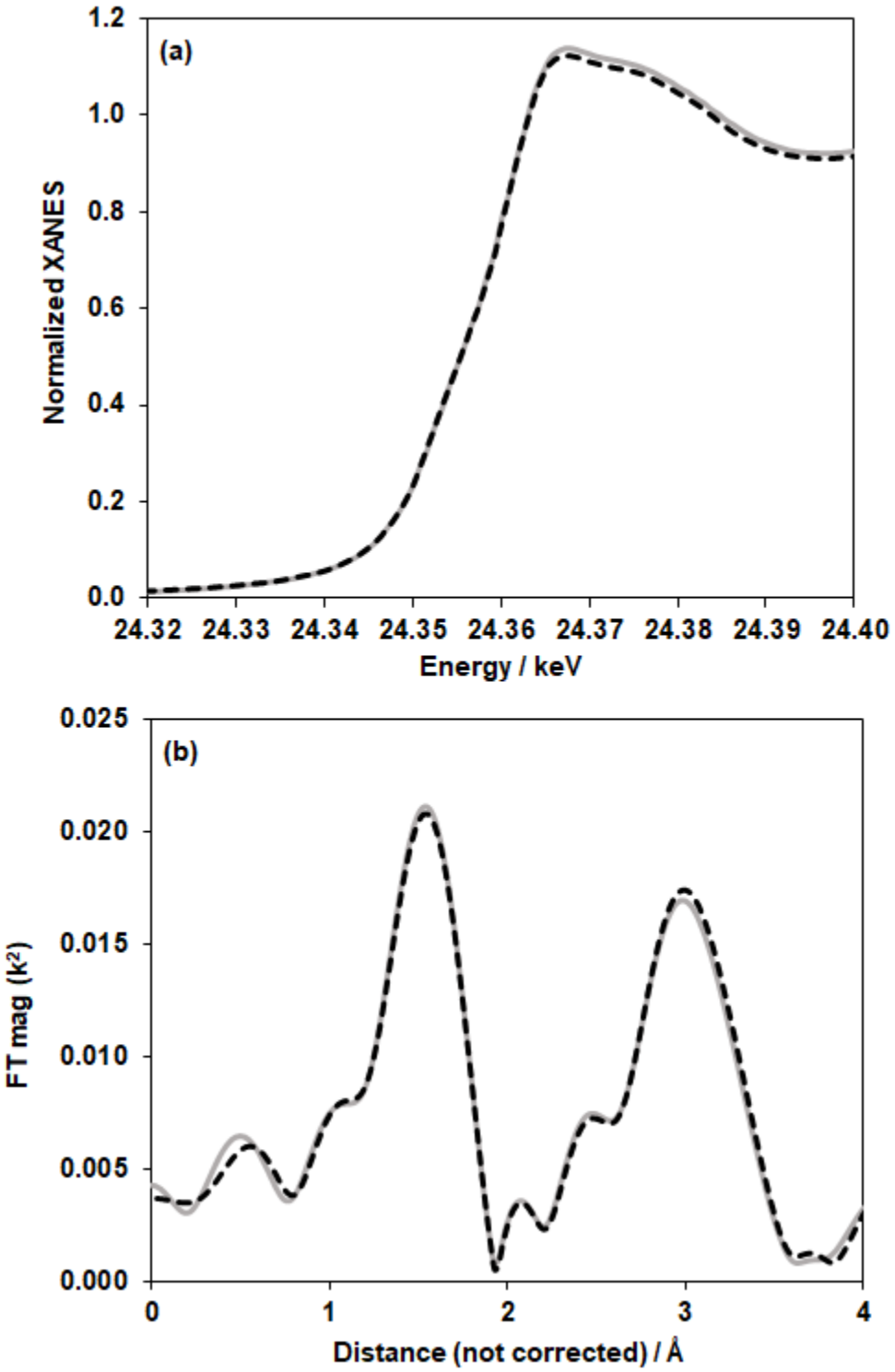

Figure 2.33. Ambient temperature Pd K-edge XANES (a) and EXAFS (b) spectra of a PdO-CHA-Si-1.4-823 sample that was treated in flowing air (1.67 cm^3 s^{-1}) to 1023 K (gray) for 0.5 h and subsequently treated in 1–2 kPa H_2O in balance air (1.67 cm^3 s^{-1}) at ambient temperature for 0.5 h (dashed black).

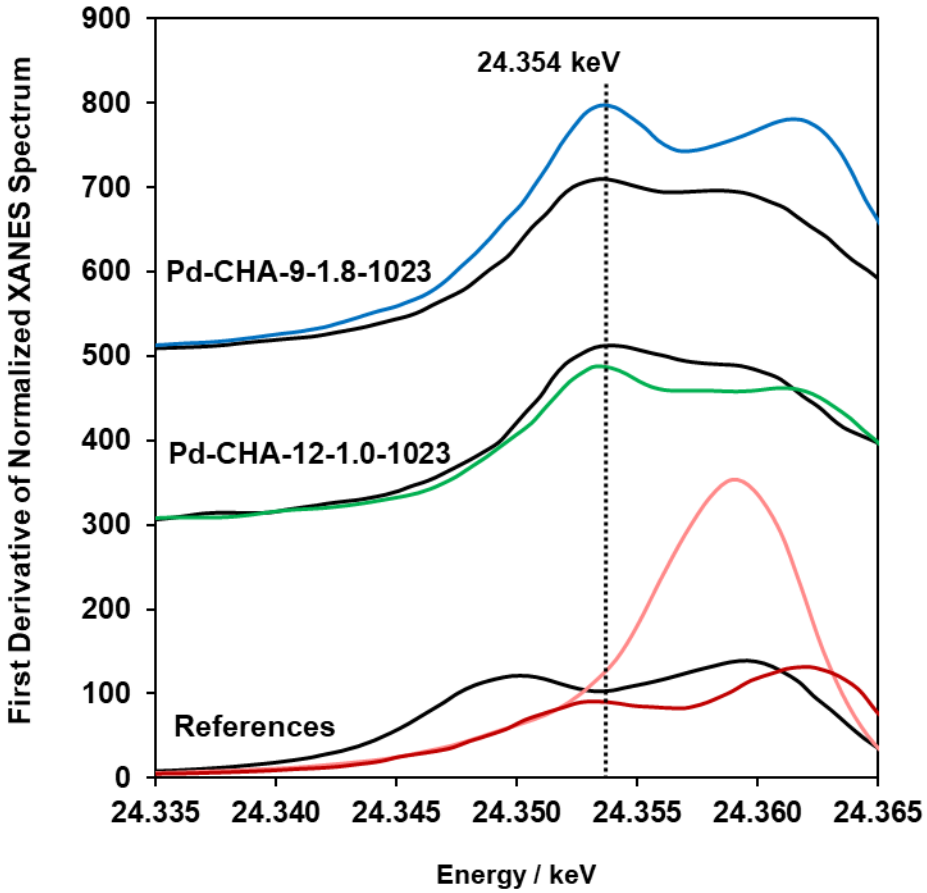

Figure 2.34. First-derivative Pd K-edge XANES analysis of Pd materials at ambient temperature. Reference compounds were collected under ambient conditions: Pd foil (black), PdO (dark red, 98% purity, Sigma Aldrich), and K_2PdCl_6 (pink, 99% purity, Sigma Aldrich). (Offset +300 units for clarity) Pd-CHA-12(24%)-1.0-1023 treated in flowing air to 1023 K (black, divided by a factor of 10 for clarity) and treated in flowing 1−2 kPa H_2O in balance air at ambient temperature (green). (Offset +500 units for clarity) Pd-CHA-9-1.8-1023 treated in flowing air to 1023 K (black, divided by a factor of 7 for clarity) and treated in flowing 1–2 kPa H_2O in balance air at ambient temperature (blue). Dashed line represents an energy of 24.354 keV.

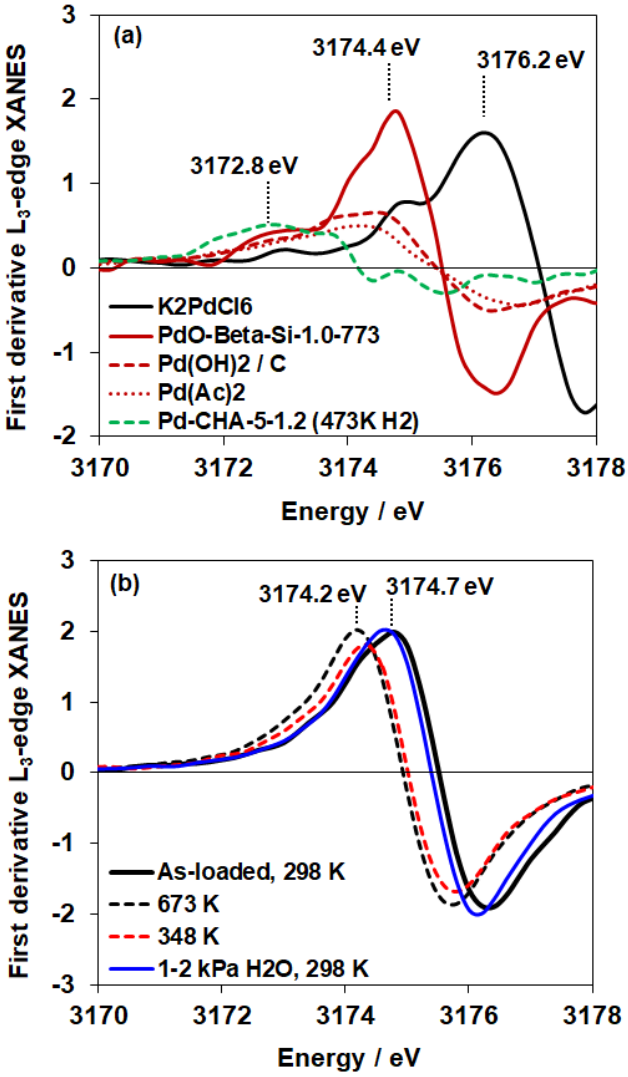

Figure 2.35. (a) First derivative analysis of Pd L_3-edge XANES for Pd reference compounds: metallic Pd nanoparticles (green dashed, treatment of Pd-CHA-5-1.4-923 in 5 kPa H_2 at 473 K), Pd(II) acetate (dotted red, 98%, Sigma Aldrich), Pd(II) hydroxide on carbon (red dashed, 20 wt%, Sigma Aldrich), agglomerated PdO domains on siliceous Beta (red line, Pd-Beta-Si-1.0-773), and Potassium hexachloropalladate(IV) (black, 99%, Sigma Aldrich). (b) First derivative analysis of L_3-edge XANES of a predominantly mononuclear sample, Pd-CHA-5-1.2-923. The sample was first scanned as-loaded in flowing He (solid black), then treated to 673 K in flowing 5 kPa O_2 in balance He (black dashed). The sample was cooled in flowing 5 kPa O_2 in He to 348 K (red dashed), then cooled to 298 K with 1−2 kPa H_2O (solid blue).

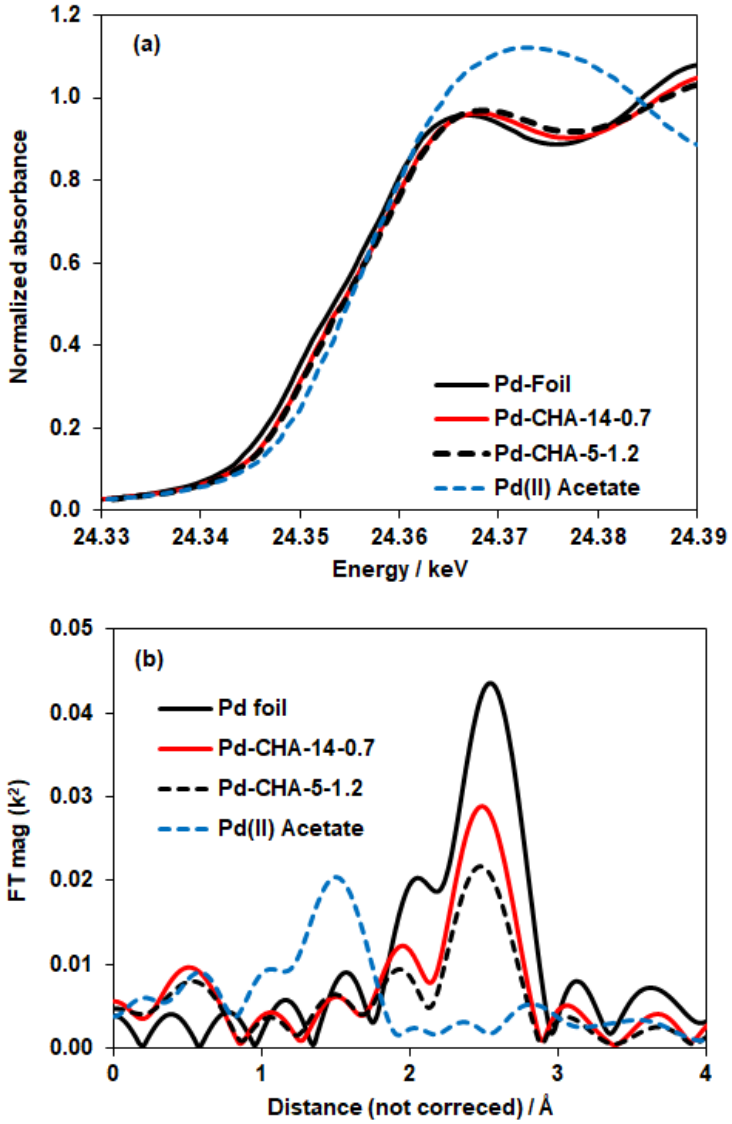

Figure 2.36. Ambient temperature Pd K-edge XANES (a) and EXAFS (b) region of Pd-CHA-14(10%)-0.7-823 (red) and Pd-CHA-5-1.2-923 (dashed black) after treatment in flowing 5 kPa H_2 to 473 K (gray) for 0.5 h. Samples were cooled in flowing UHP He with an in-line O_2 trap to decompose Pd-H species and mitigate reaction of metallic Pd with O_2. Reference spectra of Pd foil (solid black) and Pd(II) acetate (dashed blue) were collected under ambient atmosphere.

2.8.7 Temperature programmed desorption

Temperature programmed desorption (TPD) experiments were performed with a Micromeritics Autochem II 2920 Chemisorption analyzer connected to an MKS Cirrus 3 residual gas analyzer. Samples (0.03–0.06 g) were treated to 873 K (0.167 K s^{-1}) in flowing He (0.833 cm^3 s^{-1}). The H_2 was quantified using m/z = 2, NH_3 was quantified using m/z = 17 (after subtracting contributions from residual water, determined from the m/z = 17/18 fragment ratio for water and the measured m/z = 18 signal), and N_2 was quantified using m/z = 28.

The origin of the $[Pd(NH_3)_4]^{2+}$ agglomeration pathway was further investigated by monitoring the species desorbed during a TPD in inert (He) for a series of as-exchanged Pd-CHA-12(24%) samples with varied Pd loading (0.4–2.2 wt% Pd). Three distinct NH_3 desorption features with maximum desorption rates around 373, 550 and 730 K were observed. Although crystallite-scale and bed-scale re-adsorption and diffusion effects in microporous materials influence desorption peak maximum temperatures [101], [102], thus complicating their assignment to different NH_3 binding site types, we note that the NH_3 desorption peak near 550 K increased systematically with Pd loading, suggesting this peak may reflect desorption of NH_3 from $[Pd(NH_3)_4]^{2+}$ species (the d-d transition for $[Pd(NH_3)_4]^{2+}$ disappears by 598 K in air, Figure 2.1, main text) or residual NH_3 that remained physisorbed or bound to Lewis acid sites after the sample was contacted with the aqueous $Pd(NH_3)_4(NO_3)_2$ solution [103]–[105]. Additionally, a sharp decrease in NH_3 desorption rate near 573 K coincided with the evolution of H_2 and N_2, which increased systematically with Pd loading, likely as result of NH_3 or NH_4NO_3 decomposition. Consequently, the formation of H_2 at elevated temperatures (>500 K) reduced Pd^{2+} species and caused their agglomeration to metallic Pd domains (evidence of complete Pd reduction with H_2 by 500 K in Section 2.4.2.1., main text) [29]. For all Pd-containing samples, sufficient amounts of H_2 (>20 per Pd) were formed to allow for stoichiometric reduction of all Pd^{2+} species (Table 2.8). The NH_3 desorption feature centered at 730 K, which likely reflects desorption from Brønsted acid sites, did not vary systematically with Pd content. This suggests that $[Pd(NH_3)_4]^{2+}$ complexes are preferentially located at external crystallite surfaces (consistent with TEM, XPS, and diffusion-limited NH_4^+ ex-

change of mononuclear Pd^{2+}, main text) rather than at intracrystalline framework Al sites. These complexes appear to be stabilized by various counteranions, including nitrate anions in crystal form, two framework Al sites in close proximity near crystallite surfaces, or two deprotonated silanol groups that may form under incipient wetness impregnation conditions. The preferential siting of $[Pd(NH_3)_4]^{2+}$ complexes near CHA crystallite surfaces may reflect intraporous transport restrictions imposed by the larger diameter of these complexes (ca. 4.5 Å) [100] than the pore-limiting diameter of CHA (3.7 Å) [94]. From Table 2.8, the H_2 generated per Pd was >6 and the N_2 generated per Pd was >2; both values were greater than the amount expected if H_2 and N_2 only formed from $[Pd(NH_3)_4]^{2+}$ complexes. Therefore, this suggests additional species were present on the as-exchanged Pd-CHA sample that can decompose to form of H_2 at 573 K, which may lead to the reduction and agglomeration of Pd.

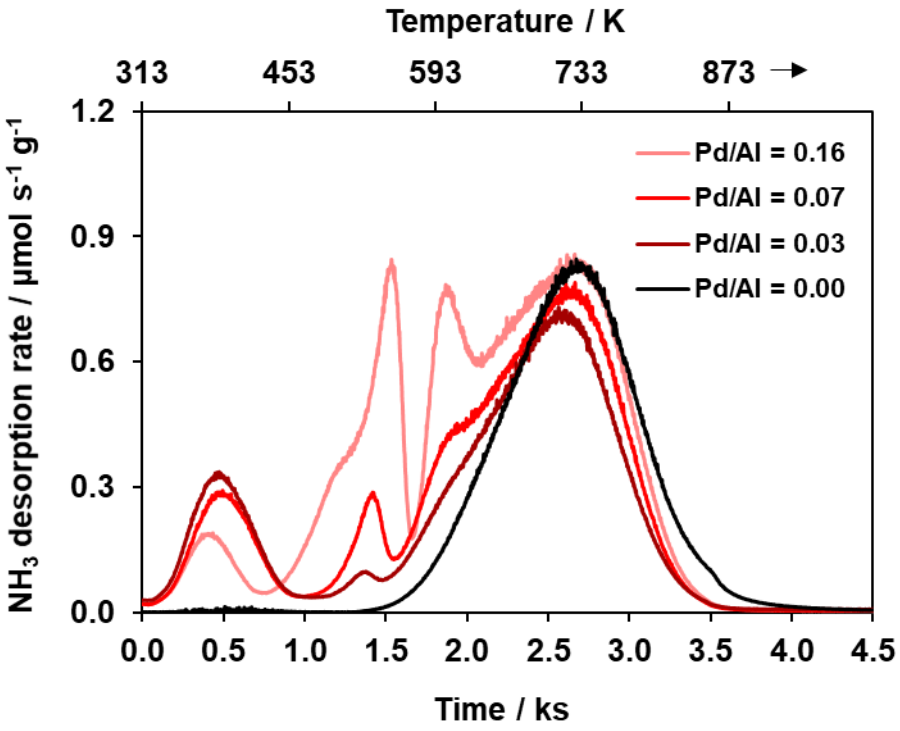

Figure 2.37. NH_3 desorption rates as a function of time and temperature for a series of as-exchanged $[Pd(NH_3)_4]^{2+}$-CHA-12(24%) zeolites of varying Pd content (0–2.2 wt% Pd). Arrow on top x-axis represents a temperature hold at 873 K.

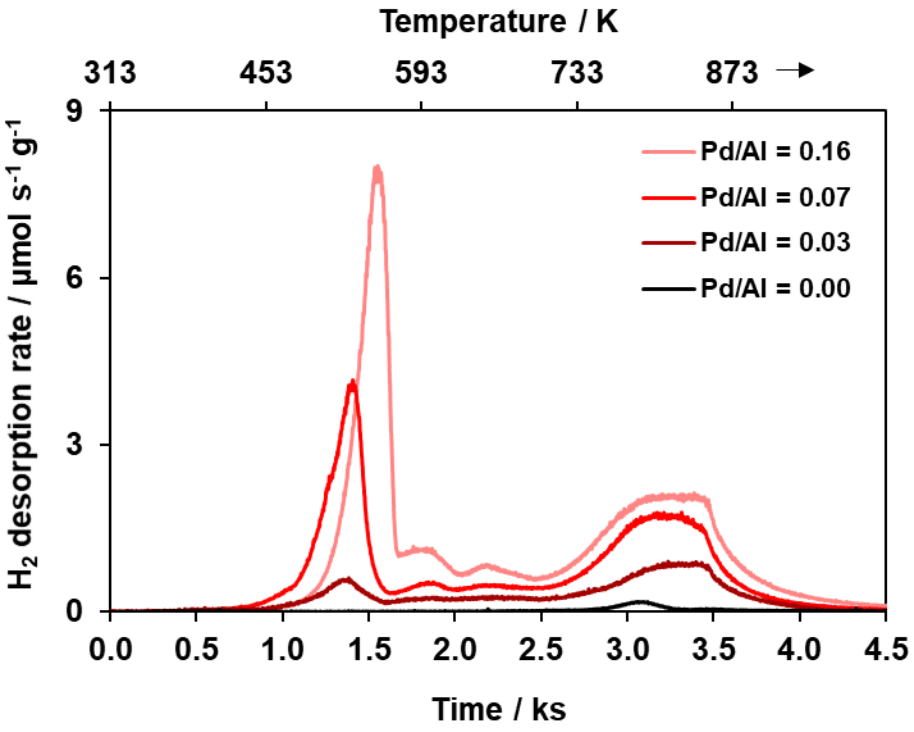

Figure 2.38. H2 desorption rates as a function of time and temperature for a series of as-exchanged $[Pd(NH_3)_4]^{2+}$-CHA-12(24%) zeolites of varying Pd content (0–2.2 wt% Pd). Arrow on top x-axis represents a temperature hold at 873 K.

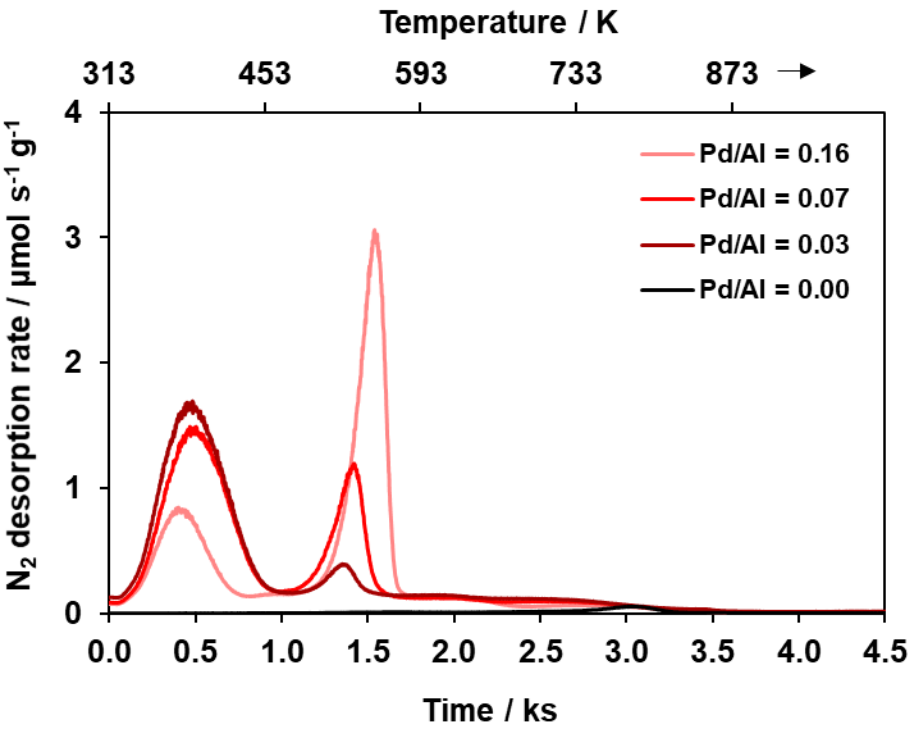

Figure 2.39. N_2 desorption rates as a function of time and temperature for a series of as-exchanged $[Pd(NH_3)_4]^{2+}$-12(24%) zeolites of varying Pd content (0–2.2 wt% Pd). Arrow on top x-axis represents a temperature hold at 873 K.

Table 2.8. NH_3, H_2, and N_2 TPD quantifications from Figures 2.37, 2.38, and 2.39 for a series of as-exchanged $[Pd(NH_3)_4]^{2+}$-CHA-12(24%) zeolites of varying Pd content (0–2.2 wt% Pd).

Sample name	Pd/Al	NH_3/Al	N_2/Al	H_2/Al	H_2/Pd
NH_4-CHA-12(24%)	0.00	0.66	0.03	0.05	–
Pd-CHA-12(24%)-0.35	0.03	0.73	1.52	0.88	34
Pd-CHA-12(24%)-1.0	0.07	0.83	1.41	2.30	31
Pd-CHA-12(24%)-2.2	0.16	1.09	1.39	3.47	22

2.8.8 H_2 temperature programmed reduction

H_2 temperature programmed reduction (TPR) experiments were performed with a Micromeritics Autochem II 2920 Chemisorption analyzer, and an internal thermal conductivity detector was used to quantify H_2 consumption. Samples (0.03–0.10 g) were pretreated in flowing air (0.83 cm^3 s^{-1}) to a designated temperature with a ramp rate of 0.167 K s^{-1}. Samples were then cooled to 373 K in air before cooling in Ar to 203 K. If noted, samples were hydrated at 303 K in 1–2 kPa H_2O in balance Ar (0.5 cm^3 s^{-1}) for 0.5 h before cooling to 203 K in Ar. Sub-ambient temperatures were achieved using a Micromeritics Cryocooler.

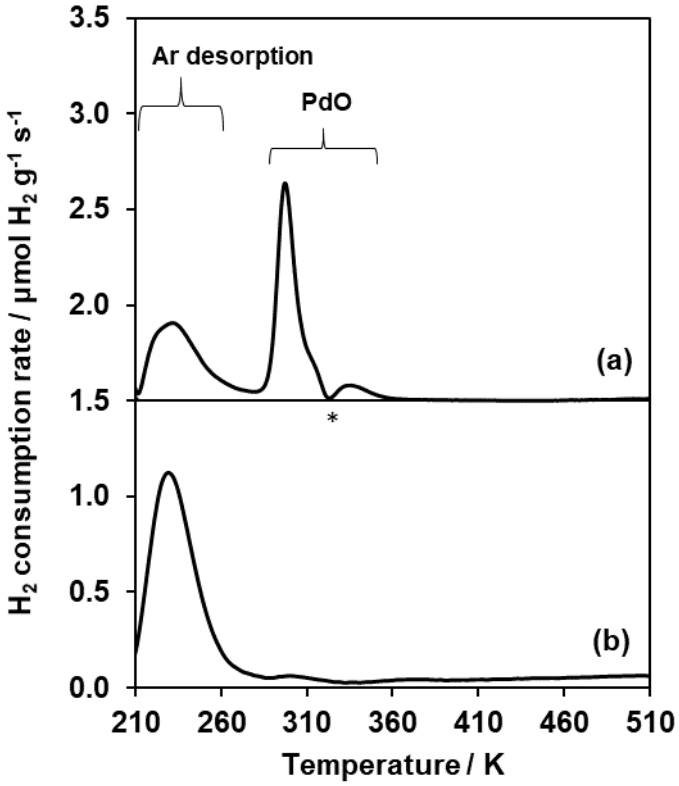

Figure 2.40. H_2 TPR profiles for (a, offset +1.5 units) PdO-CHA-Si-1.4 and (b) H-CHA-14(10%) after pretreatment in flowing air to 823 K (0.167 K s^{-1}, 0.5 cm^3 s^{-1}). H_2 consumption features are labeled for clarity. Asterisk (*) denotes Pd0-H decomposition.

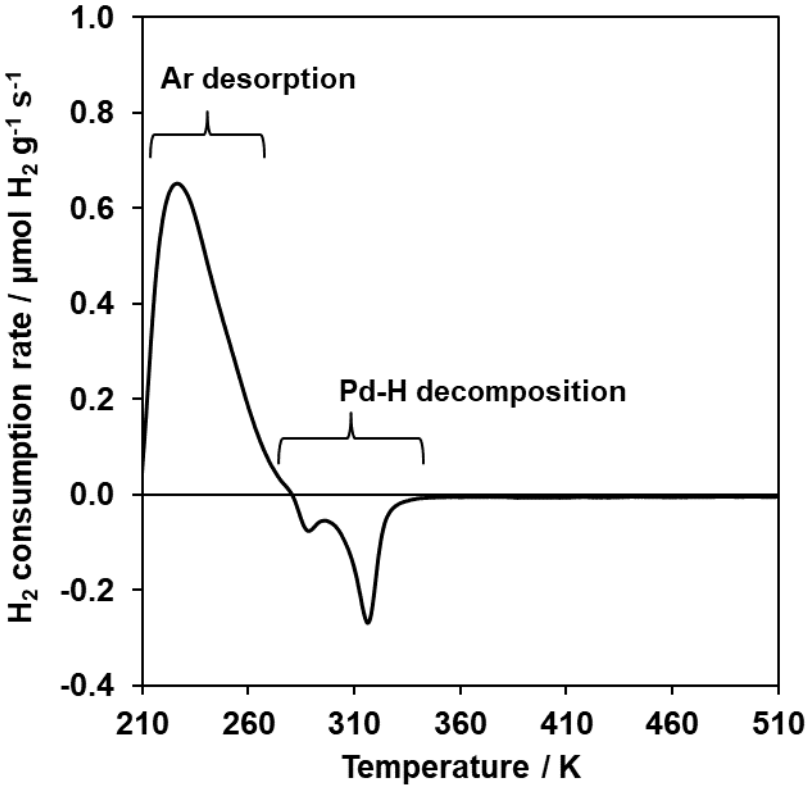

Figure 2.41. H_2 TPR profile of an as-exchanged Pd-CHA-12(24%)-1.5-298 sample pretreated in flowing He (0.83 cm^3 s^{-1}) to 773 K (0.167 K s^{-1}, 1 h).

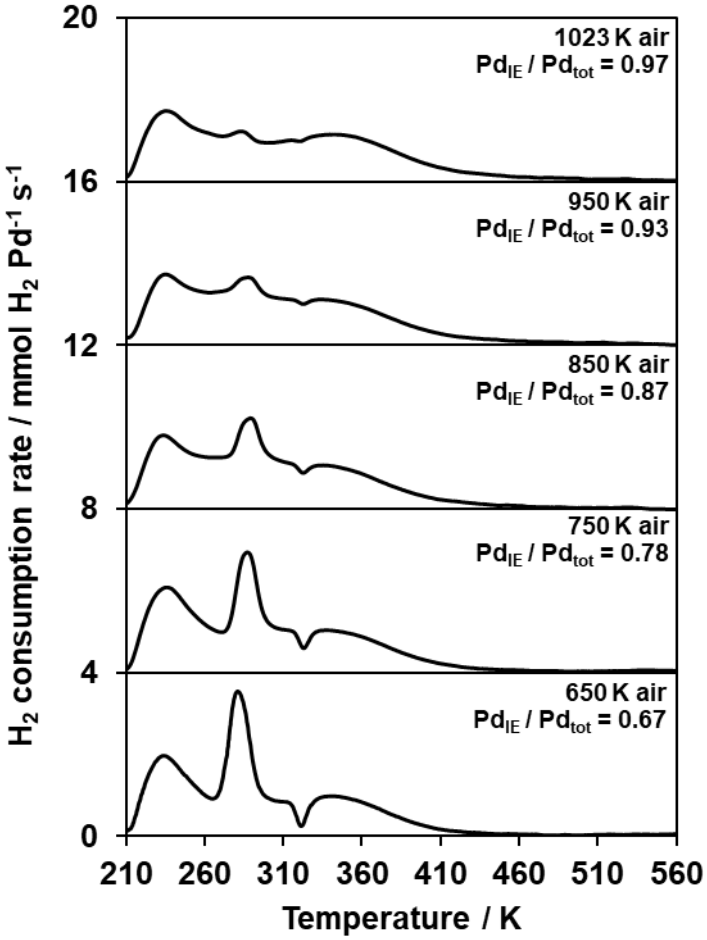

Figure 2.42. H_2 TPR profiles for a dehydrated Pd-CHA-12(24%)-1.5-298 material. The sample was first pretreated in flowing air (0.5 cm^3 s^{-1}) to 650 K (0.167 K s^{-1}) for 1 h before H_2 TPR characterization (bottom). The sample was subsequently cycled between increasing air pretreatments (750-1023 K) and H_2 TPR characterizations. Profiles are offset +4 units and listed with air pretreatment temperature and amounts of mononuclear Pd^{2+} cations (Pd_{IE}) per total Pd.

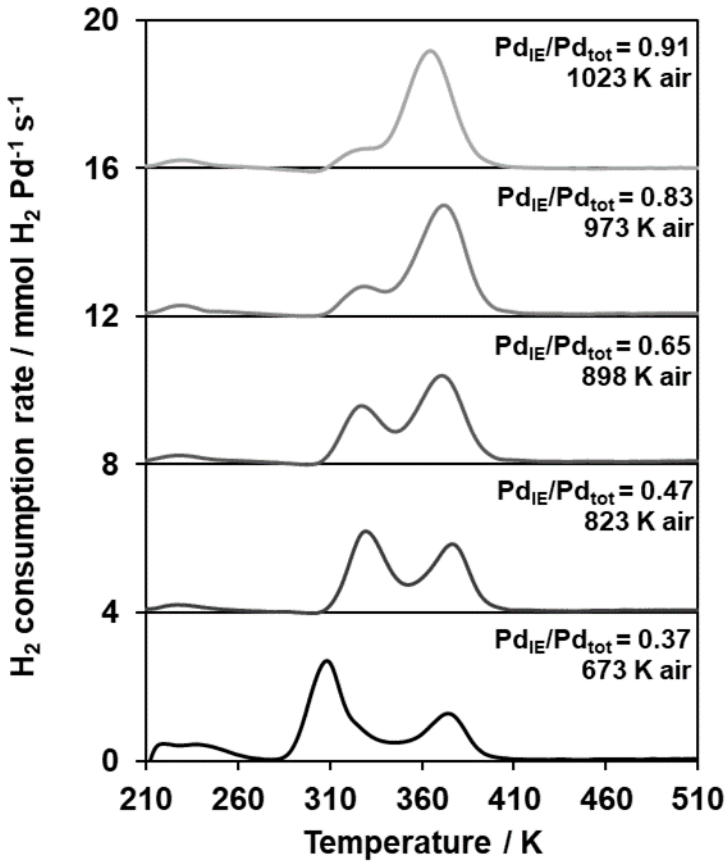

Figure 2.43. H_2 TPR profiles of a hydrated Pd-CHA-12(18%)-3.9-298 sample. The sample was first pretreated in flowing air (0.5 cm^3 s^{-1}) to 673 K (0.167 K s^{-1}) for 1 h before TPR characterization (bottom, black). The sample was subsequently cycled between increasing air pretreatments (673–1023 K, black to gray) and TPR characterizations. Profiles are offset +4 units and labeled with air pretreatment temperature and amounts of mononuclear Pd^{2+} ions (Pd_{IE}) per total Pd.

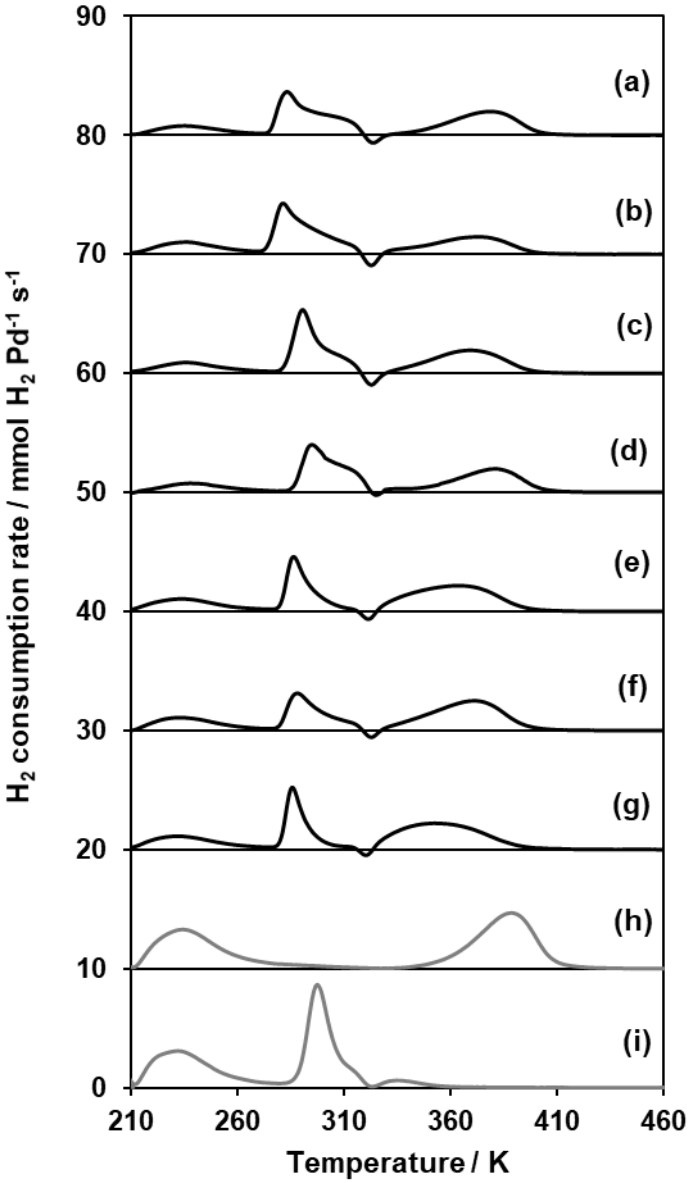

Figure 2.44. H_2 TPR profiles of hydrated Pd-CHA-12(24%)-3.3 reported in Table 2.3 of the main text and also summarized in Table 2.9. Black profiles (a-g) correspond to hydrated Pd-CHA-12(24%)-3.3 samples with different air pretreatment conditions (0.5 cm^3 s^{-1}, 0.167 K s^{-1}, 1 h, Table 2.9). Gray profiles correspond to reference TPR profiles of(h) predominantly hydrated, mononuclear Pd-CHA-5-1.2-923 and (i) PdO reference (PdO-CHA-Si-1.4-823). Profiles offset +10 units for clarity.

Table 2.9. A summary of TPR profile treatments in Figure 2.44

Profile designations in Figure 2.44	Air treatment temperature / K
(a)	773
(b)	673
(c)	773
(d)	773*
(e)	1023
(f)	773
(g)	1023

*Treatment also contained 1–2 kPa H_2O.

2.8.9 NH_4^+ back-exchange of Pd-CHA samples

Table 2.10. Effect of NH_4^+ back-exchange conditions with Pd-CHA-11-0.9-1023.

Temperature / K	NH_4NO_3 concentration	Time / days	Pd_{IE}/Pd_{tot}	Pd_{IE} content / μmol g^{-1} (TPR)	Pd_{IE} content / μmol g^{-1} (NH_4^+)
338	1.0 M	1.0	1.0	85	5.0
363	2.0 M	1.0	1.0	85	13
363	2.0 M	14	1.0	85	55

Table 2.11. Summary of H_2 TPR and NH_4^+ back-exchange with varied air treatments.

Sample Name	Air temp / K	Pd_{IE}/Pd_{tot} (TPR)	Pd_{IE} content / μmol g^{-1} (TPR)	Pd_{IE} content / μmol g^{-1} (NH_4^+)
Pd-CHA-11-0.9	823	1.0	85	14
	1023	1.0	85	5.0
Pd-CHA-12(24%)-2.2	823	0.59	120	32
	1023	0.93	190	18

2.8.10 Infrared spectroscopy

From Figure 2.5 in the main text, pretreatment of Pd-exchanged zeolites to 1023 K in flowing air increases the amount of mononuclear Pd^{2+} formed. The custom-built infrared cell [56] used cannot reach these temperatures, so samples were pretreated in flowing air (Air Zero, Indiana Oxygen) to 1023 K in a muffle furnace before preparing wafers for IR characterization (Figure 2.45 and 2.46) to maximize their mononuclear Pd^{2+} contents. Samples were then treated in the custom-built cell under flowing 20 kPa O_2 in balance He (0.83 cm^3 s^{-1}) to 723 K for 1 h (0.083 K s^{-1}) before cooling to 473 K for at least 500 scans. Four main peaks were identified in the OH stretching region of IR spectra for all samples: 3735 cm^{-1} for terminal silanol groups [106], 3660 cm^{-1} for $[PdOH]^+$ and extraframework Al [38], [87], and 3600 and 3577 cm^{-1} for Brønsted acid sites [107].

For CHA materials containing predominantly isolated Al sites (i.e., no Co^{2+}-titratable 6-MR 2Al sites), DFT calculations suggest that a plausible mononuclear Pd^{2+} species is $[PdOH]^+$ [38]. Therefore, a parent CHA zeolite was synthesized with nominally isolated Al sites (Co^{2+}/Al = 0.006), deposited with varying amounts of Pd, pretreated in flowing air to 1023 K to attempt to maximize the number of putative $[PdOH]^+$ species, and the H- and Pd-forms were characterized by IR spectroscopy (Figure 2.45). Brønsted acid site peak areas (3600, 3577 cm^{-1}) were similar for the H-form and Pd-form sample with low Pd content (Pd_{IE}/Al = 0.04), but were lower for the Pd-form sample with higher Pd content (Pd_{IE}/Al = 0.09), qualitatively consistent with the exchange of H+ sites with mononuclear Pd^{2+} sites. The Si-OH feature (3735 cm^{-1}) changed non-systematically with total Pd and mononuclear Pd^{2+} content (Figure 2.45). Lastly, a feature at 3660 cm^{-1} was visible on the Pd-exchanged samples and not clearly visible on the parent H-CHA material, qualitatively consistent with the presence of $[PdOH]^+$, although we note that contributions from OH groups from partial or fully extraframework Al sites may also appear in this range [87].

The same experimental protocol was performed, instead using a CHA parent material that contained a much larger amount of 6-MR Al pairs (24%, Co^{2+}/Al = 0.12), with analogous IR spectra shown in Figure 2.46. The Si-OH and Brønsted acid site peak areas were both higher for the Pd-exchanged sample, which suggests the H-form zeolite may have dea-

luminated to a greater extent upon treatment in air to 1023 K, consistent with prior reports that extraframework cations may protect framework Al sites against hydrolysis [108]. In the 3660 cm^{-1} region, there was no clear feature assignable to extraframework Al-associated OH groups or $[PdOH]^{+}$ sites, consistent with previously reported IR spectra of Pd-CHA samples that contained lower amounts of mononuclear Pd^{2+} than the number of 6-MR Al pairs.28 Therefore, the majority of mononuclear Pd^{2+} sites on this material are likely Z_2Pd, consistent with previous DFT and experimental results that conclude Z_2Pd is the most thermodynamically stable mononuclear Pd^{2+} species [38].

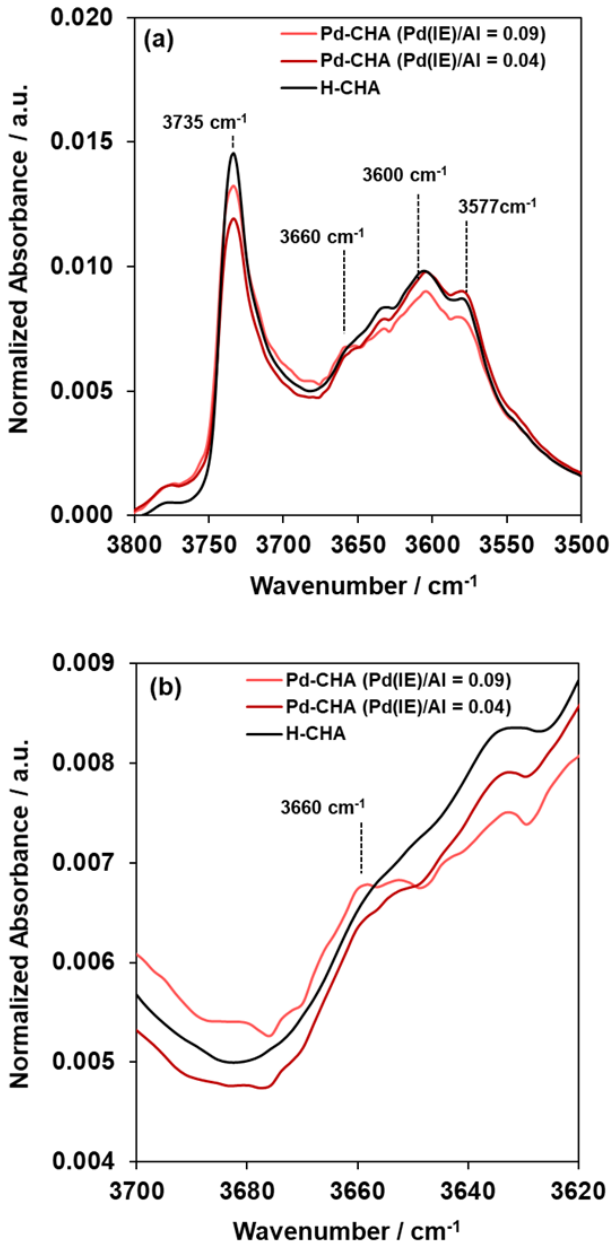

Figure 2.45. (a) OH stretching region of a parent H-CHA-15(1.2%) (black), Pd-CHA-15(1.2%)-1.2 (dark red), and Pd-CHA-15(1.2%)-2.3 (light red) treated ex situ in air to 1023 K. Samples were treated in situ in 20 kPa O_2 in balance He to 723 K before cooling to 473 K to collect spectra. The amount of mononuclear Pd^{2+} per Al (Pd(IE)/Al) measured by H_2 TPR after a 1023 K air treatment for each sample is listed in parentheses. (b) 3660 cm^{-1} region enlarged for clarity.

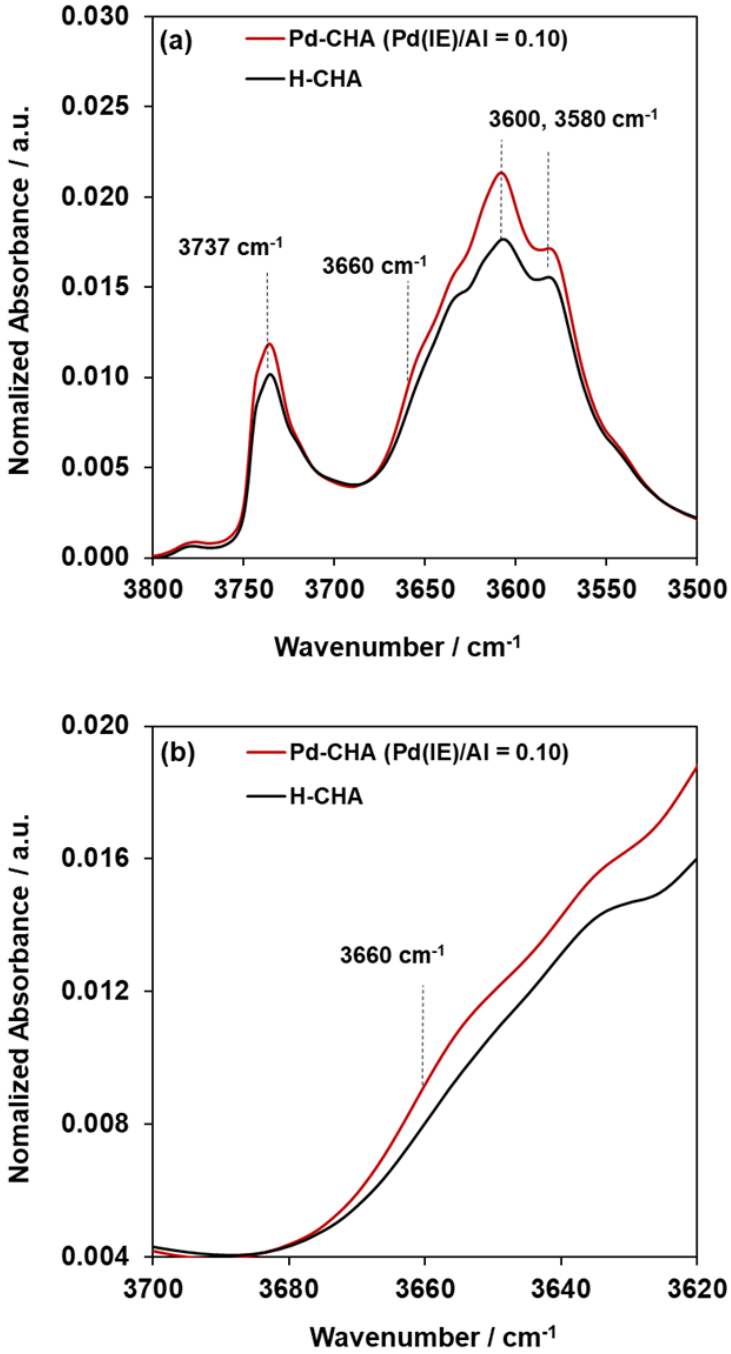

Figure 2.46. (a) OH stretching region of a parent H-CHA-12(24%) (black) and Pd-CHA-12(24%)-1.5 (red) treated ex situ in air to 1023 K. Samples were treated in situ in 20 kPa O_2 in balance He to 723 K before cooling to 473 K to collect spectra. The amount of mononuclear Pd^{2+} per Al (Pd(IE)/Al) measured by H_2 TPR after a 1023 K air treatment is listed in the parentheses. (b) 3660 cm^{-1} region enlarged for clarity.

2.8.11 O_2 chemisorption

Figure 2.47 shows O_2 chemisorption data after treatment in O_2 or H_2 to the listed temperature. The last dispersion measurement (O/Pd = 0.03, 3% dispersion) was collected after treatment to 1023 K in pure H_2, demonstrating that a higher temperature treatment in H_2 (than 573 K as used in the main text) caused significant Pd sintering and erased memory of 1023 K air treatments resulting in formation of large Pd particles.

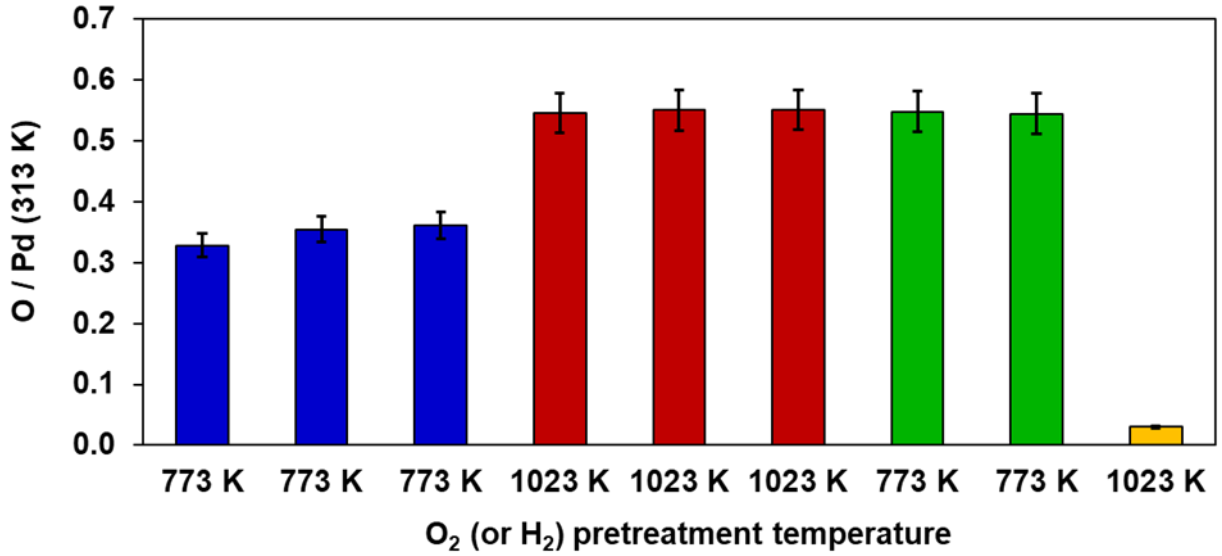

Figure 2.47. O_2 chemisorption (313 K; mol O adsorbed per Pd_{tot}) cycling experiments of a Pd-CHA-12(24%)-2.2 sample. Sample was sequentially treated in O_2 (listed left to right: blue for 773 K, red for 1023 K, and green for subsequent 773 K treatment), followed by reduction H_2 at 573 K, and then O_2 adsorption at 313 K. Last measurement (yellow) is after treatment in H_2 to 1023 K.

2.8.12 Transmission electron microscopy and energy-dispersive spectroscopy

An as-exchanged $[Pd(NH_3)_4]^{2+}$-CHA-12(24%)-1.5 sample was characterized ex situ with scanning transmission electron microscopy (HAADF-STEM) and energy-dispersive spectroscopy (EDS) (Figures 2.49, 2.50, and 2.51) after air treatments. Pd agglomerates were present on the as-exchanged $[Pd(NH_3)_4]^{2+}$-CHA-12(24%)-1.5 sample. DRUV-vis (Figure 2.18) and XAS (Table 2.6, Figure 2.30) data of as-exchanged $[Pd(NH_3)_4]^{2+}$-CHA-12(24%) samples showed the majority of the Pd is mononuclear as $[Pd(NH_3)_4]^{2+}$, suggesting that the agglomerates observed with STEM are $Pd(NH_3)_4(NO_3)_2$ crystals. The sample treated in air to 773 K also contained Pd agglomerates, likely PdO domains. The sample treated in air to 1023 K showed lower amounts of Pd agglomerates, consistent with H_2 TPR data (Figure 2.5) indicating that air treatment to progressively higher temperatures convert greater amounts of agglomerated domains into mononuclear Pd^{2+}.

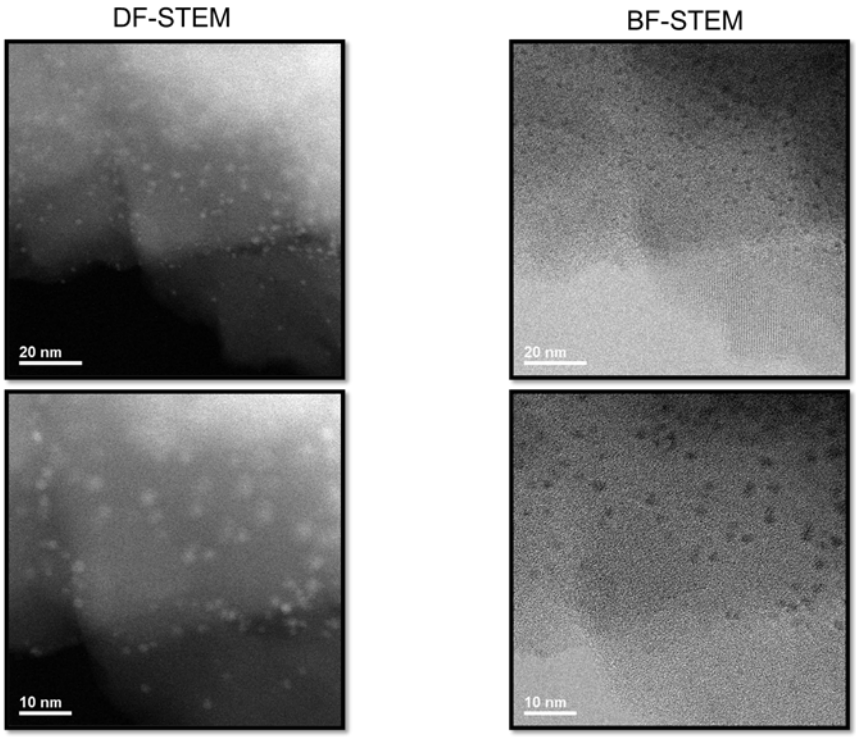

Figure 2.48. Ex situ HAADF-STEM (left) and BF-STEM (right) images of a Pd-CHA-14(10%)-0.7-823 sample.

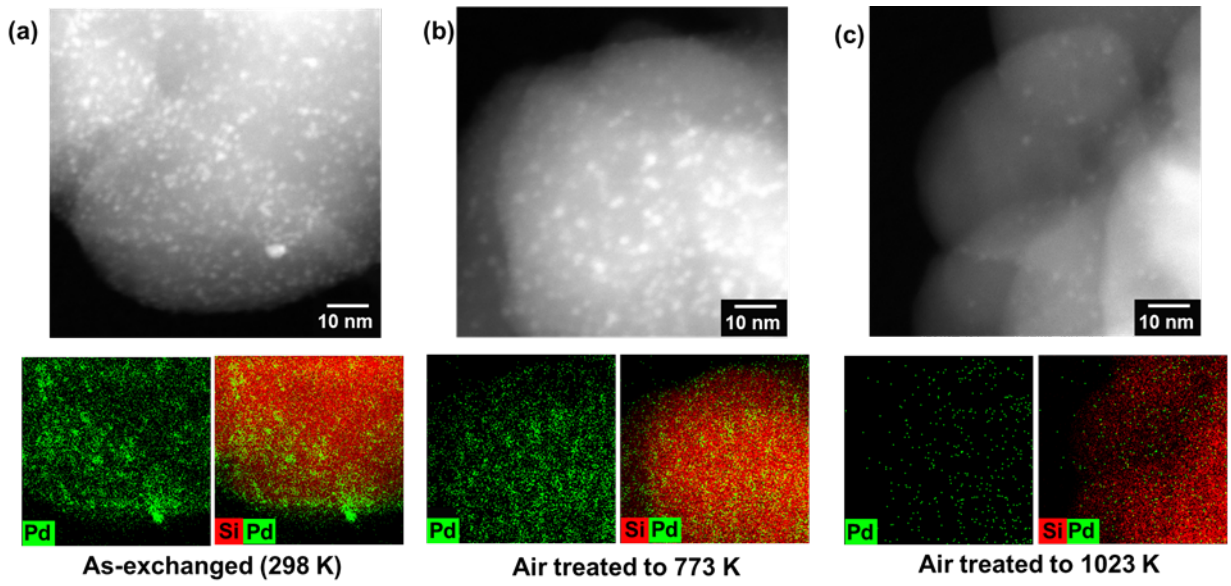

Figure 2.49. Ex situ HAADF-STEM (top panels) and EDS of Pd (green) and Si (red) at 1.25 Mx (bottom panels) of a Pd-CHA-12(24%)-1.5 sample treated in air to (a) 298 K, (b) 773 K, and (c) 1023 K.

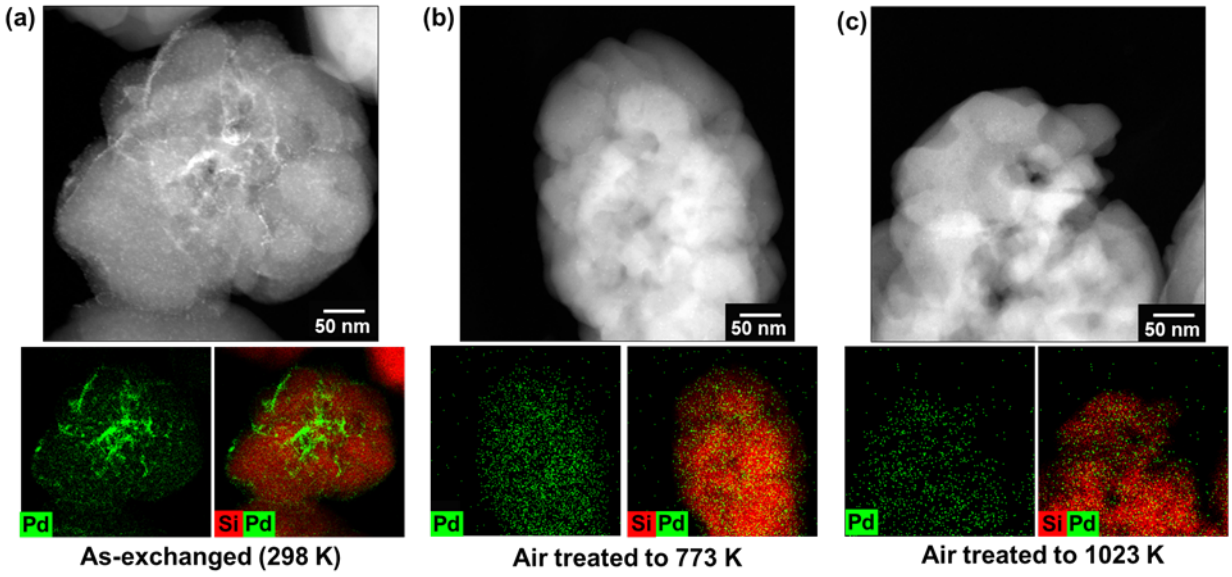

Figure 2.50. Ex situ HAADF-STEM (top panels) and EDS of Pd (green) and Si (red) at 320 kx (bottom panels) of a Pd-CHA-12(24%)-1.5 sample treated in air to (a) 298 K, (b) 773 K, and (c) 1023 K.

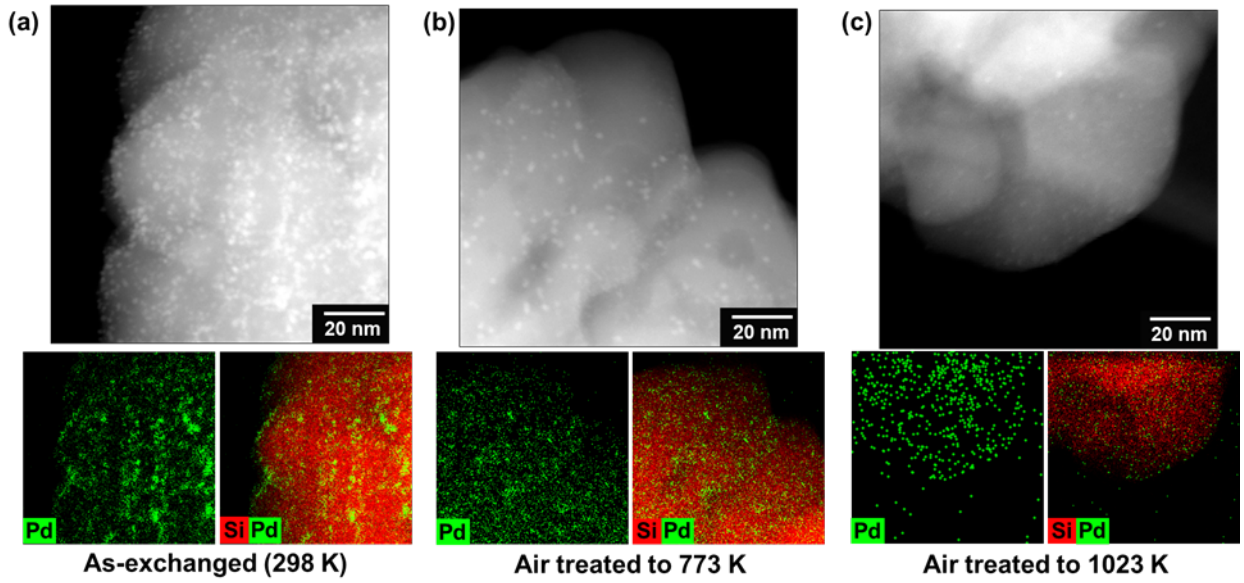

Figure 2.51. Ex situ HAADF-STEM (top panels) and EDS of Pd (green) and Si (red) at 900 kx (bottom panels) of a Pd-CHA-12(24%)-1.5 sample treated in air to (a) 298 K, (b) 773 K, and (c) 1023 K.

EDS quantifications were performed at various locations on crystallites to investigate changes in Pd spatial distribution as a function of temperature (Figures 2.52, 2.53, 2.54, 2.55, 2.56, 2.57). For all experiments, there were no clear differences in Pd atomic concentrations between the surface or center regions of the same crystallite. The low signal-to-noise caused these EDS data to be inconclusive in determining changes to Pd spatial distribution in CHA crystallites.

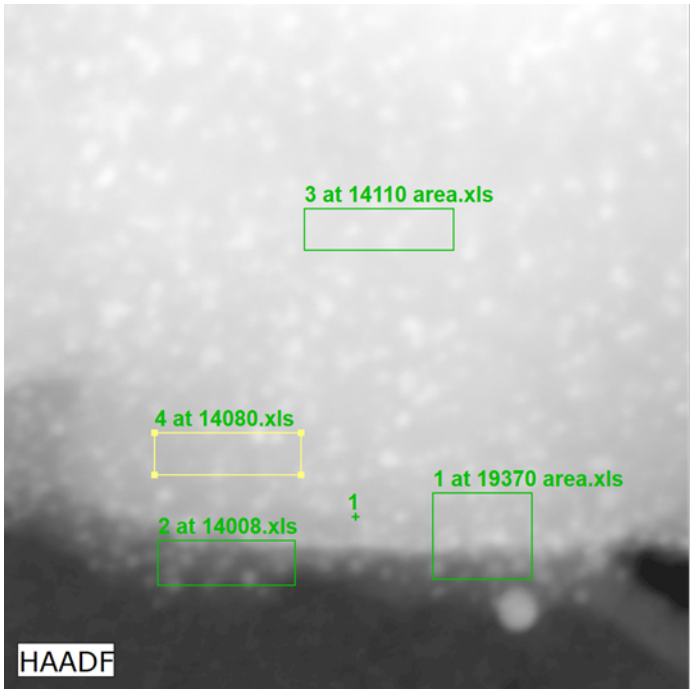

Atomic %	Spot 1 (side)	Spot 2 (side)	Spot 3 (middle)	Spot 4 (middle)
Pd	0.91	0.61	0.13	-
Si	20.15	18.10	27.58	-
Al	2.73	2.57	3.39	-

Figure 2.52. EDS spots with quantifications (1.25 Mx) for an as-exchanged Pd-CHA-12(24%)-1.5 sample previously treated in air to 298 K.

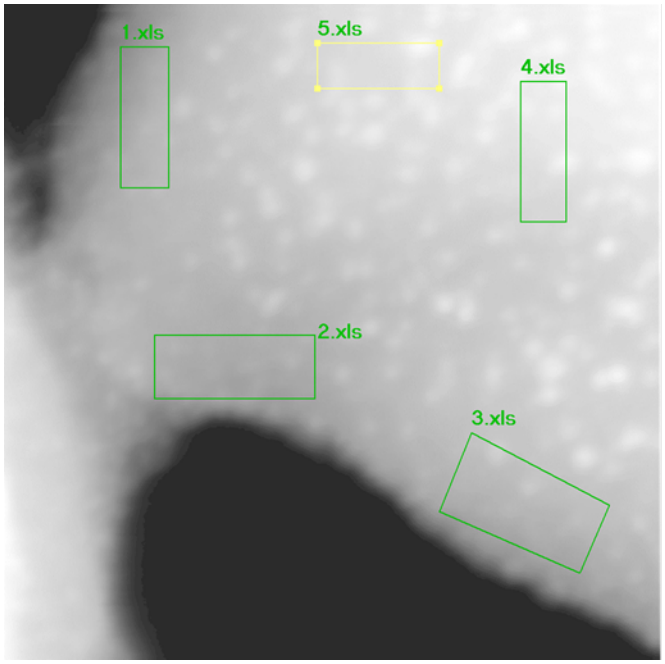

Atomic %	Spot 1 (side)	Spot 2 (side)	Spot 3 (side)	Spot 4 (middle)	Spot 5 (middle)
Pd	0.15	0.27	0.23	0.26	0.47
Si	29.36	29.07	29.22	25.70	28.10
Al	3.35	3.90	3.53	2.92	2.72

Figure 2.53. EDS spots with quantifications (1.25 Mx) for a Pd-CHA-12(24%)-1.5 sample previously treated in air to 773 K.

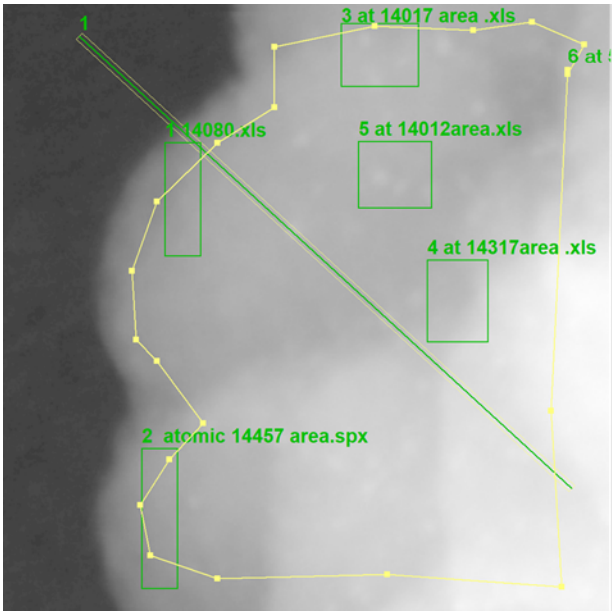

Atomic %	Spot 1 (side)	Spot 2 (side)	Spot 3 (side)	Spot 4 (middle)	Spot 5 (middle)	Spot 6 (entire area)
Pd	0.00	0.00	0.07	0.00	0.11	0.06
Si	19.72	20.77	23.63	22.35	19.51	23.33
Al	1.59	2.41	2.45	2.45	2.17	2.45

Figure 2.54. EDS spots with quantifications (1.25 Mx) for a Pd-CHA-12(24%)-1.5 sample previously treated in air to 1023 K.

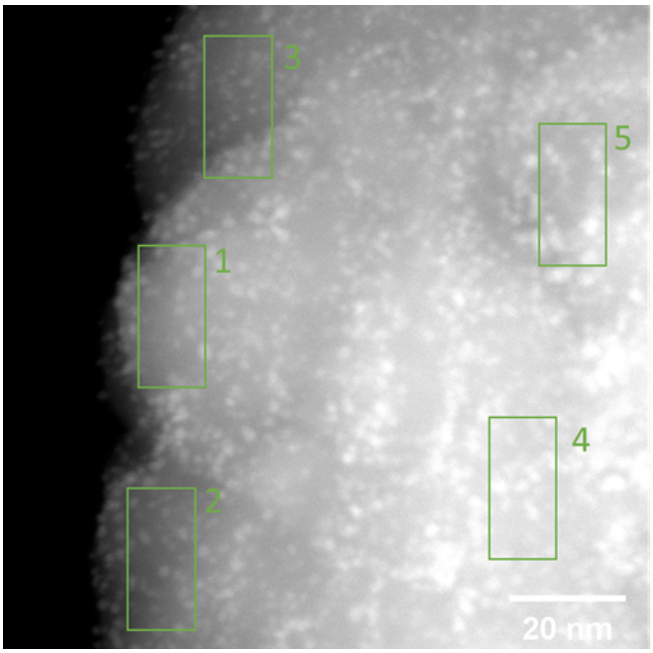

Atomic %	Spot 1 (side)	Spot 2 (side)	Spot 3 (side)	Spot 4 (middle)	Spot 5 (middle)
Pd	0.42	0.35	0.32	0.46	0.31
Si	28.56	26.42	25.23	24.40	27.77
Al	3.27	3.31	2.66	2.60	3.16

Figure 2.55. EDS spots with quantifications (900 kx) for an as-exchanged Pd-CHA-12(24%)-1.5 sample previously treated in air to 298 K.

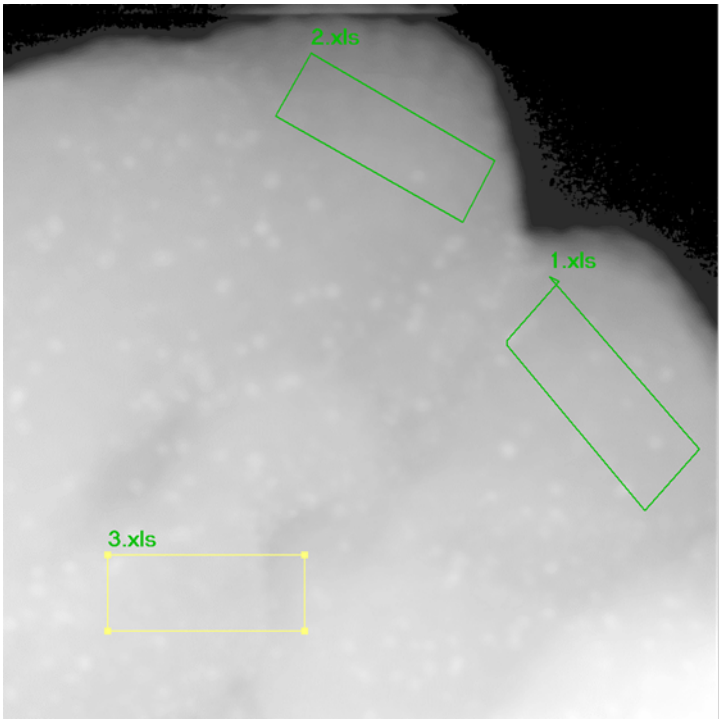

Atomic %	Spot 1 (side)	Spot 2 (side)	Spot 3 (middle)
Pd	0.07	0.05	0.15
Si	27.03	27.80	27.46
Al	3.12	3.15	2.80

Figure 2.56. EDS spots with quantifications (900 kx) for a Pd-CHA-12(24%)-1.5 sample previously treated in air to 773 K.

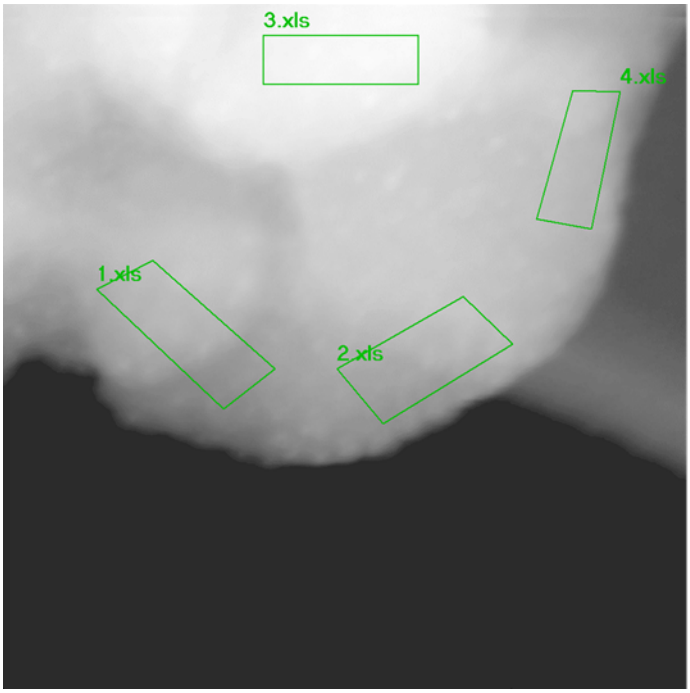

Atomic %	Spot 1 (side)	Spot 2 (side)	Spot 3 (middle)	Spot 4 (side)
Pd	0.22	0.07	0.08	0.01
Si	29.13	21.03	25.79	22.99
Al	3.69	2.94	3.21	2.99

Figure 2.57. EDS spots with quantifications (900 kx) for a Pd-CHA-12(24%)-1.5 sample previously treated in air to 1023 K.

2.8.13 X-ray photoelectron spectroscopy

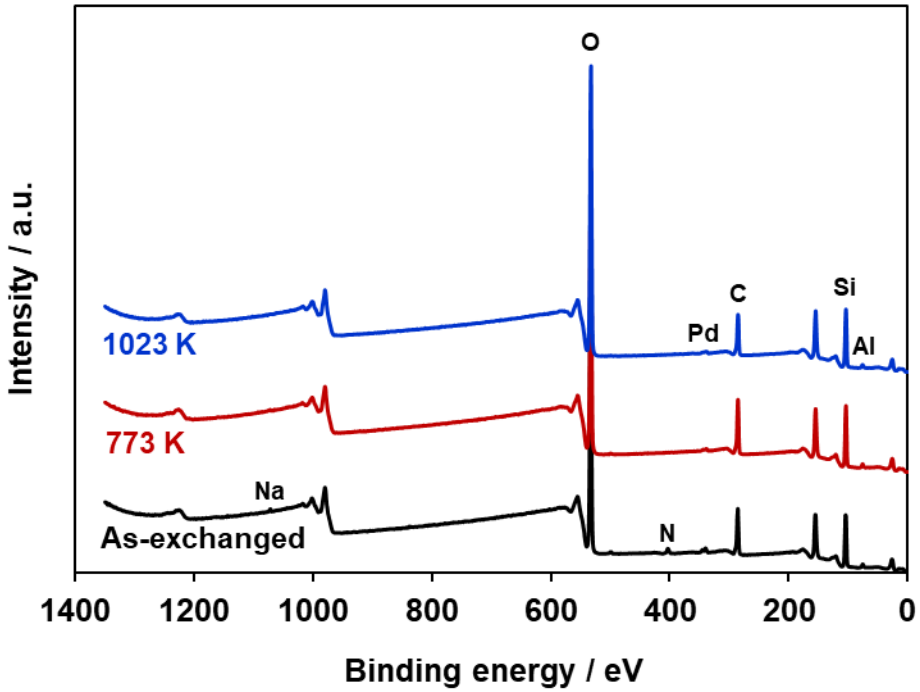

Figure 2.58. X-ray photoelectron spectra of Pd-CHA-12(24%)-1.5 samples. Bottom spectrum (black) is of the as-exchanged material, middle spectrum (red) is after treatment in air to 773 K, and top spectrum (blue) is after treatment in air to 1023 K.

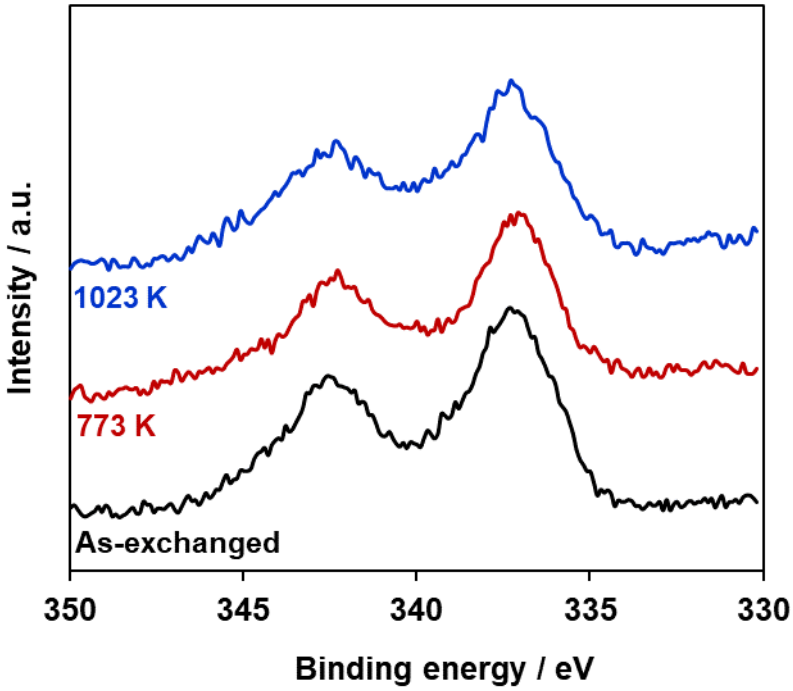

Figure 2.59. X-ray photoelectron spectra (Pd 3d binding energy range) of Pd-CHA-12(24%)-1.5 samples. Bottom spectrum (black) is of the as-exchanged material, middle spectrum (red) is after treatment in air to 773 K, and top spectrum (blue) is after treatment in air to 1023 K.

Table 2.12. Atomic surface (3-5 nm penetration depth and 400 m X-ray spot) composition percentages quantified with X-ray photoelectron spectroscopy for a Pd-CHA-12(24%)-1.5 sample after exchange, treatment in air to 773 K, and treatment in air to 1023 K.

Sample	Al / %	C / %	N / %	O / %	Pd / %	Si / %
As-exchanged	2.4	25.4	1.2	46.9	0.19	23.7
773 K air	2.3	27.9	0.0	46.0	0.15	23.5
1023 K air	2.3	25.2	0.0	47.6	0.13	24.8

3. EFFECTS OF INITIAL PD NANOPARTICLE SIZE AND WATER PRESSURE ON THE FORMATION OF MONONUCLEAR PD(II) CATIONS IN CHA ZEOLITES DURING HIGH-TEMPERATURE AIR TREATMENT

3.1 Abstract

Pd-exchanged CHA zeolites are promising materials for passive NO_x (x = 1, 2) adsorption (PNA) to mitigate low-temperature (<473 K) NO_x emissions in automotive exhaust. The structural lability of Pd leads to undesirable agglomeration and deactivation under PNA-relevant conditions and the redispersion of agglomerates to mononuclear, ion-exchanged Pd^{2+} cation sites upon high-temperature (>700 K) air regeneration treatments, yet the influence of the Pd nanoparticle size and gaseous conditions on the thermodynamic and kinetic factors influencing Pd nanoparticle conversion to ion-exchanged Pd^{2+} remain unclear. Colloidal Pd nanoparticle synthesis and deposition techniques were used to synthesize a series of model Pd-CHA zeolites containing monodisperse Pd particles (2, 7, or 14 nm) on their crystallite surfaces. These materials were treated in flowing air with and without H_2O (<6 kPa) to high temperatures (598–973 K), and the extents of metallic Pd oxidation with O_2 and subsequent conversion of PdO to ion-exchanged Pd^{2+} were quantified with H_2 temperature programmed reduction. These experimental data, together with thermodynamic predictions using DFT calculations, showed that larger Pd particles show greater resistance to bulk oxidation and conversion to ion-exchanged Pd^{2+} sites. Adding H_2O to air streams at high temperatures shift the thermodynamic preference away from Pd^{2+} ion sites toward agglomerated PdO domains, indicating that H_2O present in automotive exhaust may facilitate undesirable agglomeration. Isothermal redispersion kinetic measurements (598–673 K, air with and without H_2O) quantified the transient conversion of metallic Pd nanoparticles to agglomerated PdO and ion-exchanged Pd^{2+} sites, revealing the kinetic irrelevance of O_2 (20 kPa) and H_2O (0–2 kPa) pressures and the increased rates of conversion to Pd^{2+} ions at higher temperatures and for smaller Pd particle sizes. This study shows how combining quantitative experimental measurements on precisely-synthesized model materials with DFT predictions can

provide new insight into the fundamental thermodynamic and kinetic factors that influence the interconversion of agglomerated domains and ion-exchanged metal sites in zeolites.

3.2 Introduction

Synthetic routes to target the preparation of certain distributions of metal nanoparticle or ion-exchanged sites on aluminosilicate zeolite supports requires a fundamental understanding of the thermodynamic and kinetic factors that influence the metal structures. These concepts are particularly relevant for Pd-exchanged zeolites used for passive NO_x adsorption (PNA) [1] in automotive exhaust, because they typically contain various Pd structures [41], [109] of different nuclearity (mono- and polynuclear) [5], [25], [37] and valence (zero- to tetravalent) [6], [27], [32], [33], [110], but only extraframework, mononuclear cation sites charge-compensated by framework Al atoms (ion-exchanged Pd) [28] are the purported precursor sites for NO_x adsorption [2]. An additional complication arises from the structural lability of Pd that allows interconversion between agglomerated domains and mononuclear ion-exchanged sites [29], which depends on the size of Pd nanoparticle domain sizes and their density on the support [11]. The structural lability of Pd allows for undesirable agglomeration and deactivation under PNA-relevant conditions [4], [44], [111], [112], but also for the redispersion of agglomerates to ion-exchanged sites under high-temperature (>500 K) air [113] or NO [114] regeneration treatments via a solid-state ion-exchange mechanism. Together, these challenges and observations motivate improved fundamental understanding of the critical thermodynamic and kinetic factors that govern Pd structural interconversion in zeolites, to guide the design of PNA materials and regeneration protocols based on solid-state ion-exchange routes.

In-situ and ex-situ characterization data demonstrate that external gas conditions strongly influence the number and structures of Pd species present on zeolite supports. Pd-exchanged zeolites treated in H_2 (>5 kPa) above 573 K contain predominantly agglomerated, metallic Pd domains, evidenced by Pd-Pd bond formation (2.5 Å) with in-situ K-edge extended X-ray absorption fine structure spectroscopy [5] and diffraction peaks for metallic Pd in powder X-ray diffractograms [28]. Subsequent treatments in air to high temperatures (>523 K) result

in the oxidation of agglomerated metallic Pd with O_2 to PdO (in-situ XRD) [28] followed by disintegration of PdO domains to ion-exchanged Pd cations, evidenced by quantification of the these two structures by ex-situ H_2 temperature programmed reduction (TPR) [29]. Additionally, progressively higher air temperature treatments (723–1023 K) convert a greater fraction of PdO domains to ion-exchanged Pd, while also driving Pd deeper within zeolite crystallites so as to generate a more homogeneous spatial distribution of Pd throughout the crystallite [113]. A PdO-containing Pd-CHA zeolite (1 wt% Pd, Si/Al = 22, initially treated in air to 773 K) was hydrothermally aged (HTA) under laboratory conditions (1023 K, 15 kPa O_2, 10 kPa H_2O, balance N_2, 25 h) to simulate the lifetime of the PNA material during practical operation, resulting in increased NO_x storage per Pd with no Pd agglomerates observed by ex-situ scanning transmission electron microscopy (STEM) [10]. The addition of H_2O (10 kPa) to the high-temperature (1023 K) air stream was proposed to facilitate the mobility of Pd species to ion-exchanged Pd sites, reminiscent of reports of NH_3 facilitating the transport of Pd^{2+} and Cu^{+} ions to exchange sites in CHA zeolites [97], [115]; however, thermodynamic calculations showed that ion-exchanged Pd ions desorb H_2O ligands above 600 K at 10 kPa H_2O because entropic factors cause the Gibbs free energy of adsorption to become unfavorable [38], indicating that H_2O may have other kinetic or thermodynamic effects on the redispersion of Pd agglomerates to ion-exchanged Pd^{2+}.

The Pd structures and their spatial density initially present on a support also influences the thermodynamics of particle disintegration to mononuclear species. A series of colloidal, monodisperse Pd nanoparticles of varying particle size (2–14 nm) were deposited at a constant Pd density on γ-Al_2O_3 and treated under high-temperature (600–1000 K) conditions to determine the effect of Pd particle size on the conversion to mononuclear $Pd(OH)_2$ at Al_{III} defect sites, qualitatively estimated by methane combustion conversion [11]. Larger fractions of Pd particles were converted to mononuclear Pd species when smaller Pd particles were initially present across all temperatures tested, demonstrating the strong influence of initial Pd particle size influenced the disintegration to mononuclear $Pd(OH)_2$ [11]. The change in Gibbs free energy of adsorption of a mononuclear $Pd(OH)_2$ species at a Al_{III} site, starting from a Pd atom belonging to a 7.9 nm PdO particle, was calculated and used with the Boltzmann distribution equation to quantitatively show that lower Pd spatial densities

resulted in greater conversion to mononuclear $Pd(OH)_2$. However, the dearth of quantitative connections between DFT-predicted thermodynamic calculations and experimental quantification of different Pd site types and densities has impeded fundamental understanding of the relative importance of various thermodynamic and kinetic factors influencing the structural interconversion of Pd particles and ion-exchanged sites on supports.

Here, we combine experiment and theory to understand the influence of initial Pd nanoparticle size and external gas conditions on the thermodynamic and kinetic factors influencing structural conversion between Pd nanoparticles and ion-exchanged Pd^{2+} in CHA zeolites. A series of colloidal Pd nanoparticle solutions of monodisperse particle size (2, 7, or 14 nm) were deposited on a CHA zeolite (Si/Al = 12) at similar total Pd contents. These materials are treated to high temperatures (598–973 K) in flowing air with and without H_2O, and the number of agglomerated PdO domains and ion-exchanged Pd^{2+} sites are quantified with H_2 TPR. Thermodynamic phase diagrams are constructed for a range of Pd particle sizes under various gas environments (pressures, temperatures) to quantitatively compare with experimentally measured ion-exchanged Pd^{2+} contents on samples exposed to similar treatments. Apparent rates of conversion of metallic Pd domains to ion-exchanged Pd^{2+} sites under flowing air are measured as a function of temperature (598–673 K) and H_2O pressure (0–2 kPa) to deduce mechanistic information and determine kinetic implications of H_2O and O_2 pressures and the Pd particle size on the redispersion to ion-exchanged Pd^{2+} sites.

3.3 Methods

3.3.1 Synthesis of Pd-CHA zeolites

One Na-form CHA zeolite sample (Si/Al = 12) was provided by BASF Corporation. The Na-form CHA sample was converted to the NH_4-form by an ion-exchange treatment with 1 M of NH_4NO_3 (99.9 wt % purity NH_4NO_3, Sigma-Aldrich) in a perfluoroalkoxy alkane (PFA) container (Savillex Corporation) containing a magnetic Teflon stir bar at a ratio of 150 g of solution (g solid)$^{-1}$. The mixture was homogenized for >24 h under ambient conditions, and the solids were recovered by centrifugation. The NH_4-form sample was washed with deionized

H_2O (18.2 MΩ cm) four times (30 mL (g solid)$^{-1}$ per wash) until the pH of supernatant was constant, then placed in a static oven held at 373 K for >12 h. To prepare the H-form CHA material, the NH_4-form CHA sample was treated in flowing air (1.67 cm^3 s^{-1}, Air Zero, Indiana Oxygen) to 773 K (60 K h^{-1}) for 4 h. The fraction of framework Al in 6-MR paired configuration (defined as 2 Al sites in the 6-membered ring of CHA [20], [22]) was determined to be 0.24 (i.e., Co^{2+}/Al = 0.12) by quantification using Co^{2+} titration using procedures documented elsewhere [113].

The syntheses of colloidal Pd nanoparticle solutions were performed using protocols reported by Goodman et al. [11] Palladium(II) acetylacetonate ($Pd(acac)_2$, 35% Pd, Acros Organics), 1-dodecene (DDE, 93-95%, Acros Organics), 1-octadecene (ODE, 90%, Acros Organics), 1-tetradecene (TDE, 94%, Alfa Aesar), oleylamine (OAm, technical grade, 70%, Sigma Aldrich), oleic acid (OAc, 90%, Sigma Aldrich), trioctylphosphine (TOP, 97%, Sigma Aldrich), hexanes (99.5%, Fisher Scientific), ethanol (99.5%, Fisher Scientific), isopropanol (99.5%, Fisher Scientific), and methanol (99.8%, Fisher Scientific) were used without further purification.

Pd nanoparticles nominally of 2 nm diameter were synthesized by adding $Pd(acac)_2$ (157 mg, 0.5 mmol), DDE (11 mL), TDE (9 mL), OAm (1.64 mL), and TOP (570 μL) to a 3-neck round bottom flask under inert atmosphere. The reaction mixture was then flushed with N_2 at a Schlenk line and heated to 323 K for 0.5 h with magnetic stirring. The resultant pale-yellow mixture was then rapidly heated to 503 K under N_2 atmosphere. After 0.25 h, the solution was cooled to ambient temperature, and the nanoparticles were precipitated using ethanol (20 mL), methanol (10 mL), and isopropanol (20 mL). After centrifugation at 8500 rpm for 0.083 h, the clear supernatant was decanted, and the solids were redissolved in 5 mL hexanes. The dissolution-precipitation cleaning process was repeated three times. The cleaned nanoparticles were finally dissolved in 5 mL hexanes.

Pd nanoparticles nominally of 7 nm diameter were synthesized by adding $Pd(acac)_2$ (157 mg, 0.5 mmol), TDE (6.8 mL), ODE (13.2 mL), OAm (3.4 mL), OAc (0.8 mL), and TOP (2.4 mL) to a 3-neck round bottom flask under inert atmosphere. The reaction mixture was then heated to 323 K for 0.5 h under N_2 at a Schlenk line. The mixture was rapidly heated to 563 K for 0.25 h, then subsequently cooled to ambient temperature before ethanol (10 mL),

methanol (10 mL), and isopropanol (10 mL) were added to precipitate the Pd nanoparticles. The solids were collected by centrifugation at 8500 rpm for 0.083 h and then redissolved in 5 mL hexanes. The dissolution-precipitation cleaning process was repeated three times prior to redissolving the 7 nm Pd nanoparticles in 5 mL hexanes.

Pd nanoparticles nominally of 14 nm diameter were synthesized by adding $Pd(acac)_2$ (77 mg, 0.25 mmol), ODE (5 mL), OAc (5 mL), and TOP (0.56 mL) to a 3-neck round bottom flask under inert atmosphere. After heating to 333 K for 0.5 h under N_2 at a Schlenk line, the reaction mixture was quickly heated to 553 K. After 0.083 h, the solution was cooled to ambient temperature before ethanol (10 mL), methanol (10 mL), and isopropanol (10 mL) were added to precipitate the Pd nanoparticles. The solids collected by centrifugation (8500 rpm, 0.083 h) were redissolved in 5 mL hexanes, and the cleaning process was repeated three times. To remove the fraction of smaller nanoparticles and obtain Pd nanoparticles with narrow size distribution, size-selective precipitation using isopropanol (2.5 mL) was carried out. The grey supernatant was decanted, and 5 mL hexanes was added to redisperse the precipitated particles. This cleaning procedure was repeated two more times. Finally, the precipitated nanoparticles were dissolved in 5 mL hexanes, and 20 μL OAm was added for longer-term colloidal stability.

The as-exchanged, monodisperse Pd-CHA samples were prepared by sonicating and dispersing H-form CHA samples (0.5–1.0 g) in 20 g of hexanes, followed by dropwise addition of a colloidal Pd solution to achieve approximately 1.5 wt% Pd, assuming all Pd added would adsorb onto the zeolite sample. The mixture was sonicated again for 1 h, and the solids were recovered by centrifugation (5000 rpm, 0.083 h) then dried in a static oven at 333 K overnight. The resulting as-deposited, monodisperse Pd-CHA materials were stored in capped borosilicate vials under ambient conditions.

The 2.2 wt% Pd-CHA material used for isothermal redispersion kinetic studies was prepared via incipient wetness impregnation according to our previous report [2], wherein an aqueous $Pd(NH_3)_4(NO_3)_4$ solution was added dropwise to the NH_4-form CHA zeolite until the total pore volume was saturated while stirring with a plastic spatula. The as-exchanged $[Pd(NH_3)_4]^{2+}$-CHA material was left overnight under ambient conditions then stored in a capped borosilicate vial.

3.3.2 Pd-zeolite characterization

The Al and Pd elemental compositions were characterized with inductively coupled plasma-optical emission spectrometry (ICP-OES) using a Thermo Scientific iCAP 7000 Plus Series ICP-OES. Pd-zeolites and colloidal solutions (0.02–0.05 g) were digested with 2.5 g of hydrofluoric acid (48 wt %, Alfa Aesar) and 5.0 g of aqua regia (2:1 volume ratio of 37 wt% HCl, Mallinckrodt Chemicals and 70 wt% HNO_3, Sigma-Alrdich) for at least two days in a sealed polytetrafluoroethylene bottle. Digested samples were diluted with 50.0 g of deionized H_2O, and then further acidified with 5.0 g of nitric acid (70 wt %, Sigma-Aldrich) before ICP-OES analysis.

Transmission electron microscopy (TEM) images were acquired using an FEI Tecnai T20 TEM equipped with a 200 kV LaB_6 filament. High-angle annular dark-field scanning transmission electron microscopy (HAADF-STEM) images were collected using the FEI Talos F200X S/TEM equipped with a 200 kV X-FEG field-emission source. Colloidal solutions for TEM were prepared by drop casting onto a carbon-coated Cu grid. The Pd-exchanged CHA materials (ca. 5 mg) were sonicated in 1 mL ethanol for 15 min prior to drop casting onto Cu grids. Samples were imaged under vacuum (ca. 10 μPa).

Thermogravimetric analysis (TGA) was performed with a TA Instruments SDT Q600 thermogravimetric analyzer and differential scanning calorimeter (TGA-DSC). Samples were treated in flowing air (1.67 cm^3 s^{-1}, Air Zero, Indiana Oxygen) to 523 K (0.167 K s^{-1}) and held for 0.5 h, then further treated to 1073 K (0.167 K s^{-1}).

The amounts of agglomerated PdO and mononuclear Pd^{2+} cations were quantified with H_2 temperature programmed reduction (TPR) procedures described elsewhere [113] using a Micromeritics AutoChem II 2920 Chemisorption Analyzer equipped with a thermal conductivity detector (TCD) to quantify H_2 consumption. In brief, the TCD response factor was generated using varied partial pressures (0.5–5.0 kPa) of H_2 in balance Ar, which quantified the amount of Ag on a Ag_2O reference material (Micromeritics) to within a factor of 1.12. After a given treatment sequence, samples (0.3–0.6 g) were exposed to flowing Ar (0.50 cm^3 s^{-1}, UHP, 99.999%, Indiana Oxygen) with 1–2 kPa H_2O for >0.5 h to hydrate mononuclear Pd^{2+} cations at 303 K. Samples were then cooled to 203 K (0.167 K s^{-1}) in flowing Ar (0.167

cm^3 s^{-1}) using a Micromeritics Cryocooler II accessory. An isopropanol slurry (cooled to 184 K with liquid N_2) was inserted between the TCD detector and the sample to trap any condensable gases. The Ar stream was replaced with 5 kPa H_2 in balance Ar (0.167 cm^3 s^{-1}, certified mixture, Indiana Oxygen), and once a stable TCD signal was achieved, the sample was treated to 573 K (0.167 K s^{-1}) and held for 0.5 h. All H_2 TPR profiles and discussion of data fitting procedures are reported in supporting information.

Volumetric O_2 chemisorption experiments were performed with a Micromeritics ASAP 2020 Plus Chemisorption unit. Samples (ca. 0.2 g) were treated in flowing H_2 (UHP, 99.999%, Praxair) to 673 K or 873 K in O_2 (UHP, 99.98%, Matheson) before preparing for chemisorption. Samples were first flushed in flowing He then degassed under vacuum (<3 μmHg) for 1 h at 373 K. Next, a leak test was performed to confirm that leak rates were below the threshold of <600 μmHg h^{-1} (recommended by Micromeritics). Samples were then treated in H_2 to 573 K (0.167 K s^{-1}) for 1 h, evacuated at 573 K for 1 h, then another leak test was performed at 313 K. Then, the sample was evacuated for 0.3 h at 313 K before collecting two O_2 adsorption isotherms (313 K, 2−42 kPa), with an evacuation step after the first isotherm to remove non-chemisorbed O_2. Isothermal uptakes were linearly extrapolated to zero pressure, and the difference in uptakes at zero partial pressure yielded the amount of chemisorbed O_2. The dispersion was calculated assuming one O atom titrates one surface Pd atom.

3.3.3 Isothermal redispersion kinetics

The as-exchanged $[Pd(NH_3)_4]^{2+}$-CHA (2.2 wt% Pd) material was first pelleted then sieved to retain 180-250 μm diameter aggregates. Treatment sequences and H_2 TPR analysis were performed with a Micromeritics Autochem II 2920 Chemisorption Analyzer. Samples (0.03–0.05 g) were first pretreated in flowing H_2 in Ar (0.5 cm^3 s^{-1}; 5 kPa H_2, certified mixture, Indiana Oxygen) to 673 K for 1 h, and cooled to ambient temperature. Samples were then cycled through H_2 treatments, inert purge treatments, air treatments (i.e., isothermal redispersion treatments), and then the amounts of PdO and Pd^{2+} cations were quantified by H_2 TPR. As an example procedure for an isothermal redispersion measurement at 648 K

in air without added H_2O, the sample was treated in flowing (0.5 cm^3 s^{-1}) 5 kPa H_2 in Ar to 648 K (0.167 K s^{-1}) for 0.5 h, then the 5 kPa H_2 in Ar stream was replaced with flowing Ar (0.5 cm^3 s^{-1}; UHP, 99.999%, Indiana Oxygen) to purge the system for 0.083 h. Then, the Ar stream was replaced with flowing air (0.5 cm^3 s^{-1}; Air Zero, Indiana Oxygen) for a specified amount of time (0.003–1 h), and then rapidly cooled (0.67 K s^{-1}) from 648 K to ambient temperature in flowing Ar (0.5 cm^3 s^{-1}) Ar using a Micromeritics Cryocooler II accessory. In cycling experiments, the air exposure times were randomly varied between 0.003–1 h to avoid any systematic errors that may have been caused by this step in the procedure.

3.3.4 Details of DFT calculations

We used the Vienna ab initio simulation package (VASP, version 5.4.4) [116] to perform plane-wave, periodic DFT calculations with an energy cutoff of 400 eV and projected augmented wave (PAW) [117] pseudopotentials for core-valence interactions. We used the bulk structures reported in the Materials Project [118] database for metallic Pd and PdO, and the 24 T-site 1Al and 2Al Pd-exchanged SSZ13 species in the study by Mandal et al. [38] as initial guesses, and optimized them with the Perdew-Becke-Ernzerhof (PBE) [119] generalized gradient approximation (GGA) and Heyd-Scuseria-Erzenhof (HSE06) [116], [119]–[125] hybrid exchange-correlation functionals. Dispersion corrections were calculated using the Becke-Johnson damping (D3(BJ)-vdw) method [120], [121]. We used a convergence threshold of 10^{-8} eV and 0.01 eV/Å for the electronic energies and atomic forces, respectively. We used the Monkhorst-Pack k-point mesh detailed in the Materials Project database to sample the first Brillouin zone for bulk metallic Pd and PdO; only the Γ point was used for zeolitic structures. The optimized geometries of all structures considered in this paper have been provided in the CONTCARS attachment of the SI.

The DFT-computed 0 K energies of formation of bulk PdO ($\Delta E^{\text{form}}_{\text{PdO}_{\text{bulk}}}$), and 1Al and 2Al exchanged Pd cations ($\Delta E^{\text{form}}_{Z_*\text{PdH}_x O_y}$) were calculated as:

$$\Delta E^{form}_{PdO_{bulk}} = E_{PdO_{bulk}} - E_{Pd_{bulk}} - \frac{1}{2}E_{O_2} \tag{3.1}$$

$$\Delta E^{form}_{Z_*PdH_xO_y} = E_{Z_*PdH_xO_y} - E_{Pd_{bulk}} - E_{Z_2H_2} - \frac{x}{2}\left(E_{H_2O} - \frac{1}{2}E_{O_2}\right) - \frac{y}{2}E_{O_2} \tag{3.2}$$

where Z_* represents 1Al (Z) and 2Al (Z_2) exchange sites.

3.3.5 Details of particle size dependent models

We used the Python Materials Genomics (*Pymatgen*) package and its built-in *Slabgenerator* [126]–[128] to construct symmetric slabs of up to Miller index 2 for metallic Pd and PdO from their respective optimized bulk structures. The slab thickness was set to 10 Å, and a 15 Å vacuum space was applied to eliminate interactions between the periodic images of the surfaces in the z direction. The k-point mesh for the slabs in the x and y directions was appropriately scaled by using the k-points per reciprocal Å for the bulk structures, with a single k-point applied in the z direction. We optimized and computed the energies of the unconstrained slabs using PBE-D3(BJ)-vdw functional and the same convergence criteria as that for the bulk structures. The surface energies (γ_{slab}) of the slabs were calculated as:

$$\gamma_{slab} = \left(E_{PdO_{slab}} - n_{Pd}E_{Pd_{bulk}} - n_O\mu_O\right)/2A \tag{3.3}$$

where n_{Pd} and n_O represent the number of Pd atoms and excess or deficit O atoms in the slab, respectively, μ_O is the chemical potential of O, and A denotes the surface area of one side of the slab. The equilibrium shapes of metallic Pd and PdO nanoparticles were determined from their respective Wulff constructions which represent the minimum surface energy for a given crystal. We used the *Wulffshape* function in *Pymatgen* to generate the Wulff constructions for a range of μ_O values [129], and evaluated the corresponding shape factor (η = area/volume$^{2/3}$) and average surface energy (γ).

The dependence of the chemical potential of supported nanoparticles $\mu(d)$, assumed to be spherical, on the particle size (d) is given by the Gibbs-Thomson (G-T) equation [130]–[134]:

$$\mu\left(d\right) = \mu_{bulk} + \frac{2\gamma\rho}{d} \tag{3.4}$$

where μ_{bulk} is the chemical potential of the bulk phase, and ρ represents the volume normalized per mole of metal. The non-sphericity of nanoparticles can be accounted for by including a shape factor term in Equation 3.5 resulting in a similar expression [135], [136]:

$$\mu\left(d\right) = \mu_{bulk} + \frac{2\eta\gamma\rho}{d} \tag{3.5}$$

To validate the results of the particle size dependent models of Equations 3.4 and 3.5, we constructed nanoparticles of Pd (d_{Pd} =0.6–2 nm) and PdO (d_{Pd} = 1.4, 1.9 and 3 nm) using Atomic Simulation Environment (ASE) [137] similar to those reported in literature [138]–[140], and optimized the geometries in VASP using PBE-D3(BJ)-vdw functional with a convergence criteria of 10^{-6} eV for the electronic energies and 0.03 eV/Å for the forces on the atoms. Vacuum spacing of 20 Å was applied to eliminate interactions between periodic images of the nanoparticles, and the first Brillouin zone was sampled using only the Γ point. The optimized structures of the Pd and PdO nanoparticles have been included in the CONTCARS attachment of the SI.

3.3.6 Calculation of ab initio formation free energies and conversion of Pd nanoparticles to mononuclear Pd^{2+}

We evaluated the formation free energies of bulk PdO ($\Delta G^{\text{form}}_{\text{PdO}_{\text{bulk}}}$), and 1Al and 2Al exchanged Pd cations ($\Delta G^{\text{form}}_{Z_*\text{PdH}_x O_y}$) as a function of T, P_{H_2O}, P_{O_2} per:

$$\begin{aligned}\Delta G^{form}_{Pd_xO_{y\,bulk}}\left(T,\ P_{O_2}\right) = \Delta E^{form}_{Pd_xO_{y\,bulk}} + \Delta ZPE + \Delta E^{int}_{Pd_xO_{y\,bulk}}\left(T\right) \\ - T\Delta S_{Pd_xO_{y\,bulk}}\left(T\right) + \frac{y}{2}\Delta\mu_{O_2}\left(T, P_{O_2}\right)\end{aligned} \tag{3.6}$$

$$\begin{aligned}G^{form}_{Z_*PdH_xO_y}\left(T,\ P_{O_2}\right) = \Delta E^{form}_{Z_*PdH_xO_y} + \Delta ZPE + \Delta E^{int}_{Z_*PdH_xO_y}\left(T\right) \\ - T\Delta S_{Z_*PdH_xO_y}\left(T\right) + \frac{x}{2}\left(\Delta\mu_{H_2O}\left(T, P_{H_2O}\right) - \frac{1}{2}\Delta\mu_{O_2}\left(T, P_{O_2}\right)\right) \\ + \frac{y}{2}\Delta\mu_{O_2}\left(T, P_{O_2}\right)\end{aligned} \tag{3.7}$$

where $\Delta\mu$ is the difference the chemical potential between 0 K and reactions conditions being considered, and is calculated using the ideal gas relation. ΔZPE, ΔE^{int} and ΔS represent the zero-point energy corrections, and vibrational contributions to the internal energy and entropy, respectively, and were evaluated using the harmonic oscillator approximation for solids and gases, and the Sakur-Tetrode and rigid-rotor approximations for gas species [141]. Frequency calculations were carried out using PBE-D3(BJ)vdw functional on fully relaxed bulk phase Pd and PdO, and zeolitic structures.

The size-dependent formation free energies of PdO nanoparticles were evaluated using the following expression which includes the chemical potential of nanoparticles given by Equation 3.5:

$$\Delta G^{form}_{d_{Pd_xO_y}}(T,\ P_{H_2O},\ P_{O_2},\ d_{Pd_xO_y}) = \Delta G^{form}_{Pd_xO_{y_{bulk}}}(T,\ P_{H_2O},\ P_{O_2}) + \mu_{Pd_xO_y}\left(d_{Pd_xO_y}\right) \quad (3.8)$$

3.3.7 Details of calculations of intermediate mobile species facilitating Pd redispersion

We optimized structures of plausible neutral, gas-phase intermediates and their H_2O-solvated counterparts using the PBE functional in Gaussian 16 [142], and subsequently calculated their single point energies with the CCSD(T, full electron) method. The basis set def2-QZVPP was used for all the calculations along with an unrestricted spin state [143], [144]. Both singlet and triplet spin states were considered wherever applicable, and we used the lowest energy spin state for our subsequent analysis. The formation free energies (ΔG_{form}) of the mobile intermediate species was calculated using the following expression:

$$\begin{aligned}\Delta G^{form}_{PdH_xO_y^{(g)}}(T,\ P_{O_2}) = {} & \Delta E^{form}_{PdH_xO_y^{(g)}} + \Delta ZPE - T\Delta S_{PdH_xO_y^{(g)}}(T) \\ & + \frac{x}{2}\left(\Delta\mu_{H_2O}(T, P_{H_2O}) - \frac{1}{2}\Delta\mu_{O_2}(T, P_{O_2})\right) + \frac{y}{2}\Delta\mu_{O_2}(T, P_{O_2})\end{aligned} \quad (3.9)$$

$\Delta S_{PdH_xO_y^{(g)}}$ includes the vibrational, translational and rotational contributions to entropy. Frequency calculations for all the fully relaxed species were carried out using PBE and def2-QZVPP basis set.

3.4 Results and discussion

3.4.1 Effects of initial Pd particle size and treatment conditions on the conversion of agglomerated Pd particles to exchanged Pd^{2+} ions

Section 3.4.1.1 Synthesis of monodisperse Pd nanoparticles supported on CHA zeolites

$[Pd(NH_3)_4]^{2+}$ complexes supported on zeolites decompose and agglomerate to metallic Pd nanoparticles en route to forming exchanged, mononuclear Pd^{2+} cations that are charge-compensated by framework Al (denoted "ion-exchanged Pd^{2+}") during high-temperature (>600 K) air treatments [113]. Such agglomeration forms to a broad distribution of Pd particle sizes (1–7 nm; Figure 3.7 and 3.8, SI) before converting to ion-exchanged Pd^{2+}. This apparent log-normal particle size distribution precludes isolating particle size effects on interconversion because of the wide range of particle size-dependent free energies changes.

To isolate the effects of Pd particle size on their structural interconversion to ion-exchanged Pd^{2+} cations during high-temperature air treatments, Pd particles of monodisperse size distributions were first synthesized using solution-phase colloidal synthesis methods [11] and then supported onto the exterior of CHA zeolite crystallites (details of Pd deposition procedures in supporting information). Three different colloidal Pd nanoparticle solutions were characterized with TEM to contain monodisperse particles that were nominally 2, 7, and 14 nm in diameter (Figures 3.9, 3.10, 3.11, and 3.12, SI). These colloidal solutions were diluted in a hexane solvent and mixed with the H-form CHA zeolite powder, and then sonicated in order to deposit the oleylamine-capped Pd (denoted "as-deposited Pd-CHA"). Samples will be referred to as Pd-CHA-X, where X is the average particle size (in nm) determined by TEM on as-deposited samples.

Figure 3.1 shows ex-situ TEM images of the as-deposited Pd-CHA-X samples, and Table 3.1 lists their particle size distributions and elemental analysis data. Pd particle size distributions were similar on as-deposited Pd-CHA-X as in the colloidal precursor solutions,

demonstrating the deposition procedure used did not alter the monodisperse distributions of oleylamine-capped Pd nanoparticles. However, the deposition procedure used did result in some non-uniformities in how Pd particles were spatially distributed at external crystallite surfaces, with some localized Pd nanoparticle aggregation observed for the Pd-CHA-7 and Pd-CHA-14 samples. This aggregation of nanoparticles at crystallite exteriors may have occurred during the solvent evaporation procedure.

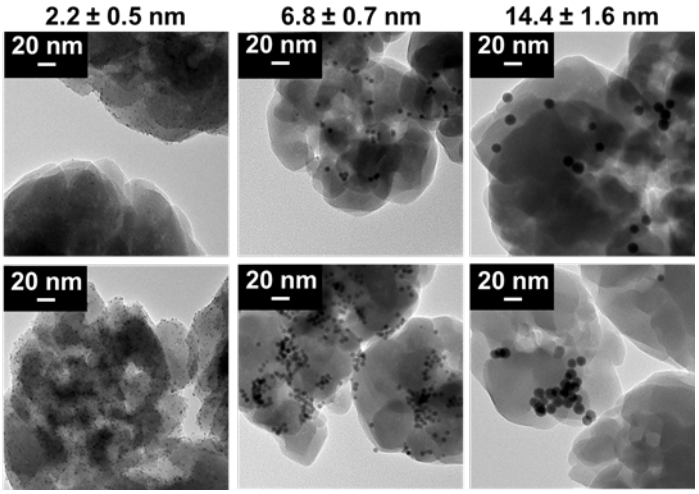

Figure 3.1. Ex-situ TEM images of the as-deposited Pd-CHA-X materials. Pd-CHA-2 (left), Pd-CHA-7 (middle), Pd-CHA-14 (right).

Table 3.1. Characterization data on as-deposited Pd-CHA-X samples. Particle size distributions are in Figures 3.13, 3.14, and 3.15, SI

Sample[a]	Nominal Pd particle size / nm	TEM characterized particle size / nm[b]	Pd wt %	Pd / Al[c]
Pd-CHA-2	2	2.2 ± 0.5	1.12	0.082
Pd-CHA-7	7	6.8 ± 0.7	0.72	0.053
Pd-CHA-14	14	14.4 ± 1.6	0.84	0.061

[a] Samples are denoted Pd-CHA-X, where X denotes the nominal Pd particle size.
[b] The average particle size plus or minus one standard deviation. Particle size distributions shown in Figures 3.13, 3.14, 3.15 (SI).
[c] Pd wt% and Pd/Al molar ratio was determined by ICP.

The as-deposited Pd-CHA materials contained oleylamine-capped Pd nanoparticles and other residual organic species, which should be removed prior to converting Pd nanoparticles to ion-exchanged Pd^{2+}. Previous reports showed that short exposure times (30 s) at high temperatures (973 K) in air led to the effective removal of organic species without causing changes to Pd particle size distribution on Al_2O_3 [145]; however, this procedure may cause hydrothermally-induced changes to the zeolite structure and hydrolysis of framework Al O Si bonds [80], [81] that would decrease the number of Brønsted acid sites [146] available to react with mobile Pd species to form ion-exchanged Pd^{2+} [44], [55], [147]. Thus, TGA was performed on the as-deposited Pd-CHA-14 sample to determine the minimum air treatment temperature required to remove >95% of the organic species, and three desorption events centered at 373, 460, and 510 K were observed (Figures 3.22 and 3.23, SI). A control experiment with the H-CHA support showed a single desorption event near 373 K, reflecting H_2O desorption from the sample. Therefore, the two higher temperature desorption features on the as-deposited Pd-CHA-14 sample (ca. 460 and 510 K) reflect the desorption or combustion of organic species, consistent with the temperatures required to removal oleylamine from Pt nanoparticles (523–573 K in air) [148]. Therefore, to remove the majority of organic species without disturbing the Pd particle size distribution, as-deposited Pd-CHA-X samples were treated in air to 548 K (60 K h^{-1}) for 4 h in a muffle furnace. Samples treated with this protocol were analyzed in a subsequent TGA experiment and did not show desorption events for organic species (460–600 K), and TGA profiles were similar to that of the parent H-CHA (Figures 3.22 and 3.23, SI), indicating that the majority of organic content was successfully removed. TEM images of Pd-CHA-X samples treated to 548 K in air showed similar Pd particle size distributions as present in their as-deposited form (Figures 3.16, 3.17, 3.18, and 3.19, SI). Therefore, we conclude that treatment of as-deposited Pd-CHA-X samples in air to 548 K will remove the majority of organic species, while retaining the Pd particle size distribution and zeolite support intact, enabling further studies of the conversion of such particles to ion-exchanged Pd^{2+} when treated to higher temperatures (>548 K).

Section 3.4.1.2 Effects of Pd particle size on Pd oxidation and structural interconversion

The as-deposited Pd-CHA-X samples were treated to high temperatures (598–873 K) in flowing air to determine the effects of Pd particle size on the extent of oxidation with O_2 and conversion to ion-exchanged Pd^{2+} cations. The amounts of agglomerated PdO domains and ion-exchanged Pd^{2+} cations after high-temperature air treatments were characterized with H_2 TPR (profiles reported in Figures 3.24, 3.25, and 3.26, SI). Previous reports concluded that agglomerated PdO domains have a lower barrier for reduction by H_2 than hydrated Pd^{2+} ion sites; thus, H_2 consumption features can be quantified and assigned to agglomerated PdO and ion-exchanged Pd^{2+} (further discussion in SI) [29], [72], [73], [113]. The total H_2 consumption (per total Pd) and the amount of ion-exchanged Pd^{2+} (per total Pd) after treatment in flowing air for Pd-CHA-X samples are reported in Figure 3.2. At a given air treatment temperature, the amount of ion-exchanged Pd^{2+} formed on CHA increased as the initial Pd nanoparticle size decreased, consistent with previous reports that smaller Pd nanoparticles (at fixed Pd density) converted to greater amounts of mononuclear $Pd(OH)_2$ on γ-Al_2O_3 [11]. For Pd-CHA-2, the total H_2 consumed per Pd was approximately unity at all air treatment temperatures studied, demonstrating that all the Pd was present in divalent form; thus, that all of the 2 nm Pd nanoparticles were oxidized to divalent Pd during the air treatment. In contrast, Pd-CHA-7 and Pd-CHA-14 showed sub-unity H_2 consumption per Pd for low-temperature air treatments (598–673 K), suggesting that a fraction of the 7 nm or 14 nm Pd nanoparticles were not fully oxidized during the air treatment, consistent with a report by Chin et al. showing that higher O_2 pressures were needed to fully oxidize larger metallic Pd particles supported on γ-Al_2O_3 at a fixed temperature of 973 K [57]. Air treatment of Pd-CHA-14 at 673 K for 1 h and 5 h formed the same amount of ion-exchanged Pd^{2+} and consumed the same amount of H_2 per Pd (Figure 3.26, SI), demonstrating that the 1 h treatments were sufficiently long for samples to reach an apparent equilibrated state. However, thermodynamic calculations predict exergonic reaction energies to convert Pd into PdO for particles between 2 and 14 nm, suggesting a kinetic barrier prevented the full oxidation of Pd nanoparticles in Pd-CHA-7 or Pd-CHA-14 at lower temperatures.

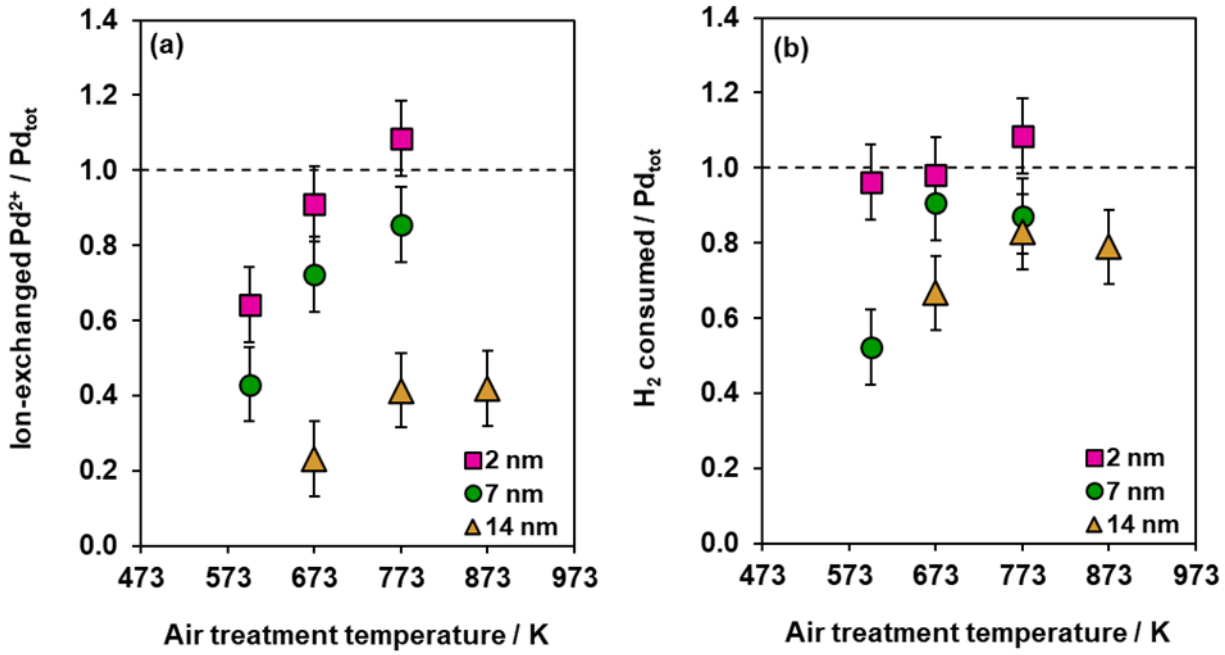

Figure 3.2. (a) The amount of ion-exchanged Pd^{2+} (per total Pd) after treatment in flowing air (593–873 K) for Pd-CHA-2 (squares), Pd-CHA-7 (circles), and Pd-CHA-14 (triangles). (b) Total H_2 consumed (per total Pd) from (a). Dashed lines represent theoretical maximum amounts. H_2 TPR profiles reported in Figures 3.24, 3.25, and 3.26, SI.

3.4.2 Thermodynamics of Pd interconversion

We next used DFT calculations and thermodynamic analyses to compute the expected fraction of Pd atoms in nanoparticles that convert to ion-exchanged Pd^{2+} as a function of the initial Pd particle size, reaction conditions, and zeolite composition. Previous studies have shown that Pd^{2+} cations charge-compensating two Al T sites (2Al) in the six-membered ring (6-MR) are the most thermodynamically stable ion-exchanged Pd^{2+} species in CHA, represented here by Z_2Pd where 'Z' denotes the substitution of framework Si with Al [6], [38]. The lowest energy Z_2Pd structure has 2Al sites in a third nearest neighbor (3NN) arrangement, followed by the (+65 kJ mol^{-1}) 2NN configuration [6], [38], [149]. One Al T sites (1Al) can be charge-compensated by Pd^{+} cations (ZPd), and by Pd^{2+} as $[PdOH]^{+}$ (ZPdOH), which are computed to be +82 and +85 kJ mol^{-1}, respectively higher in energy than 3NN Z_2Pd [6], [38], [149]. The existence of Pd^{+} after high temperature treatments

in air with and without H_2O is debated in literature [6]; while IR assignments for Pd^+-NO complexes in Pd/zeolites are reported in several studies [2], [8], [32], [75], one piece of direct characterization evidence for Pd^+ is from EPR measurements of Pd/Y zeolites performed under vacuum and after H_2 treatment at 298 K [150]. Also, ZPdOH has only been identified in detectable amounts for CHA materials containing a larger number of ion-exchanged Pd^{2+} species than the number of 2Al sites in the 6-MR [113]. The Pd content of the Pd-CHA-X samples here (Pd/Al = 0.05–0.08) are much lower than the number of available 2Al 6-MR sites quantified by Co^{2+} titration (Co^{2+}/Al = 0.12). Thus, we expect the Pd^{2+} in the 6MR 3NN configuration to be the majority cationic species in our materials; however, for comparison, we also consider 2NN Z_2Pd, ZPd and ZPdOH in the analyses below.

We used the GGA-PBE and HSE06 functionals with D3-(BJ)vdw dispersion corrections (additional details in Section 3.3.4) to compute the thermodynamics of oxidation of bulk metallic Pd with O_2 to form PdO and ion-exchanged Pd cations (Table 3.10, SI). We found that the HSE06-computed PdO formation energy (-111 kJ mol^{-1}) was consistent with the experimentally determined formation energy (-115 kJ mol^{-1}) [151], [152]; therefore, we used this functional for all subsequent calculations. The 0 K reaction energies for metallic Pd to form bulk PdO or 3NN Z_2Pd, and bulk PdO to form 3NN Z_2Pd are reported in Table 3.2. Reaction energies for the formation of 2NN Z_2Pd, ZPd and ZPdOH are much more endothermic (Table 3.10, SI).

Table 3.2. HSE06-D3(BJ)vdw-calculated 0 K energies of formation (ΔE), and formation free energies of PdO_{bulk} (ΔG^{form}_{PdO}), and 3NN Z_2Pd ($\Delta G^{form}_{Z_2Pd}$) at 598 K, 20 kPa O_2, 0.014 kPa H_2O.

Reaction	ΔE (kJ mol^{-1})	ΔG^{form} (kJ mol^{-1}) 598 K	873 K
$Pd_{bulk} + \frac{1}{2}O_2 \xrightarrow{\Delta G^{form}_{PdO}} PdO_{bulk}$	-111	-46	-16
$Pd_{bulk}+Z_2H_2+\frac{1}{2}O_2 \xrightarrow{\Delta G^{form}_{Z2Pd}} Z_2Pd+H_2O$	+8	-50	-74
$PdO_{bulk} + Z_2H_2 \rightarrow Z_2Pd + H_2O$	+119	-4	-58

We next used the HSE06-computed energies and thermodynamic relations to express the formation free energies of PdO_{bulk} and exchanged Pd cations (2NN and 3NN Z_2Pd, ZPd and ZPdOH) as a function of P_{O_2}, P_{H_2O}, and T. Table 3.2 reports ΔG^{form} values for PdO_{bulk} and 3NN Z_2Pd at conditions representative of the experimental, high-temperature air treatments (598–873 K, 20 kPa O_2, and ppm levels of impurity H_2O, estimated as 0.014 kPa H_2O) of the Pd-CHA-X samples, and Figure 3.37, SI shows the relative stabilities of Pd_{bulk}, PdO_{bulk}, and ion-exchanged Pd cations as a function of P_{O_2} and T, with 0.014 kPa H_2O. Conversion of bulk metallic Pd to 3NN Z_2Pd becomes thermodynamically favorable at $T > 576$ K (0.014 kPa H_2O, $\log(P_{O_2}/P^{\circ}) > -9.5$). These results show that structural interconversion of bulk metallic Pd to ion-exchanged Pd^{2+} is thermodynamically favorable over the range of high-temperature air treatments used experimentally.

We next accounted for particle size effects on the free energies of metallic Pd and PdO by incorporating the chemical potential, $\mu(d)$, of a particle with diameter d using a relation (Equation 3.10) similar to the Gibbs-Thomson (G-T) equation [135], [136]:

$$\mu\,(d) = \mu_{bulk} + \frac{2\eta\gamma\rho}{d} \tag{3.10}$$

where γ is the average surface energy, ρ is the volume normalized per mole of metal, and η is the computed shape factor (area/volume$^{2/3}$). We computed Wulff constructions of Pd and PdO to determine η and γ, and additional details are provided in Section 3.3.5. We validated Equation 3.10 for the particle size range of interest ($d_{\text{Pd}} = 2$–14 nm) (results shown in Figure 3.38) by explicitly computing $\mu\,(d)$ using atomistic models of Pd ($d_{\text{Pd}} = 0.6$–2 nm) and PdO ($d_{\text{Pd}} = 1.4$, 1.9, and 3 nm) nanoparticles. The size-dependent ΔG^{form} for Pd and PdO particles are calculated per:

$$\Delta G^{form}_{d_{Pd_xO_y}}(T, P_{H_2O}, P_{O_2}, d_{Pd_xO_y}) = \Delta G^{form}_{Pd_xO_{y\,bulk}}(T, P_{H_2O}, P_{O_2}) + \mu_{Pd_xO_y}(d_{Pd_xO_y}) \tag{3.11}$$

Figure 3.39 (SI) depicts the particle size-dependent thermodynamic phase diagrams incorporating metallic Pd, PdO and exchanged Pd cations (2NN and 3NN Z_2Pd, ZPd and

ZPdOH) constructed using Equation 3.11. We accounted for the expansion of particle volume during the oxidation of Pd to PdO by including a volume expansion factor of 1.36. Table 3.3 reports computed $\Delta G^{\text{form}}_{Z_{2Pd}}$ for the Pd-CHA-X samples at the high-temperature air treatments (598–873 K, 20 kPa O_2, ppm levels of H_2O). The ΔG^{form} for 2NN Z_2Pd, ZPd and ZPdOH for the Pd-CHA-X samples are significantly more endergonic, and their formation from Pd particles are not considered in subsequent thermodynamic calculations. Metallic Pd is not favorable under any of the conditions in Figure 3.39b, and formation of Z_2Pd (3NN) becomes more exergonic as either T increases or d_{Pd} decreases. Chin et al. reported an analogous trend in the Gibbs free energies for oxidation of Pd clusters (2.2–8.0 nm) with O_2 to PdO on γ-Al_2O_3, determined using volumetric O_2 isotherms that showed greater equilibrium O_2 uptakes for smaller particles at any measured O_2 pressure (0–80 kPa). The onset O_2 pressures observed experimentally at 973 K were lower for the smaller Pd clusters (22 and 35 kPa for 1.8 and 8.8 nm Pd clusters, respectively), resulting in the computed PdO formation energy at 973 K becoming more exergonic as the Pd cluster diameter decreased (-5.2 and -0.8 kJ $\text{mol}^{-1}_{\text{PdO}}$ for 1.8 and 8.8 nm Pd clusters, respectively) [57].

Table 3.3. Formation free energies of ion-exchanged Pd^{2+} ($\Delta G^{\text{form}}_{Z_{2Pd}}$, kJ mol^{-1}) for 2, 7, and 14 nm Pd particles at 598–873 K air treatment temperatures with 20 kPa O_2, 0.014 kPa H_2O.

Particle size / nm	598 K	673 K	773 K	873 K
2	-116	-123	-131	-140
7	-69	-76	-84	-93
14	-60	-66	-75	-83

To compare our thermodynamic model to the experimental data in Figure 3.2, we calculated the conversion of Pd particles to Z_2Pd (X_{Z_2Pd}) for a range of particle sizes (d_{Pd} = 2–100 nm) by considering a Boltzmann distribution of the equilibrium population of PdO particles and Z_2Pd (Equation 3.12) [11].

$$X_{Z_2Pd}(T, P_{O_2}, d_{Pd}) = \frac{(\frac{N_{2Al}}{N_{Pd}})exp(-\frac{\Delta G^{form}_{Z_2Pd} - \Delta G^{form}_{PdO}}{kT})}{(\frac{N_{2Al}}{N_{Pd}})exp(-\frac{\Delta G^{form}_{Z_2Pd} - \Delta G^{form}_{PdO}}{kT}) + 1} \tag{3.12}$$

We evaluated the conversion of Pd particles to Z_2Pd for a range of Pd/Al ratios (Figure 3.40, SI) and found that it does not have a considerable impact on X_{Z_2Pd} values until $N_{Pd}/N_{2Al} > 1$.

Figure 3.3a reports the results for the compositional parameters corresponding to the Pd-CHA-X zeolites reported in Table 3.1 and air treatment conditions in Figure 3.2. Blue and yellow regions of Figure 3.3a show conversion of metallic Pd particles to PdO, and Z_2Pd, respectively. Analogous results for the conversion of Pd particles to ZPdOH are in progress. Figure 3.3a shows that complete conversion of 2 (squares), 7 (circles), and 14 nm (triangles) Pd particles to Z_2Pd is thermodynamically feasible at all air treatment conditions in Figure 3.2 (598–873 K, 20 kPa O_2, 0.014 kPa H_2O). The predictions for $d_{Pd} = 2$ nm are consistent with the experimental results for Pd-CHA-2, which contained predominantly ion-exchanged Pd^{2+} after treatment to 673 or 773 K. However, for $d_{Pd} = 7$ and 14 nm, the computed fraction of Pd particles converted to Z_2Pd (ca. 1.00) are significantly higher than the amount of ion-exchanged Pd^{2+} observed experimentally for the Pd-CHA-7 and Pd-CHA-14 samples (593–773 K). Further, our model predicts complete oxidation of metallic Pd with O_2 to Pd^{2+} species to either agglomerated PdO or Z_2Pd under these conditions; however, a residual fraction of metallic Pd persists on both Pd-CHA-7 and Pd-CHA-14 following air treatments (<573 K for Pd-CHA-7 and 573 873 K for Pd-CHA-14). Thus, while complete conversion of large Pd particles, such as in Pd-CHA-7 and Pd-CHA-14, to ion-exchanged Pd^{2+} is not thermodynamically limited under these conditions (598-873 K, 20 kPa O_2, 0.014 kPa H_2O), kinetic barriers are likely responsible for the incomplete oxidation and/or disintegration of large Pd particles.

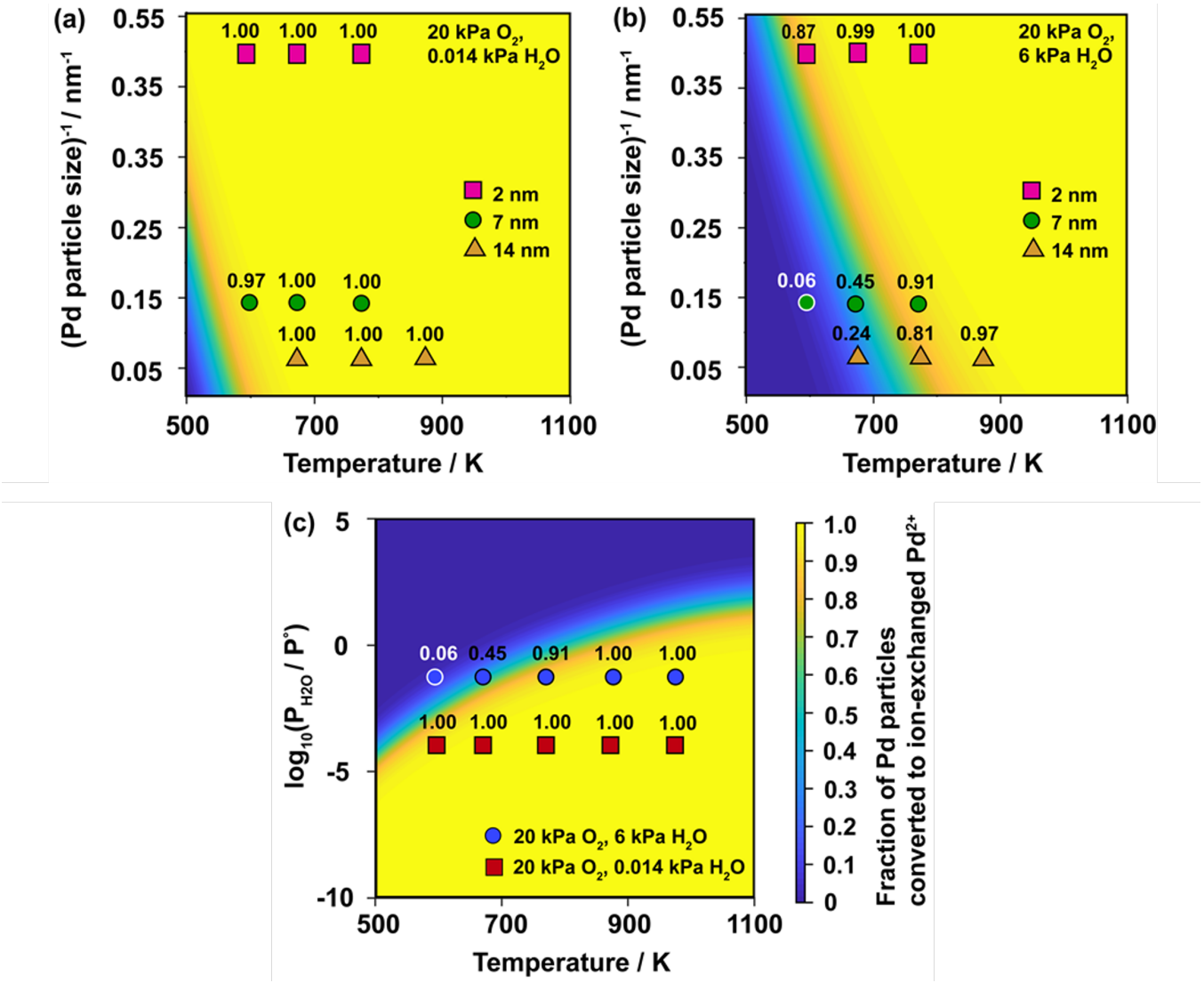

Figure 3.3. Pd particle size-dependent thermodynamic phase diagram for the conversion of Pd particles to Z_2Pd in CHA (Si/Al =12, Pd/Al = 0.06) under (a) 20 kPa O_2, 0.014 kPa H_2O and (b) 20 kPa O_2, 6 kPa H_2O, based on HSE06-D3(BJ)vdw calculated energies. The fraction of Pd particles converted to Z_2Pd for 2 nm (squares), 7 nm (circles), and 14 nm (triangles) Pd particles at the experimental air treatment conditions for Pd-CHA-X samples are labeled. (c) Thermodynamic phase diagram for the conversion of 7 nm Pd particle to ion-exchanged Pd^{2+} cations on CHA (Si/Al =12, Pd/Al = 0.06) as a function of temperature and P_{H_2O}. The fraction of Pd particles converted to ion-exchanged Pd^{2+} cations at 20 kPa O_2, 0.014 kPa H_2O (squares), and 20 kPa O_2, 6 kPa H_2O (circles) at treatment temperatures of 598–1023 K are labeled.

Previous studies have proposed that addition of H_2O to the air stream (1023 K, 10 kPa H_2O in balance air) may facilitate the mobility of Pd, causing a greater fraction of agglomerated PdO to structurally interconvert to ion-exchanged Pd^{2+} [10]. To determine the thermodynamic influence of H_2O pressure on Pd structural interconversion, we constructed phase diagrams for air treatment conditions with higher H_2O partial pressures (6 kPa). Figure 3.3b shows the fraction of Pd particles converted to Z_2Pd at the respective treatment temperatures of Pd-CHA-X samples, which are labeled for comparison with Figure 3.3a. We considered a representative Pd particle size of 7 nm to illustrate the conversion of Pd particles to Z_2Pd as a function of T and P_{H_2O} as shown in Figure 3.3c; treatment conditions of 20 kPa O_2 with 0.014 (squares) and 6 kPa (circles) H_2O, respectively are labeled. Similar phase diagrams for $d_{Pd} = 2$ and 14 nm are reported in Figure 3.41, SI. Our results demonstrate that increasing P_{H_2O} thermodynamically limits the amount of Z_2Pd formed. The inhibiting effect of H_2O is especially pronounced for larger Pd particles at $T < 773$ K. We found that $d_{Pd} = 7$ and 14 nm exhibit almost complete conversion to ion-exchanged Pd^{2+} during air treatments at $T > 600$ K in the presence of 0.014 kPa H_2O, but when P_{H_2O} is increased to 6 kPa, conversion of Pd particles decrease to 0.45 and 0.24 for 7 and 14 nm, respectively. Conversely, the effect of higher P_{H_2O} for $d_{Pd} = 2$ nm at $T > 600$ K is negligible; complete conversion of Pd particles to Z_2Pd is predicted during air treatments with 0.014 kPa H_2O as well as 6 kPa H_2O. At conditions relevant to practical applications of PNAs (3.1-4.5 kPa H_2O) an increase in P_{H_2O} favors formation of larger fractions of PdO agglomerates at $T <$ 800 K for $d_{Pd} = 2$–14 nm. The effect of H_2O favoring formation of agglomerated PdO over ion-exchanged Pd^{2+} attenuates with an increase in temperature due to the increase in the entropic contribution of H_2O as compared to the enthalpy (Figure 3.42, SI). Consequently, complete conversion of Pd particles to Z_2Pd is again predicted for all the Pd-CHA-X zeolites at $T > 800$ K.

These thermodynamic predictions suggest that adding H_2O to high-temperature air streams would inhibit the structural transformation of agglomerated PdO domains to ion-exchanged Pd^{2+} cations. Experimental investigations of this prediction involved treating the as-deposited Pd-CHA-7 sample in either flowing air with (6 kPa H_2O) and without H_2O to various temperatures, and then quantifying the ion-exchanged Pd^{2+} content and H_2 con-

sumption (per Pd) (Figure 3.4) with H_2 TPR. For treatment temperatures below 900 K, fewer ion-exchanged Pd^{2+} sites were formed after the wet air treatment than the dry air treatment (similar data on Pd-CHA-2 reported in Figures 4.4 and 3.28, SI), qualitatively consistent with the thermodynamic predictions indicating that increasing H_2O pressures should increase the agglomerated PdO content. Additionally, a larger fraction of residual metallic Pd remained after wet air treatments than dry air treatments for all temperatures below 973 K. This may be a consequence of H_2O-induced hydroxylation of the surfaces of agglomerated PdO_x domains, which has been proposed to inhibit surface O_2 activation [153], O_2 exchange from the support to Pd particles on silica and alumina supports [154], and oxidation of sub-surface metallic Pd [155]. Treatment of the as-deposited Pd-CHA-7 in air to 973 K with and without H_2O resulted in the same amount of ion-exchanged Pd^{2+} (0.80–0.85 per total Pd) and H_2 consumption (0.87–0.88 per total Pd), suggesting the inhibitory effects of co-feeding H_2O are attenuated at high temperatures because of the entropic contribution of the H_2O as a product of the ion-exchange reaction. Together, these experimental findings appear to contrast literature proposals that co-feeding H_2O facilitated the mobilization of Pd to increase the formation of ion-exchanged Pd^{2+} sites; however, we note that such reports were performed at higher temperatures (1023 K) than used here (973 K), which may be in a temperature regime where the effects of co-feeding H_2O on Pd structural interconversion are attenuated [10]. Together, these results demonstrate that co-feeding H_2O at high temperatures (673-873 K) does not facilitate the transformation of PdO to ion-exchanged Pd^{2+}, and that the treatment temperature itself was likely the dominant influence on the extent of agglomerated PdO converted to ion-exchanged Pd^{2+} cations.

Further studies were performed to determine whether the pseudo-steady state distributions of PdO and Pd^{2+} cations on Pd-CHA formed after dry or wet air treatments (673 K, 1 h) could reversibly form to the other condition. The as-deposited Pd-CHA-7 was first treated in flowing air to 673 K and held for 1 h, and then switched to a wet air stream (6 kPa H_2O) stream for 1 h (Figure 3.4). Exposure to the wet air stream decreased the H_2 consumed (per total Pd) from 0.91 (dry air only) to 0.68, which was within error of the Pd-CHA-7 sample exposed only to the wet air treatment (0.69). However, the amount of ion-exchanged Pd^{2+} (per total Pd) decreased from 0.72 (dry air only) to 0.59 (dry air followed by wet air), but

did not reach the value measured on the sample exposed only to the wet air treatment (0.43). This indicates that adding H_2O to the air stream after 1 h did not reversibly generate the distribution formed after the H_2O-only treatment; moreover, a longer treatment time (18 h) in the wet air stream following an air-only treatment did not change the ion-exchanged Pd^{2+} content or H_2 consumption per total Pd (Figure 3.29, SI), demonstrating the values reported after a 1 h treatment in Figure 3.4 reflect a pseudo steady-state distribution of agglomerated PdO and ion-exchanged Pd^{2+}. Additionally, the reverse experiment was performed where the Pd-CHA-7 sample was first treated in wet air (6 kPa H_2O) to 673 K for 1 h, followed by removing the H_2O from the air stream and holding for 1 h. The resulting ion-exchanged Pd^{2+} (per total Pd) increased slightly from 0.43 (wetted air only) to 0.49, which was significantly below the result on the sample exposed only to a dry air treatment (0.72). The partially irreversible nature of Pd structural interconversion between dry and wet (6 kPa H_2O) air treatments can be rationalized from conclusions of prior work [113] that showed sample treatment history influences the spatial distribution and particle sizes of Pd domains, which will ultimately influences the extent of Pd structural interconversion observed during a subsequent air treatment because of competing processes during Ostwald ripening and particle disintegration to form both agglomerated PdO and Pd^{2+} cations. Here, the first dry air treatment (673 K, 1 h) of Pd-CHA-7 converted the 7 nm Pd particles initially present at the exterior zeolite crystallite to different PdO domain sizes and ion-exchanged Pd^{2+} sites distributed deeper within the interior of zeolite crystallites; thus, upon subsequent addition of H_2O to the flowing air stream, there was a different distribution of PdO particle sizes with some amount of ion-exchange Pd^{2+}. Therefore, the mobile Pd species formed during Ostwald ripening would experience a different local availability of framework Al exchange sites and a different PdO particle size distribution for agglomeration events.

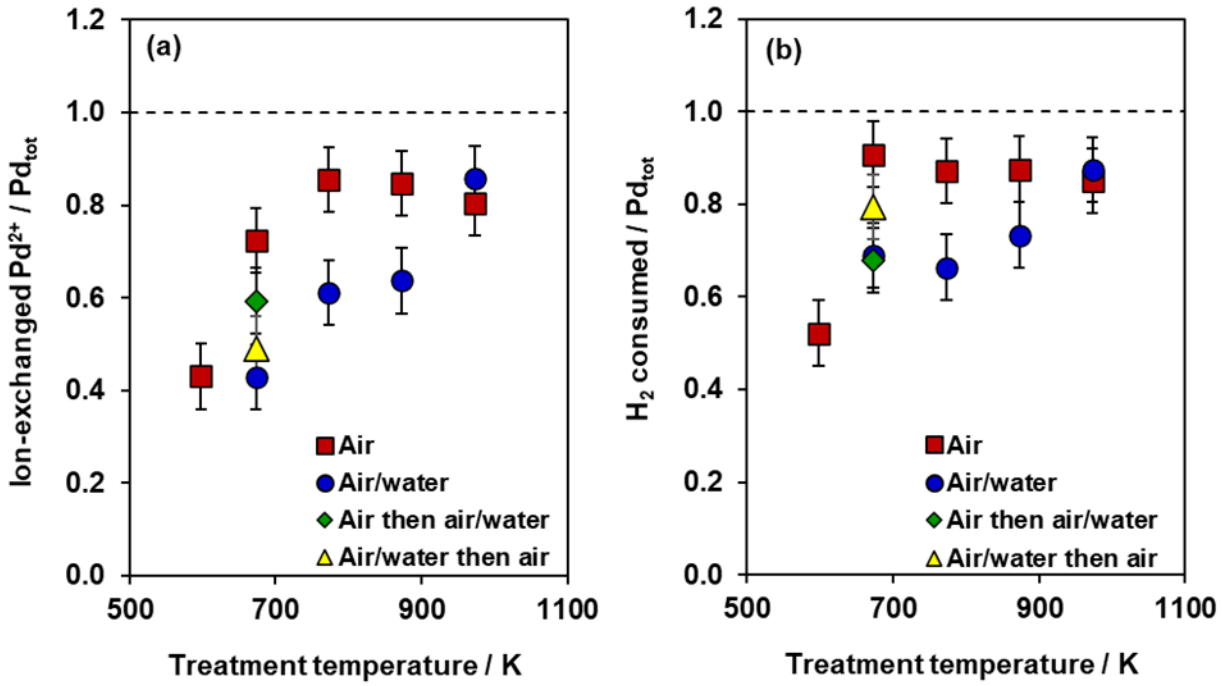

Figure 3.4. (a) The amount of ion-exchanged Pd^{2+} and (b) total H_2 consumed normalized per total Pd as a function of treatment temperature in flowing air (squares), 6 kPa H_2O in balance air (circles), air (1 h) then adding 6 kPa H_2O (1h, diamond), and 6 kPa H_2O in balance air (1 h) then air (1 h, tringle) for the Pd-CHA-7 material. Dashed line represents theoretical maximum values. H_2 TPR profiles are reported in Figure 3.30, SI.

3.4.3 Quantifying apparent rates of Pd redispersion via Ostwald ripening

The conversion of agglomerated, metallic Pd domains to ion-exchanged Pd^{2+} as a function of time was monitored under flowing air at different temperatures to deduce mechanistic information on plausible pathways for structural interconversion. An NH_4-form CHA zeolite (Si/Al = 12) was deposited with $Pd(NH_3)_4(NO_3)_2$ via incipient wetness impregnation to yield a 2.2 wt% $[Pd(NH_3)_4]^{2+}$-CHA material, which was first treated in 5 kPa H_2 to 673 K (600 K h^{-1}) for 1 h to remove amine ligands from Pd^{2+} and form agglomerated Pd^0 domains (see Figures 3.7 and 3.8 for TEM images and particle size distribution, and Figure 3.44 for O_2 chemisorption of Pd dispersion) [113]. This sample was then treated in flowing 5 kPa H_2 to high temperatures (598–673 K), purged in flowing inert (for 0.083 h), then held in flowing air for various times (0.003 1 h). The sample was then quenched (0.67 K s^{-1}) to ambient temperature with liquid N_2 blow-off gases, and then characterized by H_2 TPR. The sample was reversibly cycled through this protocol, and it was assumed the average Pd particle size did not change significantly with each subsequent cycle, as quantitatively shown in our prior work that used similar air and H_2 cycling experiments using O_2 chemisorption [113].

Figure 3.5 shows the amount of ion-exchanged Pd^{2+} as a function of time and temperature for the isothermal Pd redispersion rate measurements (further discussion on rate measurements in supporting information). The amount of ion-exchanged Pd^{2+} formed after treatment in air for 1 h increased systematically with temperature, which qualitatively agrees with thermodynamic predictions that higher temperatures facilitate the conversion of agglomerated PdO particles to ion-exchanged Pd^{2+}. Additionally, the apparent rate of formation of ion-exchanged Pd^{2+} systematically increased with temperature, consistent with an activated process for structural interconversion. Unlike previous in-situ TEM quantifications of single Ni particles disintegration rates on $MgAl_2O_4$ [156], the rates of Pd nanoparticle conversion to ion-exchanged Pd^{2+} measured with H_2 TPR quantifies the bulk rate of conversion, avoiding the sampling bias of TEM. From Figure 3.5b, the H_2 consumption per Pd was approximately unity for all time points after 10 s, suggesting the observed ion-exchanged Pd^{2+} formation rates were not limited by metallic Pd oxidation to PdO with O_2. To rule out any additional kinetic influences of O_2 on the conversion of agglomerated Pd domains to

ion-exchanged Pd^{2+} cations, the 2.2 wt% Pd-CHA material was first treated in H_2 to form predominantly metallic Pd agglomerated domains (see Figures 3.7 and 3.8 for TEM images and particle size distributions, and Figure 3.44 for O_2 chemisorption for Pd dispersion), and then was treated in flowing air at 473 K for 2 h to form predominantly agglomerated PdO domains (ion-exchanged Pd^{2+}/Pd_{tot} = 0.07, PdO/Pd_{tot} = 0.81, H_2 TPR profile in Figure 3.31, SI). Next, the air stream was replaced with an inert atmosphere (UHP He, 99.999%, with in-line O_2 and moisture trap) and treated to 648 K (600 K h^{-1}) for 1 h, and the amount of ion-exchanged Pd^{2+} (per total Pd) increased to 0.52. This observation demonstrates the mechanistic role of O_2 is likely only to oxidize metallic Pd, which was not kinetically relevant for the conditions reported in Figure 3.5; thus, the reported formation of ion-exchanged Pd^{2+} as a function of time reflects the rate of structural conversion of agglomerated domains to ion-exchanged sites.

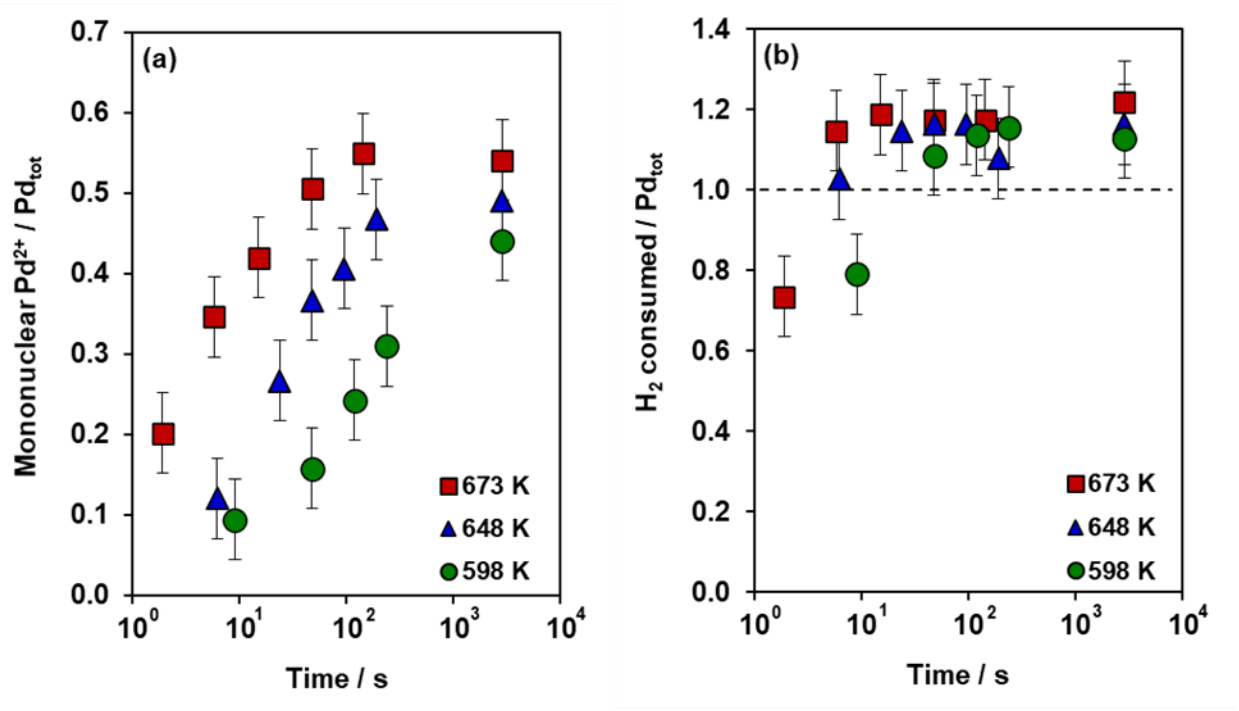

Figure 3.5. (a) The amount of ion-exchanged Pd^{2+} normalized per total Pd as a function of time during isothermal switching experiments for three different treatment temperatures (square: 673 K, triangle: 648 K, circle: 598 K) using a 2.2 wt% Pd-CHA material (Si/Al = 12) prepared via incipient wetness impregnation. (b) The total H_2 consumed normalized per total Pd from (a). Dashed line represents theoretical maximum amount. H_2 TPR profiles are in Figures 3.32, 3.33, 3.34, SI.

Preliminary energetic calculations (in progress) suggest $Pd(OH)_2$ is the most favorable species to be ejected from PdO surfaces under these conditions. Therefore, it was hypothesized that adding H_2O to the air stream may promote the rate of Pd redispersion by facilitating the hydroxylation of PdO surfaces and ejection of the $Pd(OH)_2$ mobile species, but at the expense of limiting the total extent of exchange because of thermodynamic limitations. Isothermal redispersion experiments were performed with and without 2 kPa H_2O to determine the kinetic influence of H_2O on the apparent redispersion rate (Figure 3.6). Consistent with previous thermodynamic arguments, adding 2 kPa H_2O to the air decreased the amount of ion-exchanged Pd^{2+} cations after treatment for 1 h (Figure 3.43, SI); however, when the amount of exchange was normalized to the pseudo steady-state value after 1 h (i.e., normalizing rates to the reversible fraction of Pd that can interconvert), the apparent rates of redispersion with and without H_2O were similar within error. Additionally, the H_2 consumption per total Pd was approximately unity for all time points measured, again demonstrating the rate of Pd redispersion was not limited by Pd oxidation. Therefore, co-feeding H_2O did not have a significant kinetic effect on the redispersion of PdO particles to ion-exchanged Pd^{2+} and, for this material and conditions of these measurements, H_2O apparently only influences the thermodynamics of the redispersion process.

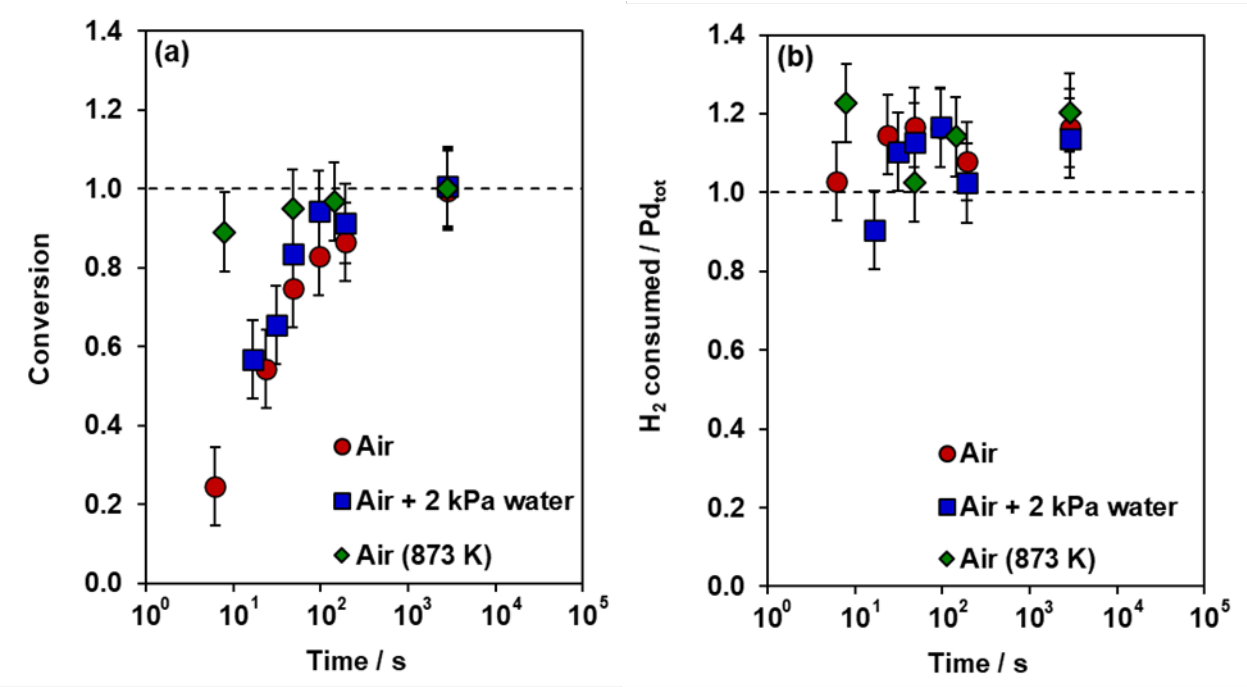

Figure 3.6. (a) The amount of ion-exchanged Pd^{2+} (normalized per ion-exchanged Pd^{2+} content after treatment for 1 h, and denoted as conversion) as a function of time during isothermal switching experiments (648 K) in air (circles), 2 kPa H_2O in balance air (squares), and air after treatment in air to 873 K (diamonds) using a 2.2 wt% Pd-CHA material (Si/Al = 12) prepared via incipient wetness impregnation. H_2 TPR profiles are in Figures 3.33, 3.35, and 3.36, SI. (b) H_2 consumed normalized to total Pd of materials in (a).

Pd particle size can influence the kinetics and thermodynamics of converting Pd particles to ion-exchanged Pd^{2+} sites, as larger particles show higher barriers for Pd oxidation to PdO in the presence of O_2 and subsequent redispersion to ion-exchanged Pd^{2+}. Therefore, the 2.2 wt% Pd-CHA material (cycled between 598–673 K air treatments for redispersion kinetic measurements) was then treated in flowing air to 873 K to alter the particle size distribution with the goal of disentangling Pd particle size effects on the apparent rate of redispersion. Air treatment to 873 K decreased the average particle size (HAADF-STEM images in Figure 3.20 and particle size distribution in Figure 3.21, SI) from 2.9 to 2.1 nm (assuming a log-normal distribution) and increased the Pd dispersion (O_2 chemisorption, Figure 3.44, SI) from 0.19 to 0.52, corroborating prior reports that showed the average Pd particle size decreased as the air treatment temperature increased [57]. Time-dependent redispersion measurements of the 2.2 wt% Pd-CHA material previously treated in air at 873 K showed faster apparent rates of redispersion to ion-exchanged Pd^{2+}. Notably, the shortest time point of 10 s resulted in almost complete conversion (ca. 0.9) of the Pd species that reversibly convert between agglomerated domains and ion-exchanged Pd^{2+}. Additionally, all of the redispersion rates measured for the 873 K air-treated material showed H_2 consumptions per Pd near unity, again demonstrating the kinetic irrelevance of O_2. The greater kinetic barriers associated with disintegration to ion-exchanged Pd^{2+} sites rationalize why materials initially containing larger Pd nanoparticles contained greater dispersions (measured with CO chemisorption) than initially smaller Pd nanoparticles after aging protocols (cyclic O_2/CO injections at 1173 K) [157], consistent with proposals that the constant sintering kinetic parameter (K_I) in the Wynblatt and Gjostein Ostwald-ripening model [158] (Equation 3.13) increases as the initial particle size (D_0) decreases:

$$D\left(t\right) = D_0 \left(1 + \frac{8K_I t}{\left(D_0\right)^3}\right)^{\frac{1}{3}} \tag{3.13}$$

where D(t) is the size of the particles as a function of time (t). Taken together, these data suggest smaller Pd nanoparticles disintegrate at a faster rate for structural interconversion to ion-exchanged Pd^{2+}.

3.5 Conclusions

Precise catalyst synthesis techniques, quantitative site characterization methods, and DFT calculations were combined to examine the relative importance of various thermodynamic and kinetic factors governing the interconversion of Pd nanoparticles and ion-exchanged Pd^{2+} cation sites in CHA zeolites under high temperature (593–973 K) air treatments with and without H_2O. A series of model Pd-CHA materials was synthesized via deposition of colloidal Pd nanoparticle suspensions onto H-CHA supports to prepare monodisperse Pd particles of different size (2–14 nm) deposited at zeolite crystallite surfaces, to facilitate quantitative measurements of Pd particle redispersion rates and their dependence on initial Pd particle size. Smaller Pd nanoparticles (2 nm) more readily converted to ion-exchanged Pd^{2+} species in air, and the conversion of larger metallic Pd nanoparticles (7, 14 nm) to PdO domains and ion-exchanged Pd^{2+} were observed to be lower than the thermodynamic distributions predicted by DFT calculations, which demonstrates larger metallic particles have kinetic barriers for oxidation with O_2 to PdO and for the subsequent disintegration of PdO to ion-exchanged Pd^{2+} sites. Additionally, increasing the H_2O partial pressure shifts the thermodynamic distribution away from Pd^{2+} sites and toward agglomerated PdO domains, suggesting that H_2O present in exhaust streams may facilitate Pd deactivation to agglomerated phases, contrary to prior literature proposals that adding H_2O to air facilitates Pd redispersion to ion-exchanged sites [10].

Quantitative measurements of metallic Pd nanoparticle conversion to ion-exchanged Pd^{2+} sites in air with and without H_2O, performed isothermally (598–673 K) with varying treatment time (0.003 -1.0 h), were leveraged to deduce mechanistic information of the redispersion process. After 10 s of treatment time, the oxidation of metallic Pd with O_2 is complete, and thus kinetically relevant for apparent rates of conversion to ion-exchanged Pd^{2+} sites beyond 10 s, which increased systematically as a function of temperature. Additionally, a predominantly PdO-containing CHA material treated in He to 648 K resulted in PdO conversion to ion-exchanged Pd^{2+} sites similar to that observed in air, suggesting the dominant mechanistic role of O_2 is to oxidize agglomerated metallic Pd to PdO. Under these conditions, DFT calculations predict $Pd(OH)_2$ as the most thermodynamically favorable mobile

Pd species, suggesting that adding H_2O to the air stream may facilitate hydroxylation of the PdO surface to increase the rate of forming $Pd(OH)_2$ intermediates. Experiments performed to add H_2O (2 kPa) to the air stream (648 K), however, lowered the amount of ion-exchanged Pd^{2+} sites for all isothermal redispersion measurements, but rates normalized by the fraction of Pd that reversible interconverts between particles to ion-exchanged Pd^{2+} sites did not depend on H_2O pressure (0–2 kPa). This observation demonstrates that H_2O more strongly influences the thermodynamics rather than the kinetics of Pd structural interconversion. Finally, a Pd-CHA sample treated in air to 873 K before isothermal redispersion measurements altered the particle size distribution toward smaller particles, which underwent redispersion to ion-exchanged Pd^{2+} site at a faster apparent rate, demonstrating that smaller Pd nanoparticles more easily disintegrate to mobile Pd species that adsorb at and exchange with Brønsted acid sites during Ostwald ripening processes.

We conclude both the initial Pd nanoparticle size and gas phase conditions influence critical thermodynamic and kinetic factors that govern Pd redispersion to ion-exchanged Pd^{2+} sites, which are the desired precursor Pd structures for PNA applications. Smaller Pd nanoparticles resulted in faster disintegration rates and greater thermodynamic preference to form ion-exchanged Pd^{2+}, consistent with previous reports that showed the kinetic rate parameter of Ostwald-ripening (in the Wynblatt and Gjostein model [158]) increased as the initial particle size decreased. Additionally, these results demonstrate that, in addition to H_2 and CO, the H_2O present in automotive exhaust increases the thermodynamic preference for forming agglomerated PdO structures and thus may negatively impact the long-term stability and viability of Pd-zeolite materials for PNA. The use of H_2 TPR to quantify the number of agglomerated PdO and ion-exchanged Pd^{2+} sites in the bulk of the sample, which avoids uncertainties associated with selective imaging techniques, provides a promising method to estimate rates of structural interconversion and compare to DFT predictions. Altogether, the quantitative connections between theory and experiment lend fundamental insights into the key thermodynamic and kinetic factors of solid-state ion-exchange mechanisms to prepare metal-zeolites with intended metal speciation and structures.

3.6 Acknowledgements

The authors thank the Department of Energy, Energy Efficiency and Renewable Energy (DE-EE000821) (T.M.L, H.H.L., R.G.) and UVA Engineering Research and Innovation Award (K.M., C.P.) for the financial support throughout the development of this project. The authors acknowledge Research Computing at the University of Virginia for the computational resources and technical support. Additionally, the authors thank Dr. Xinyi Wei (BASF Corporation) for providing the CHA material and all other members of the collaborative research team from the University of Kentucky, University of California Berkeley, Ford Motor Company, Oak Ridge National Laboratory, and BASF for helpful technical discussions.

3.7 Supporting Information

3.7.1 Colloidal Pd nanoparticle synthesis and deposition

Table 3.4. Colloidal Pd nanoparticle solutions, Pd compositions measured by inductively coupled plasma, and amounts of compounds used for metal deposition to prepare Pd-CHA.

Particle Size / nm	Pd wt %	mass colloidal Pd solution / g	mass H-CHA / g	mass hexanes / g
2	0.69	1.95	0.91	20.
7	0.73	1.87	0.90	20.
14	0.31	1.95	0.41	20.

3.7.2 Transmission electron microscopy and particle size distributions

The Pd nanoparticle sizes were estimated with transmission electron microscopy (TEM). ImageJ software quantified the 2-D projected area of the nanoparticles, and the diameter was estimated assuming a circle (i.e., projected area = π [diameter/2]^2). Table 3.5 contains a summary of all TEM characterizations.

Table 3.5. *Ex-situ* TEM characterization data for all samples after listed treatment conditions

Sample name	Treatment conditions	Number of particles imaged	Average particle size / nm	98% Confidence interval / nm	Standard deviation / nm
2.2 wt % Pd-CHA	673 K, 5 kPa H_2	164	2.9[a]	–	± 0.5[b]
2.2 wt % Pd-CHA	973 K in air, then 673 K in 5 kPa H_2	179	2.1[a]	–	±0.4[b]
2 nm (colloidal solution)	Ambient conditions	164	2.2	± 0.1	± 0.5
Pd-CHA-2	Ambient conditions	164	2.2	± 0.1	± 0.5
Pd-CHA-2	548 K , air	–	2.2	± 0.1	± 0.5
7 nm (colloidal solution)	Ambient conditions	161	6.9	± 0.1	± 0.7
Pd-CHA-7	Ambient conditions	112	6.8	± 0.1	± 0.7
Pd-CHA-7	548 K, air	72	6.6	± 0.2	± 0.7
14 nm (colloidal solution)	Ambient conditions	378	14.0	± 0.3	± 2.3
Pd-CHA-14	Ambient conditions	73	14.4	± 0.5	± 1.6
Pd-CHA-14	548 K, air	74	13.5	± 0.4	± 1.3

[a] Assuming a log-normal distribution.
[b] Standard deviation of log-normal distribution ($\sigma(\ln(x))$)

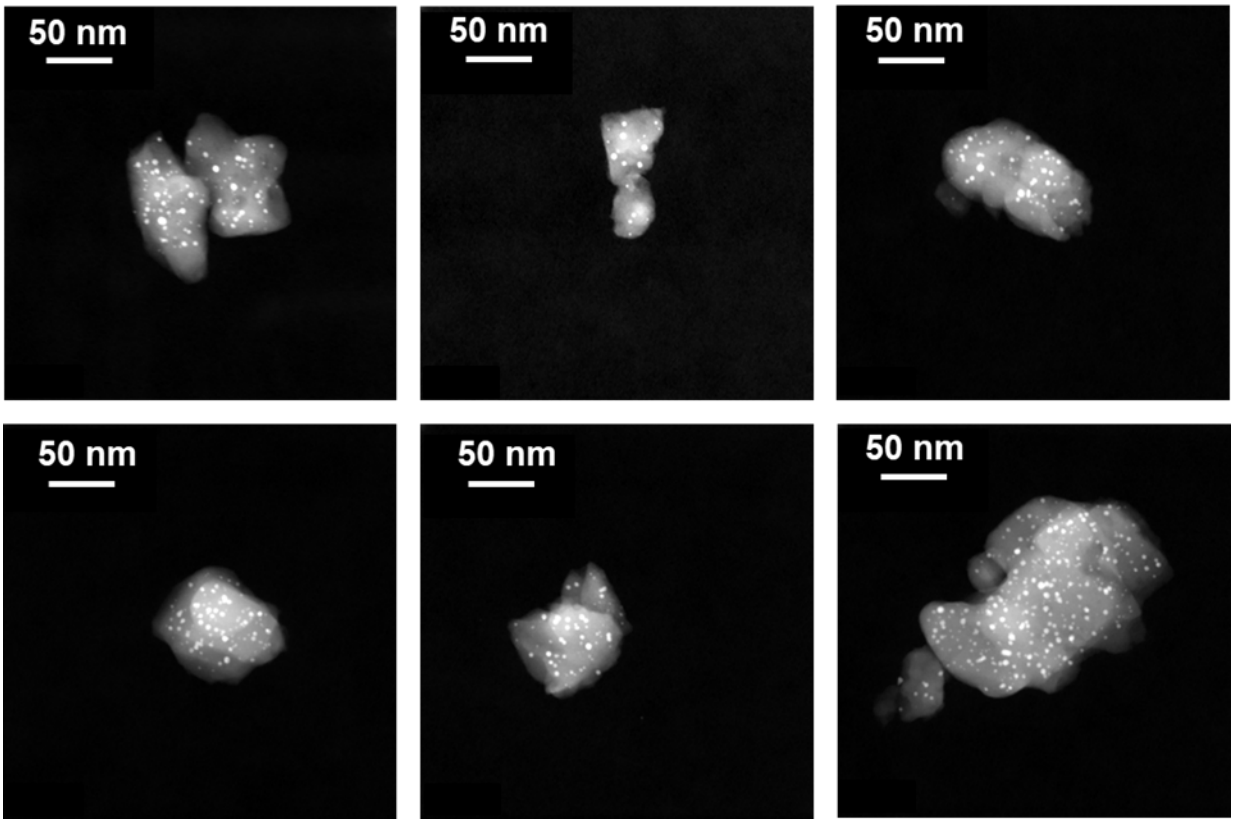

Figure 3.7. Ex-situ HAADF-STEM images (340 kx resolution) of the as-exchanged 2.2 wt% Pd-CHA sample synthesized via incipient wetness impregnation after treatment in flowing H_2 (5 kPa) at 673 K for 1 h. Histogram is reported in Figure 3.8

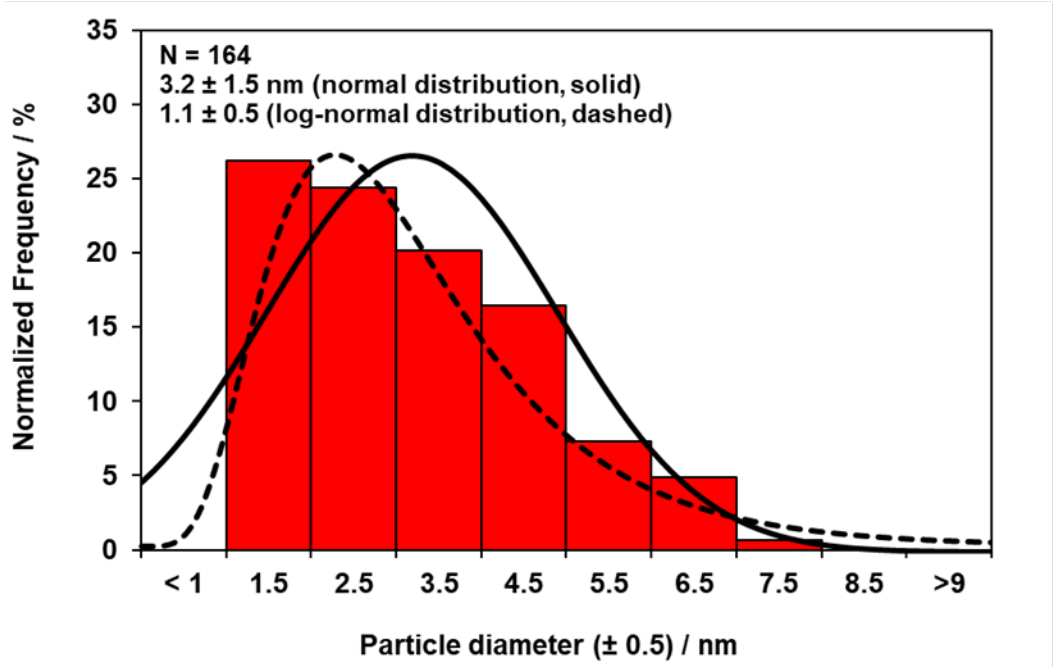

Figure 3.8. Histogram (normalized frequency), normal distribution (solid black line), and log-normal distribution (dashed black line) for the as-exchanged 2.2 wt% Pd-CHA material after treatment in flowing H_2 (5 kPa) at 673 K for 1 h. Histogram bins contain particles ± 0.5 nm from bin listing. The total number of particles imaged was 164, and the average particle size was 3.2 nm with a 98% confidence interval of 0.3 nm and standard deviation of 1.5 nm, assuming a normal distribution. The mean (average of ln(x)) of the log-normal distribution was 1.1 (corresponding to an average particle size of 2.9 nm) with a standard deviation (σ(ln(x)) of 0.5.

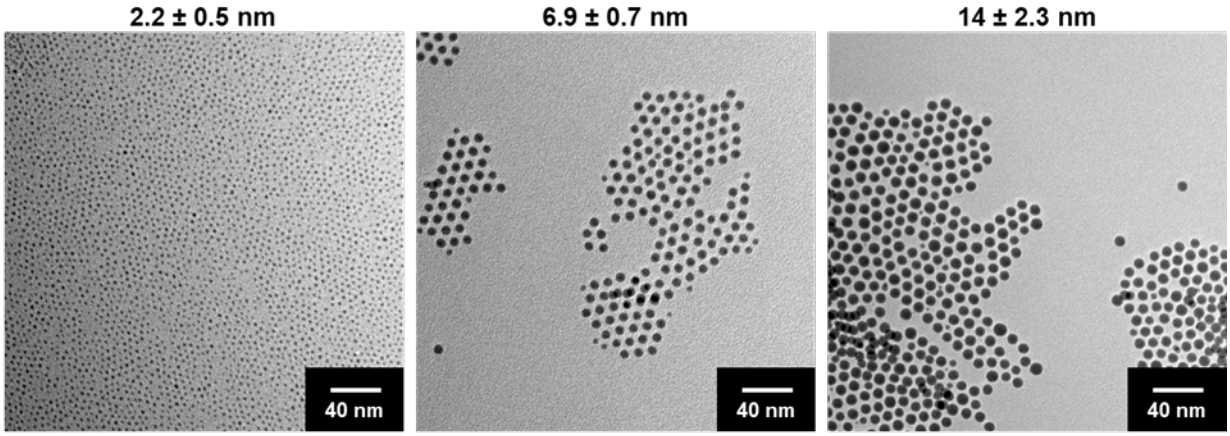

Figure 3.9. Ex-situ TEM images (71 kx resolution) of the colloidal Pd nanoparticle solutions. (Far left) nominally 2 nm particles, (middle) nominally 7 nm particles, (right) nominally 14 nm particles. Histograms are reported in Figures 3.10, 3.11, 3.12.

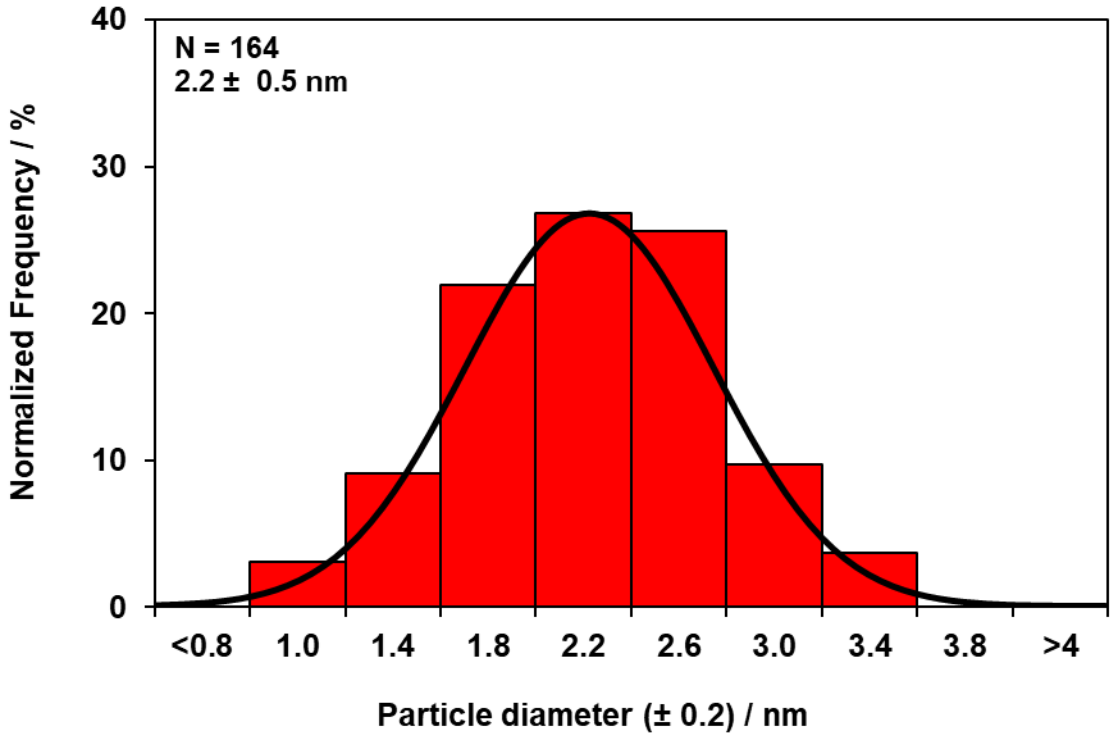

Figure 3.10. Histogram (normalized frequency) and normal distribution (black line) for the nominally 2 nm colloidal Pd nanoparticle solution. Histogram bins contain particles ± 0.2 nm from bin listing. The total number of particles imaged was 164, and the average particle size was 2.2 nm with a 98% confidence interval of 0.1 nm and standard deviation of 0.5 nm.

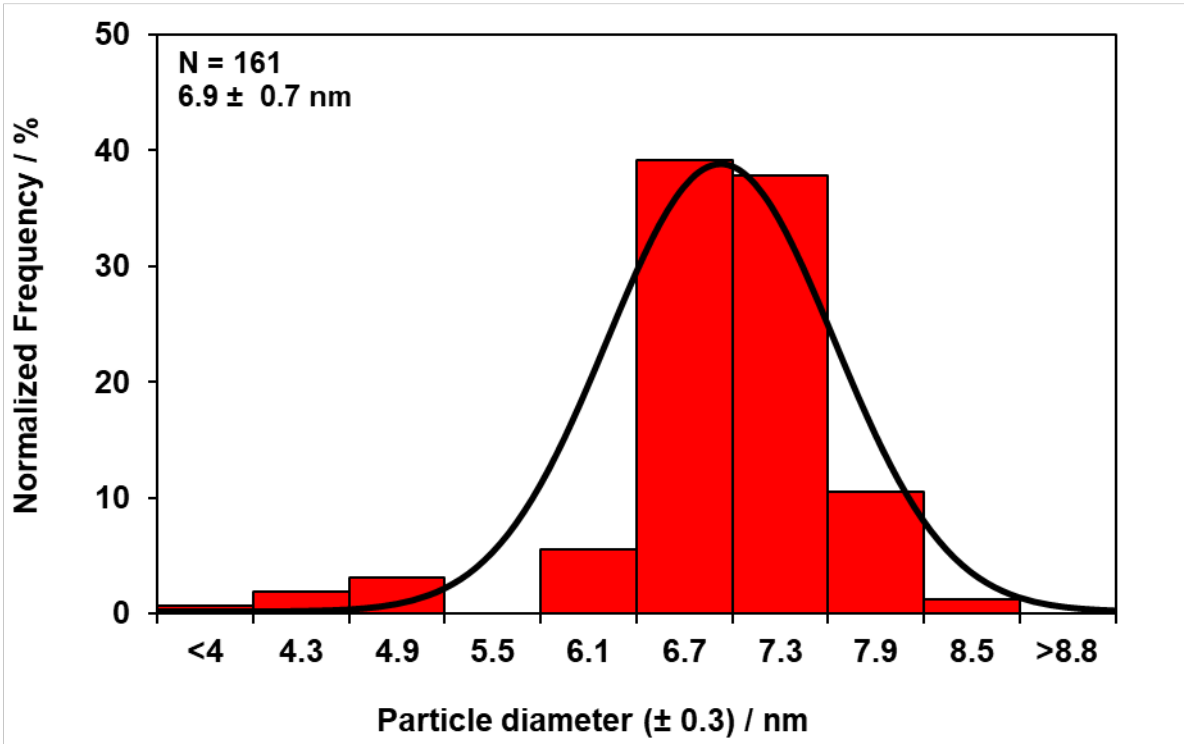

Figure 3.11. Histogram (normalized frequency) and normal distribution (black line) for the nominally 7 nm colloidal Pd nanoparticle solution. Histogram bins contain particles ± 0.3 nm from bin listing. The total number of particles imaged was 161, and the average particle size was 6.9 nm with a 98% confidence interval of 0.1 nm and standard deviation of 0.7 nm.

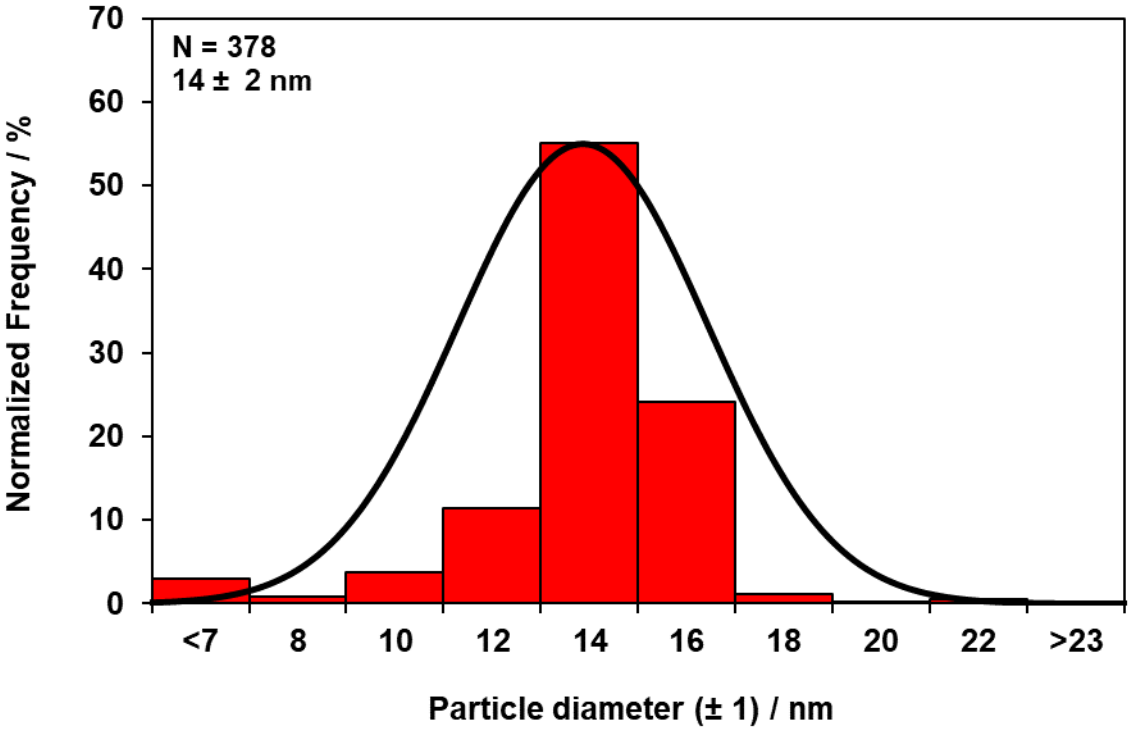

Figure 3.12. Histogram (normalized frequency) and normal distribution (black line)for the nominally 14 nm colloidal Pd nanoparticle solution. Histogram bins contain particles ± 1 nm from bin listing. The total number of particles imaged was 378, and the average particle size was 14 nm with a 98% confidence interval of 0.3 nm and standard deviation of 2.3 nm.

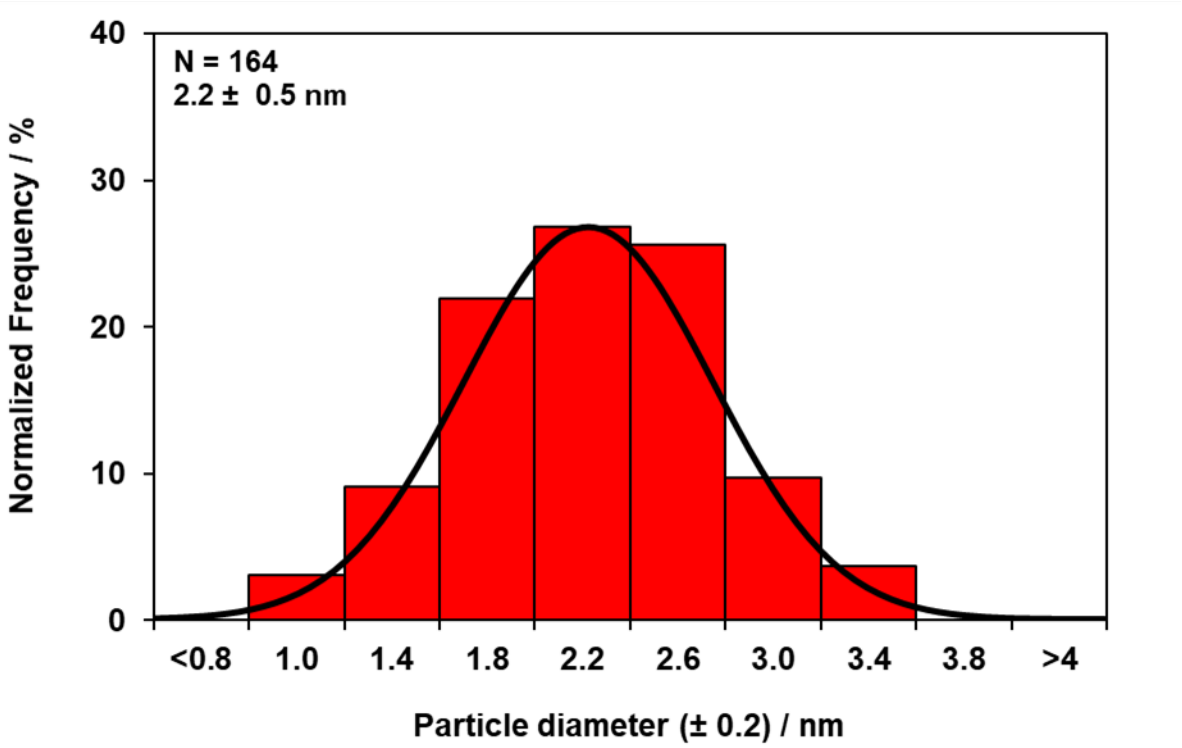

Figure 3.13. Histogram (normalized frequency) and normal distribution (black line) for the as-exchanged Pd-CHA-2 material. Histogram bins contain particles ± 0.2 nm from bin listing. The total number of particles imaged was 164, and the average particle size was 2.2 nm with a 98% confidence interval of 0.1 nm and standard deviation of 0.5 nm.

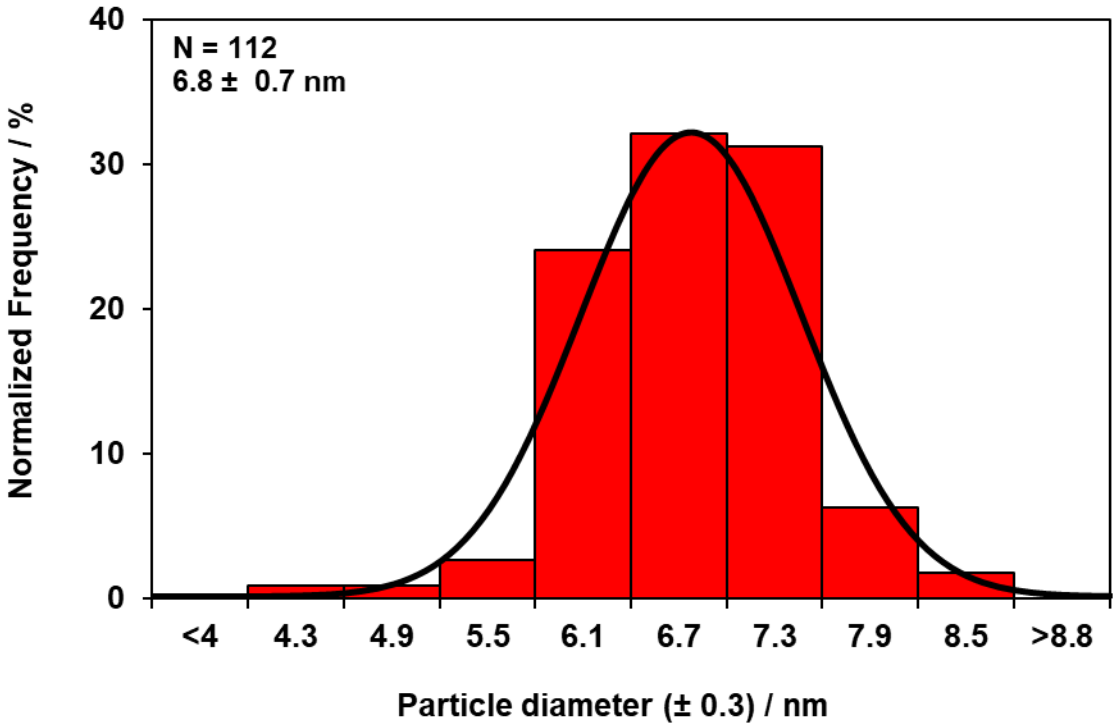

Figure 3.14. Histogram (normalized frequency) and normal distribution (black line) for the nominally 7 nm colloidal Pd nanoparticle solution. Histogram bins contain particles ± 0.3 nm from bin listing. The total number of particles imaged was 112, and the average particle size was 6.8 nm with a 98% confidence interval of 0.2 nm and standard deviation of 0.7 nm.

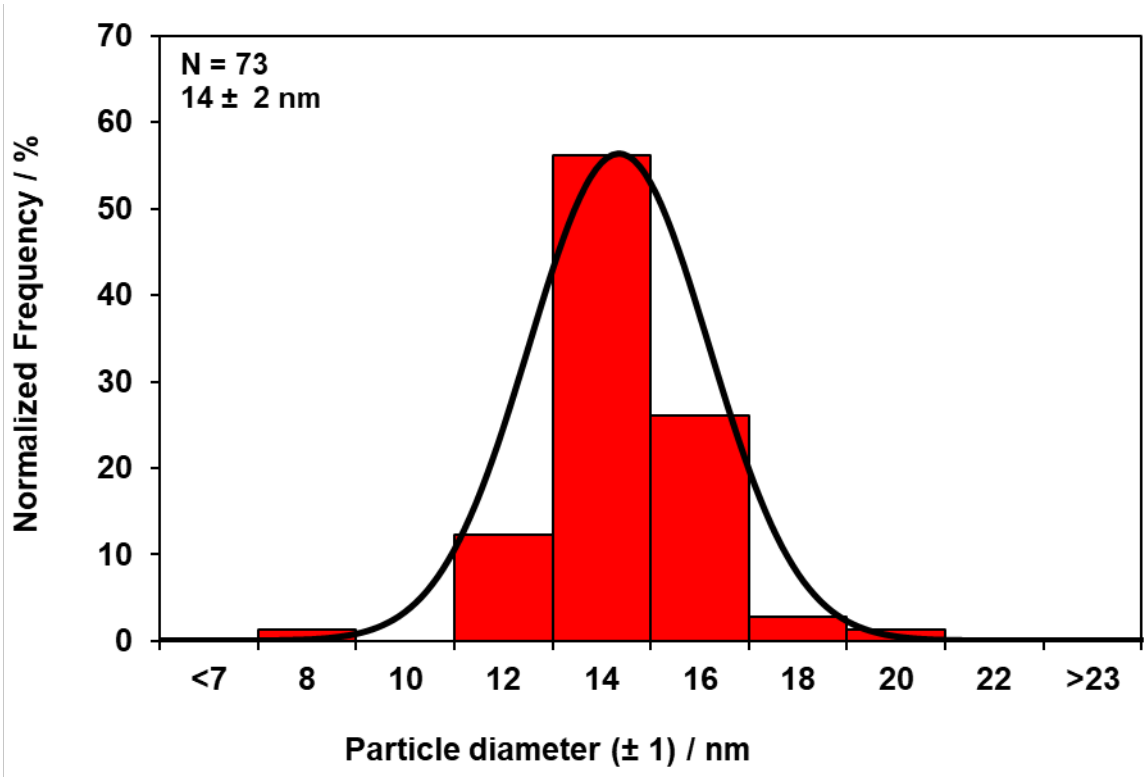

Figure 3.15. Histogram (normalized frequency) and normal distribution (black line) for the nominally 14 nm colloidal Pd nanoparticle solution. Histogram bins contain particles ± 1 nm from bin listing. The total number of particles imaged was 73, and the average particle size was 14.0 nm with a 98% confidence interval of 0.5 nm and standard deviation of 1.6 nm.

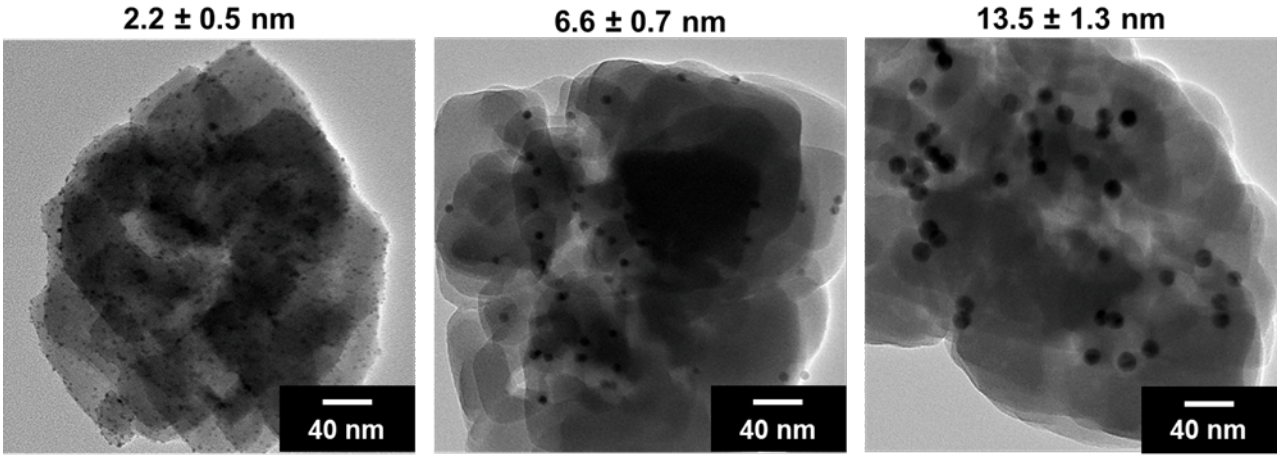

Figure 3.16. Ex-situ TEM images of the air-treated (548 K) Pd-CHA-X materials. Pd-CHA-2 (left), Pd-CHA-7 (middle), Pd-CHA-14 (right). Histograms are plotted in Figures 3.17, 3.18, and 3.19.

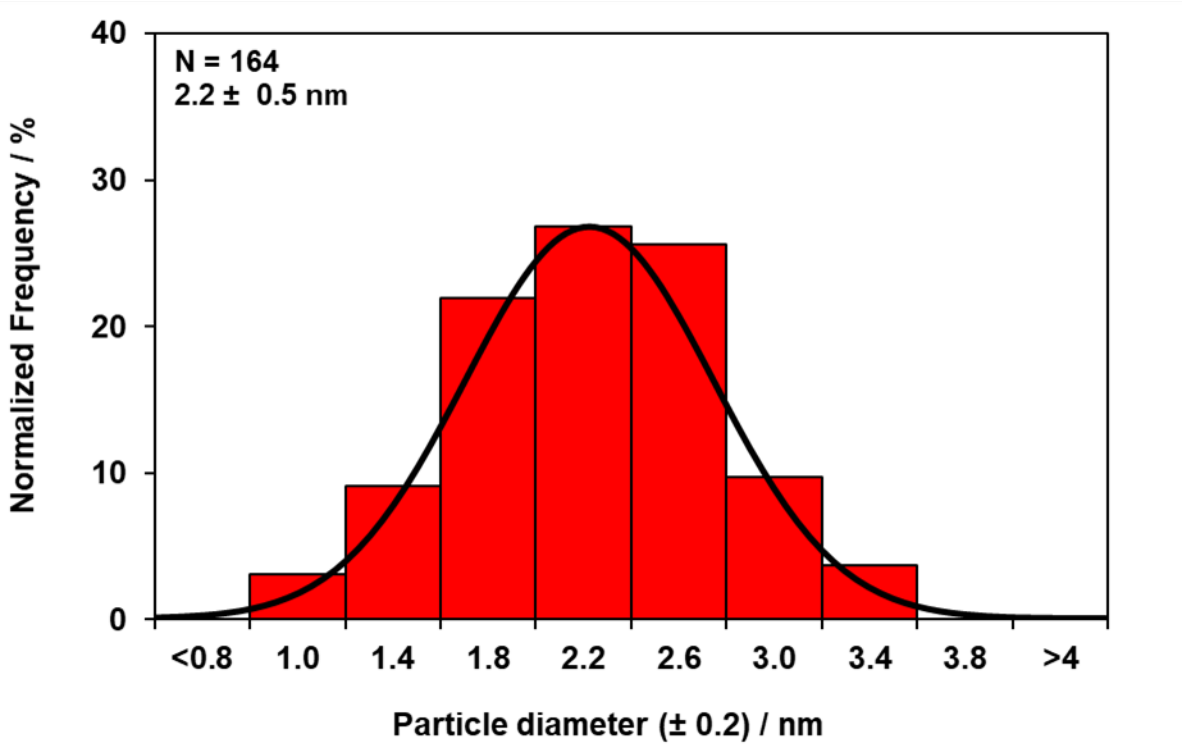

Figure 3.17. Histogram (normalized frequency) and normal distribution (black line) for the nominally 2 nm colloidal Pd nanoparticle solution after treatment in flowing air to 548 K (60 K h^{-1}) for 4 h. Histogram bins contain particles ± 0.2 nm from bin listing. The total number of particles imaged was 164, and the average particle size was 2.2 nm with a 98% confidence interval of 0.1 nm and standard deviation of 0.5 nm.

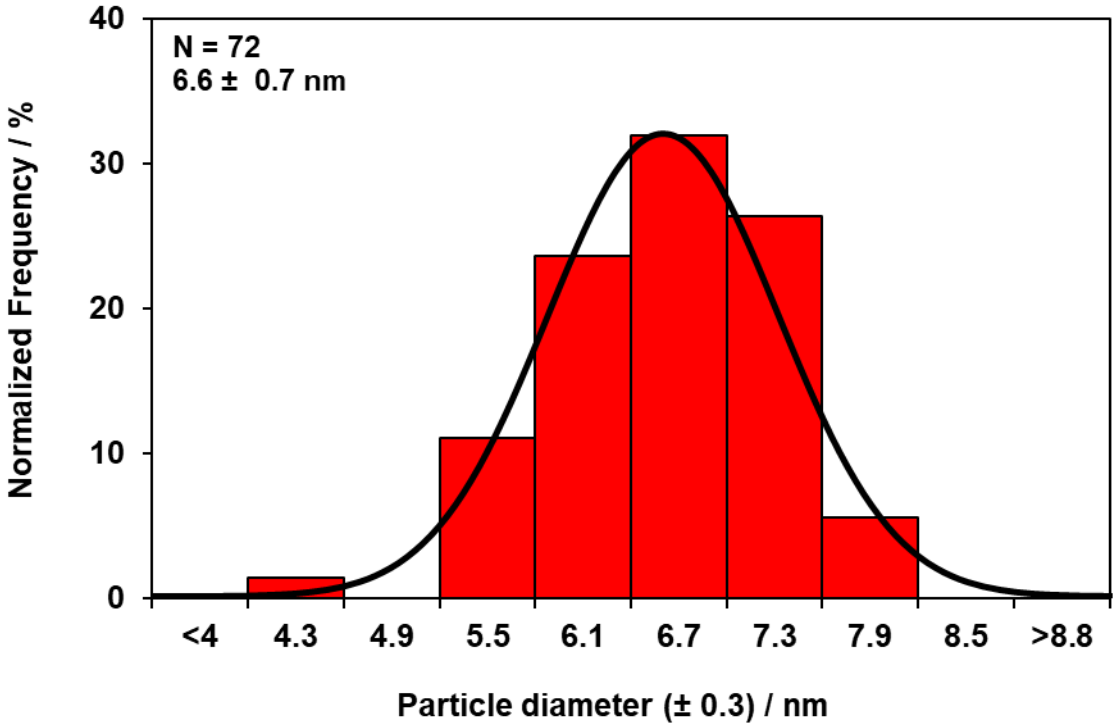

Figure 3.18. Histogram (normalized frequency) and normal distribution (black line) for the nominally 7 nm colloidal Pd nanoparticle solution after treatment in flowing air to 548 K (60 K h^{-1}) for 4 h. Histogram bins contain particles ± 0.3 nm from bin listing. The total number of particles imaged was 72, and the average particle size was 6.6 nm with a 98% confidence interval of 0.2 nm and standard deviation of 0.7 nm.

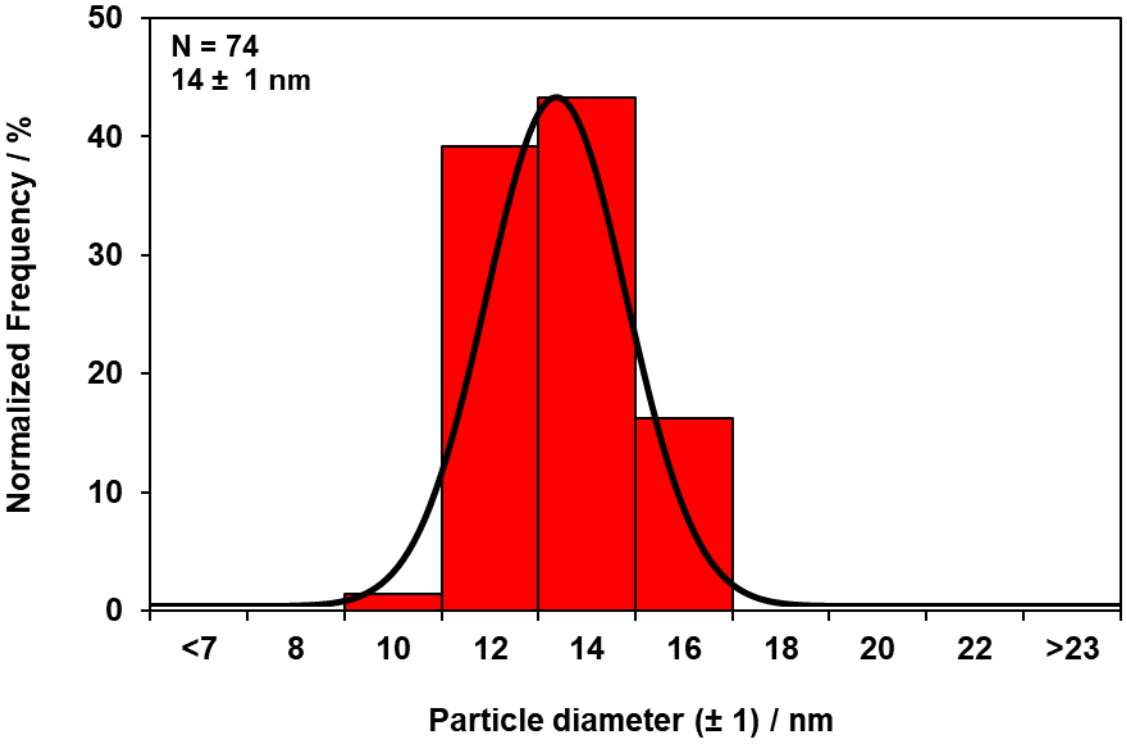

Figure 3.19. Histogram (normalized frequency) and normal distribution (black line) for the nominally 14 nm colloidal Pd nanoparticle solution after treatment in flowing air to 548 K (60 K h^{-1}) for 4 h. Histogram bins contain particles ± 1 nm from bin listing. The total number of particles imaged was 74, and the average particle size was 13.5 nm with a 98% confidence interval of 0.4 nm and standard deviation of 1.3 nm.

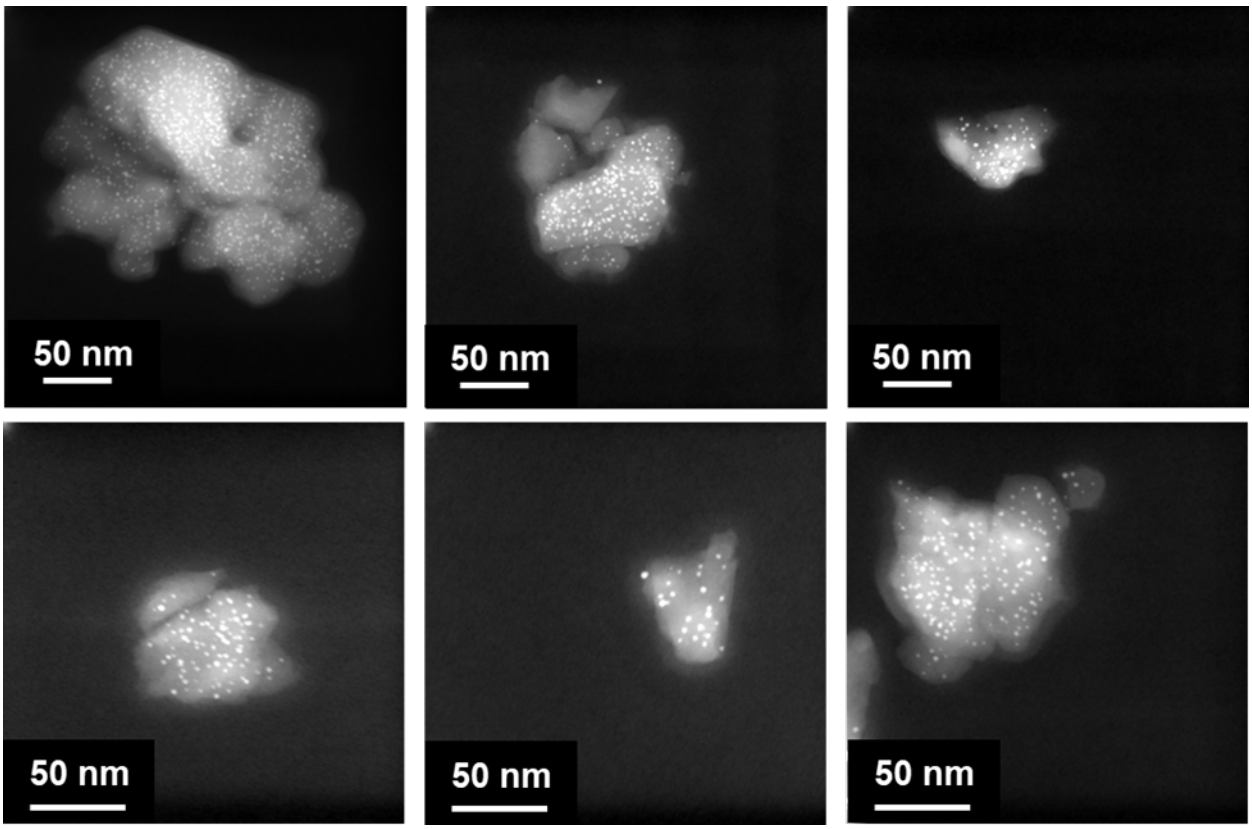

Figure 3.20. Ex-situ HAADF-STEM images (340 kx resolution for top panels and 470 kx resolution for bottom panels) of the as-exchanged Pd-CHA sample after treatment in flowing H_2 (5 kPa) at 673 K for 1 h, then air at 873 K for 1 h. Histogram is reported in Figure 3.21.

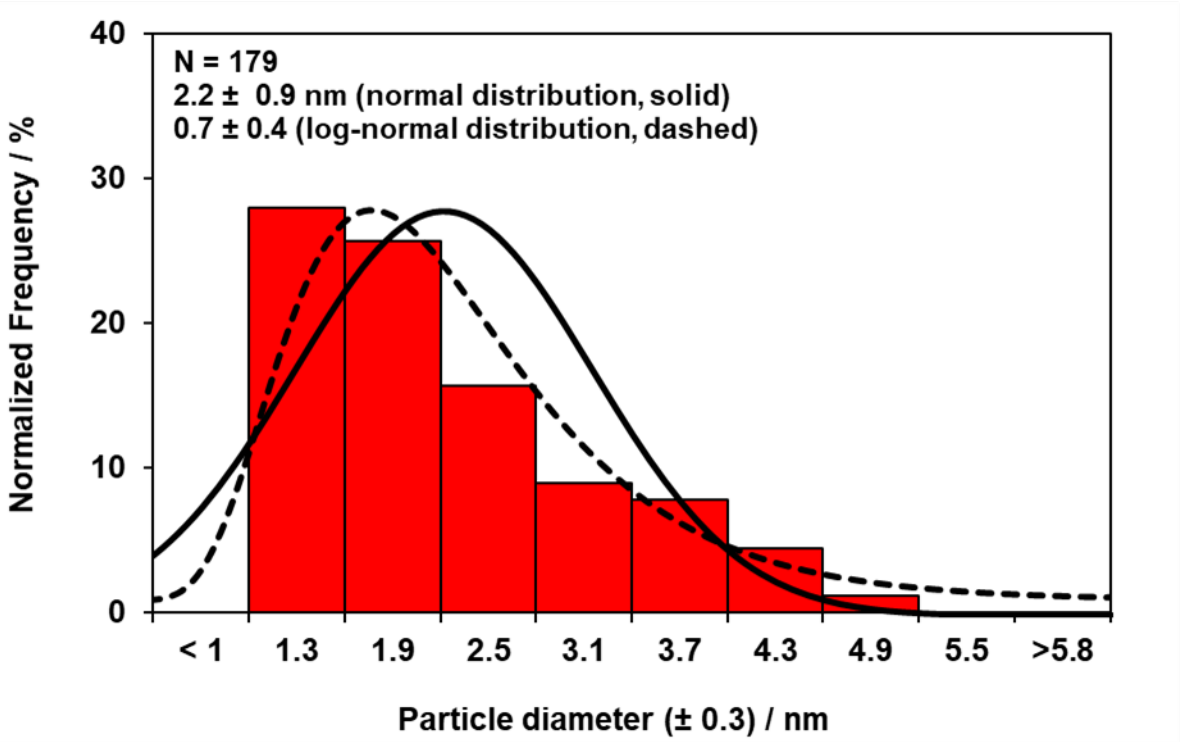

Figure 3.21. Histogram (normalized frequency), normal distribution (solid black line), and log-normal distribution (dashed black line) for the as-exchanged 2.2 wt% Pd-CHA material after treatment in flowing H_2 (5 kPa) at 673 K for 1 h, treatment in air to 873 K for 1 h, then treatment in flowing H_2 (5 kPa) to 573 K for 1 h. Histogram bins contain particles ± 0.3 nm from bin listing. The total number of particles imaged was 179, and the average particle size was 2.2 nm with a 98% confidence interval of 0.2 nm and standard deviation of 1.0 nm, assuming a normal distribution. The mean (average of ln(x)) of the log-normal distribution was 0.7 (corresponding to an average particle size of 2.1 nm) with a standard deviation (σ(ln(x)) of 0.4.

3.7.3 Thermal gravimetric analysis

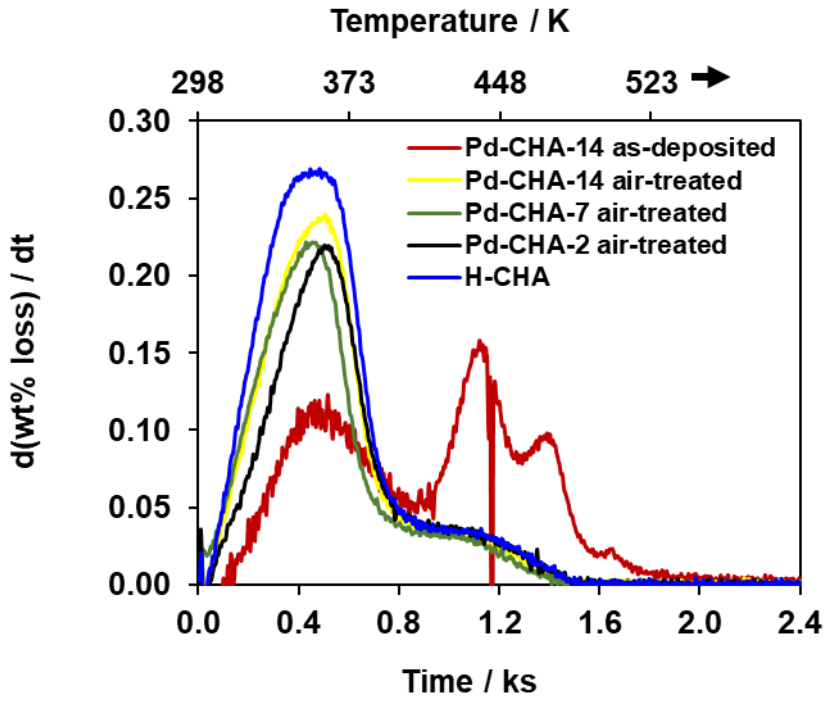

Figure 3.22. TGA weight loss derivative profiles (298 523 K, hold at 523 K) of as-deposited Pd-CHA-14 nm Pd-CHA (red), air-treated (548 K, 60 K h^{-1}, 4 h) monodisperse Pd-CHA materials (yellow for Pd-CHA-14, green for Pd-CHA-7, and black for Pd-CHA-2), and H-CHA support (blue).

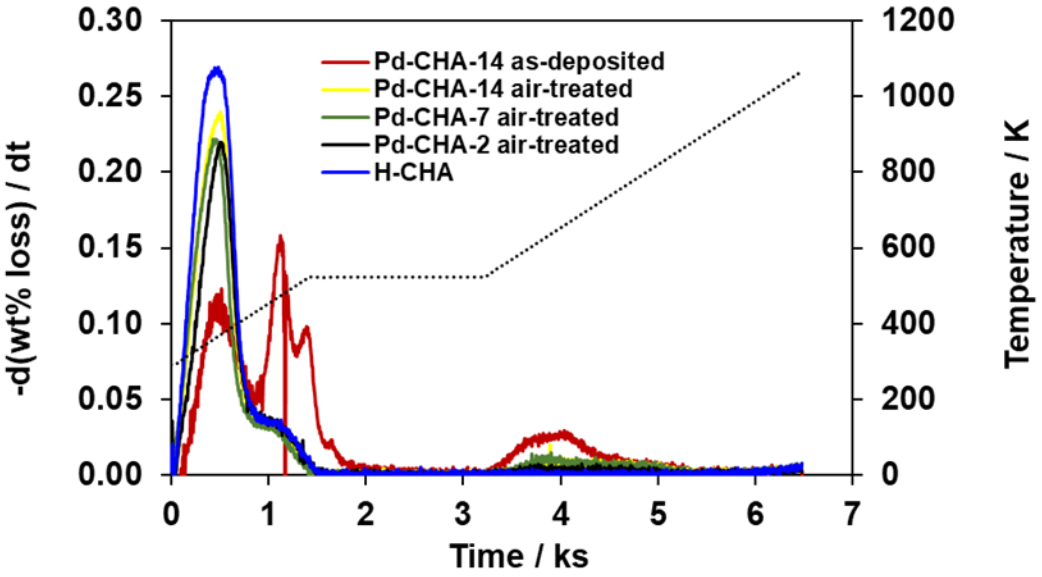

Figure 3.23. TGA weight loss derivative profiles (298–1073 K) of as-deposited Pd-CHA-14 (red), air-treated (548 K, 60 K h^{-1}, 4 h) monodisperse Pd-CHA-X materials (yellow for Pd-CHA-14, green for Pd-CHA-7, and black for Pd-CHA-2), and H-CHA support (blue). Dotted line is for temperature (secondary y-axis).

3.7.4 H_2 temperature programmed reduction

H_2 temperature programmed reduction (TPR) was leveraged to quantify agglomerated PdO domains and mononuclear, exchanged Pd^{2+} (ion-exchanged Pd^{2+}) species in Pd-exchanged zeolites. Even with the hydration step before H_2 TPR characterization to better separate the PdO domains (reduction temperatures between 260 310 K) from the ion-exchanged Pd^{2+} (reduction temperature of c.a. 380 K), some H_2 TPR profiles are ambiguous; a detailed discussion can be found in our prior report [113]. For profiles that do not have clearly separable peak boundaries, two Gaussian curves were fitted for agglomerated PdO and ion-exchanged Pd^{2+} domains. Profiles that required Gaussian deconvolution will be plotted with the experimental profile, Gaussian fits, and the sum of the Gaussian fits to demonstrate the efficacy of the fitting procedure. We note that the reduction features are not an exact Gaussian shape (see Figure 3.24; the 773 K air-treated sample was predominantly ion-exchanged Pd^{2+}, yet the profile was asymmetrical), but using Gaussian fits yield a better estimate of each component than using a strict temperature cutoff to separate each component. For the most difficult Gaussian deconvolutions (for the isothermal reduction kinetic measurements), the Gaussian peak center for the ion-exchanged Pd^{2+} was set to 383 K and allowed to vary +/- 5 K during the fitting process, and the agglomerated PdO Gaussian fits were allowed to vary over a wider range to obtain the best fit for the TPR profile. This methodology was chosen because hydrated, ion-exchanged Pd^{2+} always contained a single, distinct temperature of reduction near 383 K, whereas agglomerated PdO features occurred over a wider temperature range likely reflecting polydispersity in the particle size distribution, demonstrating the structures of the PdO agglomerates can change as a function of treatment time and influence the temperatures of reduction with H_2. Given the absence of PdO structural characterization before H_2 TPR characterization, changes in temperature of reduction for agglomerated PdO particles are not interpreted.

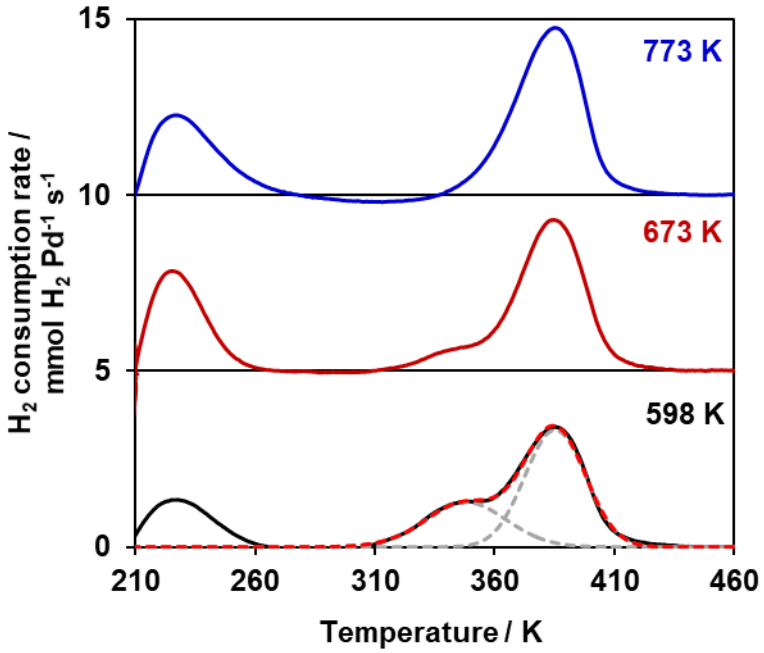

Figure 3.24. H_2 TPR profiles of the Pd-CHA-2 material after treatment in flowing (0.5 cm^3 s^{-1}) air to 598 K (black), 673 K (red, offset +5 units), and 773 K (blue, offset + 10 units) for 1 h. Quantifications are plotted in Figure 3.1, main text. Dashed gray lines for 598 K air treatment are for two Gaussian fits for agglomerated PdO particles (centered near 340 K) and ion-exchanged Pd^{2+} (centered near 390 K). Dashed red line is the sum of the two Gaussians.

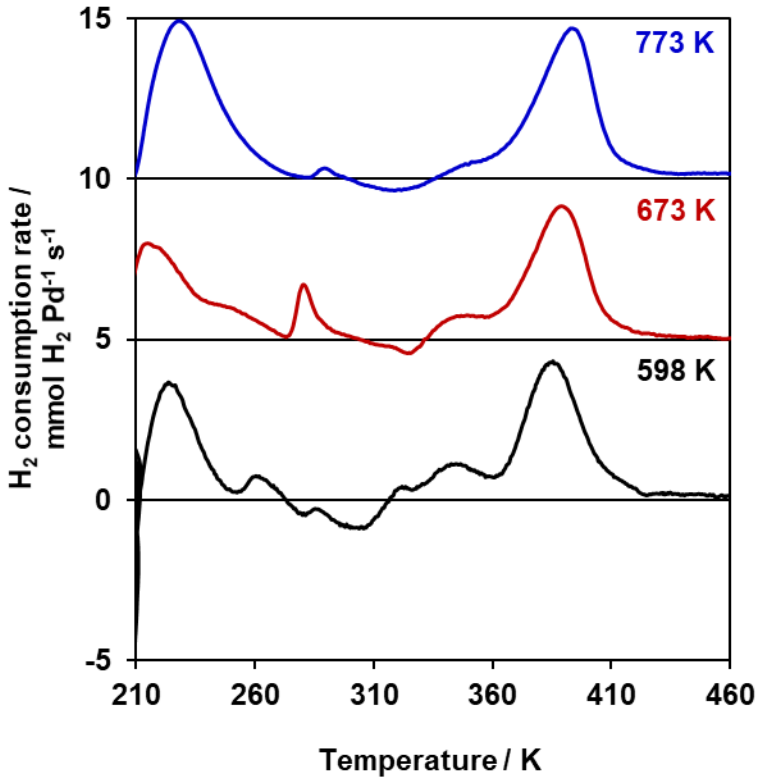

Figure 3.25. H_2 TPR profiles of the Pd-CHA-7 material after treatment in flowing (0.5 cm^3 s^{-1}) air to 598 K (black), 673 K (red, offset +5 units), and 773 K (blue, offset + 10 units) for 1 h. Quantifications are plotted in Figure 3.1.

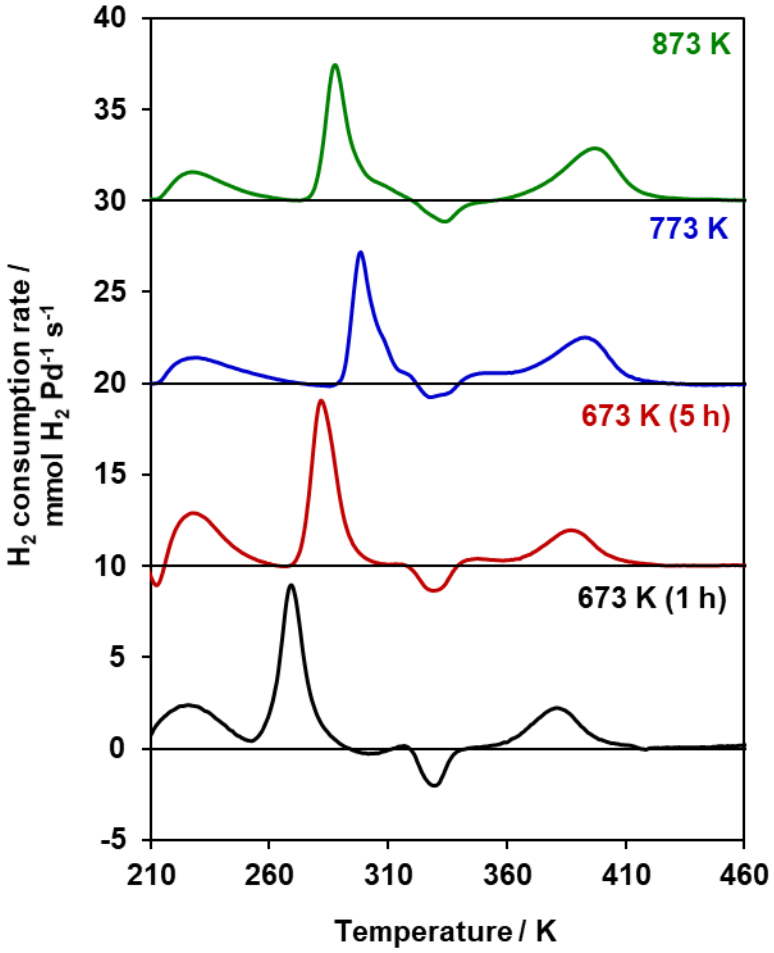

Figure 3.26. H_2 TPR profiles of the Pd-CHA-14 material after treatment in flowing (0.5 cm^3 s^{-1}) air to 673 K (black, 1 h), 673 K (red, offset +10 units, 5 h), 773 K (blue, offset + 20 units, 1 h), and 873 K (green, offset +30 units, 1 h). Quantifications are plotted in Figure 3.1.

Table 3.6. H_2 TPR quantifications of the Pd-CHA-14 material treated in air to 673 K for 5 h and 1 h.

Time	H_2 / Pd_{tot}	IE Pd^{2+} / Pd_{tot}	PdO / Pd_{tot}
1 h	0.41	0.25	0.66
5 h	0.43	0.23	0.66

The Pd-CHA-2 material was treated in flowing air (with and without H_2O) to high temperatures (598–773 K), similar to the Pd-CHA-7 material (Figure 3.4). Unlike the Pd-CHA-7 material, adding 6 kPa H_2O to the air stream did not significantly impact the amount of ion-exchanged Pd^{2+} at lower temperatures (598 673 K) for the Pd-CHA-2 material but did decrease the ion-exchanged Pd^{2+} content after treatment in air to 773 K. Increasing the H_2O pressure to 10 kPa at 673 K did result in a lower amount of ion-exchanged Pd^{2+} (outside of error) than the air-only treatment, again demonstrating higher H_2O partial pressures convert greater fractions of ion-exchanged Pd^{2+} to agglomerated PdO domains. For all conditions studied on the Pd-CHA-2 material, the H_2 consumption per Pd was approximately unity for all treatment conditions in Figure 3.27, demonstrating the majority of Pd was divalent as agglomerated PdO domains or ion-exchanged Pd^{2+}. This observation with the Pd-CHA-2 material contrasts the Pd-CHA-7 material, which showed sub-unity H_2 consumption per total Pd when 6 kPa H_2O was co-fed with air between 673–873 K, but was mostly divalent (>85%) after treatment in air-only.

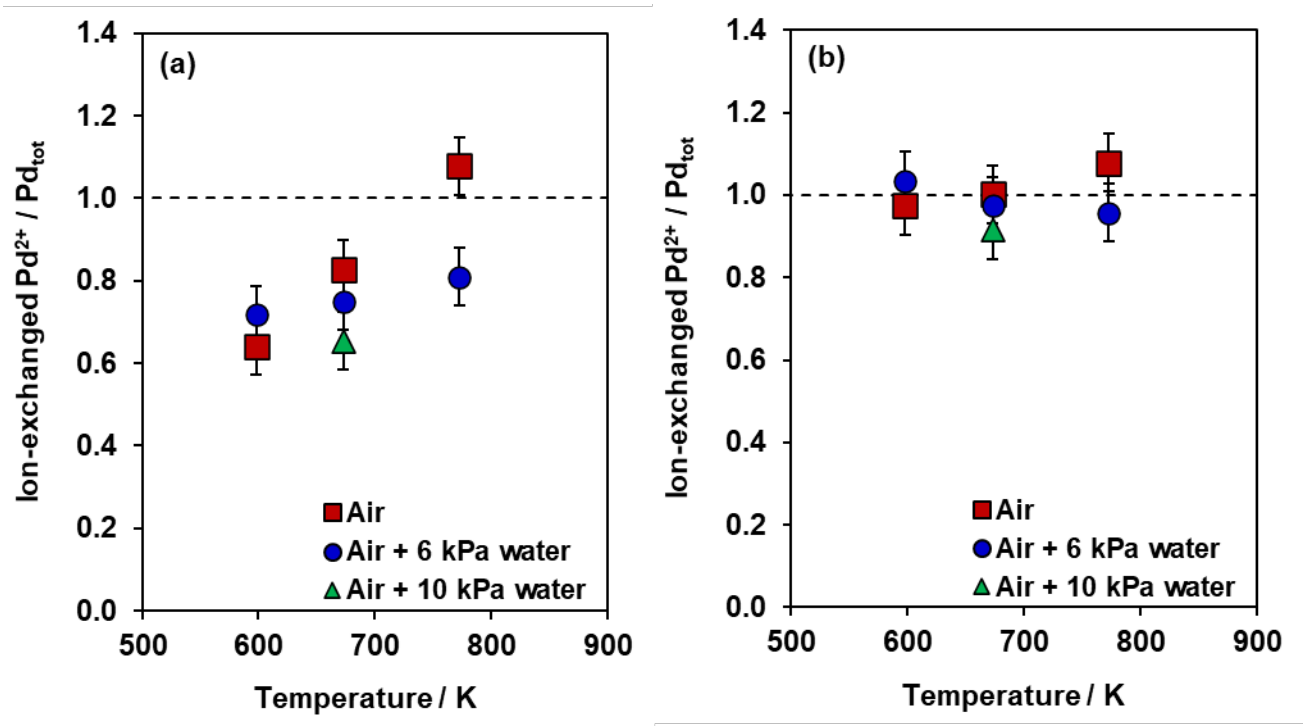

Figure 3.27. (a) The amount of ion-exchanged Pd^{2+} and (b) total H_2 consumed normalized per total Pd as a function of treatment temperature in flowing air (squares), 6 kPa water in balance air (circles), and 10 kPa water in balance air (tringle) for the Pd-CHA-2 material. Dashed line represents theoretical maximums. See above for discussion of data. H_2 TPR profiles are found in Figure 3.28.

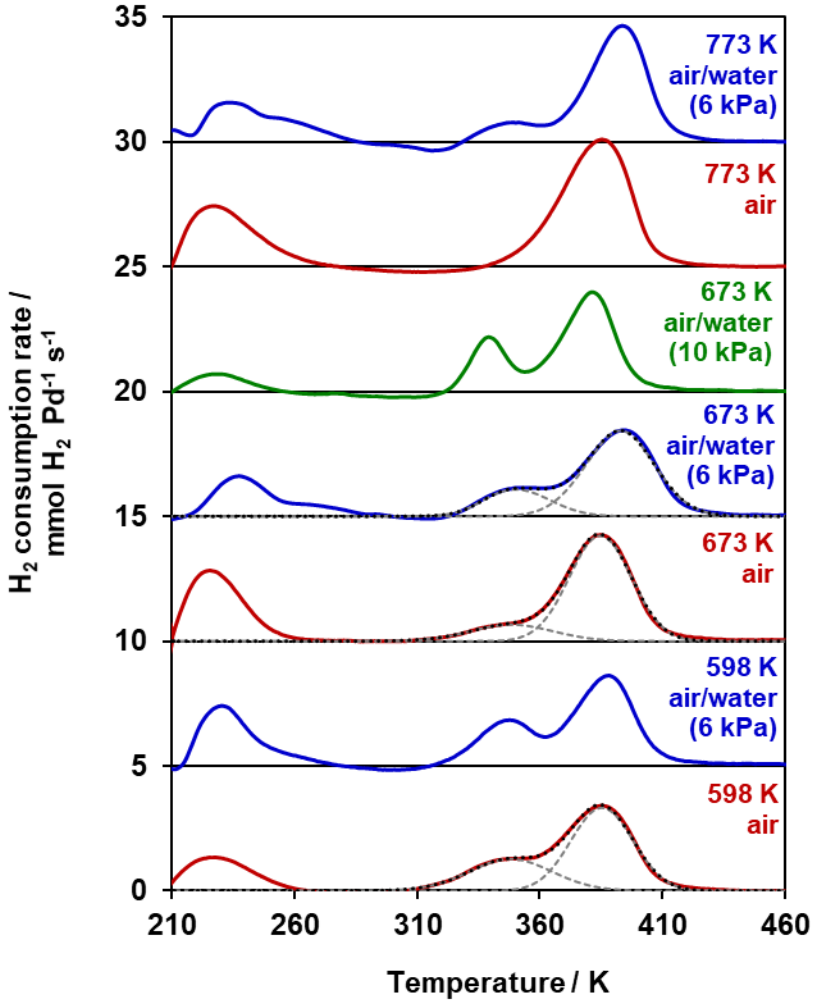

Figure 3.28. H_2 TPR profiles of the Pd-CHA-2 material after treatment in flowing air (with and without water) for 1 h. Profiles are offset by +5 unit increments and labeled for clarity. Quantifications are plotted in Figure 3.27. For profiles that required fitting, gray dashed lines are for Gaussian fits of agglomerated PdO domains and ion-exchanged Pd^{2+}, and the dotted black lines are for the sum of the respective Gaussian fits.

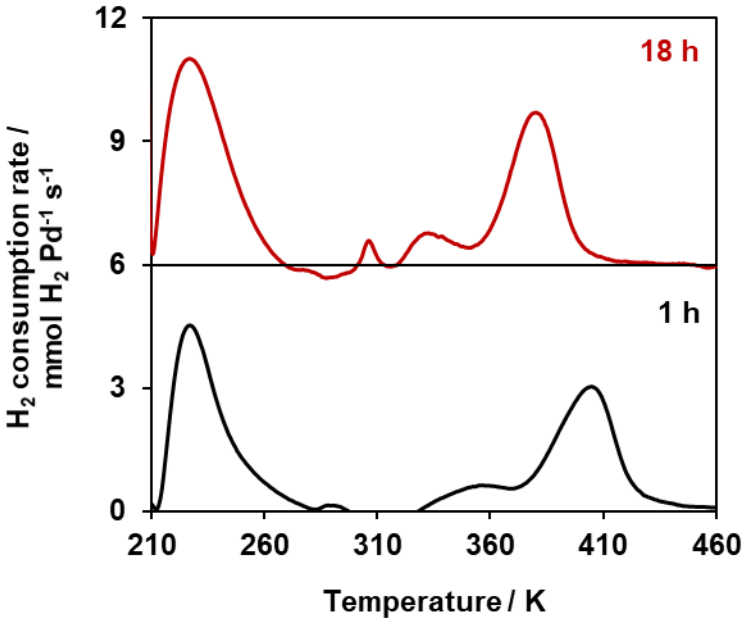

Figure 3.29. H_2 TPR profiles of the Pd-CHA-7 material after treatment in flowing air with 6 kPa water for 1 h (black) and 18 h (red, offset + 6 units) at 673 K.

Table 3.7. H_2 TPR quantifications of the Pd-CHA-7 material after treatment in flowing air with 6 kPa water for 1 and 18 h at 673 K

Time	H_2 / Pd_{tot}	IE Pd^{2+} / Pd_{tot}	PdO / Pd_{tot}
1 h	0.68	0.59	0.09
18 h	0.71	0.61	0.10

Table 3.8. Quantifications of H_2 TPR characterization of the Pd-CHA-7 material after various treatments. H_2 TPR profiles are in Figure 3.30.

Conditions	Temperature / K	Water Pressure / kPa	H_2 / Pd_{tot}	Pd^{2+}_{IE} / Pd_{tot}	PdO / Pd_{tot}
Air-only	598	–	0.52	0.43	0.09
	673	–	0.91	0.72	0.19
	773	–	0.87	0.86	0.02
	873	–	0.88	0.85	0.03
	973	–	0.85	0.80	0.05
Air with water	673	6.0	0.69	0.43	0.26
	773	6.0	0.66	0.61	0.05
	873	6.0	0.73	0.64	0.10
	973	6.0	0.87	0.86	0.02
Air (1 h) then air/water (1h)	673	6.0	0.68	0.59	0.09
Air (1 h) then air/water (4h)	673	6.0	0.64	0.62	0.02
Air (1 h) then air/water (18h)	673	6.0	0.71	0.61	0.10
Water/air (1 h) then air (1 h)	673	6.0	0.79	0.49	0.30

Table 3.9. H_2 TPR quantifications of the H_2 TPR profiles in Figure 3.31 of the 2.2 wt% Pd-CHA (Si/Al = 12) sample.

Conditions	H_2 / Pd_{tot}	IE Pd^{2+} / Pd_{tot}	PdO / Pd_{tot}
2 h, 473 K	0.88	0.07	0.81
5 h, 473 K	0.97	0.08	0.89
2 h in air at 473 K, then 1 h at 648 K in He	0.94	0.52	0.43

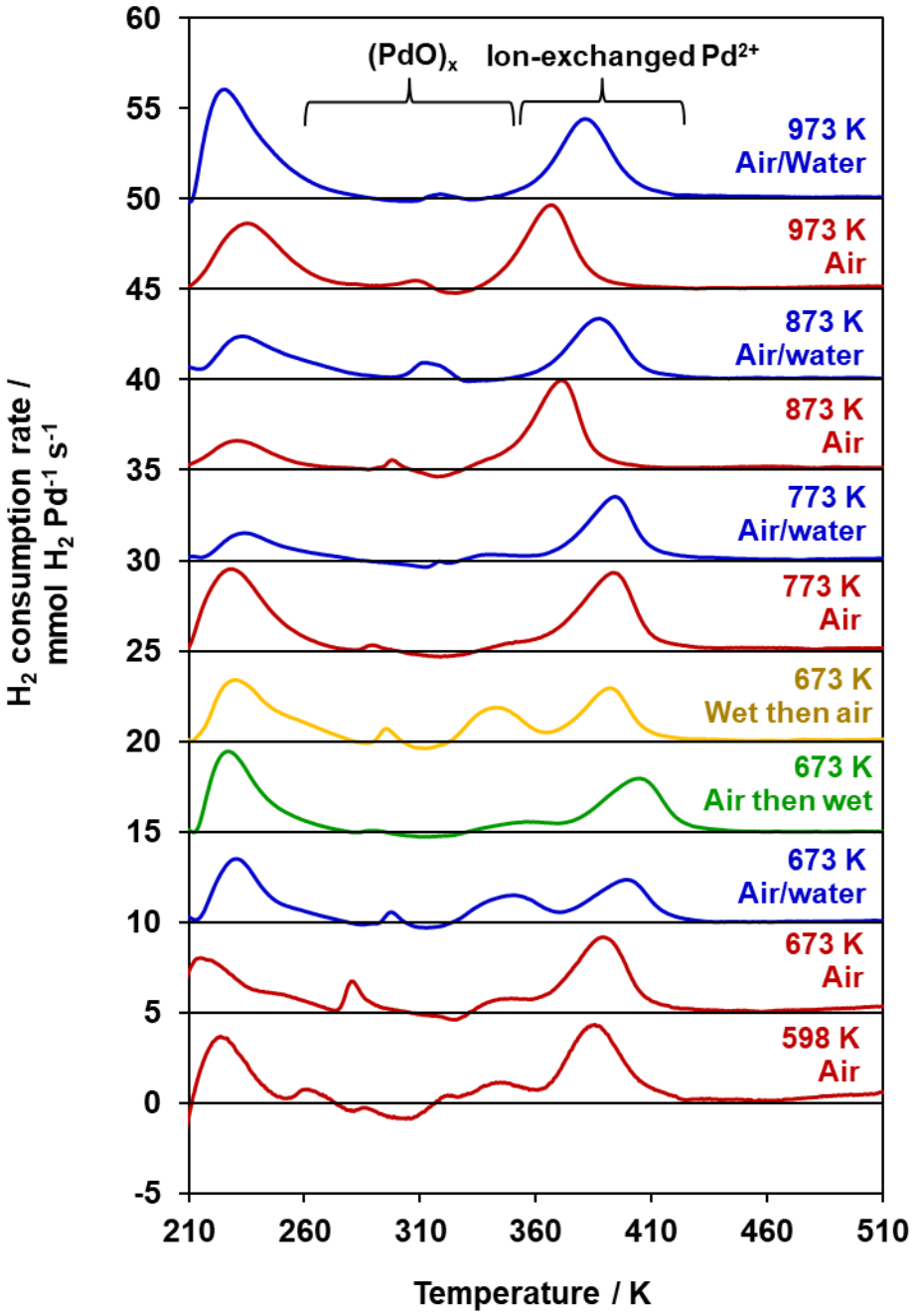

Figure 3.30. H_2 TPR profiles of the Pd-CHA-7 material (reported in Figure 3.4 of the main text) after various treatments, which are listed next to profile. Profiles are offset +5 units for clarity. H_2 TPR quantifications are listed in Table 3.8.

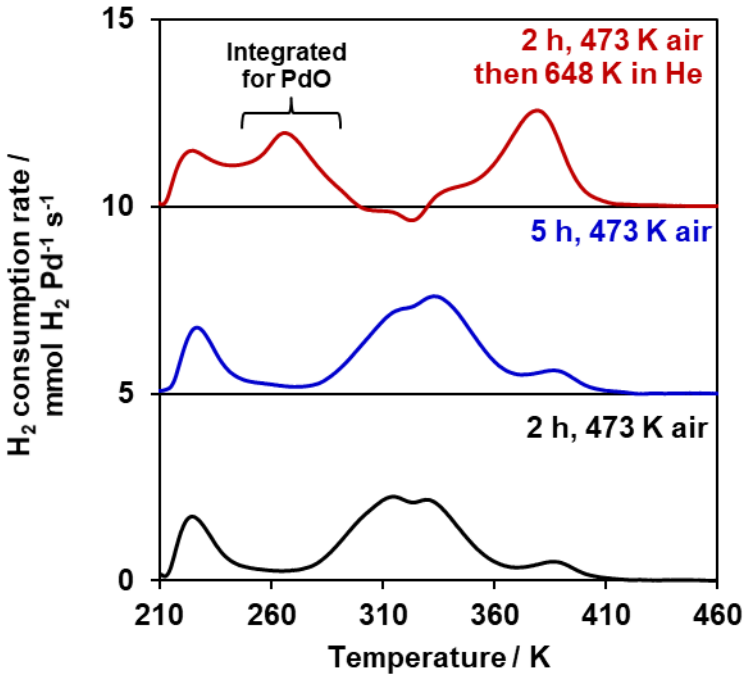

Figure 3.31. H_2 TPR profiles of a 2.2 wt% Pd-CHA (Si/Al = 12) material after treatment in flowing air to 473 K for 2 h (black), 473 K for 5 h (blue, offset +5 units), and 473 K in air for 2 h, then 648 K in flowing He for 1 h (red, offset + 10 units). Bracket region denotes an integrated region attributed to agglomerated PdO domains for the +10 units offset profile.

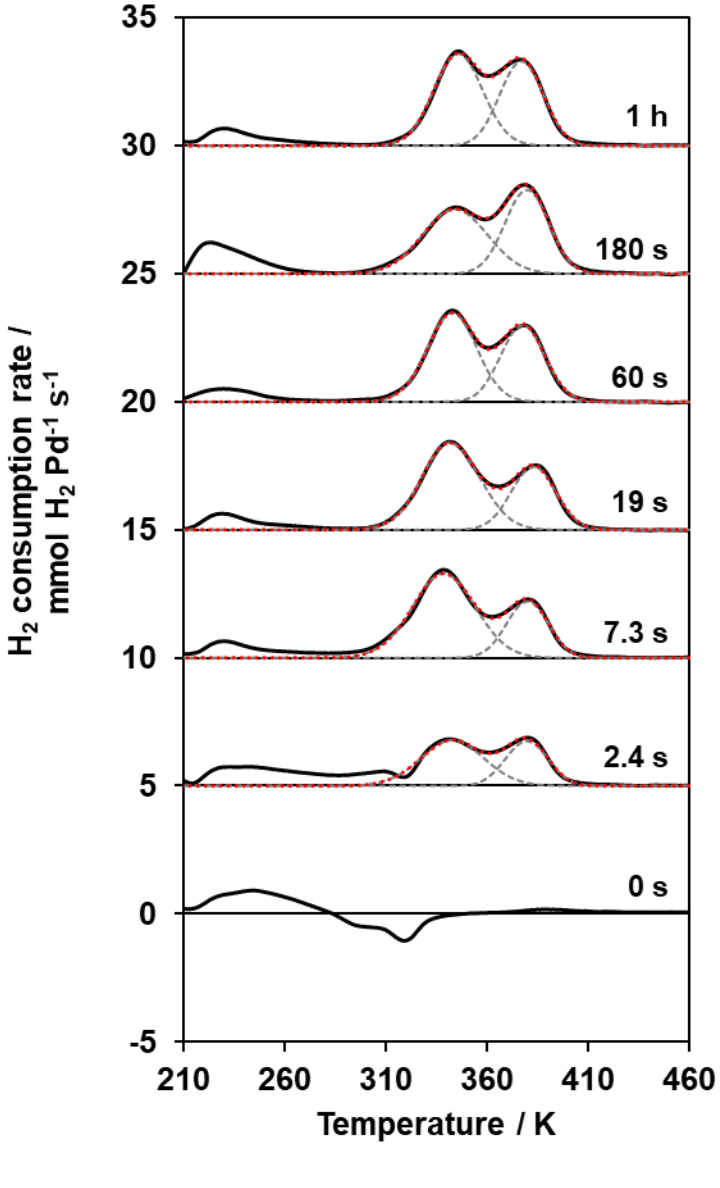

Figure 3.32. H_2 TPR characterization of the 2.2 wt% Pd-CHA material after isothermal redispersion experiments at 673 K. Air exposure times are listed by profiles (offset +5 units for clarity). Gaussian peak deconvolutions were performed to determine agglomerated PdO more and ion-exchanged contents more accurately. Dotted gray lines are for PdO (lower temperature) and ion-exchanged Pd^{2+} (highest temperature) Gaussian deconvolutions, dotted red lines are the sum of the Gaussian fits, and the black lines are for the experimentally measured H_2 consumption rate.

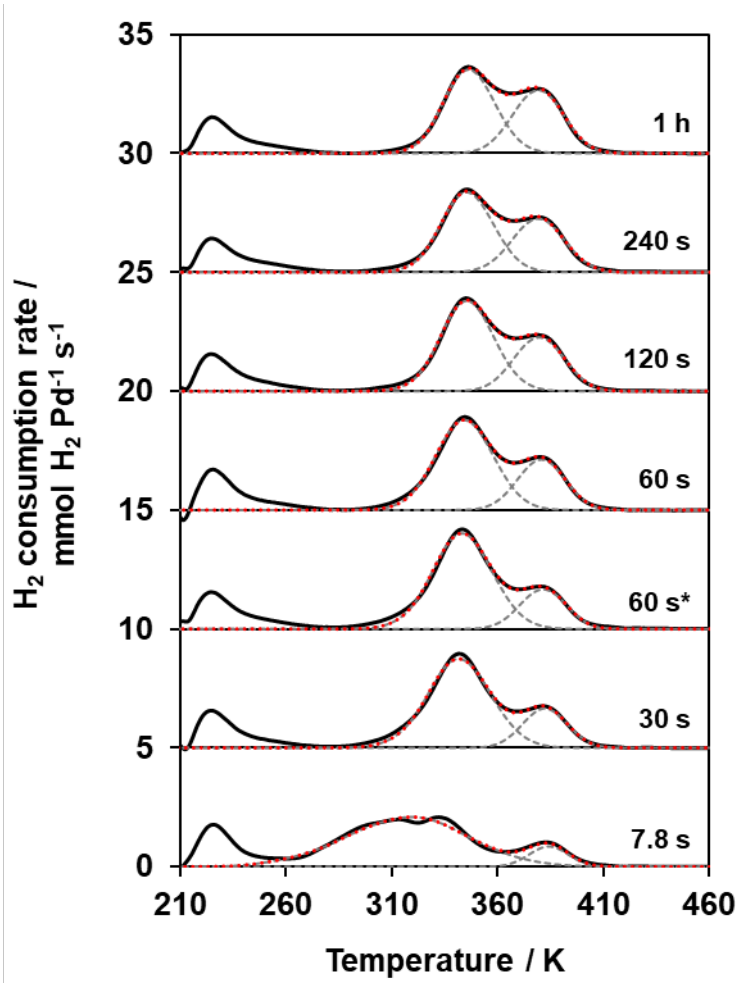

Figure 3.33. H_2 TPR characterization of the 2.2 wt% Pd-CHA material after isothermal redispersion experiments at 648 K. Air exposure times are listed by profiles (offset +5 units for clarity). Gaussian peak deconvolutions were performed to determine agglomerated PdO more and ion-exchanged contents more accurately. Dotted gray lines are for PdO (lower temperature) and ion-exchanged Pd^{2+} (highest temperature) Gaussian deconvolutions, dotted red lines are the sum of the Gaussian fits, and the black lines are for the experimentally measured H_2 consumption rate.

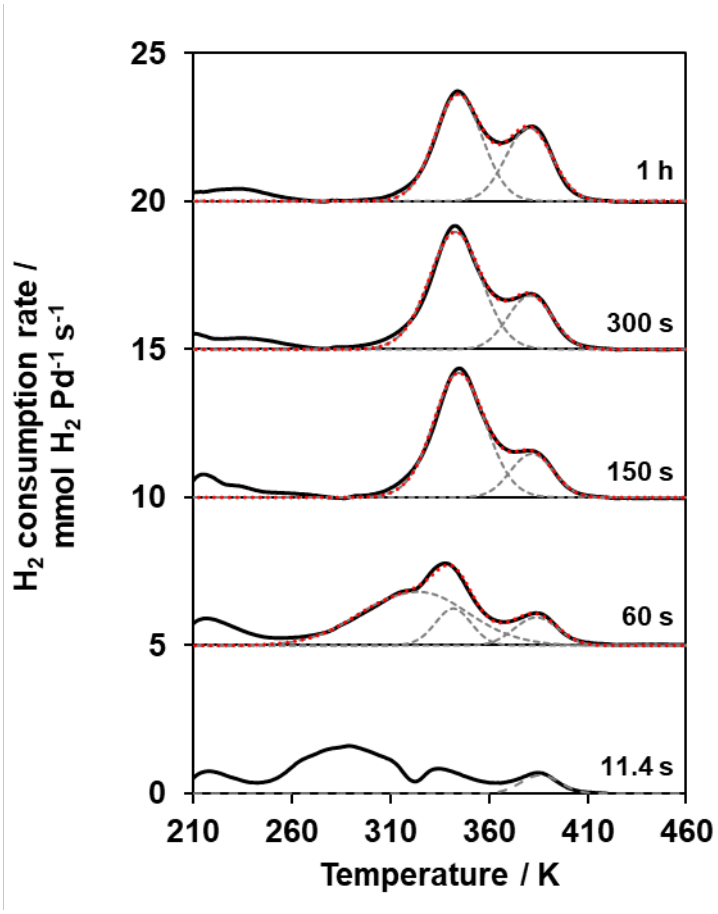

Figure 3.34. H_2 TPR characterization of the 2.2 wt% Pd-CHA material after isothermal redispersion experiments at 598 K. Air exposure times are listed by profiles (offset +5 units for clarity). Gaussian peak deconvolutions were performed to determine agglomerated PdO more and ion-exchanged contents more accurately. Dotted gray lines are for PdO (lower temperatures) and ion-exchanged Pd^{2+} (highest temperature) Gaussian deconvolutions, dotted red lines are the sum of the Gaussian fits, and the black lines are for the experimentally measured H_2 consumption rate. For the 11.4 s trial, the entire profile was integrated to determine H_2 consumed per Pd, and the ion-exchanged Pd^{2+} content was estimated with a Gaussian.

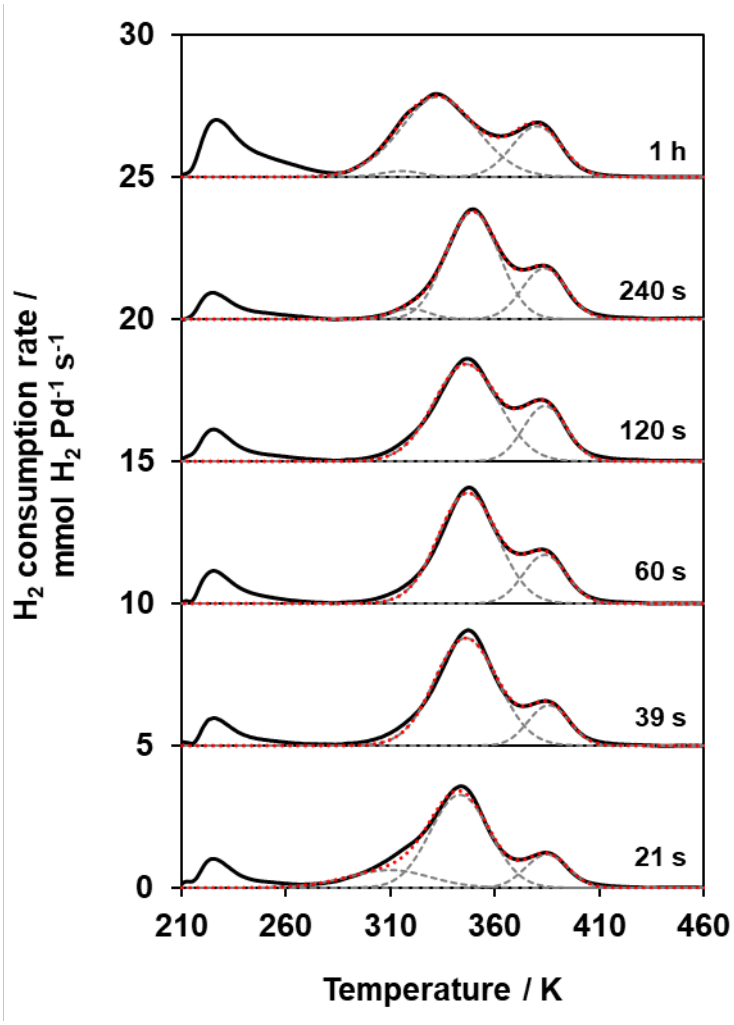

Figure 3.35. H_2 TPR characterization of the 2.2 wt% Pd-CHA material after isothermal redispersion experiments in wetted (2 kPa H_2O) air at 648 K. Wetted air exposure times are listed by profiles (offset +5 units for clarity). Gaussian peak deconvolutions were performed to determine agglomerated PdO more and ion-exchanged contents more accurately. Dotted gray lines are for PdO (lower temperatures) and ion-exchanged Pd^{2+} (highest temperature) Gaussian deconvolutions, dotted red lines are the sum of the Gaussian fits, and the black lines are for the experimentally measured H_2 consumption rate.

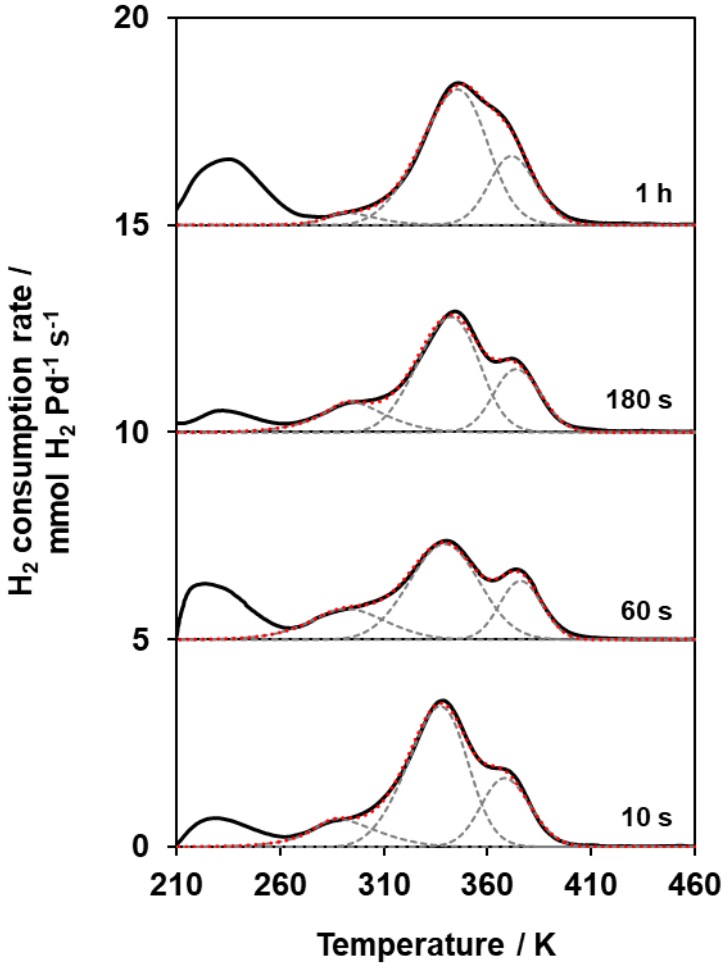

Figure 3.36. H_2 TPR characterization of the 2.2 wt% Pd-CHA (treated in air to 873 K for 1 h before each redispersion sequence, particle size distribution in Figure 3.21, O_2 chemisorption dispersion measurements in Figure 3.44) material after isothermal redispersion experiments in air at 648 K. Wetted air exposure times are listed by profiles (offset +5 units for clarity). Gaussian peak deconvolutions were performed to determine agglomerated PdO more and ion-exchanged contents more accurately. Dotted gray lines are for PdO (lower temperatures) and ion-exchanged Pd^{2+} (highest temperature) Gaussian deconvolutions, dotted red lines are the sum of the Gaussian fits, and the black lines are for the experimentally measured H_2 consumption rate.

3.7.5 Thermodynamic calculations

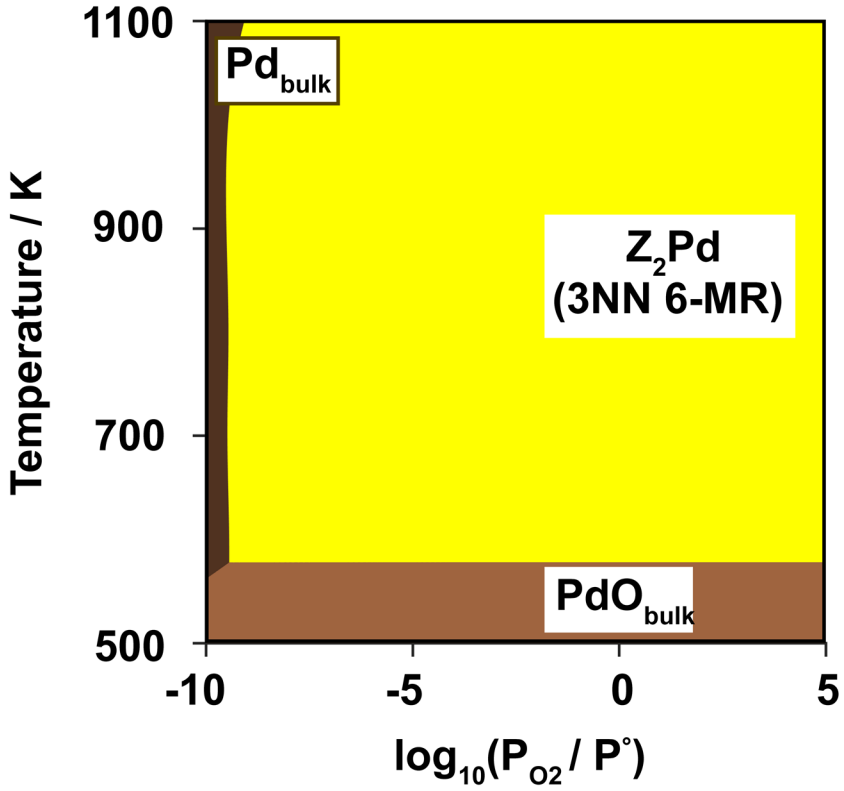

Figure 3.37. Thermodynamic bulk phase diagram based on HSE06-D3(BJ)vdw calculated energies at 0.014 kPa H_2O

Table 3.10. GGA-PBE and HSE06-calculated 0 K energies of formation (ΔE) of PdO_{bulk}, 3NN and 2NN Z_2Pd, ZPd and ZPdOH. The formation free energies of PdO_{bulk} (ΔG^{form}_{PdO}), 3NN ($\Delta G^{form}_{3NN\ Z_2Pd}$), and 2NN Z2Pd ($\Delta G^{form}_{2NN\ Z_2Pd}$), ZPd ($\Delta G^{form}_{ZPd}$) and ZPdOH ($\Delta G^{form}_{ZPdOH}$) at 598 K, 20 kPa O_2, 0.014 kPa H_2O have been calculated using HSE06-D3(BJ)vdw energies.

Reaction	ΔG (kJ mol^{-1})	ΔE^{form} (kJ mol^{-1}) GGA-PBE	HSE06
$Pd_{bulk} + 0.5O_2 \xrightarrow{\Delta G^{form}_{PdO}} PdO_{bulk}$	-46	-89	-111
$Pd_{bulk} + Z_2H_2 + 0.5O_2 \xrightarrow{\Delta G^{form}_{3NN\ Z2Pd}} Z_2Pd + H_2O$	-50	+29	+8
$PdO_{bulk} + Z_2H_2 \rightarrow 3NN\ Z_2Pd + H_2O$	-4	+118	+119
$Pd_{bulk} + Z_2H_2 + 0.5O_2 \xrightarrow{\Delta G^{form}_{2NN\ Z2Pd}} Z_2Pd + H_2O$	+12	+94	+73
$PdO_{bulk} + Z_2H_2 \rightarrow 2NN\ Z_2Pd + H_2O$	+58	+183	+184
$Pd_{bulk} + Z_2H_2 + 0.5(H_2O - 0.5O_2) \xrightarrow{\Delta G^{form}_{ZPd}} ZPd/ZH$	+45	+111	+36
$PdO_{bulk} + Z_2H_2 + 0.5(H_2O - 0.5O_2) \rightarrow ZPd/ZH + H_2O$	+91	+200	+147
$Pd_{bulk} + Z_2H_2 + 0.5O_2 \xrightarrow{\Delta G^{form}_{ZPdOH}} ZPdOH/ZH$	+29	+62	+35
$PdO_{bulk} + Z_2H_2 \rightarrow ZPdOH/ZH$	+75	+151	+146

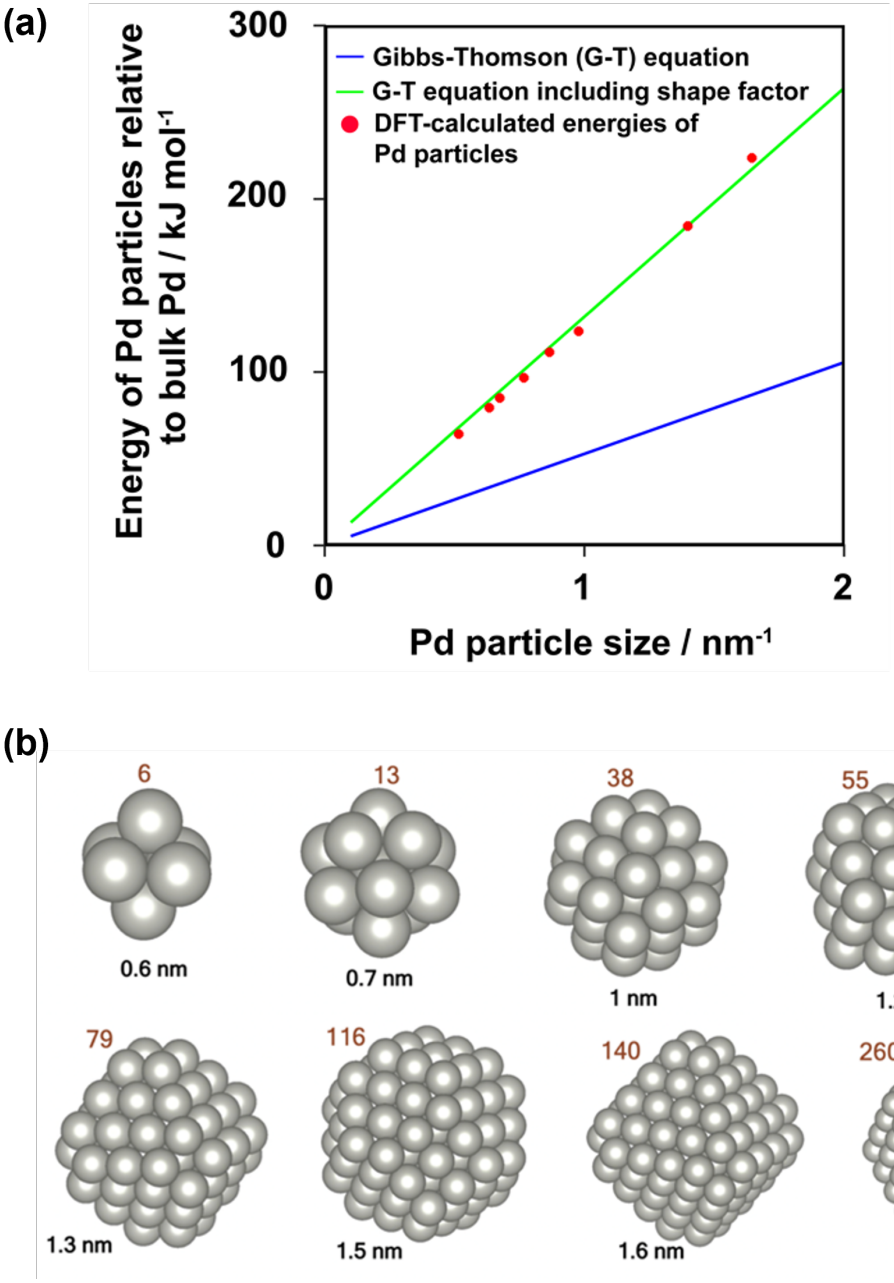

Figure 3.38. (a) Comparison of particle size-dependent thermodynamic models with DFT-computed energies of Pd nanoparticles. (b) Optimized structures of the Pd nanoparticles considered

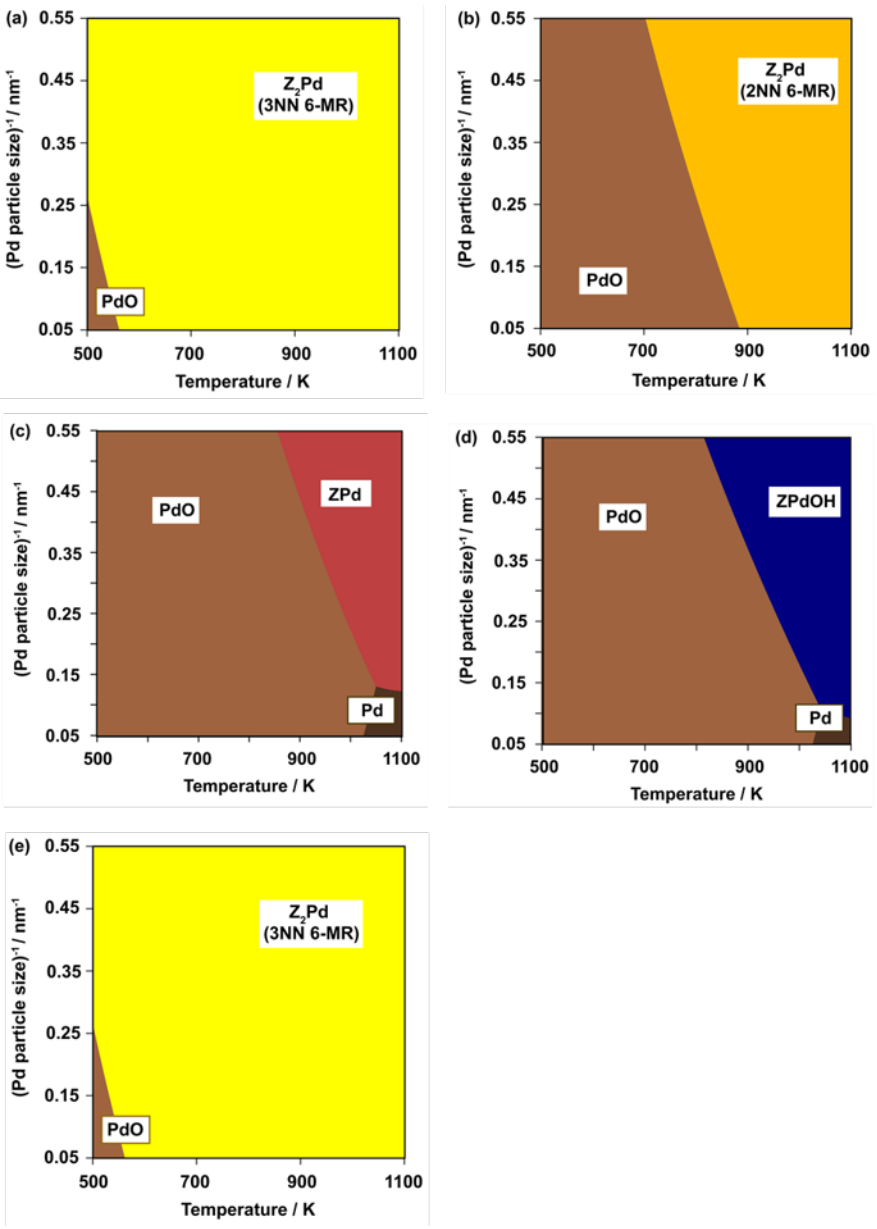

Figure 3.39. Particle size dependent thermodynamic phase diagram based on HSE06-D3(BJ)vdw calculated energies for conversion of Pd particle sizes ranging from 1.8 to 100 nm to exchanged cations at 2Al sites as (a) Pd^{2+} at 2NN 6-MR (3NN 6-MR Z_2Pd), and (b) 2NN 6-MR Z_2Pd, and at 1Al sites as (c) Pd^{+} (ZPd), and (d) $[PdOH]^{+}$ (ZPdOH). (e) Combined phase diagram of all the Pd-exchanged species at 1Al and 2Al sites shown in (a)-(d). Air treatment conditions of 0.014 kPa H_2O and 20 kPa O_2 are used.

Table 3.11. Formation free energies (ΔG^{form}) of ion-exchanged Pd^{2+} at 3NN and 2NN 2Al sites, and Pd^{+} and $[PdOH]^{+}$ exchanged at 1Al sites for 2, 7, and 14 nm Pd particles at air treatment temperature of 598 K with 20 kPa O_2, 0.014 kPa H_2O

Pd particle size / nm	Z_2Pd (3NN 6-MR)	Z_2Pd (2NN 6-MR)	ZPd	ZPdOH
2	-116	-51	-21	-37
7	-69	-4	+26	+11
14	-60	+5	+36	+20

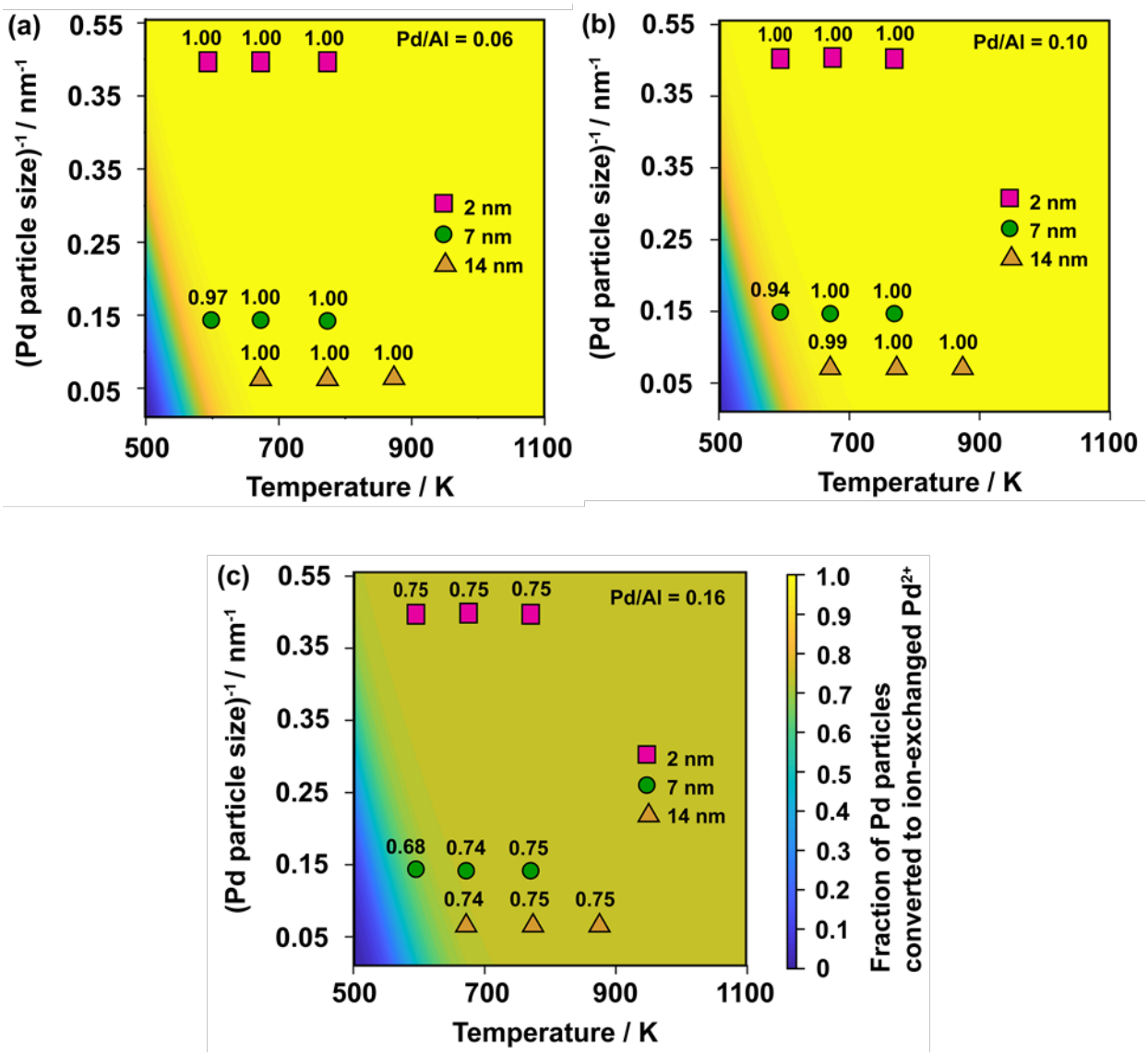

Figure 3.40. Size-dependent thermodynamic phase diagram for Pd/Al ratios of (a) 0.06, (b) 0.10, and (c) 0.16 based on HSE06-D3(BJ)vdw calculated energies at 20 kPa O_2, 0.014 kPa H_2O.

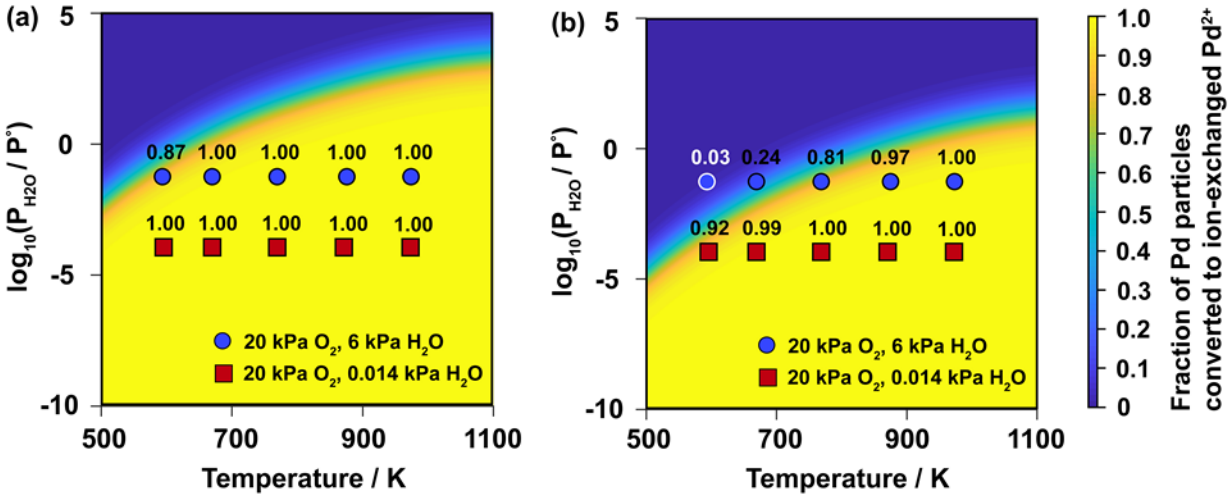

Figure 3.41. Thermodynamic phase diagram for the conversion of (a) d_{Pd} = 2 nm, and (b) d_{Pd} = 14 nm to ion-exchanged Pd^{2+} cations on CHA (Si/Al =12, Pd/Al = 0.06) as a function of temperature and P_{H_2O}. The fraction of Pd particles converted to ion-exchanged Pd^{2+} cations at 20 kPa O_2, 0.014 kPa H_2O (squares), and 20 kPa O_2, 6 kPa H_2O (circles) at treatment temperatures of 598–1023 K are labeled.

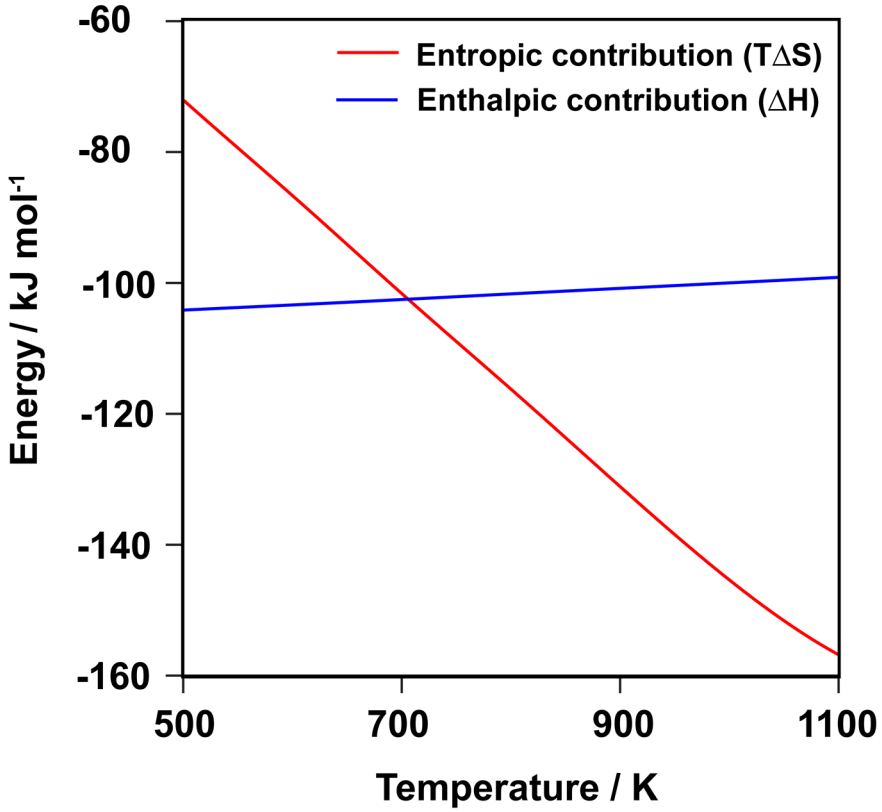

Figure 3.42. Comparison of enthalpy and entropy contributions to the conversion of $d_{Pd} = 7$ nm to Z_2Pd based on HSE06-D3(BJ)vdw calculated energies at 20 kPa O_2, 6 kPa H_2O

3.7.6 Isothermal Pd structural interconversion rates

Isothermal Pd redispersion measurements were collected at different space velocities to determine if external mass transfer Figure 3.43 is the same plot as Figure 3.6 in the main text, but two different space velocities were added for the air-only and wetted air. The flow rate was decreased from 0.5 to 0.25 cm^3 s^{-1} for the air-only 60 s time point and increase from 0.5 to 1.0 cm^3 s^{-1} for the wetted 39 s time point. Both experiments resulted in changes of ion-exchanged Pd^{2+}, demonstrating these measurements are do not solely reflect intrinsic kinetics and cannot be modeled as well-mixed, batch reactors in excess O_2. Therefore, we forego kinetic fitting of the data and only make qualitative conclusions.

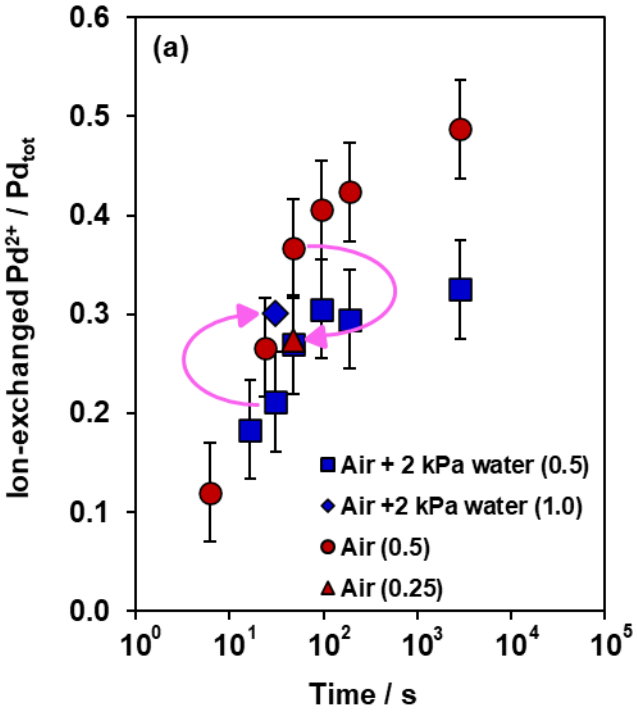

Figure 3.43. The amount of ion-exchanged Pd^{2+} normalized per total Pd as a function of time during isothermal switching experiments (648 K) in air (circles, triangle) or 2 kPa water in balance air (squares, diamond). The flowrates (in cm^3 s^{-1}) for each measurement are given in parentheses in the legend.

3.7.7 O_2 chemisorption

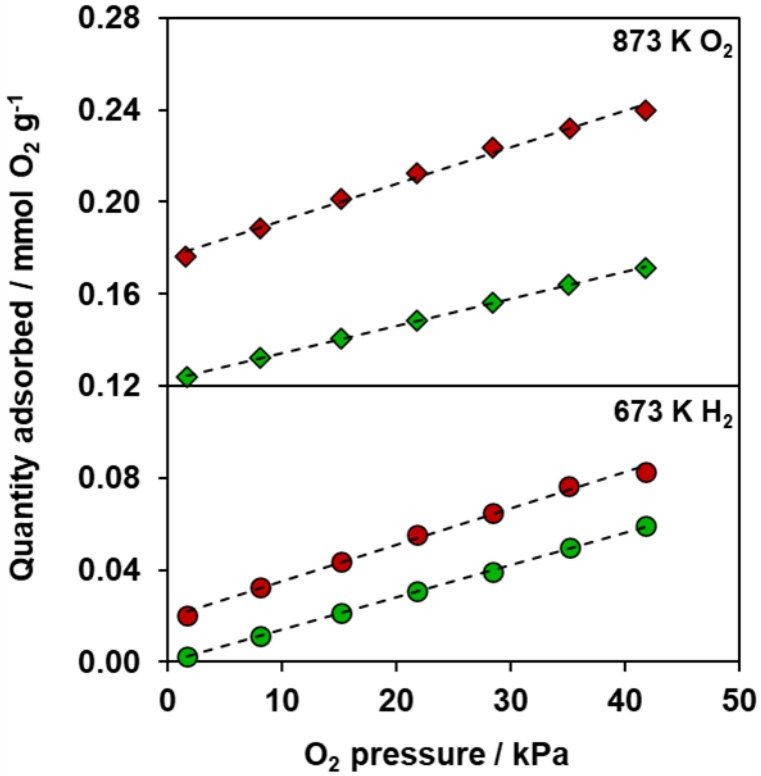

Figure 3.44. O_2 chemisorption (313 K) experiment of a 2.2 wt% Pd-CHA material. The as-exchanged material was treated in flowing H_2 (103 kPa) to 673 K for 1 h before performing O_2 chemisorption characterization (no offset, circles). Following, the sample was treated in flowing O_2 (103 kPa) to 873 K for 1 h, cooled to ambient temperatures, treated in flowing H_2 to 573 K, then prepared for O_2 chemisorption (triangles, offset +0.12 mmol O_2 g^{-1}). Quantifications are reported in Table 3.12.

Table 3.12. O_2 chemisorption qualifications from Figure 3.44

Treatment	mmol O_2 chemisorbed g^{-1}	Dispersion (O/Pd_{tot})
673 K, 103 kPa H_2	0.019	0.19
873 K, 103 kPa O_2, then 573 K, 103 kPa H_2	0.053	0.52

4. MICROPOROUS MATERIALS FOR THE STORAGE AND CONVERSION OF FORMALDEHYDE IN AUTOMOTIVE EXHAUST AFTERTREATMENT

4.1 Abstract

A series of Beta zeolites of varied material properties (e.g., silanol density, framework heteroatom identity and density, and extraframework metal species) was tested for formaldehyde storage and release under simulated exhaust conditions (100–1000 ppm formaldehyde, 1–2 kPa H_2O, balance air) to determine key material variables for automotive abatement applications. Two purely siliceous Beta zeolite materials stored formaldehyde (191–230 μmol g^{-1}), and the major products released during a temperature ramp (0.167 K s^{-1}) in air were formaldehyde, carbon monoxide, and carbon dioxide. The siliceous supports showed high selectivity among desorption products to carbon monoxide and carbon dioxide (0.90–0.95). The addition of framework Al heteroatoms (Si/Al = 12.5) did not significantly increase the total formaldehyde storage (242 μmol g^{-1}), but decreased the onset temperature of formaldehyde desorption from 420 K to 375 K, and lowered the selectivity to carbon monoxide and carbon dioxide from 0.90 to 0.75, relative to the purely siliceous supports. One framework Sn-substituted Beta zeolite material (Si/Sn = 41) contained the highest per-mass formaldehyde storage (301 μmol g^{-1}) of all materials tested here and a high selectivity (0.99) to carbon monoxide and carbon dioxide among desorption products. Lowering the Sn atom density (Si/Sn = 109) decreased the total formaldehyde storage to 140 μmol g^{-1} but did not change the selectivity of 0.99 to carbon monoxide and carbon dioxide. Lastly, extraframework SnO_x supported on siliceous Beta resulted in a formaldehyde storage of 246 μmol g^{-1} and a selectivity to carbon monoixide and carbond dioxide of 1.00, demonstrating extraframework SnO_x species may be a beneficial material property for the mitigation of formaldehyde pollution in automotive exhaust.

4.2 Introduction

A significant fraction of automotive engine exhaust pollution occurs during engine start-up when downstream abatement technologies are below their operating temperature window to efficiently convert pollutants. This highly transient process (i.e., temperature fluctuations between ambient and 1000 K) may be leveraged to design materials that passively adsorb pollutants and subsequently desorb them at higher temperatures compatible with catalytic abatement technologies, as demonstrated for NO_x storage with Pd-zeolites [1], [3] The United States Environmental Protection Agency also regulates aldehyde emissions, but unlike the Pd-zeolite technology, a scientific breakthrough has not been discovered, motivating an exploratory study to identify key material properties for aldehyde abatement, focusing on formaldehyde as a representative aldehyde.

Microporous, crystalline materials of the Beta topology have been proposed as effective hydrocarbon traps [159] and, therefore, may be a promising candidate for aldehyde storage. The large-pore Beta framework contains 12 membered-rings (MR), resulting in a lower diffusion barrier of longer-chained hydrocarbons compared to medium-pore (10-MR, such as MFI) and small-pore (8-MR, such as CHA) zeolite materials. However, the Beta topology is more prone to structural collapse under realistic conditions of automotive exhaust applications (i.e., hydrothermal aging) and may limit its practical implementation [160]. Additionally, incorporation of Sn and Zr Lewis acid heteroatoms in microporous materials have been proposed to bind aldehyde and ketone functional groups in the presence of water [12], [13], suggesting the Lewis acid-substituted Beta materials are promising materials for passive aldehyde adsorption for automotive applications.

Here, we investigate the influence of various microporous material properties on the storage and conversion of formaldehyde under simple exhaust conditions. A suite of Beta materials was synthesized with varied silanol defect densities, framework heteroatom identities (e.g., Al, Sn), and extraframework metals, then tested with a standardized formaldehyde storage and desorption protocol. The evolved species were quantified with gas-phase FTIR and related to changes in material properties. These efforts identify relevant material characteristics for the efficacy of aldehyde traps for vehicular abatement systems.

4.3 Methods

4.3.1 Materials synthesis and characterization

One Al-Beta zeolite (Si/Al = 12.5, CP814E) was sourced from Zeolyst International. To prepare the dealuminated Si-Beta material, one gram of the commercially supplied Al-Beta was mixed with 25 mL of concentrated nitric acid (69 wt%, Avantor) in a covered perfluoroalkoxy alkane (PFA) container (Savillex Corp.) for 24 h under ambient conditions. The solids were recovered with centrifugation and washed with deionized water until the pH of the supernatant was constant. The recovered solids were dried in a static oven controlled to 373 K overnight. The Sn-Beta materials were synthesized following previously reported post-synthetic grafting [161] and hydrothermal synthesis procedures [162]. The purely siliceous, fluoride-mediated Beta material was prepared following previously reported methods [113]. The SnO_x-Si-Beta material was prepared via incipient wetness impregnation using tin(IV) chloride pentahydrate dissolved in deionized water. The tin-containing solution was deposited dropwise on a purely siliceous Beta material until the total pore volume was saturated. The as-deposited material was stored under ambient conditions overnight before treatment in a muffle furnace under flowing air to 773 K (60 K h^{-1}) for 2 h.

Elemental compositions were estimated with atomic absorption spectroscopy (AAS) using a PerkinElmer model AAnalyst 300. Solid samples (0.02–0.05 g) were first digested with 2.5 g of hydrofluoric acid (48 wt%, Alfa Aesar) for at least 2 days then diluted with 50 g of deionized water. Sn and Al contents of samples were determined from calibration curves generated with standards of known concentration.

4.3.2 Formaldehyde adsorption and desorption tests

0.2 g of paraformaldehyde (95%, Sigma Aldrich) were mixed with 0.5 g of silica gel particles (1.2–3.3 mm diameter) and supported between two quartz wool plugs in a 0.325-inch diameter Pyrex tube. A flowing (0.833 cm^3 s^{-1}) stream of wetted (1–2 kPa) air (Air Zero, Indiana Oxygen) was passed through the paraformaldehyde bed under ambient conditions to generate a gas-phase formaldehyde concentration of 100–1000 ppm. After a stable bypass

formaldehyde concentration was achieved, the formaldehyde-containing stream was switched over the adsorbent bed (c.a. 0.05 g), which was pelleted and sieved to retain 180–250 μm diameter particles and supported between two plugs of quartz wool in a 0.325-inch diameter Pyrex tube held at 348 K. After the formaldehyde concentration stabilized to the bypass concentration, the paraformaldehyde bed and water bubbler were bypassed. The temperature programmed desorption (TPD, 0.167 K s^{-1}) was performed once the formaldehyde concentration reached undetectable values, and the desorbed gas phase products were quantified with an in-line MKS Multigas 2030 FTIR analyzer.

4.4 Results and Discussion

4.4.1 Formaldehyde storage over purely siliceous supports

Two purely siliceous Beta zeolites were synthesized to understand the influence of a metal-free support on the storage and release of formaldehyde in an exhaust stream, specifically focusing on silanol density as the material property of interest. First, a fluoride-mediated Si-Beta (denoted as Si-Beta-F) was synthesized and tested for formaldehyde storage and release, where fluoride-mediated Beta syntheses are reported to contain lower amounts of silanol groups compared to hydroxide-mediated syntheses because the fluoride anions charge-compensate the cationic, organic structure directing agent (SDA) instead of anionic framework siloxy (Si-O^-) groups that convert to silanol groups upon removal of the SDA [163]–[167]. Here, neither semiquantitative water adsorption isotherms [168] nor quantitative deuterated acetonitrile adsorption IR (303 K) [162] experiments were used to estimate the number of silanol groups, and it was assumed the reproduced fluoride-mediated synthesis yielded a low silanol defect material [169].

Figure 4.1 shows the TPD profile of the Si-Beta-F material after adsorption of formaldehyde, and Table 1 shows the material characterizations and TPD quantifications for all materials tested in this study. The TPD profile of the Si-Beta-F material contained three main desorbed species: carbon monoxide, carbon dioxide, and formaldehyde. In the absence of metals, the purely siliceous support stored gas-phase formaldehyde and, upon treatment to 573 K in flowing air, converted the majority (>95%) of stored formaldehyde to carbon

monoxide and carbon dioxide, with carbon dioxide comprising the major desorption product. This result demonstrates that a purely siliceous support can both store and convert formaldehyde to more environmentally benign products such as carbon monoxide and carbon dioxide.

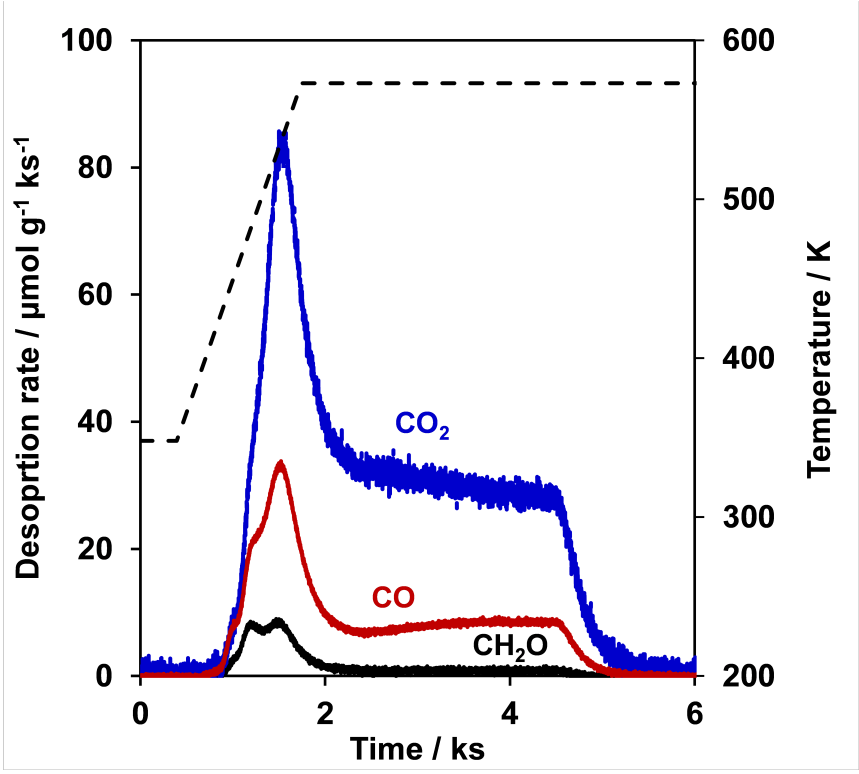

Figure 4.1. TPD profile of the Si-Beta-F material under flowing air after adsorption of formaldehyde. Black profile is for formaldehyde, red profile is for carbon monoxide, blue profile is for carbon dioxide, and dashed black line is for temperature (on the secondary y-axis)

Table 4.1. A summary of the materials compositions and TPD quantifications. 'M' denotes the framework heteroatom or extraframework metal species (i.e., Al, Sn). Selectivity of desorbed products is defined as the molar sum carbon monoxide and dioxide divided by the total storage.

Sample	Si / M	μmol M / g	Total mol stored / M	μmol CH_2O / g	μmol CO / g	μmol CO_2 / g	Total μmol stored / g	Selectivity
Si-Beta-F	–	–	–	8	43	140	191	0.96
Dealuminated Si-Beta	–	–	–	21	69	140	230	0.91
Al-Beta	12.5	1240	0.2	60	71	111	242	0.75
Sn-Beta-41	41	390	0.8	4	102	195	301	0.99
Sn-Beta-109	109	151	0.9	2	87	51	140	0.99
SnOx-Si-Beta	209	68	3.6	1	25	220	246	1.00

For the purely siliceous Si-Beta-F material, it was hypothesized that the silanol defects could be the sites responsible for formaldehyde storage. Therefore, a commercially supplied Al-Beta (Si/Al = 12.5, CP814E, Zeolyst) was dealuminated in concentrated nitric acid to remove the majority of the Al heteroatoms (denoted as dealuminated Si-Beta), increasing the number of silanol defects. Again, the amount of silanol groups were not quantified, but were assumed to be a greater density in the dealuminated Si-Beta than the Si-Beta-F material. The dealuminated Si-Beta material was then tested for formaldehyde storage and release in Figure 4.2. From the TPD profile, carbon dioxide was again the major desorbed product. The selectivity of desorbed products to carbon monoxide and carbon dioxide was 0.90, which was similar to the 0.95 selectivity of the Si-Beta-F material. The dealuminated Si-Beta material showed a total formaldehyde storage 230 μmol per gram compared to 191 μmol per gram for the Si-Beta-F material, suggesting the increase in silanol density could increase total formaldehyde storage; however, this interpretation on influence of silanol density is contingent on future work quantify the silanol densities present on these materials.

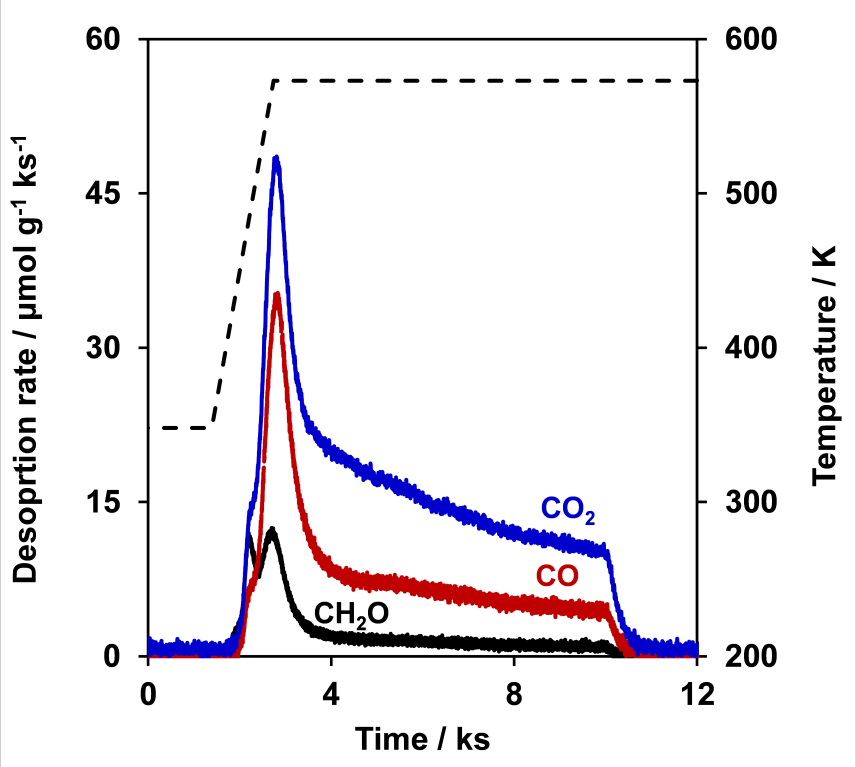

Figure 4.2. TPD profile of the dealuminated Si-Beta material under flowing air after adsorption of formaldehyde. Black profile is for formaldehyde, red profile is for carbon monoxide, blue profile is for carbon dioxide, and dashed black line is for temperature (on the secondary y-axis).

4.4.2 Influence of heteroatom identity and extraframework metals on formaldehyde storage and conversion

Isomorphous substitution of framework Si atoms with different heteroatoms (e.g., Al, Sn) can introduce different binding and active site functions, such as Brønsted acid sites or Lewis acid sites, within microporous environments. Here, a commercially supplied, Al-substituted Beta material (denoted Al-Beta, Si/Al = 12.5, CP814E) was tested for formaldehyde storage to determine if Brønsted acid sites can store or convert formaldehyde (Figure 4.3). The onset temperature (c.a. 375 K) of formaldehyde desorption occurred before carbon monoxide and carbon dioxide (c.a. 420 K), which contrasts the purely siliceous supports (Figures 4.1 and 4.2) that showed similar onset temperatures (c.a. 420 K) of desorption for all three major species. Additionally, the selectivity of desorbed products to carbon monoxide and carbon dioxide was 0.75, compared to >0.9 for the purely siliceous supports. The difference in onset temperature of desorption of formaldehyde and selectivity between the Al-Beta and the siliceous Beta materials could be a consequence of the adsorbate structure of formaldehyde at Brønsted acid sites compared to that at silanol groups. The total formaldehyde storage of the Al-Beta (242 μmol g^{-1}) was below the total number of framework Al sites (0.2 total mol stored / Al), which suggests only a subset of framework Al store formaldehyde. Together, this data suggests incorporation of Brønsted acid sites in microporous materials decreases the temperature of desorption of formaldehyde and decreases the selectivity to more environmentally benign products compared to purely siliceous supports.

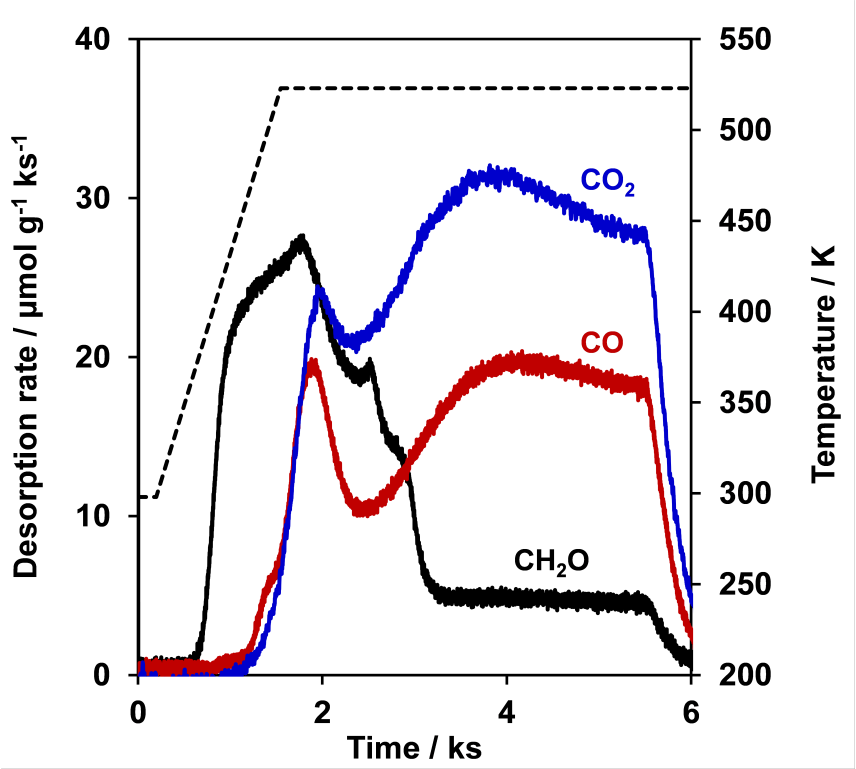

Figure 4.3. TPD profile of the Al-Beta material under flowing air after adsorption of formaldehyde. Black profile is for formaldehyde, red profile is for carbon monoxide, blue profile is for carbon dioxide, and dashed black line is for temperature (on the secondary y-axis).

Previous reports showed the incorporation of framework Sn and Zr (i.e., Lewis acids) heteroatoms in microporous materials can bind aldehyde and ketone functional groups in the presence of water,[5,6] suggesting framework Sn-substituted Beta materials may be effective formaldehyde traps. Therefore, two Sn-Beta materials were synthesized with different bulk Sn densities, where the highest Sn density sample (Si/Sn = 41) will be denoted as Sn-Beta-41 and the lower Sn density sample (Si/Sn = 109) will be denoted as Sn-Beta-109. The two materials were tested for formaldehyde storage, and the TPD profiles are plotted in Figures 4.4 and 4.5. The Sn-Beta-41 material showed the greatest total storage of all materials tested in this study with 301 μmol g^{-1}, and the Sn-Beta-109 material showed a total storage of 140 μmol g^{-1}. Both Sn-Beta materials showed high selectivity (0.99) to carbon monoxide and carbon dioxide, suggesting Sn-incorporated Beta materials are more effective at converting stored formaldehyde to more environmentally benign compounds compared to the purely siliceous Beta (selectivity = 0.91 0.95) and Al-substituted Beta (selectivity = 0.75) materials. These Sn-Beta materials were not characterized to determine the fraction of Sn that are present in framework versus extraframework locations, which suggests extraframework SnO_x could also influence the adsorption and chemistries for formaldehyde storage.

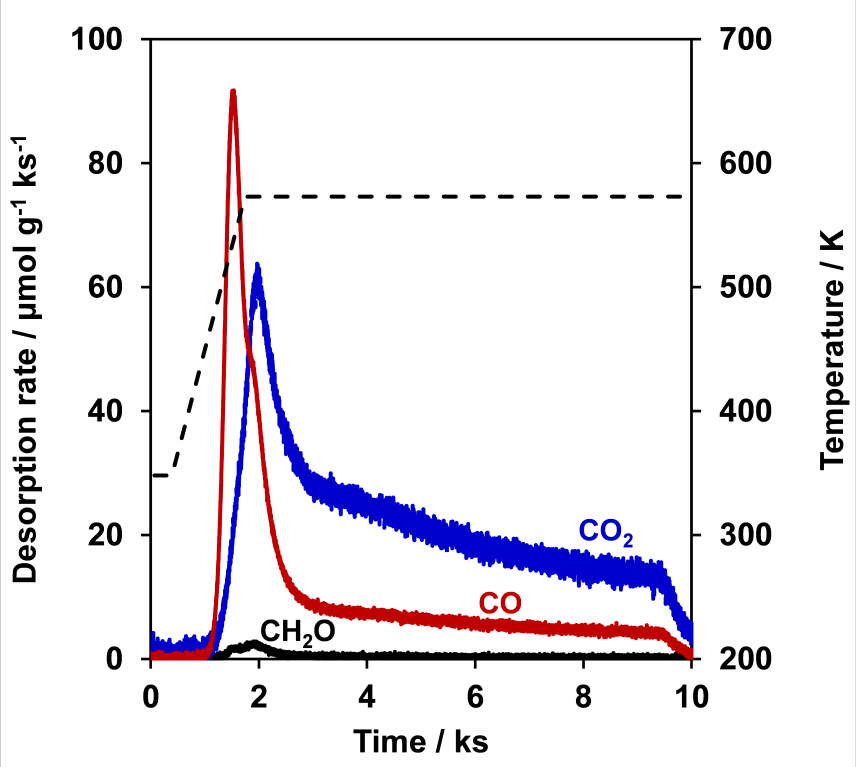

Figure 4.4. TPD profile of the Sn-Beta-41 material under flowing air after adsorption of formaldehyde. Black profile is for formaldehyde, red profile is for carbon monoxide, blue profile is for carbon dioxide, and dashed black line is for temperature (on the secondary y-axis).

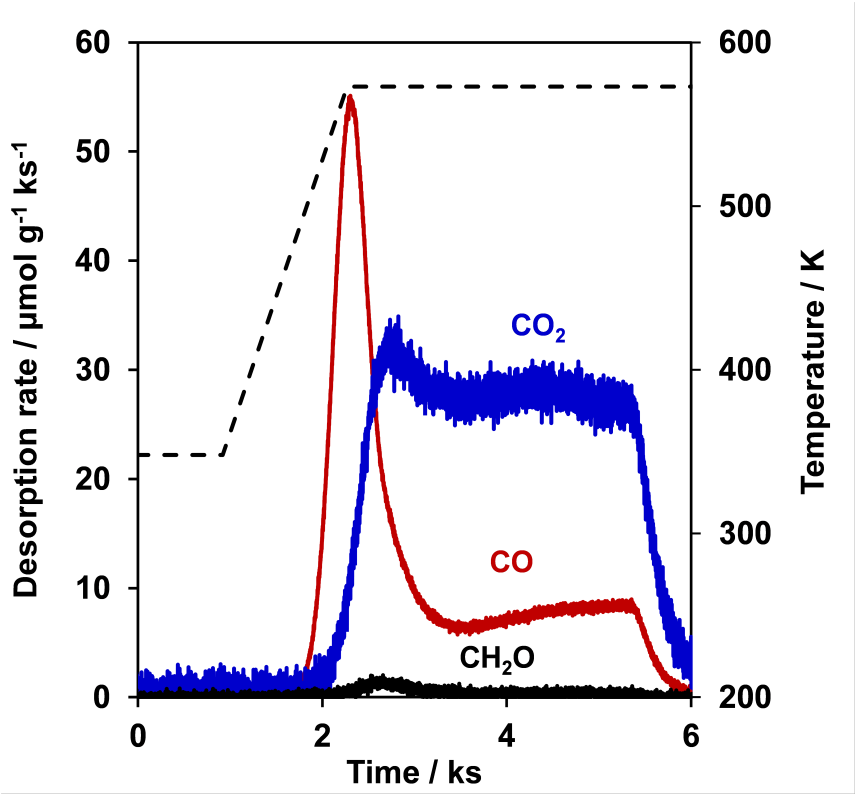

Figure 4.5. TPD profile of the Sn-Beta-109 material under flowing air after adsorption of formaldehyde. Black profile is for formaldehyde, red profile is for carbon monoxide, blue profile is for carbon dioxide, and dashed black line is for temperature (on the secondary y-axis).

To determine if extraframework SnO_x particles influences the processes involved in formaldehyde adsorption and conversion, a purely siliceous Beta material was deposited with $SnCl_4$ and treated in flowing air to 773 K to form predominantly SnO_x particles (denoted as SnO_x-Si-Beta). The SnO_x-Si-Beta material was tested for formaldehyde storage, and the resultant TPD profile is provided in Figure 4.6. The SnO_x-Si-Beta material showed the highest selectivity to carbon monoxide and carbon dioxide of all the materials studied (1.00), demonstrating SnO_x particles may catalyze the conversion of formaldehyde to carbon monoxide and carbon dioxide in the presence of air. Therefore, these preliminary results suggest the addition of SnO_x particles to microporous materials may facilitate the oxidation of formaldehyde to more environmentally benign products during temperature desorption in air.

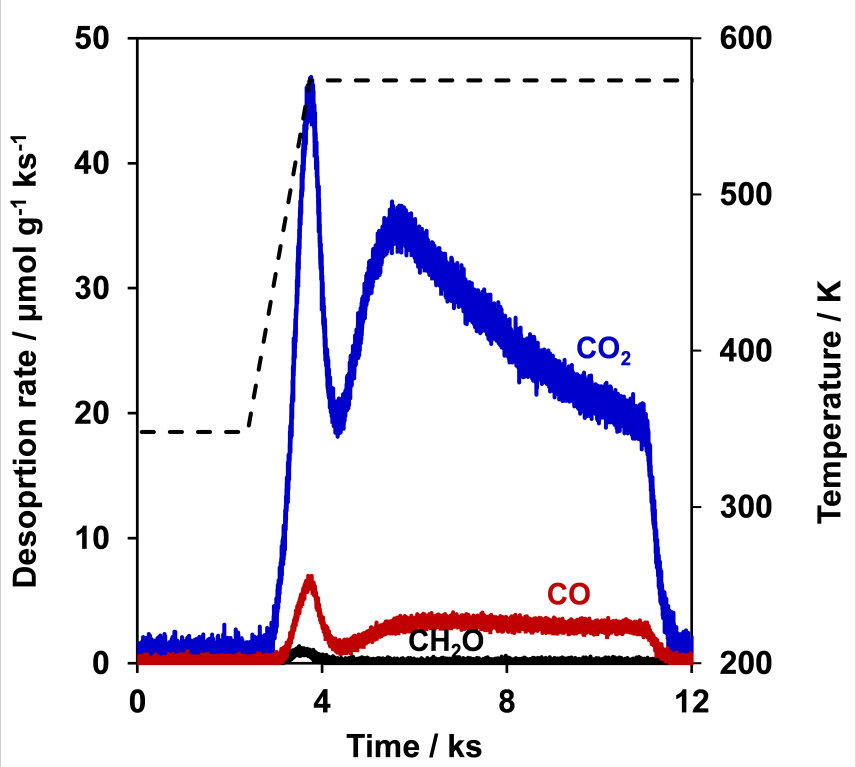

Figure 4.6. TPD profile of the SnO_x-Si-Beta material under flowing air after adsorption of formaldehyde. Black profile is for formaldehyde, red profile is for carbon monoxide, blue profile is for carbon dioxide, and dashed black line is for temperature (on the secondary y-axis).

4.5 Conclusions

A series of microporous Beta samples were synthesized with varying material properties including silanol density, framework heteroatom identity, and extraframework species to identify key material properties for the abatement of formaldehyde in automotive exhaust. Purely siliceous Beta materials stored formaldehyde and converted the majority (>0.9) of adsorbed formaldehyde to carbon monoxide and carbon dioxide, suggesting silanol groups may store formaldehyde. The addition of framework Al sites, forming Brønsted acid sites, did not significantly change the total storage, but decreased the selectivity of desorbed products to carbon monoxide and carbon dioxide from 0.9 to 0.75 and decreased the onset temperature of desorption of formaldehyde. Incorporation of framework Sn heteroatoms resulted in a greater selectivity to carbon monoxide and carbon dioxide (0.99); additionally, the intentional precipitation of SnO_x particles on siliceous Beta resulted in the highest selectivity to carbon monoxide and carbon dioxide (1.00).

These exploratory results suggests that siliceous surfaces can store formaldehyde, and the addition of heteroatoms to the framework does not significantly change the total per-mass formaldehyde storage. However, the addition of some heteroatoms may have deleterious effects (e.g., Al) where greater amounts of formaldehyde are released at lower temperatures below the operating temperature window of downstream formaldehyde oxidation catalysts. The addition of Sn heteroatoms or extraframework SnO_x on purely siliceous supports showed promise as materials for both the storage and conversion of formaldehyde to environmentally benign products.

4.6 Acknowledgements

The authors would like to acknowledge the Ford-Purdue University Alliance for funding this project, and Dr. Bean Getsoian at Ford for helpful technical discussions and contributions. Additionally, the authors would like to thank Dr. Jason S. Bates, Dr. Juan Carlos Vega-Vila, Dr. James W. Harris, Dr. Michael J. Cordon, and Dr. Young Gul Hur for their contributions to material synthesis and formaldehyde adsorption experiments.

REFERENCES

[1] R. R. Rajaram, H.-Y. Chen, and D. Liu, *Passive NOx adsorber*, 2014. [Online]. Available: https://patents.google.com/patent/US10005075B2/en?oq=10%2C005075.

[2] K. Khivantsev, N. R. Jaegers, L. Kovarik, J. C. Hanson, F. (Tao, Y. Tang, X. Zhang, I. Z. Koleva, H. A. Aleksandrov, G. N. Vayssilov, Y. Wang, F. Gao, and J. Szanyi, "Achieving Atomic Dispersion of Highly Loaded Transition Metals in Small-Pore Zeolite SSZ-13: High-Capacity and High-Efficiency Low-Temperature CO and Passive NOx Adsorbers," *Angewandte Chemie*, vol. 130, no. 51, pp. 16 914–16 919, Dec. 2018, ISSN: 0044-8249. DOI: 10.1002/ange.201809343. [Online]. Available: https://onlinelibrary.wiley.com/doi/abs/10.1002/ange.201809343.

[3] H. Chen, J. E. Collier, D. Liu, L. Mantarosie, D. Durán-Martín, V. Novák, R. R. Rajaram, and D. Thompsett, "Low Temperature NO Storage of Zeolite Supported Pd for Low Temperature Diesel Engine Emission Control," *Catalysis Letters*, vol. 146, no. 9, pp. 1706–1711, Sep. 2016, ISSN: 1011-372X. DOI: 10.1007/s10562-016-1794-6. [Online]. Available: http://link.springer.com/10.1007/s10562-016-1794-6.

[4] J. Lee, Y. Kim, S. Hwang, E. Lee, H. Lee, C. H. Kim, and D. H. Kim, "Deactivation of Pd/Zeolites passive NOx adsorber induced by NO and H2O: Comparative study of Pd/ZSM-5 and Pd/SSZ-13," *Catalysis Today*, vol. 360, pp. 350–355, Jan. 2021, ISSN: 09205861. DOI: 10.1016/j.cattod.2020.01.039.

[5] Y. S. Ryou, J. Lee, Y. Kim, S. Hwang, H. Lee, C. H. Kim, and D. H. Kim, "Effect of reduction treatments (H2 vs. CO) on the NO adsorption ability and the physicochemical properties of Pd/SSZ-13 passive NOx adsorber for cold start application," *Applied Catalysis A: General*, vol. 569, pp. 28–34, Jan. 2019, ISSN: 0926860X. DOI: 10.1016/j.apcata.2018.10.016. [Online]. Available: https://linkinghub.elsevier.com/retrieve/pii/S0926860X18305143.

[6] J. Van der Mynsbrugge, M. Head-Gordon, and A. T. Bell, "Computational Modeling Predicts the Stability of Both Pd+ and Pd2+ Ion-Exchanged into H-CHA," *Journal of Materials Chemistry A*, DOI: 10.1039/d0ta11254b, 2021, ISSN: 2050-7488. DOI: 10.1039/d0ta11254b.

[7] M. Ambast, K. Karinshak, B. M. M. Rahman, L. C. Grabow, and M. P. Harold, "Passive NOx adsorption on Pd/H-ZSM-5: Experiments and modeling," *Applied Catalysis B: Environmental*, vol. 269, p. 118 802, 2020, ISSN: 09263373. DOI: 10.1016/j.apcatb.2020.118802. [Online]. Available: https://doi.org/10.1016/j.apcatb.2020.118802.

[8] C. Descorme, P. Gelin, M. Primet, and C. Lecuyer, "Infrared study of nitrogen monoxide adsorption on palladium ion-exchanged ZSM-5 catalysts," *Catalysis Letters*, vol. 41, no. 3-4, pp. 133–138, 1996, ISSN: 1011-372X. DOI: 10.1007/BF00811479. [Online]. Available: http://link.springer.com/10.1007/BF00811479.

[9] Y. Zheng, L. Kovarik, M. H. Engelhard, Y. Wang, Y. Wang, F. Gao, and J. Szanyi, "Low-Temperature Pd/Zeolite Passive NOx Adsorbers: Structure, Performance, and Adsorption Chemistry," *Journal of Physical Chemistry C*, vol. 121, no. 29, pp. 15 793–15 803, 2017, ISSN: 19327455. DOI: 10.1021/acs.jpcc.7b04312. [Online]. Available: https://pubs.acs.org/doi/pdf/10.1021/acs.jpcc.7b04312.

[10] Y. S. Ryou, J. Lee, S. J. Cho, H. Lee, C. H. Kim, and D. H. Kim, "Activation of Pd/SSZ-13 catalyst by hydrothermal aging treatment in passive NO adsorption performance at low temperature for cold start application," *Applied Catalysis B: Environmental*, vol. 212, pp. 140–149, 2017, ISSN: 09263373. DOI: 10.1016/j.apcatb.2017.04.077. [Online]. Available: http://dx.doi.org/10.1016/j.apcatb.2017.04.077.

[11] E. D. Goodman, A. C. Johnston-Peck, E. M. Dietze, C. J. Wrasman, A. S. Hoffman, F. Abild-Pedersen, S. R. Bare, P. N. Plessow, and M. Cargnello, "Catalyst deactivation via decomposition into single atoms and the role of metal loading," *Nature Catalysis*, vol. 2, no. 9, pp. 748–755, 2019, ISSN: 25201158. DOI: 10.1038/s41929-019-0328-1. [Online]. Available: http://dx.doi.org/10.1038/s41929-019-0328-1.

[12] M. Renz, T. Blasco, A. Corma, V. Fornés, R. Jensen, and L. Nemeth, "Selective and Shape-Selective Baeyer–Villiger Oxidations of Aromatic Aldehydes and Cyclic Ketones with Sn-Beta Zeolites and H2O2," *Chemistry - A European Journal*, vol. 8, no. 20, pp. 4708–4717, Oct. 2002, ISSN: 09476539. DOI: 10.1002/1521-3765(20021018)8:20<4708::AID-CHEM4708>3.0.CO;2-U. [Online]. Available: https://onlinelibrary.wiley.com/doi/10.1002/1521-3765(20021018)8:20%3C4708::AID-CHEM4708%3E3.0.CO;2-U.

[13] M. Moliner, Y. Román-Leshkov, and M. E. Davis, "Tin-containing zeolites are highly active catalysts for the isomerization of glucose in water," *Proceedings of the National Academy of Sciences of the United States of America*, vol. 107, no. 14, pp. 6164–6168, Apr. 2010, ISSN: 00278424. DOI: 10.1073/pnas.1002358107. [Online]. Available: https://www.pnas.org/content/107/14/6164%20https://www.pnas.org/content/107/14/6164.abstract.

[14] J. Lee, Y. Ryou, S. Hwang, Y. Kim, S. J. Cho, H. Lee, C. H. Kim, and D. H. Kim, "Comparative study of the mobility of Pd species in SSZ-13 and ZSM-5, and its implication for their activity as passive NOX adsorbers (PNAs) after hydro-thermal aging," *Catalysis Science and Technology*, vol. 9, no. 1, pp. 163–173, Jan. 2019, ISSN: 20444761. DOI: 10.1039/c8cy02088d. [Online]. Available: https://pubs.rsc.org/en/content/articlehtml/2019/cy/c8cy02088d%20https://pubs.rsc.org/en/content/articlelanding/2019/cy/c8cy02088d.

[15] L. L. Sheu, H. Knözinger, and W. M. Sachtler, "Ship-in-a-bottle formation of Pd13(CO)x clusters in zeolite NaY," *Catalysis Letters*, vol. 2, no. 3, pp. 129–137, May 1989, ISSN: 1011372X. DOI: 10.1007/BF00775061.

[16] T. Otto, S. I. Zones, and E. Iglesia, "Challenges and strategies in the encapsulation and stabilization of monodisperse Au clusters within zeolites," *Journal of Catalysis*, vol. 339, pp. 195–208, Jul. 2016, ISSN: 0021-9517. DOI: 10.1016/J.JCAT.2016.04.015. [Online]. Available: https://www.sciencedirect.com/science/article/pii/S0021951716300264.

[17] M. Moliner, J. E. Gabay, C. E. Kliewer, R. T. Carr, J. Guzman, G. L. Casty, P. Serna, and A. Corma, "Reversible Transformation of Pt Nanoparticles into Single Atoms inside High-Silica Chabazite Zeolite," *Journal of the American Chemical Society*, vol. 138, no. 48, pp. 15 743–15 750, Dec. 2016, ISSN: 0002-7863. DOI: 10.1021/jacs.6b10169. [Online]. Available: http://pubs.acs.org/doi/10.1021/jacs.6b10169.

[18] Y. Román-Leshkov, M. Moliner, and M. E. Davis, "Impact of controlling the site distribution of al atoms on catalytic properties in ferrierite-type zeolites," *Journal of Physical Chemistry C*, vol. 115, no. 4, pp. 1096–1102, Feb. 2011, ISSN: 19327447. DOI: 10.1021/jp106247g.

[19] V. Pashkova, P. Klein, J. Dedecek, V. Tokarová, and B. Wichterlová, "Incorporation of Al at ZSM-5 hydrothermal synthesis. Tuning of Al pairs in the framework," *Microporous and Mesoporous Materials*, vol. 202, pp. 138–146, Jan. 2015, ISSN: 1387-1811. DOI: 10.1016/J.MICROMESO.2014.09.056. [Online]. Available: https://www.sciencedirect.com/science/article/pii/S1387181114005708.

[20] J. R. Di Iorio and R. Gounder, "Controlling the Isolation and Pairing of Aluminum in Chabazite Zeolites Using Mixtures of Organic and Inorganic Structure-Directing Agents," *Chemistry of Materials*, vol. 28, no. 7, pp. 2236–2247, Apr. 2016, ISSN: 15205002. DOI: 10.1021/acs.chemmater.6b00181. [Online]. Available: http://pubs.acs.org/doi/abs/10.1021/acs.chemmater.6b00181.

[21] R. W. Borry, Y. H. Kim, A. Huffsmith, J. A. Reimer, and E. Iglesia, "Structure and density of Mo and acid sites in Mo-exchanged H-ZSM5 catalysts for nonoxidative methane conversion," *Journal of Physical Chemistry B*, vol. 103, no. 28, pp. 5787–5796, 1999, ISSN: 10895647. DOI: 10.1021/jp990866v. [Online]. Available: https://pubs.acs.org/sharingguidelines.

[22] J. R. Di Iorio, S. Li, C. B. Jones, C. T. Nimlos, Y. Wang, E. Kunkes, V. Vattipalli, S. Prasad, A. Moini, W. F. Schneider, and R. Gounder, "Cooperative and Competitive Occlusion of Organic and Inorganic Structure-Directing Agents within Chabazite Zeolites Influences Their Aluminum Arrangement," *Journal of the American Chemical Society*, vol. 142, no. 10, pp. 4807–4819, Mar. 2020, ISSN: 15205126. DOI: 10.1021/jacs.9b13817. [Online]. Available: https://pubs.acs.org/doi/abs/10.1021/jacs.9b13817.

[23] C. Paolucci, A. A. Parekh, I. Khurana, J. R. Di Iorio, H. Li, J. D. Albarracin Caballero, A. J. Shih, T. Anggara, W. N. Delgass, J. T. Miller, F. H. Ribeiro, R. Gounder, and W. F. Schneider, "Catalysis in a Cage: Condition-Dependent Speciation and Dynamics of Exchanged Cu Cations in SSZ-13 Zeolites," *Journal of the American Chemical Society*, vol. 138, no. 18, pp. 6028–6048, May 2016, ISSN: 0002-7863. DOI: 10.1021/jacs.6b02651. [Online]. Available: http://pubs.acs.org/doi/abs/10.1021/jacs.6b02651.

[24] G. K. Reddy, C. Ling, T. C. Peck, and H. Jia, "Understanding the chemical state of palladium during the direct NO decomposition-influence of pretreatment environment and reaction temperature," *RSC Advances*, vol. 7, no. 32, pp. 19 645–19 655, Apr. 2017, ISSN: 20462069. DOI: 10.1039/c7ra00836h.

[25] M. Moliner, J. Gabay, C. Kliewer, P. Serna, and A. Corma, "Trapping of Metal Atoms and Metal Clusters by Chabazite under Severe Redox Stress," *ACS Catalysis*, vol. 8, no. 10, pp. 9520–9528, Oct. 2018, ISSN: 21555435. DOI: 10.1021/acscatal.8b01717. [Online]. Available: http://pubs.acs.org/doi/10.1021/acscatal.8b01717.

[26] J. Lee, Y. Ryou, S. J. Cho, H. Lee, C. H. Kim, and D. H. Kim, "Investigation of the active sites and optimum Pd/Al of Pd/ZSM–5 passive NO adsorbers for the cold-start application: Evidence of isolated-Pd species obtained after a high-temperature thermal treatment," *Applied Catalysis B: Environmental*, vol. 226, pp. 71–82, Jun. 2018, ISSN: 0926-3373. DOI: 10.1016/J.APCATB.2017.12.031. [Online]. Available: https://www.sciencedirect.com/science/article/pii/S0926337317311803.

[27] G. Bergeret, P. Gallezot, and B. Imelik, "X-ray study of the activation, reduction, and reoxidation of palladium in Y-type zeolites," *Journal of Physical Chemistry*, vol. 85, no. 4, pp. 411–416, 1981, ISSN: 00223654. DOI: 10.1021/j150604a020. [Online]. Available: https://pubs.acs.org/sharingguidelines.

[28] P. Gallezot and B. Imelik, "X-Ray Diffraction Study of Palladium Y Zeolite," in *Molecular Sieves*, Advances in Chemistry Series, 1973, ch. 5, pp. 66–73. DOI: 10.1021/ba-1973-0121.ch005.

[29] S. Homeyer and W. Sachtler, "Oxidative redispersion of palladium and formation of PdO particles in NaY: An Application of High Precision TPR," *Applied Catalysis*, vol. 54, no. 1, pp. 189–202, Sep. 1989, ISSN: 0166-9834. DOI: 10.1016/S0166-9834(00)82364-7. [Online]. Available: https://www-sciencedirect-com.ezproxy.lib.purdue.edu/science/article/pii/S0166983400823647.

[30] K. Khivantsev, F. Gao, L. Kovarik, Y. Wang, and J. Szanyi, "Molecular Level Understanding of How Oxygen and Carbon Monoxide Improve NO x Storage in Palladium/SSZ-13 Passive NOx Adsorbers: The Role of NO+ and Pd(II)(CO)(NO) Species," *The Journal of Physical Chemistry C*, vol. 122, no. 20, pp. 10 820–10 827, May 2018, ISSN: 1932-7447. DOI: 10.1021/acs.jpcc.8b01007. [Online]. Available: http://pubs.acs.org/doi/10.1021/acs.jpcc.8b01007.

[31] Y. Taarit, J. C. Vedrine, J. F. Dutel, and C. Naccache, "EPR investigation of the structure and reactivity of Pd(I) species generated in synthetic mordenite-type zeolite," *Journal of Magnetic Resonance (1969)*, vol. 31, no. 2, pp. 251–257, Aug. 1978, ISSN: 00222364. DOI: 10.1016/0022-2364(78)90187-7.

[32] K. Khivantsev, N. R. Jaegers, I. Z. Koleva, H. A. Aleksandrov, L. Kovarik, M. Engelhard, F. Gao, Y. Wang, G. N. Vayssilov, and J. Szanyi, "Stabilization of Super Electrophilic Pd+2 Cations in Small-Pore SSZ-13 Zeolite," *Journal of Physical Chemistry C*, vol. 124, no. 1, pp. 309–321, 2019, ISSN: 19327455. DOI: 10.1021/acs.jpcc.9b06760. [Online]. Available: https://pubs.acs.org/sharingguidelines.

[33] J. Michalik, M. Heming, and L. Kevan, "Trivalent and monovalent palladium cations in PdNa-X zeolite: Electron spin resonance and electron spin echo modulation spectroscopic studies," *The Journal of Physical Chemistry*, vol. 90, no. 10, pp. 2132–2136, 1986, ISSN: 00223654. DOI: 10.1021/j100401a029. [Online]. Available: https://pubs.acs.org/sharingguidelines.

[34] A. Gupta, S. B. Kang, and M. P. Harold, "NOx uptake and release on Pd/SSZ-13: Impact Of Feed composition and temperature," *Catalysis Today*, vol. 360, pp. 411–425, 2020, ISSN: 09205861. DOI: 10.1016/j.cattod.2020.01.018. [Online]. Available: www.elsevier.com/locate/cattod.

[35] M. Ogura, M. Hayashi, S. Kage, M. Matsukata, and E. Kikuchi, "Determination of active palladium species in ZSM-5 zeolite for selective reduction of nitric oxide with methane," *Applied Catalysis B: Environmental*, vol. 23, no. 4, pp. 247–257, Dec. 1999, ISSN: 09263373. DOI: 10.1016/S0926-3373(99)00082-X.

[36] K. Khivantsev, N. R. Jaegers, L. Kovarik, M. Wang, J. Z. Hu, Y. Wang, M. A. Derewinski, and J. Szanyi, "The superior hydrothermal stability of Pd/SSZ-39 in low temperature passive NOx adsorption (PNA) and methane combustion," *Applied Catalysis B: Environmental*, vol. 280, p. 1 194 492, 2021, ISSN: 09263373. DOI: 10.1016/j.apcatb.2020.119449.

[37] K. Okumura, J. Amano, N. Yasunobu, and M. Niwa, "X-ray Absorption Fine Structure Study of the Formation of the Highly Dispersed PdO over ZSM-5 and the Structural Change of Pd Induced by Adsorption of NO," *Journal of Physical Chemistry B*, vol. 104, no. 5, pp. 1050–1057, 2000, ISSN: 10895647. DOI: 10.1021/jp993182w. [Online]. Available: https://pubs.acs.org/doi/abs/10.1021/jp993182w.

[38] K. Mandal, Y. Gu, K. S. Westendorff, S. Li, J. A. Pihl, L. C. Grabow, W. S. Epling, and C. Paolucci, "Condition-Dependent Pd Speciation and NO adsorption in Pd/Zeolites," *ACS Catalysis*, vol. 10, pp. 12 801–12 818, Sep. 2020, ISSN: 2155-5435. DOI: 10.1021/acscatal.0c03585. [Online]. Available: https://pubs.acs.org/doi/10.1021/acscatal.0c03585.

[39] I. Friberg, N. Sadokhina, and L. Olsson, "The effect of Si/Al ratio of zeolite supported Pd for complete CH4 oxidation in the presence of water vapor and SO2," *Applied Catalysis B: Environmental*, vol. 250, pp. 117–131, Aug. 2019, ISSN: 09263373. DOI: 10.1016/j.apcatb.2019.03.005.

[40] O. Mihai, L. Trandafilović, T. Wentworth, F. F. Torres, and L. Olsson, "The Effect of Si/Al Ratio for Pd/BEA and Pd/SSZ-13 Used as Passive NOx Adsorbers," *Topics in Catalysis*, vol. 61, no. 18-19, pp. 2007–2020, Nov. 2018, ISSN: 1022-5528. DOI: 10.1007/s11244-018-1017-z. [Online]. Available: http://link.springer.com/10.1007/s11244-018-1017-z.

[41] Y. S. Ryou, J. Lee, H. Lee, C. H. Kim, and D. H. Kim, "Effect of various activation conditions on the low temperature NO adsorption performance of Pd/SSZ-13 passive NOx adsorber," *Catalysis Today*, vol. 320, pp. 175–180, Dec. 2017, ISSN: 09205861. DOI: 10.1016/j.cattod.2017.11.030. [Online]. Available: https://www.sciencedirect.com/science/article/pii/S092058611730809X.

[42] E. J. Peterson, A. T. DeLaRiva, S. Lin, R. S. Johnson, H. Guo, J. T. Miller, J. H. Kwak, C. H. Peden, B. Kiefer, L. F. Allard, F. H. Ribeiro, and A. K. Datye, "Low-temperature carbon monoxide oxidation catalysed by regenerable atomically dispersed palladium on alumina," *Nature Communications*, vol. 5, p. 4885, 2014, ISSN: 20411723. DOI: 10.1038/ncomms5885.

[43] Z. Zhang, G. Mestl, H. Knözinger, and W. M. Sachtler, "Effects of calcination program and rehydration on palladium dispersion in zeolites NaY and 5A," *Applied Catalysis A, General*, vol. 89, no. 2, pp. 155–168, 1992, ISSN: 0926860X. DOI: 10.1016/0926-860X(92)80230-A. [Online]. Available: https://ac.els-cdn.com/0926860X9280230A/1-s2.0-0926860X9280230A-main.pdf?_tid=49b158c1-45f3-4550-8eda-3f7c40cf6221&acdnat=1531768423_906bbf0e51a9549f2bb1a9937e622077.

[44] Y. Gu, R. P. Zelinsky, Y. R. Chen, and W. S. Epling, "Investigation of an irreversible NOx storage degradation Mode on a Pd/BEA passive NOx adsorber," *Applied Catalysis B: Environmental*, vol. 258, p. 118 032, Dec. 2019, ISSN: 09263373. DOI: 10.1016/j.apcatb.2019.118032.

[45] S. B. Simonsen, I. Chorkendorff, S. Dahl, M. Skoglundh, J. Sehested, and S. Helveg, "Direct observations of oxygen-induced platinum nanoparticle ripening studied by in situ TEM," *Journal of the American Chemical Society*, vol. 132, no. 23, pp. 7968–7975, 2010, ISSN: 00027863. DOI: 10.1021/ja910094r. [Online]. Available: https://pubs.acs.org/sharingguidelines.

[46] D. W. Fickel and R. F. Lobo, "Copper Coordination in Cu-SSZ-13 and Cu-SSZ-16 Investigated by Variable-Temperature XRD," *The Journal of Physical Chemistry C*, vol. 114, no. 3, pp. 1633–1640, Jan. 2010, ISSN: 1932-7447. DOI: 10.1021/jp9105025. [Online]. Available: http://pubs.acs.org/doi/abs/10.1021/jp9105025.

[47] S. A. Bates, A. A. Verma, C. Paolucci, A. A. Parekh, T. Anggara, A. Yezerets, W. F. Schneider, J. T. Miller, W. N. Delgass, and F. H. Ribeiro, "Identification of the active Cu site in standard selective catalytic reduction with ammonia on Cu-SSZ-13," *Journal of Catalysis*, vol. 312, pp. 87–97, 2014, ISSN: 00219517. DOI: 10.1016/j.jcat.2014.01.004. [Online]. Available: http://www.sciencedirect.com/science/article/pii/S0021951714000141.

[48] J. R. Di Iorio, C. T. Nimlos, and R. Gounder, "Introducing catalytic diversity into single-site chabazite zeolites of fixed composition via synthetic control of active site proximity," *ACS Catalysis*, vol. 7, no. 10, pp. 6663–6674, 2017, ISSN: 21555435. DOI: 10.1021/acscatal.7b01273. [Online]. Available: https://pubs.acs.org/doi/abs/10.1021/acscatal.7b01273.

[49] E. A. Eilertsen, B. Arstad, S. Svelle, and K. P. Lillerud, "Single parameter synthesis of high silica CHA zeolites from fluoride media," *Microporous and Mesoporous Materials*, vol. 153, pp. 94–99, May 2012, ISSN: 13871811. DOI: 10.1016/j.micromeso.2011.12.026.

[50] H. Hoser, S. Krazyzanowski, and F. Trifiró, "Optical spectra of Co-zeolites," *Journal of the Chemical Society, Faraday Transactions 1: Physical Chemistry in Condensed Phases*, vol. 71, no. 0, pp. 665–669, Jan. 1975, ISSN: 03009599. DOI: 10.1039/F19757100665. [Online]. Available: https://pubs.rsc.org/en/content/articlehtml/1975/f1/f19757100665%20https://pubs.rsc.org/en/content/articlelanding/1975/f1/f19757100665.

[51] A. A. Verberckmoes, B. M. Weckhuysen, and R. A. Schoonheydt, "Spectroscopy and coordination chemistry of cobalt in molecular sieves," *Microporous and Mesoporous Materials*, vol. 22, no. 1-3, pp. 165–178, Jun. 1998, ISSN: 13871811. DOI: 10.1016/S1387-1811(98)00091-2. [Online]. Available: https://lirias.kuleuven.be/1582098.

[52] T. B. Bolin, T. Wu, N. Schweitzer, R. Lobo-Lapidus, A. J. Kropf, H. Wang, Y. Hu, J. T. Miller, and S. M. Heald, "In situ intermediate-energy X-ray catalysis research at the advanced photon source beamline 9-BM," *Catalysis Today*, vol. 205, pp. 141–147, Apr. 2013, ISSN: 09205861. DOI: 10.1016/j.cattod.2012.09.034.

[53] S. Lee, B. Lee, S. Seifert, S. Vajda, and R. E. Winans, "Simultaneous measurement of X-ray small angle scattering, absorption and reactivity: A continuous flow catalysis reactor," *Nuclear Instruments and Methods in Physics Research, Section A: Accelerators, Spectrometers, Detectors and Associated Equipment*, vol. 649, no. 1, pp. 200–203, Sep. 2011, ISSN: 01689002. DOI: 10.1016/j.nima.2010.12.172.

[54] M. Jiang, J. Wang, J. Wang, and M. Shen, "The influence of Si/Al ratios on adsorption and desorption characterizations of Pd/Beta served as cold-start catalysts," *Materials*, vol. 12, no. 7, p. 1045, Mar. 2019, ISSN: 19961944. DOI: 10.3390/ma12071045. [Online]. Available: https://www.mdpi.com/1996-1944/12/7/1045.

[55] L. Castoldi, R. Matarrese, S. Morandi, P. Ticali, and L. Lietti, "Low-temperature Pd/FER NOx adsorbers: Operando FT-IR spectroscopy and performance analysis," *Catalysis Today*, vol. 360, pp. 317–325, Feb. 2021, ISSN: 09205861. DOI: 10.1016/j.cattod.2020.02.019.

[56] J. Wang, V. F. Kispersky, W. Nicholas Delgass, and F. H. Ribeiro, "Determination of the Au active site and surface active species via operando transmission FTIR and isotopic transient experiments on 2.3 wt.% Au/TiO2 for the WGS reaction," *Journal of Catalysis*, vol. 289, pp. 171–178, May 2012, ISSN: 00219517. DOI: 10.1016/j.jcat.2012.02.008.

[57] Y. H. C. Chin, M. García-Diéguez, and E. Iglesia, "Dynamics and thermodynamics of Pd-PdO phase transitions: Effects of pd cluster size and kinetic implications for catalytic methane combustion," *Journal of Physical Chemistry C*, vol. 120, no. 3, pp. 1446–1460, 2016, ISSN: 19327455. DOI: 10.1021/acs.jpcc.5b06677. [Online]. Available: https://pubs.acs.org/sharingguidelines.

[58] M. Behrens and R. Schlögl, "X-Ray Diffraction and Small Angle X-Ray Scattering," in *Characterization of Solid Materials and Heterogeneous Catalysts: From Structure to Surface Reactivity: Part Two: Macroscopic Techniques*, vol. 1, Wiley-VCH, Apr. 2012, pp. 611–653, ISBN: 9783527326877. DOI: 10.1002/9783527645329.

[59] D. Spielbauer, H. Zeilinger, and H. Knozinger, "Adsorption of Palladium-Ammino-Aquo Complexes on gamma-Alumina and Silica," *Langmuir*, vol. 9, pp. 460–466, 1993. [Online]. Available: https://doi.org/10.1021/la00026a017.

[60] L. Rasmussen and K. Jorgensen, "Palladium (II) Complexes," *Acta Chemica Scandinavica*, vol. 22, pp. 2313–2323, 1968.

[61] A. Sauvage, P. Massiani, M. Briend, D. Barthomeuf, and F. Bozon-Verduraz, "Comparison of Pd(NH3)42+ decomposition and Pd2+ reduction in zeolites NaY, NaX and CsX," *Journal of the Chemical Society, Faraday Transactions*, vol. 91, no. 18, pp. 3291–3297, Jan. 1995, ISSN: 09565000. DOI: 10.1039/FT9959103291.

[62] L. I. Elding and L. F. Olsson, "Electronic Spectra of Square-Planar Complexes Electronic Absorption Spectra of Square-Planar Chloro-Aqua and Bromo-Aqua Complexes of Palladium(II) and Platinum(II)," *The Journal of Physical Chemistry*, vol. 82, no. 1, p. 69, 1978. [Online]. Available: https://doi.org/10.1021/j100490a018.

[63] T. Nedoseykina, P. Plyusnin, Y. Shubin, and S. Korenev, "XAFS investigation of Pd(II) amine / Au(IV) chloride and its thermolysis products," in *Journal of Thermal Analysis and Calorimetry*, vol. 102, Nov. 2010, pp. 703–708. DOI: 10.1007/s10973-010-0723-y. [Online]. Available: https://akjournals-com.ezproxy.lib.purdue.edu/view/journals/10973/102/2/article-p703.xml.

[64] Z. Zhang, W. M. Sachtler, and H. Chen, "Identification by diffuse reflectance and EXAFS of the changes in coordination of NaY entrapped Pd(NH3)x2+ ion during calcination," *Zeolites*, vol. 10, no. 8, pp. 784–789, 1990, ISSN: 01442449. DOI: 10.1016/0144-2449(90)90062-V.

[65] L. Jiao and J. R. Regalbuto, "The synthesis of highly dispersed noble and base metals on silica via strong electrostatic adsorption: I. Amorphous silica," *Journal of Catalysis*, vol. 260, pp. 329–341, 2008. DOI: 10.1016/j.jcat.2008.09.022. [Online]. Available: www.elsevier.com/locate/jcat.

[66] W. Reagan, A. Chester, and G. Kerr, "Studies of the thermal decomposition and catalytic properties of some platinum and palladium ammine zeolites," *Journal of Catalysis*, vol. 69, no. 1, pp. 89–100, May 1981, ISSN: 0021-9517. DOI: 10.1016/0021-9517(81)90131-7. [Online]. Available: https://www.sciencedirect.com/science/article/pii/0021951781901317.

[67] J. H. Tsai and L. K. Frevel, *Ammine complex of palladium nitrate and method of preparation*, 1973.

[68] K. I. Shimizu, F. Okada, Y. Nakamura, A. Satsuma, and T. Hattori, "Mechanism of NO reduction by CH4 in the presence of O2 over Pd-H-mordenite," *Journal of Catalysis*, vol. 195, no. 1, pp. 151–160, Oct. 2000, ISSN: 00219517. DOI: 10.1006/jcat.2000.2964.

[69] E. K. Dann, E. K. Gibson, R. A. Catlow, P. Collier, T. Eralp Erden, D. Gianolio, C. Hardacre, A. Kroner, A. Raj, A. Goguet, and P. P. Wells, "Combined in Situ XAFS/DRIFTS Studies of the Evolution of Nanoparticle Structures from Molecular Precursors," *Chemistry of Materials*, vol. 29, no. 17, pp. 7515–7523, 2017, ISSN: 15205002. DOI: 10.1021/acs.chemmater.7b02552. [Online]. Available: https://pubs.acs.org/sharingguidelines.

[70] S. Homeyer and W. Sachtler, "Elementary steps in the formation of highly dispersed palladium in NaY: II. Particle formation and growth," *Journal of Catalysis*, vol. 118, no. 1, pp. 266–274, Jul. 1989, ISSN: 0021-9517. DOI: 10.1016/0021-9517(89)90316-3. [Online]. Available: https://www-sciencedirect-com.ezproxy.lib.purdue.edu/science/article/pii/0021951789903163.

[71] N. K. Nag, "A study on the formation of palladium hydride in a carbon-supported palladium catalyst," *Journal of Physical Chemistry B*, vol. 105, no. 25, pp. 5945–5949, Jun. 2001, ISSN: 10895647. DOI: 10.1021/jp004535q.

[72] B. T. Carvill, B. A. Lerner, Z. C. Zhang, and W. M. Sachtler, "Preparation of metal/zeolite catalysts: Formation of palladium aquocomplexes in the precursor of palladium-mordenite catalysts," *Journal of Catalysis*, vol. 143, no. 1, pp. 314–317, Sep. 1993, ISSN: 10902694. DOI: 10.1006/jcat.1993.1277.

[73] J. Lee, J. Kim, Y. Kim, S. Hwang, H. Lee, C. H. Kim, and D. H. Kim, "Improving NOx storage and CO oxidation abilities of Pd/SSZ-13 by increasing its hydrophobicity," *Applied Catalysis B: Environmental*, vol. 277, p. 119 190, 2020, ISSN: 09263373. DOI: 10.1016/j.apcatb.2020.119190. [Online]. Available: https://doi.org/10.1016/j.apcatb.2020.119190.

[74] D. Mei, F. Gao, J. Szanyi, and Y. Wang, "Mechanistic insight into the passive NOx adsorption in the highly dispersed Pd/HBEA zeolite," *Applied Catalysis A: General*, vol. 569, pp. 181–189, Jan. 2019, ISSN: 0926860X. DOI: 10.1016/j.apcata.2018.10.037.

[75] K. Khivantsev, N. R. Jaegers, L. Kovarik, S. Prodinger, M. A. Derewinski, Y. Wang, F. Gao, and J. Szanyi, "Palladium/Beta zeolite passive NOx adsorbers (PNA): Clarification of PNA chemistry and the effects of CO and zeolite crystallite size on PNA performance," *Applied Catalysis A: General*, vol. 569, pp. 141–148, Jan. 2019, ISSN: 0926860X. DOI: 10.1016/j.apcata.2018.10.021.

[76] C. Descorme, P. Gélin, C. Lécuyer, and M. Primet, "Catalytic reduction of nitric oxide by methane in the presence of oxygen on palladium-exchanged mordenite zeolites," *Journal of Catalysis*, vol. 177, no. 2, pp. 352–362, 1998, ISSN: 00219517. DOI: 10.1006/jcat.1998.2112.

[77] A. Vu, J. Luo, J. Li, and W. S. Epling, "Effects of CO on Pd/BEA Passive NOx Adsorbers," *Catalysis Letters*, vol. 147, no. 3, pp. 745–750, Mar. 2017, ISSN: 1011-372X. DOI: 10.1007/s10562-017-1976-x. [Online]. Available: http://link.springer.com/10.1007/s10562-017-1976-x.

[78] S. M. Pugh, P. A. Wright, D. J. Law, N. Thompson, and S. E. Ashbrook, "Facile, Room-Temperature 17O Enrichment of Zeolite Frameworks Revealed by Solid-State NMR Spectroscopy," *Journal of the American Chemical Society*, vol. 142, no. 2, pp. 900–906, Jan. 2020, ISSN: 15205126. DOI: 10.1021/jacs.9b10528. [Online]. Available: https://pubs.acs.org/doi/abs/10.1021/jacs.9b10528.

[79] C. J. Heard, L. Grajciar, C. M. Rice, S. M. Pugh, P. Nachtigall, S. E. Ashbrook, and R. E. Morris, "Fast room temperature lability of aluminosilicate zeolites," *Nature Communications*, vol. 10, no. 1, pp. 1–7, Dec. 2019, ISSN: 20411723. DOI: 10.1038/s41467-019-12752-y. [Online]. Available: https://doi.org/10.1038/s41467-019-12752-y.

[80] G. T. Kerr, "The Intracrystalline Rearrangement of Constitutive Water in Hydrogen Zeolite Y," *Journal of Physical Chemistry*, vol. 71, pp. 4155–4156, 1967. [Online]. Available: http://pubs.acs.org/doi/pdf/10.1021/j100871a079.

[81] G. T. Kerr, "Chemistry of crystalline aluminosilicates. VII. Thermal decomposition products of ammonium zeolite Y," *Journal of Catalysis*, vol. 15, no. 2, pp. 200–204, 1969, ISSN: 10902694. DOI: 10.1016/0021-9517(69)90024-4.

[82] F. Gao, Y. Wang, M. Kollár, N. M. Washton, J. Szanyi, and C. H. Peden, "A comparative kinetics study between Cu/SSZ-13 and Fe/SSZ-13 SCR catalysts," *Catalysis Today*, vol. 258, pp. 347–358, 2015, ISSN: 09205861. DOI: 10.1016/j.cattod.2015.01.025. [Online]. Available: http://www.sciencedirect.com/science/article/pii/S0920586115000747.

[83] Q. L. Wang, G. Giannetto, M. Torrealba, G. Perot, C. Kappenstein, and M. Guisnet, "Dealumination of zeolites II. Kinetic study of the dealumination by hydrothermal treatment of a NH4NaY zeolite," *Journal of Catalysis*, vol. 130, no. 2, pp. 459–470, Aug. 1991, ISSN: 10902694. DOI: 10.1016/0021-9517(91)90128-Q. [Online]. Available: http://linkinghub.elsevier.com/retrieve/pii/002195179190128Q.

[84] L. H. Ong, M. Dömök, R. Olindo, A. C. Van Veen, and J. A. Lercher, "Dealumination of HZSM-5 via steam-treatment," *Microporous and Mesoporous Materials*, vol. 164, pp. 9–20, Dec. 2012, ISSN: 13871811. DOI: 10.1016/j.micromeso.2012.07.033. [Online]. Available: http://linkinghub.elsevier.com/retrieve/pii/S1387181112004659.

[85] D. Wang, Y. Jangjou, Y. Liu, M. K. Sharma, J. Luo, J. Li, K. Kamasamudram, and W. S. Epling, "A comparison of hydrothermal aging effects on NH3-SCR of NOx over Cu-SSZ-13 and Cu-SAPO-34 catalysts," *Applied Catalysis B: Environmental*, vol. 165, pp. 438–445, Apr. 2015. [Online]. Available: https://www-sciencedirect-com.ezproxy.lib.purdue.edu/science/article/pii/S092633731400633X%20http://dx.doi.org/10.1016/j.apcatb.2014.10.020.

[86] D. D. Hibbitts, R. Gounder, C. T. Nimlos, A. J. Hoffman, Y. G. Hur, B. J. Lee, and J. R. Di Iorio, "Experimental and theoretical assessments of aluminum proximity in MFI zeolites and its alteration by organic and inorganic structure-directing agents," *Chemistry of Materials*, vol. 32, no. 21, pp. 9277–9298, Oct. 2020, ISSN: 15205002. DOI: 10.1021/acs.chemmater.0c03154.

[87] Y. Zhang, R. Zhao, M. Sanchez-Sanchez, G. L. Haller, J. Hu, R. Bermejo-Deval, Y. Liu, and J. A. Lercher, "Promotion of protolytic pentane conversion on H-MFI zeolite by proximity of extra-framework aluminum oxide and Bronsted acid sites," *Journal of Catalysis*, vol. 370, pp. 424–433, Feb. 2019, ISSN: 10902694. DOI: 10.1016/j.jcat.2019.01.006.

[88] T. W. Hansen, A. T. Delariva, S. R. Challa, and A. K. Datye, "Sintering of catalytic nanoparticles: Particle migration or ostwald ripening?" *Accounts of Chemical Research*, vol. 46, no. 8, pp. 1720–1730, 2013, ISSN: 00014842. DOI: 10.1021/ar3002427. [Online]. Available: https://pubs.acs.org/sharingguidelines.

[89] J. R. Theis and C. K. Lambert, "Mechanistic assessment of low temperature NOx adsorbers for cold start NOx control on diesel engines," *Catalysis Today*, vol. 320, pp. 181–195, Jan. 2019, ISSN: 09205861. DOI: 10.1016/j.cattod.2017.12.014.

[90] A. Holm, E. D. Goodman, J. H. Stenlid, A. Aitbekova, R. Zelaya, B. T. Diroll, A. C. Johnston-Peck, K. C. Kao, C. W. Frank, L. G. Pettersson, and M. Cargnello, "Nanoscale Spatial Distribution of Supported Nanoparticles Controls Activity and Stability in Powder Catalysts for CO Oxidation and Photocatalytic H2 Evolution," *Journal of the American Chemical Society*, vol. 142, no. 34, pp. 14 481–14 494, Aug. 2020, ISSN: 15205126. DOI: 10.1021/jacs.0c03842. [Online]. Available: https://pubs.acs.org/doi/abs/10.1021/jacs.0c03842.

[91] L. Liu and A. Corma, "Confining isolated atoms and clusters in crystalline porous materials for catalysis," *Nature Reviews Materials*, pp. 41 578–020, 2020, ISSN: 2058-8437. DOI: 10.1038/s41578-020-00250-3. [Online]. Available: https://doi.org/10.1038/s41578-020-00250-3.

[92] D. W. Fickel, E. D'Addio, J. A. Lauterbach, and R. F. Lobo, "The ammonia selective catalytic reduction activity of copper-exchanged small-pore zeolites," *Applied Catalysis B: Environmental*, vol. 102, no. 3-4, pp. 441–448, Feb. 2011, ISSN: 09263373. DOI: 10.1016/j.apcatb.2010.12.022. [Online]. Available: http://linkinghub.elsevier.com/retrieve/pii/S0926337310005539.

[93] M. A. Camblor, A. Corma, and S. Valencia, "Spontaneous nucleation and growth of pure silica zeolite-β free of connectivity defects," *Chemical Communications*, no. 20, pp. 2365–2366, 1996, ISSN: 13597345. DOI: 10.1039/cc9960002365.

[94] C. Baerlocher and L. B. McCusker, *Database of Zeolite Structures*. [Online]. Available: http://www.iza-structure.org/databases.

[95] M. Calligaris, G. Nardin, and L. Randaccio, "Cation site location in hydrated chabazites. Crystal structure of potassium- and silver- exchanged chabazites," *Zeolites*, vol. 3, no. 3, pp. 205–208, Jul. 1983, ISSN: 01442449. DOI: 10.1016/0144-2449(83)90008-8.

[96] W. A. Brantley, Z. Cai, E. Papazoglou, J. C. Mitchell, S. J. Kerber, G. P. Mann, and T. L. Barr, "X-ray diffraction studies of oxidized high-palladium alloys," *Dental Materials*, vol. 12, no. 5-6, pp. 333–341, Sep. 1996, ISSN: 01095641. DOI: 10.1016/s0109-5641(96)80043-1.

[97] H. Zhao, X. Chen, A. Bhat, Y. Li, and J. W. Schwank, "Understanding the chemistry during the preparation of Pd/SSZ-13 for the low-temperature NO adsorption: The role of NH4-SSZ-13 support," *Applied Catalysis B: Environmental*, vol. 282, 2021, ISSN: 09263373. DOI: 10.1016/j.apcatb.2020.119611. [Online]. Available: https://www.sciencedirect.com/science/article/abs/pii/S0926337320310262.

[98] P. Holoborodko, *Smooth noise-robust differentiators*. [Online]. Available: http://www.holoborodko.com/pavel/numerical-methods/numerical-derivative/smooth-low-noise-differentiators/.

[99] J. Waser, H. A. Levy, and S. W. Peterson, "The structure of PdO," *Acta Crystallographica*, vol. 6, no. 7, pp. 661–663, Jul. 1953, ISSN: 0365-110X. DOI: 10.1107/s0365110x53001800. [Online]. Available: https://onlinelibrary.wiley.com/doi/full/10.1107/S0365110X53001800%20https://onlinelibrary.wiley.com/doi/abs/10.1107/S0365110X53001800%20https://onlinelibrary.wiley.com/doi/10.1107/S0365110X53001800.

[100] T. Grassl and N. Korber, "Tetraamminepalladium(II) dichloride ammonia tetrasolvate," *Acta Crystallographica Section E: Structure Reports Online*, vol. 70, no. 7, pp. i32–i32, Jun. 2014, ISSN: 16005368. DOI: 10.1107/S1600536814012355. [Online]. Available: https://doi.org/10.1107/S1600536814012355].

[101] R. J. Gorte, "Design parameters for temperature programmed desorption from porous catalysts," *Journal of Catalysis*, vol. 75, no. 1, pp. 164–174, May 1982, ISSN: 10902694. DOI: 10.1016/0021-9517(82)90131-2.

[102] R. Demmin and R. Gorte, "Design parameters for temperature-programmed desorption from a packed bed," *Journal of Catalysis*, vol. 90, no. 1, pp. 32–39, Nov. 1984, ISSN: 0021-9517. DOI: 10.1016/0021-9517(84)90081-2. [Online]. Available: https://www.sciencedirect.com/science/article/pii/0021951784900812?via%3Dihub.

[103] J. R. Di Iorio, S. A. Bates, A. A. Verma, W. N. Delgass, F. H. Ribeiro, J. T. Miller, and R. Gounder, "The Dynamic Nature of Brønsted Acid Sites in Cu–Zeolites During NOx Selective Catalytic Reduction: Quantification by Gas-Phase Ammonia Titration," *Topics in Catalysis*, vol. 58, no. 7-9, pp. 424–434, May 2015, ISSN: 1022-5528. DOI: 10.1007/s11244-015-0387-8. [Online]. Available: http://link.springer.com/10.1007/s11244-015-0387-8.

[104] S. A. Bates, W. N. Delgass, F. H. Ribeiro, J. T. Miller, and R. Gounder, "Methods for NH3 titration of Brønsted acid sites in Cu-zeolites that catalyze the selective catalytic reduction of NOx with NH3," *Journal of Catalysis*, vol. 312, pp. 26–36, 2014, ISSN: 00219517. DOI: 10.1016/j.jcat.2013.12.020. [Online]. Available: http://www.sciencedirect.com/science/article/pii/S0021951714000086.

[105] G. L. Woolery and G. H. Kuehl, "On the nature of framework Brønsted and Lewis acid sites in ZSM-5," *Zeolites*, vol. 19, no. 4, pp. 288–296, Oct. 1997, ISSN: 01442449. DOI: 10.1016/S0144-2449(97)00086-9.

[106] A. A. Gabrienko, I. G. Danilova, S. S. Arzumanov, A. V. Toktarev, D. Freude, and A. G. Stepanov, "Strong acidity of silanol groups of zeolite beta: Evidence from the studies by IR spectroscopy of adsorbed CO and 1H MAS NMR," *Microporous and Mesoporous Materials*, vol. 131, no. 1-3, pp. 210–216, Jun. 2010, ISSN: 13871811. DOI: 10.1016/j.micromeso.2009.12.025.

[107] M. Sierka and J. Sauer, "Proton mobility in chabazite, faujasite, and ZSM-5 zeolite catalysts. Comparison based on ab initio calculations," *Journal of Physical Chemistry B*, vol. 105, no. 8, pp. 1603–1613, Mar. 2001, ISSN: 10895647. DOI: 10.1021/jp004081x. [Online]. Available: https://pubs.acs.org/doi/abs/10.1021/jp004081x.

[108] F. Gao, Y. Wang, N. M. Washton, M. Kollár, J. Szanyi, and C. H. F. Peden, "Effects of Alkali and Alkaline Earth Cocations on the Activity and Hydrothermal Stability of Cu/SSZ-13 NH3–SCR Catalysts," *ACS Catalysis*, vol. 5, no. 11, pp. 6780–6791, Nov. 2015, ISSN: 2155-5435. DOI: 10.1021/acscatal.5b01621. [Online]. Available: http://pubs.acs.org/doi/10.1021/acscatal.5b01621.

[109] B. Wen, Q. Sun, and W. M. Sachtler, "Function of Pdn0 cluster, Pd2+(oxo-) ions, and PdO clusters in the catalytic reduction of NO with methane over Pd/MFI catalysts," *Journal of Catalysis*, vol. 204, no. 2, pp. 314–323, Dec. 2001, ISSN: 00219517. DOI: 10.1006/jcat.2001.3401. [Online]. Available: http://www.sciencedirect.com/science/article/pii/S0021951701934013.

[110] S. N. Gandhi, G. D. Lei, and W. M. Sachtler, "Identification of Pd3+ ions in zeolite L by temperature programmed reduction and electron paramagnetic resonance spectroscopy," *Catalysis Letters*, vol. 17, no. 1-2, pp. 117–126, Mar. 1993, ISSN: 1011372X. DOI: 10.1007/BF00763933.

[111] E. Bello, V. J. Margarit, E. M. Gallego, F. Schuetze, C. Hengst, A. Corma, and M. Moliner, "Deactivation and regeneration studies on Pd-containing medium pore zeolites as passive NOx adsorbers (PNAs) in cold-start applications," *Microporous and Mesoporous Materials*, vol. 302, p. 110 222, Apr. 2020, ISSN: 13871811. DOI: 10.1016/j.micromeso.2020.110222. [Online]. Available: https://www.sciencedirect.com/science/article/pii/S1387181120302250.

[112] J. R. Theis and J. A. Ura, "Assessment of zeolite-based Low temperature NOx adsorbers: Effect of reductants during multiple sequential cold starts," *Catalysis Today*, vol. 360, pp. 340–349, Jan. 2021, ISSN: 09205861. DOI: 10.1016/j.cattod.2020.01.040.

[113] T. M. Lardinois, J. S. Bates, H. H. Lippie, C. K. Russell, J. T. Miller, H. M. Meyer, K. A. Unocic, V. Prikhodko, X. Wei, C. K. Lambert, A. B. Getsoian, and R. Gounder, "Structural Interconversion between Agglomerated Palladium Domains and Mononuclear Pd(II) Cations in Chabazite Zeolites," *Chemistry of Materials*, Feb. 2021, ISSN: 0897-4756. DOI: 10.1021/acs.chemmater.0c04465. [Online]. Available: https://pubs.acs.org/doi/abs/10.1021/acs.chemmater.0c04465.

[114] S. Yasumura, H. Ide, T. Ueda, Y. Jing, C. Liu, K. Kon, T. Toyao, Z. Maeno, and K.-i. Shimizu, "Transformation of Bulk Pd to Pd Cations in Small-Pore CHA Zeolites Facilitated by NO," *JACS Au*, Jan. 2021, ISSN: 2691-3704. DOI: 10.1021/jacsau.0c00112. [Online]. Available: https://dx.doi.org/10.1021/jacsau.0c00112.

[115] S. Shwan, M. Skoglundh, L. F. Lundegaard, R. R. Tiruvalam, T. V. Janssens, A. Carlsson, and P. N. Vennestrøm, "Solid-State Ion-Exchange of Copper into Zeolites Facilitated by Ammonia at Low Temperature," *ACS Catalysis*, vol. 5, no. 1, pp. 16–19, Jan. 2015, ISSN: 2155-5435. DOI: 10.1021/cs5015139. [Online]. Available: http://pubs.acs.org/doi/10.1021/cs5015139.

[116] G. Kresse and J. Furthmüller, "Efficient iterative schemes for ab initio total-energy calculations using a plane-wave basis set," *Physical Review B*, vol. 54, no. 16, p. 11 186, Oct. 1996. DOI: 10.1103/PhysRevB.54.11169. [Online]. Available: https://journals.aps.org/prb/abstract/10.1103/PhysRevB.54.11169.

[117] P. E. Blöchl, "Projector augmented-wave method," *Physical Review B*, vol. 50, no. 24, p. 17 953, Dec. 1994. DOI: 10.1103/PhysRevB.50.17953. [Online]. Available: https://journals.aps.org/prb/abstract/10.1103/PhysRevB.50.17953.

[118] A. Jain, S. P. Ong, G. Hautier, W. Chen, W. D. Richards, S. Dacek, S. Cholia, D. Gunter, D. Skinner, G. Ceder, and K. A. Persson, "Commentary: The Materials Project: A materials genome approach to accelerating materials innovation," *APL Materials*, vol. 1, no. 1, p. 011 002, Jul. 2013. DOI: 10.1063/1.4812323. [Online]. Available: https://aip.scitation.org/doi/abs/10.1063/1.4812323.

[119] J. P. Perdew and Y. Wang, "Accurate and simple analytic representation of the electron-gas correlation energy," *Physical Review B*, vol. 45, no. 23, p. 13 244, Jun. 1992. DOI: 10.1103/PhysRevB.45.13244. [Online]. Available: https://journals.aps.org/prb/abstract/10.1103/PhysRevB.45.13244.

[120] S. Grimme, J. Antony, S. Ehrlich, and H. Krieg, "A consistent and accurate ab initio parametrization of density functional dispersion correction (DFT-D) for the 94 elements H-Pu," *The Journal of Chemical Physics*, vol. 132, no. 15, p. 154 104, Apr. 2010, ISSN: 0021-9606. DOI: 10.1063/1.3382344. [Online]. Available: https://aip.scitation.org/doi/abs/10.1063/1.3382344.

[121] S. Grimme, S. Ehrlich, and L. Goerigk, "Effect of the damping function in dispersion corrected density functional theory," *Journal of Computational Chemistry*, vol. 32, no. 7, pp. 1456–1465, May 2011, ISSN: 1096-987X. DOI: 10.1002/JCC.21759. [Online]. Available: https://onlinelibrary.wiley.com/doi/full/10.1002/jcc.21759%20https://onlinelibrary.wiley.com/doi/abs/10.1002/jcc.21759%20https://onlinelibrary.wiley.com/doi/10.1002/jcc.21759.

[122] J. Heyd, G. E. Scuseria, and M. Ernzerhof, "Hybrid functionals based on a screened Coulomb potential," *The Journal of Chemical Physics*, vol. 118, no. 18, p. 8207, Apr. 2003, ISSN: 0021-9606. DOI: 10.1063/1.1564060. [Online]. Available: https://aip.scitation.org/doi/abs/10.1063/1.1564060.

[123] J. Heyd and G. E. Scuseria, "Efficient hybrid density functional calculations in solids: Assessment of the Heyd–Scuseria–Ernzerhof screened Coulomb hybrid functional," *The Journal of Chemical Physics*, vol. 121, no. 3, p. 1187, Jul. 2004, ISSN: 0021-9606. DOI: 10.1063/1.1760074. [Online]. Available: https://aip.scitation.org/doi/abs/10.1063/1.1760074.

[124] J. Heyd, G. E. Scuseria, and M. Ernzerhof, "Erratum: "Hybrid functionals based on a screened Coulomb potential" [J. Chem. Phys. 118, 8207 (2003)]," *The Journal of Chemical Physics*, vol. 124, no. 21, p. 219 906, Jun. 2006, ISSN: 0021-9606. DOI: 10.1063/1.2204597. [Online]. Available: https://aip.scitation.org/doi/abs/10.1063/1.2204597.

[125] A. V. Krukau, O. A. Vydrov, A. F. Izmaylov, and G. E. Scuseria, "Influence of the exchange screening parameter on the performance of screened hybrid functionals," *The Journal of Chemical Physics*, vol. 125, no. 22, p. 224 106, Dec. 2006, ISSN: 0021-9606. DOI: 10.1063/1.2404663. [Online]. Available: https://aip.scitation.org/doi/abs/10.1063/1.2404663.

[126] S. P. Ong, W. D. Richards, A. Jain, G. Hautier, M. Kocher, S. Cholia, D. Gunter, V. L. Chevrier, K. A. Persson, and G. Ceder, "Python Materials Genomics (pymatgen): A robust, open-source python library for materials analysis," *Computational Materials Science*, vol. 68, pp. 314–319, Feb. 2013, ISSN: 0927-0256. DOI: 10.1016/J.COMMATSCI.2012.10.028.

[127] R. Tran, Z. Xu, B. Radhakrishnan, D. Winston, W. Sun, K. A. Persson, and S. P. Ong, "Surface energies of elemental crystals," *Scientific Data 2016 3:1*, vol. 3, no. 1, pp. 1–13, Sep. 2016, ISSN: 2052-4463. DOI: 10.1038/sdata.2016.80. [Online]. Available: https://www.nature.com/articles/sdata201680.

[128] W. Sun and G. Ceder, "Efficient creation and convergence of surface slabs," *Surface Science*, vol. 617, pp. 53–59, Nov. 2013, ISSN: 0039-6028. DOI: 10.1016/J.SUSC.2013.05.016.

[129] G. Wulff, "XXV. Zur Frage der Geschwindigkeit des Wachsthums und der Auflösung der Krystallflächen," *Zeitschrift für Kristallographie - Crystalline Materials*, vol. 34, no. 1-6, pp. 449–530, Dec. 1901, ISSN: 2196-7105. DOI: 10.1524/ZKRI.1901.34.1.449. [Online]. Available: https://www.degruyter.com/document/doi/10.1524/zkri.1901.34.1.449/html.

[130] P. Wynblatt and N. A. Gjostein, "Particle growth in model supported metal catalysts—I. Theory," *Acta Metallurgica*, vol. 24, no. 12, pp. 1165–1174, Dec. 1976, ISSN: 0001-6160. DOI: 10.1016/0001-6160(76)90034-1.

[131] S. C. Parker and C. T. Campbell, "Kinetic model for sintering of supported metal particles with improved size-dependent energetics and applications to Au on TiO2(110)," *Physical Review B*, vol. 75, no. 3, p. 035 430, Jan. 2007. DOI: 10.1103/PhysRevB.75.035430. [Online]. Available: https://journals.aps.org/prb/abstract/10.1103/PhysRevB.75.035430.

[132] X. Lai and D. W. Goodman, "Structure–reactivity correlations for oxide-supported metal catalysts: new perspectives from STM," *Journal of Molecular Catalysis A: Chemical*, vol. 162, no. 1-2, pp. 33–50, Nov. 2000, ISSN: 1381-1169. DOI: 10.1016/S1381-1169(00)00320-4.

[133] M. J. Jak, C. Konstapel, A. Van Kreuningen, J. Verhoeven, and J. W. Frenken, "Scanning tunnelling microscopy study of the growth of small palladium particles on TiO2 (110)," *Surface Science*, vol. 457, no. 3, pp. 295–310, Jun. 2000, ISSN: 0039-6028. DOI: 10.1016/S0039-6028(00)00431-3.

[134] R. Ouyang, J. X. Liu, and W. X. Li, "Atomistic theory of ostwald ripening and disintegration of supported metal particles under reaction conditions," *Journal of the American Chemical Society*, vol. 135, no. 5, pp. 1760–1771, 2013, ISSN: 00027863. DOI: 10.1021/ja3087054. [Online]. Available: https://pubs.acs.org/sharingguidelines.

[135] W. Sun, D. A. Kitchaev, D. Kramer, and G. Ceder, "Non-equilibrium crystallization pathways of manganese oxides in aqueous solution," *Nature Communications 2019 10:1*, vol. 10, no. 1, pp. 1–9, Feb. 2019, ISSN: 2041-1723. DOI: 10.1038/s41467-019-08494-6. [Online]. Available: https://www.nature.com/articles/s41467-019-08494-6.

[136] A. Shrestha, X. Gao, J. C. Hicks, and C. Paolucci, "Nanoparticle Size Effects on Phase Stability for Molybdenum and Tungsten Carbides," *Chemistry of Materials*, vol. 33, no. 12, pp. 4606–4620, Jun. 2021. DOI: 10.1021/ACS.CHEMMATER.1C01120. [Online]. Available: https://pubs.acs.org/doi/abs/10.1021/acs.chemmater.1c01120.

[137] A. H. Larsen, J. J. Mortensen, J. Blomqvist, I. E. Castelli, R. Christensen, M. Dułak, J. Friis, M. N. Groves, B. Hammer, C. Hargus, E. D. Hermes, P. C. Jennings, P. B. Jensen, J. Kermode, J. R. Kitchin, E. L. Kolsbjerg, J. Kubal, K. Kaasbjerg, S. Lysgaard, J. B. Maronsson, T. Maxson, T. Olsen, L. Pastewka, A. Peterson, C. Rostgaard, J. Schiøtz, O. Schütt, M. Strange, K. S. Thygesen, T. Vegge, L. Vilhelmsen, M. Walter, Z. Zeng, and K. W. Jacobsen, "The atomic simulation environment—a Python library for working with atoms," *Journal of Physics: Condensed Matter*, vol. 29, no. 27, p. 273 002, Jun. 2017, ISSN: 0953-8984. DOI: 10.1088/1361-648X/AA680E. [Online]. Available: https://iopscience.iop.org/article/10.1088/1361-648X/aa680e%20https://iopscience.iop.org/article/10.1088/1361-648X/aa680e/meta.

[138] I. V. Yudanov, M. Metzner, A. Genest, and N. Rösch, "Size-Dependence of Adsorption Properties of Metal Nanoparticles: A Density Functional Study on Palladium Nanoclusters," *Journal of Physical Chemistry C*, vol. 112, no. 51, pp. 20 269–20 275, 2008. DOI: 10.1021/JP8075673. [Online]. Available: https://pubs.acs.org/doi/full/10.1021/jp8075673.

[139] I. V. Yudanov, A. Genest, and N. Rösch, "DFT Studies of Palladium Model Catalysts: Structure and Size Effects," *Journal of Cluster Science 2011 22:3*, vol. 22, no. 3, pp. 433–448, Jun. 2011, ISSN: 1572-8862. DOI: 10.1007/S10876-011-0392-4. [Online]. Available: https://link.springer.com/article/10.1007/s10876-011-0392-4.

[140] D. González, B. Camino, J. Heras-Domingo, A. Rimola, L. Rodríguez-Santiago, X. Solans-Monfort, and M. Sodupe, "BCN-M: A Free Computational Tool for Generating Wulff-like Nanoparticle Models with Controlled Stoichiometry," *The Journal of Physical Chemistry C*, vol. 124, pp. 1227–1237, 2019. DOI: 10.1021/ACS.JPCC.9B10506. [Online]. Available: https://pubs.acs.org/doi/abs/10.1021/acs.jpcc.9b10506.

[141] D. McQuarrie and J. D. Simon, *Molecular Thermodynamics*. University Science Books, 1999, ISBN: 978-1891389054.

[142] M. J. Frisch, G. W. Trucks, H. B. Schlegel, G. E. Scuseria, M. A. Robb, J. R. Cheeseman, G. Scalmani, V. Barone, G. A. Petersson, H. Nakatsuji, X. Li, M. Caricato, A. V. Marenich, J. Bloino, B. G. Janesko, R. Gomperts, B. Mennucci, H. P. Hratchian, J. V. Ortiz, A. F. Izmaylov, J. L. Sonnenberg, D. Williams-Young, F. Ding, F. Lipparini, F. Egidi, J. Goings, B. Peng, A. Petrone, T. Henderson, D. Ranasinghe, V. G. Zakrzewski, J. Gao, N. Rega, G. Zheng, W. Liang, M. Hada, M. Ehara, K. Toyota, R. Fukuda, J. Hasegawa, M. Ishida, T. Nakajima, Y. Honda, O. Kitao, H. Nakai, T. Vreven, K. Throssell, J. Montgomery J. A., J. E. Peralta, F. Ogliaro, M. J. Bearpark, J. J. Heyd, E. N. Brothers, K. N. Kudin, V. N. Staroverov, T. A. Keith, R. Kobayashi, J. Normand, K. Raghavachari, A. P. Rendell, J. C. Burant, S. S. Iyengar, J. Tomasi, M. Cossi, J. M. Millam, M. Klene, C. Adamo, R. Cammi, J. W. Ochterski, R. L. Martin, K. Morokuma, O. Farkas, J. B. Foresman, and D. J. Fox, *Gaussian 16*, Wallingford, CT, 2016.

[143] R. A. Kendall, T. H. D. Jr., and R. J. Harrison, "Electron affinities of the first-row atoms revisited. Systematic basis sets and wave functions," *The Journal of Chemical Physics*, vol. 96, no. 9, p. 6796, Jun. 1998, ISSN: 0021-9606. DOI: 10.1063/1.462569. [Online]. Available: https://aip.scitation.org/doi/abs/10.1063/1.462569.

[144] D. E. Woon and T. H. D. Jr., "Gaussian basis sets for use in correlated molecular calculations. III. The atoms aluminum through argon," *The Journal of Chemical Physics*, vol. 98, no. 2, p. 1358, Aug. 1998, ISSN: 0021-9606. DOI: 10.1063/1.464303. [Online]. Available: https://aip.scitation.org/doi/abs/10.1063/1.464303.

[145] M. Cargnello, C. Chen, B. T. Diroll, V. V. Doan-Nguyen, R. J. Gorte, and C. B. Murray, "Efficient removal of organic ligands from supported nanocrystals by fast thermal annealing enables catalytic studies on well-defined active phases," *Journal of the American Chemical Society*, vol. 137, no. 21, pp. 6906–6911, Jun. 2015, ISSN: 15205126. DOI: 10.1021/jacs.5b03333. [Online]. Available: https://pubs.acs.org/doi/abs/10.1021/jacs.5b03333.

[146] J. D. Albarracin-Caballero, I. Khurana, J. R. Di Iorio, A. J. Shih, J. E. Schmidt, M. Dusselier, M. E. Davis, A. Yezerets, J. T. Miller, F. H. Ribeiro, R. Gounder, A. Godiksen, S. Mossin, P. Beato, M. W. Anderson, O. Terasaki, and B. M. Weckhuysen, "Structural and kinetic changes to small-pore Cu-zeolites after hydrothermal aging treatments and selective catalytic reduction of NO _x with ammonia," *React. Chem. Eng.*, vol. 2, no. 2, pp. 168–179, 2017, ISSN: 2058-9883. DOI: 10.1039/C6RE00198J. [Online]. Available: http://xlink.rsc.org/?DOI=C6RE00198J.

[147] B. J. Adelman and W. M. Sachtler, "The effect of zeolitic protons on NO(x) reduction over Pd/ZSM-5 catalysts," *Applied Catalysis B: Environmental*, vol. 14, no. 1-2, pp. 1–11, Dec. 1997, ISSN: 09263373. DOI: 10.1016/S0926-3373(97)00007-6.

[148] Q. Zhao, H. Li, X. Zhang, S. Yu, S. Wang, and G. Sun, "Platinum in-situ catalytic oleylamine combustion removal process for carbon supported platinum nanoparticles," *Journal of Energy Chemistry*, vol. 41, pp. 120–125, Feb. 2020, ISSN: 20954956. DOI: 10.1016/j.jechem.2019.05.006.

[149] H. Aljama, M. Head-Gordon, A. Bell, and A. T. Bell, "Assessing the stability of Pd-exchanged sites in zeolites with the aid of a high throughput quantum chemistry workkow Assessing the stability of Pd-exchanged sites in zeolites with the aid of a high throughput quantum chemistry workflow," May 2021. DOI: 10.21203/rs.3.rs-396201/v1. [Online]. Available: https://doi.org/10.21203/rs.3.rs-396201/v1.

[150] M. Che, J. F. Dutel, P. Gallezot, and M. Primet, "A study of the chemisorption of nitric oxide on PdY zeolite. Evidence for a room temperature oxidative dissolution of Pd crystallites," *Journal of Physical Chemistry*, vol. 80, no. 21, pp. 2371–2381, Oct. 1976, ISSN: 00223654. DOI: 10.1021/j100562a011. [Online]. Available: http://pubs.acs.org/doi/abs/10.1021/j100562a011.

[151] J. E. Saal, S. Kirklin, M. Aykol, B. Meredig, and C. Wolverton, "Materials design and discovery with high-throughput density functional theory: The open quantum materials database (OQMD)," *JOM*, vol. 65, no. 11, pp. 1501–1509, Nov. 2013, ISSN: 10474838. DOI: 10.1007/s11837-013-0755-4. [Online]. Available: http://oqmd.org,.

[152] S. Kirklin, J. E. Saal, B. Meredig, A. Thompson, J. W. Doak, M. Aykol, S. Rühl, and C. Wolverton, "The Open Quantum Materials Database (OQMD): Assessing the accuracy of DFT formation energies," *npj Computational Materials*, vol. 1, no. 1, pp. 1–15, Dec. 2015, ISSN: 20573960. DOI: 10.1038/npjcompumats.2015.10. [Online]. Available: www.oqmd.org/download..

[153] A. Toso, S. Colussi, J. Llorca, and A. Trovarelli, "The dynamics of PdO-Pd phase transformation in the presence of water over Si-doped Pd/CeO2 methane oxidation catalysts," *Applied Catalysis A: General*, vol. 574, pp. 79–86, Mar. 2019, ISSN: 0926860X. DOI: 10.1016/j.apcata.2019.01.023. [Online]. Available: https://doi.org/10.1016/j.apcata.2019.01.023.

[154] W. R. Schwartz, D. Ciuparu, and L. D. Pfefferle, "Combustion of methane over palladium-based catalysts: Catalytic deactivation and role of the support," *Journal of Physical Chemistry C*, vol. 116, no. 15, pp. 8587–8593, 2012, ISSN: 19327447. DOI: 10.1021/jp212236e. [Online]. Available: https://pubs.acs.org/sharingguidelines.

[155] X. Li, X. Wang, K. Roy, J. A. Van Bokhoven, and L. Artiglia, "Role of Water on the Structure of Palladium for Complete Oxidation of Methane," *ACS Catalysis*, vol. 10, no. 10, pp. 5783–5792, 2020, ISSN: 21555435. DOI: 10.1021/acscatal.0c01069. [Online]. Available: https://dx.doi.org/10.1021/acscatal.0c01069.

[156] S. R. Challa, A. T. Delariva, T. W. Hansen, S. Helveg, J. Sehested, P. L. Hansen, F. Garzon, and A. K. Datye, "Relating Rates of Catalyst Sintering to the Disappearance of Individual Nanoparticles during Ostwald Ripening," *J. Am. Chem. Soc*, vol. 133, pp. 20 672–20 675, 2011. DOI: 10.1021/ja208324n. [Online]. Available: https://pubs.acs.org/sharingguidelines.

[157] S. B. Kang, J. B. Lim, D. Jo, I. S. Nam, B. K. Cho, S. B. Hong, C. H. Kim, and S. H. Oh, "Ostwald-ripening sintering kinetics of Pd-based three-way catalyst: Importance of initial particle size of Pd," *Chemical Engineering Journal*, vol. 316, pp. 631–644, May 2017, ISSN: 13858947. DOI: 10.1016/j.cej.2017.01.136.

[158] P. Wynblatt and N. A. Gjostein, *Supported metal crystallites*, Jan. 1975. DOI: 10.1016/0079-6786(75)90013-8.

[159] G. S. Bugosh and M. P. Harold, "Impact of Zeolite Beta on Hydrocarbon Trapping and Light-Off Behavior on Pt/Pd/BEA/Al2O3 Monolith Catalysts," *Emission Control Science and Technology*, vol. 3, no. 2, pp. 123–134, Jun. 2017, ISSN: 21993637. DOI: 10.1007/s40825-017-0061-7. [Online]. Available: https://link.springer.com/article/10.1007/s40825-017-0061-7.

[160] P. G. Blakeman, E. M. Burkholder, H.-Y. Chen, J. E. Collier, J. M. Fedeyko, H. Jobson, and R. R. Rajaram, "The role of pore size on the thermal stability of zeolite supported Cu SCR catalysts," *Catalysis Today*, vol. 231, pp. 56–63, 2014, ISSN: 09205861. DOI: 10.1016/j.cattod.2013.10.047. [Online]. Available: http://www.sciencedirect.com/science/article/pii/S0920586113005221.

[161] J. C. Vega-Vila, J. W. Harris, and R. Gounder, "Controlled insertion of tin atoms into zeolite framework vacancies and consequences for glucose isomerization catalysis," *Journal of Catalysis*, vol. 344, pp. 108–120, Dec. 2016, ISSN: 10902694. DOI: 10.1016/j.jcat.2016.09.011.

[162] J. W. Harris, M. J. Cordon, J. R. Di Iorio, J. C. Vega-Vila, F. H. Ribeiro, and R. Gounder, "Titration and quantification of open and closed Lewis acid sites in Sn-Beta zeolites that catalyze glucose isomerization," *Journal of Catalysis*, vol. 335, pp. 141–154, Mar. 2016, ISSN: 0021-9517. DOI: 10.1016/J.JCAT.2015.12.024. [Online]. Available: https://www.sciencedirect.com/science/article/pii/S0021951715004170.

[163] A. Corma, L. T. Nemeth, M. Renz, and S. Valencia, "Sn-zeolite beta as a heterogeneous chemoselective catalyst for Baeyer-Villiger oxidations," *Nature*, vol. 412, no. 6845, pp. 423–425, Jul. 2001, ISSN: 00280836. DOI: 10.1038/35086546. [Online]. Available: www.nature.com.

[164] A. Corma and S. Valencia, "Stannosilicate Molecular Sieves," *US Patent*, no. 19, pp. 1–5, Dec. 1999. [Online]. Available: https://patents.google.com/patent/US5968473A/en.

[165] C. C. Chang, Z. Wang, P. Dornath, H. Je Cho, and W. Fan, "Rapid synthesis of Sn-Beta for the isomerization of cellulosic sugars," *RSC Advances*, vol. 2, no. 28, pp. 10 475–10 477, Nov. 2012, ISSN: 20462069. DOI: 10.1039/c2ra21381h. [Online]. Available: https://pubs.rsc.org/en/content/articlehtml/2012/ra/c2ra21381h%20https://pubs.rsc.org/en/content/articlelanding/2012/ra/c2ra21381h.

[166] H. Koller, R. F. Lobo, S. L. Burkett, and M. E. Davis, "SiO-...HOSi hydrogen bonds in As-synthesized high-silica zeolites," *Journal of physical chemistry*, vol. 99, no. 33, pp. 12 588–12 596, 1995, ISSN: 00223654. DOI: 10.1021/j100033a036. [Online]. Available: https://pubs.acs.org/doi/abs/10.1021/j100033a036.

[167] J. L. Guth, H. Kessler, J. M. Higel, J. M. Lamblin, J. Patarin, A. Seive, J. M. Chezeau, and R. Wey, "Zeolite Synthesis in the Presence of Fluoride Ions," in, Jul. 1989, pp. 176–195. DOI: 10.1021/bk-1989-0398.ch013. [Online]. Available: https://pubs.acs.org/doi/abs/10.1021/bk-1989-0398.ch013.

[168] R. Gounder and M. E. Davis, "Beyond shape selective catalysis with zeolites: Hydrophobic void spaces in zeolites enable catalysis in liquid water," *AIChE Journal*, vol. 59, no. 9, pp. 3349–3358, Sep. 2013, ISSN: 00011541. DOI: 10.1002/aic.14016. [Online]. Available: https://aiche.onlinelibrary.wiley.com/doi/full/10.1002/aic.14016%20https://aiche.onlinelibrary.wiley.com/doi/abs/10.1002/aic.14016%20https://aiche.onlinelibrary.wiley.com/doi/10.1002/aic.14016.

[169] M. J. Cordon, J. W. Harris, J. C. Vega-Vila, J. S. Bates, S. Kaur, M. Gupta, M. E. Witzke, E. C. Wegener, J. T. Miller, D. W. Flaherty, D. D. Hibbitts, and R. Gounder, "Dominant Role of Entropy in Stabilizing Sugar Isomerization Transition States within Hydrophobic Zeolite Pores," *Journal of the American Chemical Society*, 2018, ISSN: 15205126. DOI: 10.1021/jacs.8b08336. [Online]. Available: https://pubs.acs.org/sharingguidelines.

[170] J. Song, Y. Wang, E. D. Walter, N. M. Washton, D. Mei, L. Kovarik, M. H. Engelhard, S. Prodinger, Y. Wang, C. H. F. Peden, and F. Gao, "Toward Rational Design of Cu/SSZ-13 Selective Catalytic Reduction Catalysts: Implications from Atomic-Level Understanding of Hydrothermal Stability," *ACS Catalysis*, vol. 7, no. 12, pp. 8214–8227, Dec. 2017, ISSN: 2155-5435. DOI: 10.1021/acscatal.7b03020. [Online]. Available: http://pubs.acs.org/doi/10.1021/acscatal.7b03020.

[171] C. Paolucci, I. Khurana, A. A. Parekh, S. Li, A. J. Shih, H. Li, J. R. Di Iorio, J. D. Albarracin-Caballero, A. Yezerets, J. T. Miller, W. N. Delgass, F. H. Ribeiro, W. F. Schneider, and R. Gounder, "Dynamic multinuclear sites formed by mobilized copper ions in NOx selective catalytic reduction," *Science*, vol. 357, no. 6354, pp. 898–903, Sep. 2017, ISSN: 10959203. DOI: 10.1126/science.aan5630. [Online]. Available: http://science.sciencemag.org/.

[172] L. Ma, Y. Cheng, G. Cavataio, R. W. McCabe, L. Fu, and J. Li, "Characterization of commercial Cu-SSZ-13 and Cu-SAPO-34 catalysts with hydrothermal treatment for NH3-SCR of NOx in diesel exhaust," *Chemical Engineering Journal*, vol. 225, pp. 323–330, Jun. 2013, ISSN: 1385-8947. DOI: 10.1016/J.CEJ.2013.03.078. [Online]. Available: https://www.sciencedirect.com/science/article/pii/S1385894713004038.

[173] C.-Y. Hu, K. Shih, and J. O. Leckie, "Formation of copper aluminate spinel and cuprous aluminate delafossite to thermally stabilize simulated copper-laden sludge," *Journal of Hazardous Materials*, vol. 181, no. 1-3, pp. 399–404, Sep. 2010, ISSN: 0304-3894. DOI: 10.1016/J.JHAZMAT.2010.05.024. [Online]. Available: https://www.sciencedirect.com/science/article/pii/S0304389410006072.

[174] M.-F. Luo, P. Fang, M. He, and Y.-L. Xie, "In situ XRD, Raman, and TPR studies of CuO/Al 2 O 3 catalysts for CO oxidation," *Journal of Molecular Catalysis A: Chemical*, vol. 239, pp. 243–248, 2005. DOI: 10.1016/j.molcata.2005.06.029. [Online]. Available: https://ac.els-cdn.com/S1381116905004164/1-s2.0-S1381116905004164-main.pdf?_tid=777c3308-dcb5-4ee9-88f6-09e5f372cd99&acdnat=1545342419_dfb45c6297508b2790cd3abc1740d7c2.

[175] M. Kumar, H. Luo, Y. Románroмán-Leshkov, and J. D. Rimer, "SSZ-13 Crystallization by Particle Attachment and Deterministic Pathways to Crystal Size Control," *J. Am. Chem. Soc*, vol. 137, pp. 13 007–13 017, 2015. DOI: 10.1021/jacs.5b07477. [Online]. Available: https://pubs.acs.org/sharingguidelines.

[176] Z. Li, M. T. Navarro, J. Martínez-Triguero, J. Yu, and A. Corma, "Synthesis of nano-SSZ-13 and its application in the reaction of methanol to olefins," *Catalysis Science and Technology*, vol. 6, no. 15, pp. 5856–5863, Jul. 2016, ISSN: 20444761. DOI: 10.1039/c6cy00433d. [Online]. Available: www.rsc.org/catalysis.

A. SYNTHESIS OF ENCAPSULATED PD SPECIES IN CHA ZEOLITES

One goal of the Pd-zeolite project was to study how the distribution of Pd species (PdO, ion-exchanged Pd^{2+}) was influenced by the method of introducing Pd onto the zeolite support. We investigated commonly used aqueous-phase methods, but also attempted direct Pd encapsulation methods, colloquially termed 'one-pot' syntheses. Similar to the direct synthesis of ion-exchanged Cu-CHA using tetraethylpentamine (TEPA)-solvated Cu^{2+} ions, it was hypothesized that Pd^{2+} solvated by NH_3 or TEPA could serve as a structure directing agent (SDA) along with trimethyladamantylammonium hydroxide (TMAdaOH) to crystallize the CHA topology and also result in the siting of two proximal framework Al to charge-compensate the Pd^{2+} center. Experiments were performed to determine how the Pd precursor and Pd, Na, and H_2O contents influence CHA crystallization and the amounts of ion-exchanged Pd^{2+} formed All synthesis experiments were performed at 433 K with molar synthesis gel ratios of Si/Al = 15 and (Na+SDA)/Si = 0.5, where the SDAs were $TMAda^+$, $[Pd(NH_3)_4]^{2+}$, and $[Pd\text{-}TEPA]^{2+}$. The TEPA precursor was a TEPA·5 HCl solid. Tables A.1 and A.2 contain the synthetic mixtures used, and Figures A.1 and A.2 contain the X-ray diffraction (XRD) patterns to assess crystallinity and zeolite topology.

Table A.1. Synthesis mixtures using Pd-TEPA as the precursor to directly synthesize Pd-CHA. Syntheses A-C used 5 wt % Pd-TEPA with Pd:TEPA= 1 and syntheses D and E used 4.67 wt % Pd-TEPA with Pd:TEPA = 0.47. Typical total mixture masses were 5-15 grams.

Sample	Na:SDA	SDA:Si	Pd-TEPA:SDA	Pd-TEPA:Si	H_2O:Si	TMAda:Si
A	1	0.25	0.050	0.013	20	0.24
B	1	0.25	0.025	0.006	20	0.24
C	1	0.25	0.050	0.013	40	0.24
D	1	0.25	0.025	0.006	20	0.24
E	0	0.50	0.025	0.013	20	0.49

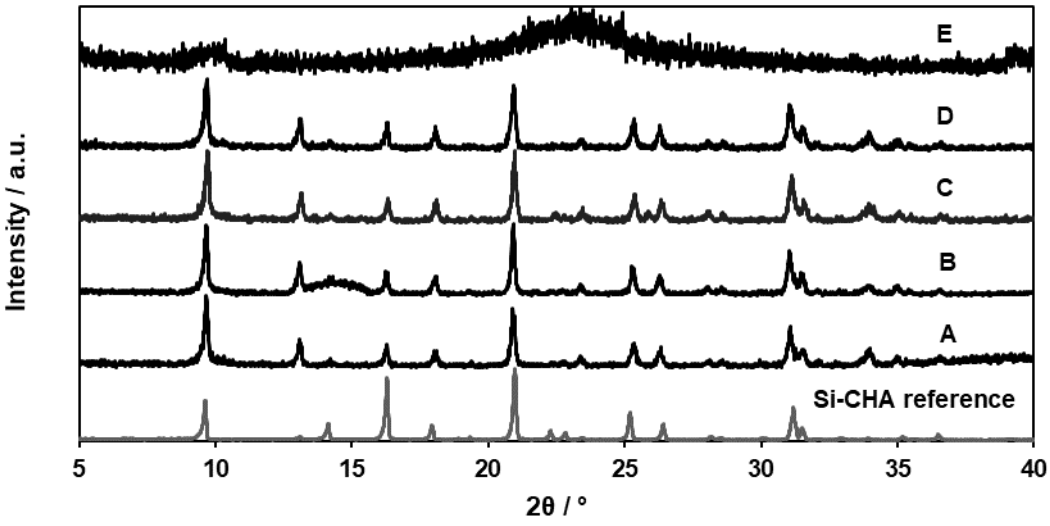

Figure A.1. XRD patterns of zeolites synthesized with Pd-TEPA after treatment in flowing air to 853 K and cooling to ambient. Bottom XRD pattern is for a reference Si-CHA material. Samples A, B, C, D, E refer to the samples in Table A.1.

Table A.2. Synthesis mixtures with 10 wt% $(NH_3)_4Pd(NO_3)_2$ as the precursor to directly synthesize Pd-CHA. Typical total mixture masses were 5–15 grams.

Sample	Na:SDA	SDA:Si	Pd:SDA	Pd:Si	H_2O:Si	TMAda:Si
A	0	0.50	0.050	0.025	20	0.48
B	0	0.50	0.025	0.013	20	0.49
C	0	0.50	0.050	0.025	40	0.48
D	1	0.25	0.050	0.013	20	0.24
E	1	0.25	0.050	0.013	40	0.24

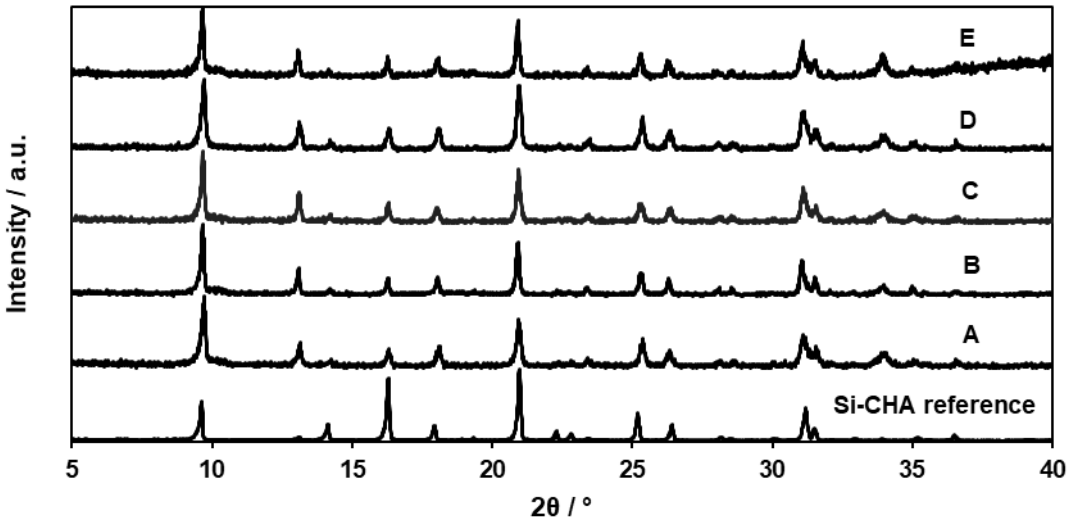

Figure A.2. XRD patterns of zeolites synthesized with $(NH_3)_4Pd(NO_3)_2$ after treatment in flowing air to 853 K. Bottom XRD pattern is for a reference Si-CHA material. Samples A, B, C, D, E refer to the samples in Table A.2.

The Pd content was characterized for samples that contained the CHA topology. Additionally, Pd-zeolites were equilibrated with a 1 M NH_4NO_3 solution for 24 hours at 353 K (300 mL g^{-1}) to estimate the ion-exchanged Pd^{2+} content, which occurred before the findings in Chapter 2 that showed Pd back-exchanged with NH_4^+ is diffusion limited and not an equilibrated procedure. The Pd content in the supernatant was quantified as the amount of ion-exchanged Pd^{2+} that were removed upon NH_4^+ exchange.

Table A.3. Characterization of Pd-CHA zeolites synthesized with Pd-TEPA from Table A.1. Ion-exchanged Pd^{2+} was quantified with NH_4^+ back-exchange experiments.

Sample	Pd wt %	Ion-exchanged Pd^{2+} / Pd_{tot}
A	0.10	0.12
B	0.15	0.24
C	0.12	0.19
D	0.07	0.18
E	--	--

Table A.4. Characterization of Pd-CHA zeolites synthesized with 10 wt % $(NH_3)_4Pd(NO_3)_2$ from Table A.2. Ion-exchanged Pd was quantified with NH_4^+ back-exchange experiments

Sample	Pd wt %	Ion-exchanged Pd^{2+} / Pd_{tot}
A	0.32	0.26
B	0.22	0.05
C	0.42	0.06
D	0.25	0.23
E	0.38	0.03

Given the fraction of ion-exchanged Pd^{2+} was always less than 0.3 and the samples were visibly black (indicating Pd agglomeration occurred), the incomplete encapsulation of both Pd-amine SDAs (Pd-TEPA or $Pd(NH_3)_4$) was further investigated. Solution phase ultraviolet-visible (UV-Vis) spectroscopy was performed on the Pd-amine synthesis mixtures to elucidate the ligand environment around Pd (Figure A.3).

Both the Pd-TEPA and $Pd(NH_3)_4(NO_3)_2$ solutions contained an absorption peak centered around 300 nm, which can be attributed to the d-d transition of Pd-amine complexes.

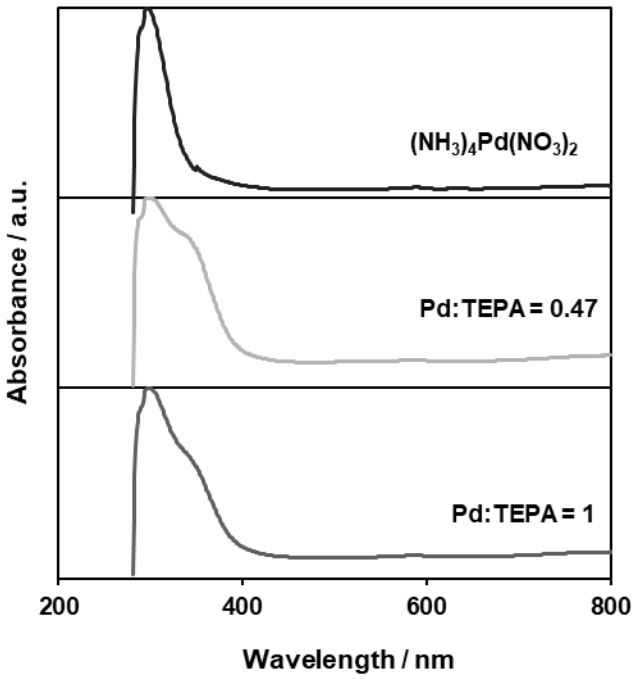

Figure A.3. Transmission UV-Vis spectra of Pd-containing solutions used for syntheses collected under ambient conditions.

Since TEPA is stabilized in an HCl matrix, the absorption feature at 350 nm is assigned to Pd-chloro complexes. Although these absorption bands were not quantified, the identified Pd-chloro complexation ($[PdCl_x(NR_2)_{4-x}]^{2-x}$, where R is a continuation of the TEPA chain) is undesirable because these species will not direct two negative framework Al sites. Therefore, strategies to synthesize predominately Pd-TEPA complexes were further investigated.

The TEPA·5 HCl solid was dissolved in water, and the undesirable Cl^- anions were precipitated out with a stoichiometric amount of $AgNO_3$ as AgCl. The solution was centrifuged, and the resultant TEPA solution was decanted. Subsequently, $Pd(NO_3)_2$ was dissolved in the TEPA solution. The resultant Pd-TEPA mixture was mixed with other zeolite synthesis components, and the UV-Vis spectra were collected in Figure A.4.

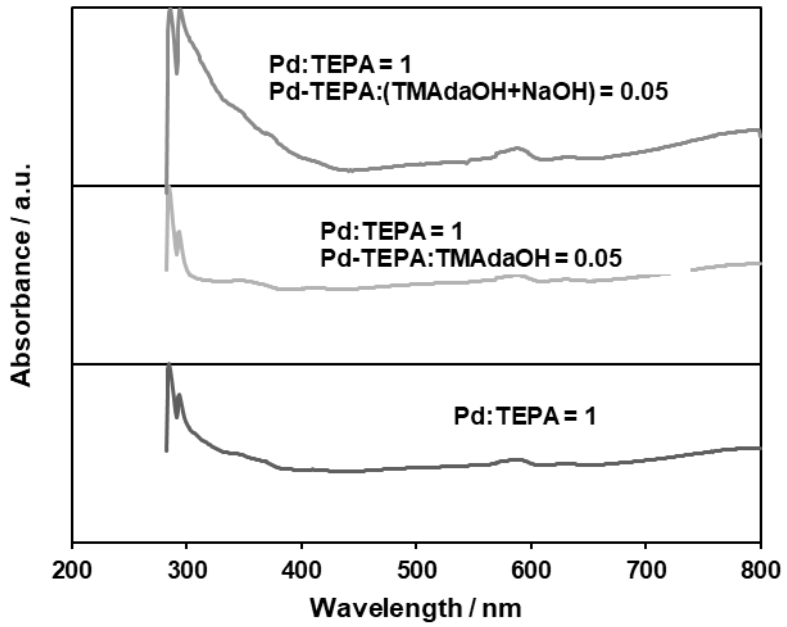

Figure A.4. Transmission UV-Vis spectra of Pd-TEPA solutions used for syntheses collected under ambient conditions after removal of Cl^- species with $Ag(NO_3)$.

All of the Pd-TEPA solutions contained peaks centered around 300 nm, which can be attributed to the d-d transition of a Pd-amine complex. None of the solutions contained an observable absorption feature near 350 nm for Pd-chloro complexes, indicating that Cl^- was successfully removed from the solution in the form of AgCl. Additionally, introduction of other synthetic ingredients, such as TMAdaOH and NaOH, did not influence the amine-ligand environment around Pd. However, crystallization of Pd-CHA with these Pd precursors also resulted in low fractions of ion-exchanged Pd^{2+} (per total Pd) of less than 0.2, indicating that amine-solvated Pd complexes were not stable under hydrothermal (433 K) synthesis conditions. This was corroborated by experiments where the Pd-ammine synthesis mixtures were heated without silica to 373 K, in which Pd precipitation from solution was observed, demonstrating that both NH_3 and TEPA cannot stabilize Pd^{2+} cations under hydrothermal conditions as required for the crystallization of CHA. Moving forward, direct Pd encapsulation in zeolites will not be a viable strategy for synthesizing Pd-zeolites with a high fraction of ion-exchanged Pd. Instead, incipient wetness impregnation or aqueous

ion-exchange will be used for future Pd depositions because ion-exchanged Pd^{2+} fractions greater than 0.5 can be achieved for both BEA and CHA (Si/Al = 12) zeolites after air treatments to 873 K.

B. HYDROTHERMAL DEACTIVATION OF MONONUCLEAR CU STRUCTURES TO AGGLOMERATED PHASES IN CHA ZEOLITES FOR NH_3 SELECTIVE CATALYTIC REDUCTION OF NITROGEN OXIDES

A series of CHA zeolites was synthesized at a fixed Al density (Si/Al = 15) with systematic variations in Al arrangement (6-MR paired Al measured by Co^{2+} titration [20]) to vary the Cu speciation (Z_2Cu or ZCuOH) at a fixed Cu density, in order to study the propensity of each Cu ion site to undergo deactivation under hydrothermal conditions. Samples were subject to aqueous ion-exchange to achieve ca. 2 wt% Cu, and the amount of each Cu site was estimated with NH_3 TPD and summarized in Table B.1. Samples will be labeled Cu(XX)-Z, where XX is the percentage of ion-exchanged Cu^{2+} sites in the Z_2Cu configuration.

Table B.1. A summary of Cu deposition procedures and estimation of Z2Cu and ZCuOH structures.

Sample name	Ex-change time	Molarity of $Cu(NO_3)_2$	pH control with dropwise 0.1 M NH_4OH	Cu wt %	Z_2Cu / Cu_{tot}	Si / Al (±1)
Cu(85)-Z	Stable pH	0.15	4	1.9	0.85	12
Cu(29)-Z	4 hours	0.2	No	2.0	0.29	14
Cu(17)-Z	0.5 hours	0.005	No	1.9	0.17	14

Cu-CHA zeolites that were hydrothermally aged (1023 K, 10 kPa H_2O in balance air, 16 h) will be labeled Cu(XX)-Z-HTA. Standard SCR rates (normalized per Cu), apparent activation energies (E_a), and reaction orders were measured on the fresh and hydrothermally aged Cu-CHA zeolite samples (Table B.2) to determine if the decrease in SCR rate was related to changes in the speciation of Cu (Figure B.1).

All fresh samples showed similar SCR rates (7.9 ± 0.7 mol NO mmol Cu^{-1} s^{-1}), apparent activation energies (61 ± 6 kJ mol^{-1}), and apparent kinetic orders for each reactant (±0.1), demonstrating that all SCR rates on fresh catalysts were measured in a similar kinetic regime and can be considered catalytically equivalent, consistent with prior reports that

Table B.2. SCR rates, apparent activation energies, reactant orders, and extraframework Al (Al_{ex}, quantified with ^{27}Al MAS NMR) for three Cu-CHA zeolites with fixed Al density and Cu density but varying Cu speciation, before and after HTA.

Kinetic Measurement	Cu(85)-Z	Cu(85)-Z-HTA	Cu(29)-Z	Cu(29)-Z-HTA	Cu(17)-Z	Cu(17)-Z-HTA
Rate (mol NO s^{-1} g^{-1})	2.41E-06	1.06E-06	2.56E-06	1.99E-06	2.59E-06	1.68E-06
Rate (mol NO s^{-1} mol Cu^{-1})	0.008	0.0035	0.0072	0.0057	0.0085	0.0055
Eapp (kJ mol^{-1})	56	43	61	56	67	59
NO order	0.6	0.6	0.73	0.8	0.7	n.m.
O_2 order	0.4	0.4	0.3	0.3	0.4	n.m.
NH_3 order	-0.1	0	-0.33	-0.1	-0.3	n.m.
Al_{ex} / Al_{tot}	0.12	n.m.	0	n.m.	0.13	n.m.

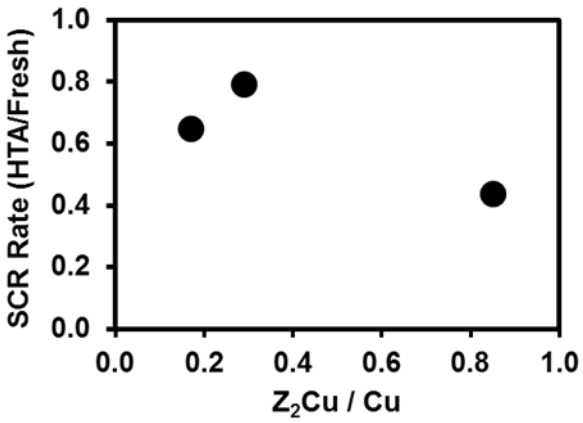

Figure B.1. The relative decrease in SCR rate of fresh and HTA Cu-CHA zeolite samples as a function of Cu speciation.

low-temperature SCR rates are independent of Cu speciation because NH_3 solvation creates similar Cu-amine complexes *in situ* [23]. The results in Figure B.1 show that Cu-CHA zeolite samples at a fixed Al and Cu density, but varied distributions of Cu ion sites, deactivate to different extents under hydrothermal aging conditions. This result suggests that samples with a higher fraction of ZCuOH sites may be less likely to hydrothermally deactivate than Z_2Cu sites, contradicting previously published reports [170]. However, the E_a value for Cu(85)-Z-HTA was 43 kJ mol^{-1}, which is outside of error of the other measured E_a value (60 kJ mol^{-1}) for fresh and HTA Cu-zeolites. The lower E_a value for the Cu(85)-Z-HTA sample indicates this catalyst may be operating in a different kinetic regime, and thus comparison to other fresh and HTA catalysts is not straightforward. Additionally, Paolucci et al. [171] reported on the non-mean field kinetic phenomena that arises when Cu densities fall below a critical threshold at a given Al density, because the oxidation half-cycle that forms binuclear $[Cu\text{-}O_2\text{-}Cu]^{2+}$ intermediates, and this results in a positive order in O_2; thus, normalization of rates by the number of Cu is also insufficient for direct kinetic comparison. Additionally, the three zeolite supports used in this study were synthesized using different recipes, which may influence their structural changes upon hydrothermal aging. Thus, instead of direct comparison via SCR kinetics, fresh and HTA samples were characterized were used to better

understand the parameters that accelerate HTA and agglomeration of Cu sites to an inactive phase.

NO and NH_3 solid-state exchange experiments were adapted from prior literature [115] and performed on intrapellet mixtures of H-CHA (Si/Al = 15) with either CuO or $CuAl_2O_4$ (2 wt% Cu) to study the how each agglomerated Cu domain may interconvert to form Cu ion sites on the zeolite support under HTA conditions (Figure B.2).

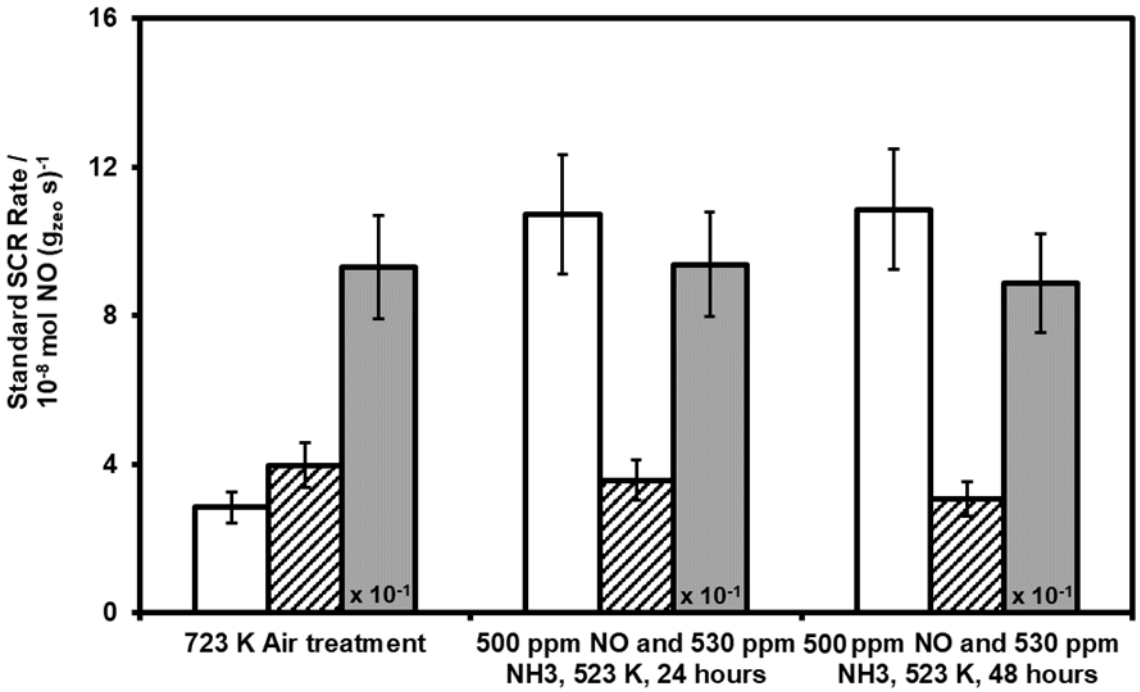

Figure B.2. The SCR rate normalized to mass of catalyst measured after sequential treatments at 723 K in air then 500 ppm NO and 530 ppm NH3 at 523 K for 24 and 48 hours. White bars are for CuO and H-CHA zeolite (Si/Al = 15) mixture. Striped bars are for CuAl2O4 and H-CHA zeolite mixture. Gray bars are for Cu(85)-Z-HTA. The rates plotted for the HTA sample were divided by a factor of 10 for graphical comparison.

Samples were first pretreated in flowing air to 723 K (5 K min^{-1}), then cooled to 473 K to measure standard SCR rates. Next, samples were heated to 523 K (5 K min^{-1}) and held in 500 ppm NO and 530 ppm NH_3 in balance N_2 for 24 hours, then the samples were cooled back down to 473 K to measure SCR rates. Finally, samples were heated back up to 523 K (5 K min^{-1}) under the same NO and NH_3 treatment, but held for 48 hours, before cooling to

473 K to measuring the SCR rate a final time. The CuO/H-CHA mixture had an increase in the SCR rate (per Cu) after treatment in NO and NH_3, consistent with literature proposals that CuO can migrate under these conditions to form SCR active sites (i.e., ion-exchanged Cu^{2+}) on the zeolite support [115]. The $CuAl_2O_4$ and H-CHA zeolite mixture was not able to transform to SCR active sites after any NO and NH_3 treatment, and likewise, the Cu(85)-Z-HTA sample did not generate more SCR active sites. These results suggest that CuO can reversibly transform into Cu ion sites under NH_3 and NO environments at 523 K, but that $CuAl_2O_4$ cannot. These results do not clearly demonstrate the nature of the inactive Cu species present in Cu(85)-Z-HTA. It is estimated that approximately 4% of Cu in the CuO / H-CHA mixture transformed into SCR active sites. If 4% of the inactive Cu formed on the Cu(85)Z-HTA sample were able to transform into SCR active sites, then this would have been within the error of the SCR rate measurement. Additionally, the amount of interfacial Cu relative to the total Cu available to reduce in NO and NH_3 will be different for intrapellet mixtures than for particles formed inside or on the surface of CHA crystallites from HTA [172]. Another factor to consider is the rate of transport at CuO and H-CHA interfaces (i.e., intercrystalline transport) relative to intracrystalline Cu transport, both of which are not well understood. Lastly, smaller CuO clusters stabilized inside the zeolite micropores might have different reduction potentials than bulk CuO due to constrained environments or stabilization through van der Waals interactions, influencing the barrier for NO and NH_3 reduction.

Hu et al. [173] synthesized $CuAl_2O_4$ by heating a physical mixture of CuO and Al_2O_3 to 1023 K in dry flowing air, evidenced by decreases in the XRD peak intensities assigned to CuO and increases those for $CuAl_2O_4$. Additionally, CuO supported on Al_2O_3 was found to form $CuAl_2O_4$ when treated to 973 K in flowing air [174]. The reproduction of the Hu et al. report (Figure B.3) suggests that $CuAl_2O_4$ formation is possible under HTA conditions. HTA of zeolites is known to generate extraframework Al (Al_{ex}) species, which could react with Cu species (e.g., ZCuOH, Z_2Cu, CuO) to form $CuAl_2O_4$. Therefore, Figure B.4 plots the relative SCR rate before and after HTA as a function of Al_{ex} measured by ^{27}Al MAS NMR to determine if Al_{ex} may accelerated HTA deactivation.

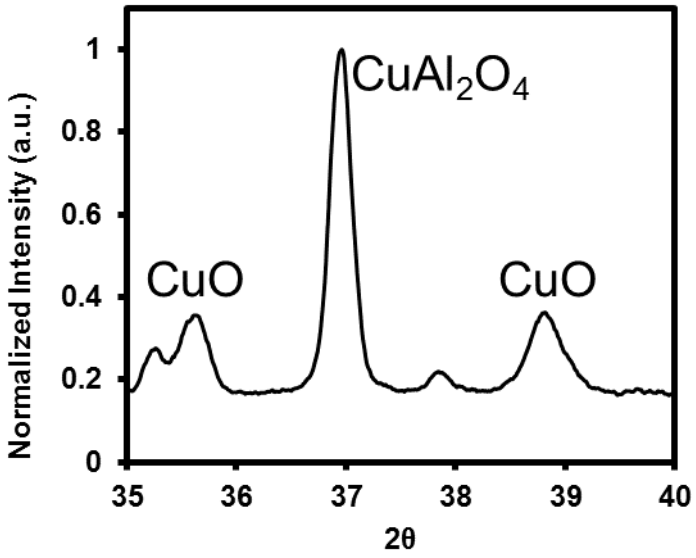

Figure B.3. Ex-situ XRD (Cu Kα) pattern of an intimate mixture of γ-Al2O3 and CuO after treatment in air to 1023 K for 24 h.

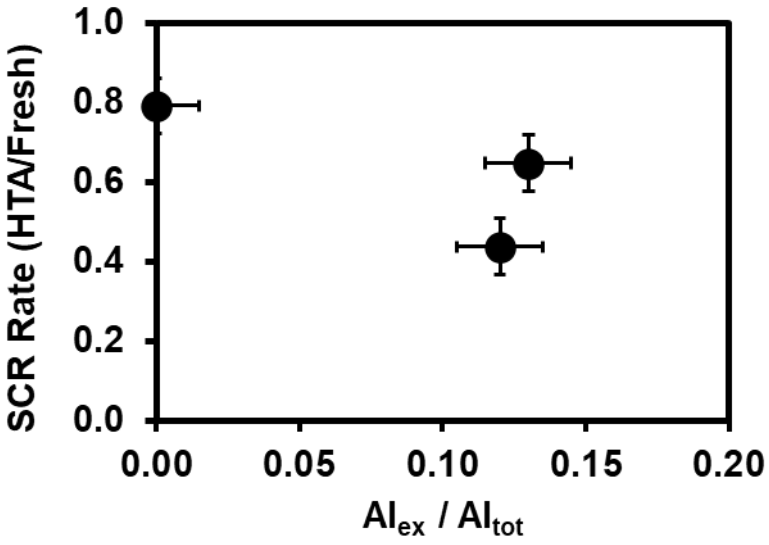

Figure B.4. The relative SCR rate of fresh and HTA Cu-CHA catalysts plotted as a function of the initial fraction of Al that is extraframework. The relative SCR rate was calculated by dividing the HTA SCR rate by the fresh SCR rate. Al_{ex} was quantified with ^{27}Al MAS NMR on the hydrated, parent H-form zeolite before Cu exchange.

From Figure B.4, it is hypothesized that Cu-zeolites with a higher initial fraction of Al_{ex} are less hydrothermally stable, evidenced by a greater extent of SCR deactivation, because Al_{ex} sites serve as thermodynamically favorable sites to react with Cu to form $CuAl_2O_4$. However, there is a dearth of unambiguous characterization of CuO and $CuAl_2O_4$ in the literature, likely because these particles are small (< 3 nm), and XRD patterns of HTA Cu-CHA zeolites show no diffraction peaks for CuO or $CuAl_2O_4$. In attempt to form XRD-observable Cu particles, the less hydrothermally stable framework of zeolite Beta (Si/Al = 11) was exchanged with $Cu(NO_3)_2$ and treated using an HTA protocol for 48 hours at 1223 K (Figure B.5), yet, the resultant XRD pattern still lacked diffraction peaks assignable to CuO and $CuAl_2O_4$.

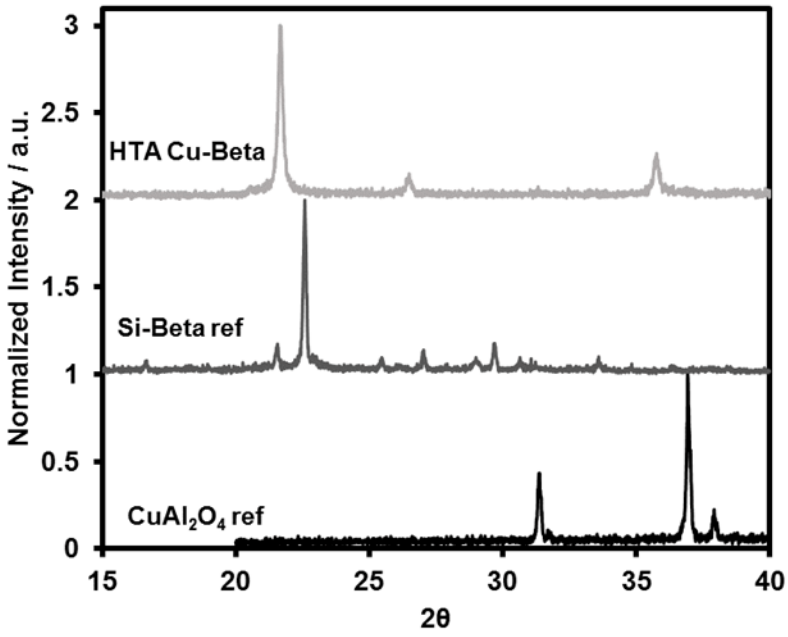

Figure B.5. Ex-situ XRD (Cu Kα) pattern of $CuAl_2O_4$ (bottom), Siliceous Beta (middle), and HTA (1223 K, 48 hours) Cu-Beta.

C. NO AND CO ADSORPTION SPECTROSCOPY OF Pd-ZEOLITES: DIFFUSE REFLECTANCE ULTRAVIOLET-VISIBLE AND PD L_3-EDGE X-RAY ABSORPTION

Diffuse Reflectance Ultraviolet-Visible (DRUV-Vis) spectroscopy was used to study the Pd speciation and coordination environment *in situ* under NO and CO-containing streams. A series of model Pd samples were prepared with varied fractions of ion-exchanged Pd^{2+} and PdO (the fraction of ion-exchanged Pd^{2+} per total Pd listed in parenthesis after sample name), and DRUV-Vis spectra were collected *in situ* after dehydration (Figure C.1).

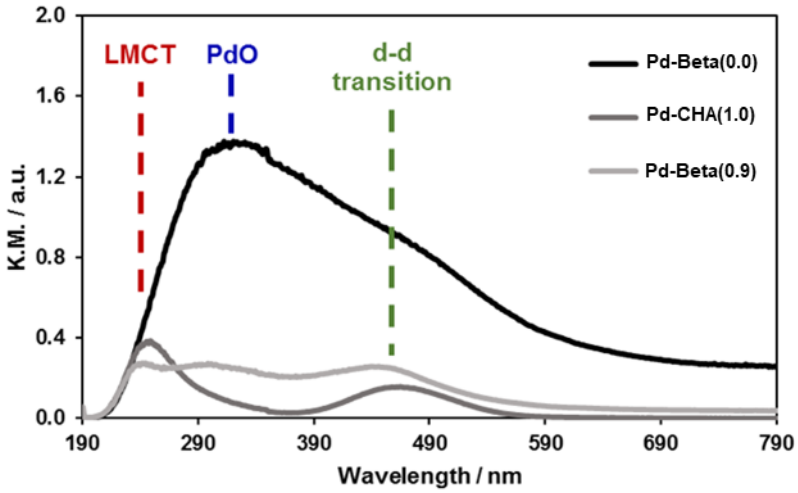

Figure C.1. DRUV-Vis spectra of Pd-zeolites dehydrated in flowing (50 cm^3 min^{-1}) air at 723 K for 30 minutes. Spectra were collected at 290 K. The characterized fractions of ion-exchanged Pd^{2+} to total Pd are in parentheses in legend. Ligand to metal charge transfer (LMCT, red) bands are assigned to absorptions around 250 nm, PdO particles show absorption features around 320 nm (blue), and d-d transitions are around 440 nm (green).

The Pd-CHA(1.0) sample with predominantly ion-exchanged Pd^{2+} showed two absorption features: LMCT (250 nm) and d-d transitions (440 nm). The Pd-Beta(0.0) sample (PdO deposited on purely siliceous Beta) contained a single, intense absorption feature at 320 nm for PdO particles, with a barely visible d-d transition shoulder. The small percentage

(<10%) of PdO in the Pd-Beta(0.9) sample resulted in the appearance of a PdO absorption feature, demonstrating the sensitivity of DRUV-Vis to detect agglomerated PdO particles.

NO adsorption was studied on a H-CHA (Si/Al = 6) to identify any non-Pd related UV-Vis absorption from NO adsorption occurs. A single UV-Vis absorption feature for a non-Pd NO binding site was centered at 280 nm in Figure C.2. Treating the NO-adsorbed H-form zeolite in flowing air to higher temperatures attenuated the absorption feature near 280 nm, suggesting NO was desorbing from the zeolite. Treatment in flowing air to 573 K was unable to regenerate the spectrum of the dehydrated sample, suggesting NO was still adsorbed on non-Pd sites.

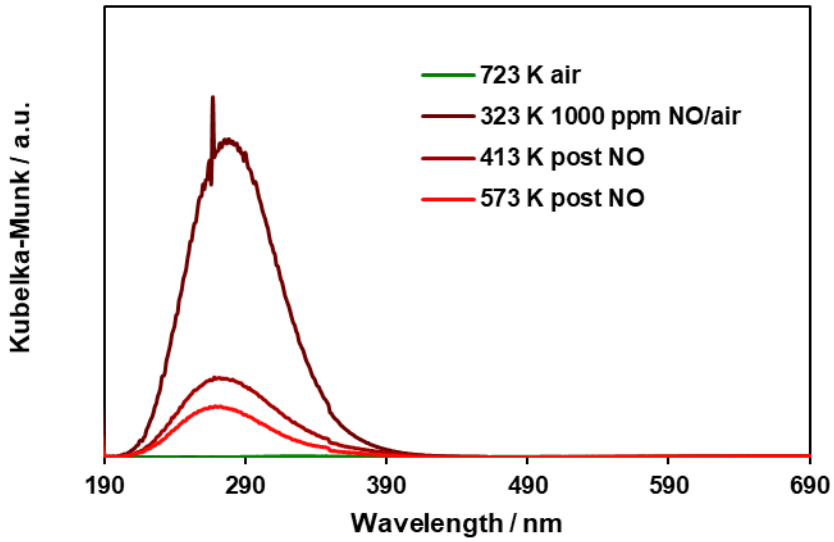

Figure C.2. DRUV-Vis spectra of H-CHA (Si/Al = 6) treated in flowing (50 cm^3 min^{-1}) air to 723 K, then exposed to 1000 ppm NO in balance air at 348 K. Once the spectra stabilized indicating the sample has equilibrated, NO flow was cut off and the sample was treated to higher temperatures in air. Spectra for samples treated to temperatures above 473 K were collected after cooling to 293 K.

An analogous NO adsorption/desorption experiment was performed with Pd-CHA(1.0) (Figure C.3). Flowing NO in air resulted in significant spectral changes. The absence of absorption between 390-590 nm for the H-form sample (Figure C.2) allows for unambiguous detection and characterization of NO adsorption on Pd sites. From Figure C.3, NO exposure induces a broadening of the d-d transition, with a peak maximum shift from 470 nm to 450

nm. After treatment in flowing air to 413 K, the d-d peak maximum shifted closer to 470 nm, but still showed some breadth. After 573 K in flowing air, the spectrum collected of Pd-CHA(1.0) after NO exposure was similar to the spectrum of the dehydrated sample, suggesting all Pd-bound NO desorbed by this temperature.

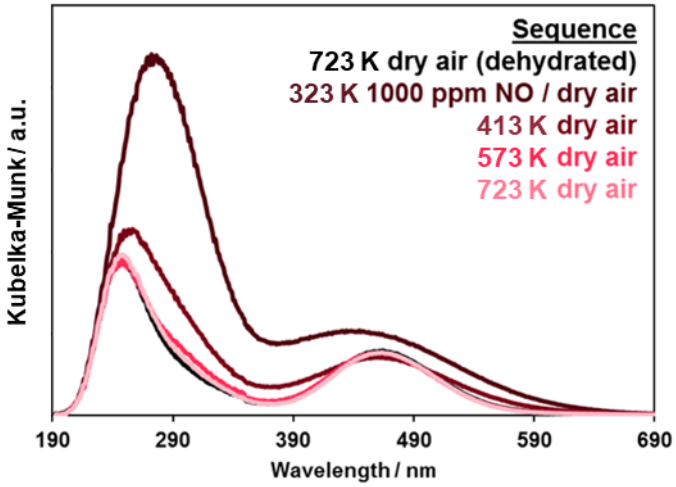

Figure C.3. DRUV-Vis spectra of Pd-CHA(1.0) treated in flowing (50 cm^3 min^{-1}) air to 723 K, then exposed to 1000 ppm NO in balance air at 323 K. Once the spectra stropped changing, NO flow was cut off and the sample was ramped to higher temperatures. Spectra for samples treated to temperatures above 473 K were collected after cooling to 293 K.

CO and NO co-adsorption has been reported to increase the temperature at which NO desorbs, which has been proposed to be due to the formation of a CO/NO co-adsorbed complex on exchanged, mononuclear Pd [30]. A DRUV-Vis experiment was performed (Figure C.4) following similar procedures. Flowing 2000 ppm CO in balance air over the sample resulted in three absorption features: LMCT (295 nm), d-d transition (420 nm), and an unknown feature (550 nm). CO caused the LMCT peak maximum to shift to higher wavelengths (250 to 295 nm) and the d-d transition maximum to shift to lower wavelengths (470 to 420 nm). When NO was introduced to the CO-containing stream, the unknown 550 nm feature disappeared and the resulting spectrum was similar to the NO-only spectrum, suggesting that NO outcompetes CO for adsorption sites or NO/CO co-adsorbed complexes give rise to similar DRUV-Vis spectra as NO adsorbed complexes. After treating the post

CO and NO co-adsorption experiment in flowing air to 723 K, the original spectrum of the dehydrated sample was fully recovered.

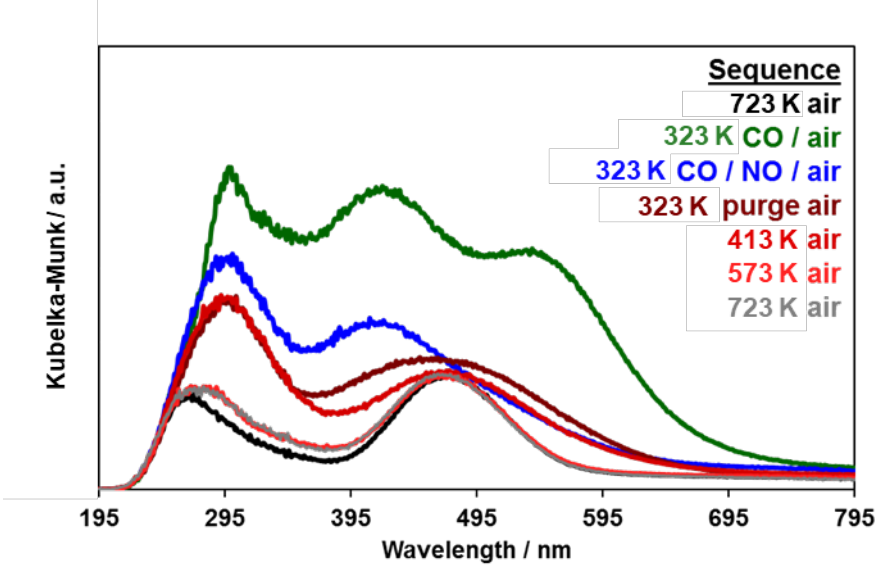

Figure C.4. DRUV-Vis spectra of Pd-CHA(1.0) previously treated in flowing air to 923 K. The sample was first dehydrated at 723 K in flowing air (50 cm^3 min^{-1}) then exposed to 2000 ppm CO in balance air at 323 K. Once the spectra stropped changing, 1000 ppm NO flow was added. The sample was then purged in dry air at 323 K, then ramped to higher temperatures. Spectra for samples treated to temperatures above 473 K were collected after cooling to 293 K.

Autoreduction of Pd has been proposed in literature to occur in inert environments (Figure C.5), as reported for other metal-exchanged zeolites [43]. Under He flow, some autoreduction was observed, evidenced by the increase in total absorbance. Introducing approximately 3 kPa of water into the inert stream at 723 K appeared to increase the extent of autoreduction, evidenced by a sample that visually appeared darker black after the experiment. Overall, the pretreatment conditions of Pd-zeolites influence the form of Pd: treating in dry air ($>$ 573 K) results in a distribution of ion-exchanged Pd and PdO particles, treating in hydrogen ($>$ 473 K) converts all Pd to metallic particles, and treating in wet inert (He) at 723 K reduces Pd^{2+} to metallic Pd particles.

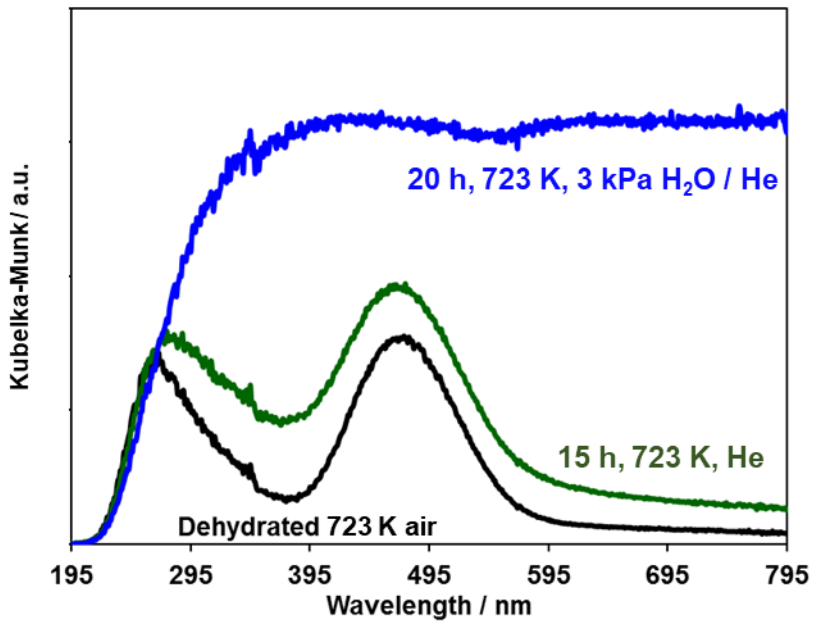

Figure C.5. DRUV-Vis spectra of Pd-CHA(1.0) previously treated in flowing air to 923 K. The sample was first dehydrated at 723 K in flowing air (50 cm^3 min^{-1}, black) and treated in flowing UHP He (50 cm^3 min^{-1}) for 15 hours at 723 K. The sample was cooled down under He flow and scanned at 290 K (green). The flowing He stream was then sent though a water bubbler, resulting in ~3 kPa H_2O / He stream. The sample was ramped to 723 K and held in flowing, wet He for 20 hours. The sample was then cooled to 290 K and scanned (blue).

Fluorescence Pd L_3-edge XANES was also used to study the Pd species in CHA zeolites under conditions relevant for passive NO_x adsorption. First, a series of Pd standards of different oxidation states and ligand environments were characterized. From Figure C.6, it was observed that a derivative of the L_3-edge XANES spectra can discriminate between different oxidation states of Pd complexes. The edge energies for metallic Pd^0, Pd^{2+}, and Pd^{4+} are approximately 3172.8, 3174, and 3176 eV, respectively. Additionally for the Pd^{2+} standards, the ligands and coordination environment around Pd appear to significantly change the white line intensity, yet only slightly (+/- 0.2 eV) change the edge energy.

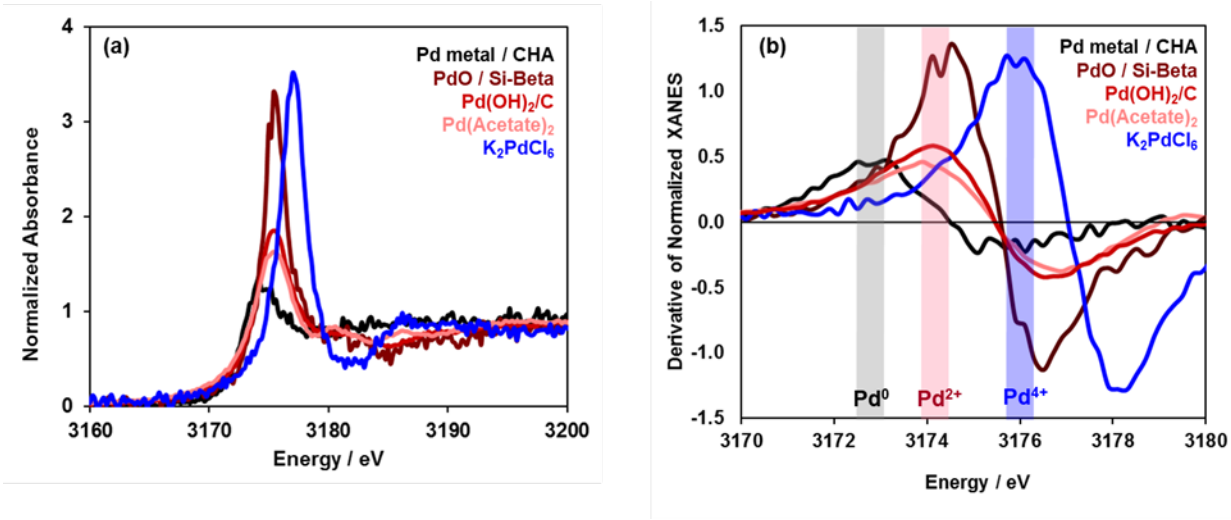

Figure C.6. (a) Series of Pd standards characterized with Pd L_3-edge XANES. 4 scans were averaged. Pd metal / CHA (black) was prepared by reducing a 1.2 wt% Pd-CHA zeolite in 5 kPa H_2 at 473 K, PdO / Si-Beta (dark red) was prepared by depositing $Pd(NH_3)_4(NO_3)_2$ on purely siliceous beta zeolite and treating in flowing air to 823 K, $Pd(OH)_2$ (red) was scanned as-loaded, $Pd(Acetate)_2$ (light pink) was scanned as-loaded, and K_2PdCl_6 (blue) was scanned as-loaded. (b) The derivative of (a) was plotted to clearly identify edge energies of the different Pd standards. The black spectrum is a Pd^0 reference (3172.8 eV), red spectra are Pd^{2+} references (3174 eV), and blue is a Pd^{4+} reference (3176 eV). Shaded regions are peak maximums (edge energies) for the labeled Pd oxidation sate standard.

A Pd-CHA (Si/Al = 4.5, 1.2 wt% Pd) sample was synthesized with predominantly (>95%) ion-exchanged Pd^{2+} and characterized with L_3-edge XANES after dehydration and re-hydration (Figure C.7). Regardless if Pd^{2+} was dehydrated and ligated to four zeolite

oxygen atoms or hydrated and ligated to four water molecules, the edge energy was approximately 3174 eV, aligned with the Pd divalent standards. There was a slight difference in edge energy between a dehydrated (3174 eV) and hydrated Pd^{2+} cation (3174.3 eV), but the difference is not significant enough to conclude that reduction occurred. This slight difference in edge energy is most likely due to a change in ligand environments from oxygen atoms in water those in zeolite lattices, as observed for the divalent Pd standards in Figure C.6 that varied in edge energy from 3173.9 to 3174.3 eV. Lastly, there was no systematic trend in white line intensity as a function of temperature for dehydrated Pd^{2+} cations in Figure C.7. Therefore, changes in white line intensity for in-situ NO adsorption/desorption studies can be attributed to changes in ligand environment and not thermal effects or changes in oxidation state.

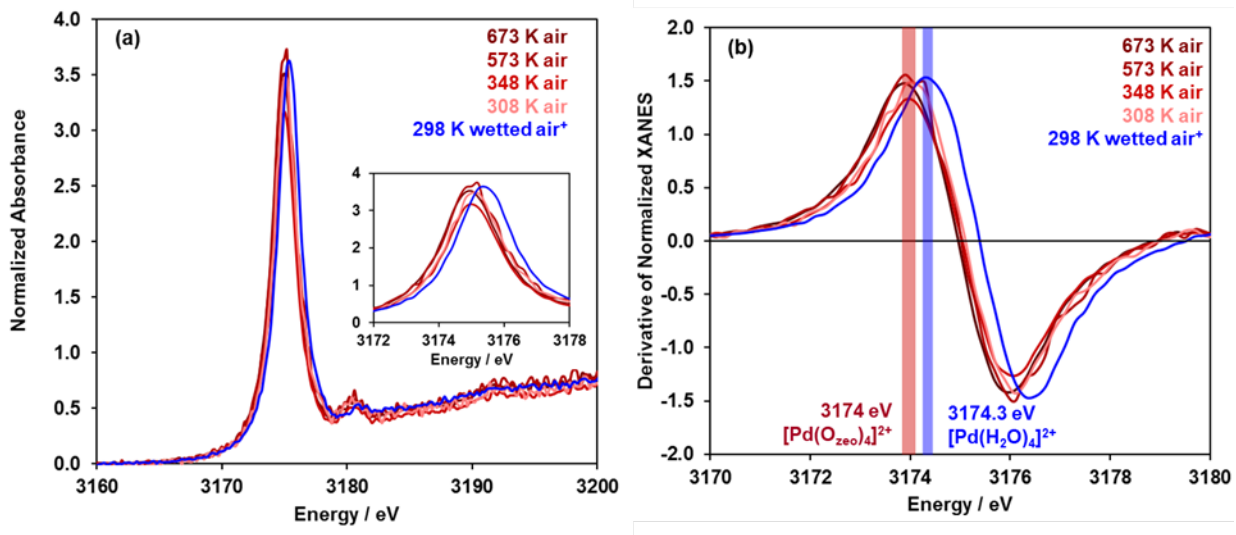

Figure C.7. (a) Pd L_3-XANES spectra of dehydrated Pd-CHA (Si/Al = 4.5, 1.2 wt% Pd, predominantly ion-exchanged Pd^{2+}) (reds) at various temperatures (308 673 K) and rehydrated in wetted (1–3 kPa H_2O) air at 298 K (blue). Inset is for clarity when comparing white line intensity. (b) The derivative of (a) to clearly identify edge energies. Shaded regions on right are to show edge energy for a zeolite ligated (red) or water ligated (blue) ion-exchanged Pd^{2+} cation.

To further investigate NO adsorption/desorption on Pd-zeolites, the same Pd-CHA sample (Si/Al = 4.5, 1.2 wt% Pd) was treated *in-situ* while collecting L_3-edge XANES in Figure C.8. After dehydrating the sample (673 K, air), NO exposure caused a significant decrease

in the white line intensity (Figure C.8), suggesting NO has ligated to Pd^{2+} cations. From Figure C.8, the change in white line intensity did not change the edge energy of the Pd-zeolite sample, suggesting there was no change in oxidation state upon adsorption of NO. Treatment of the sample after NO adsorption to 413 K in air resulted in similar spectra measured before NO exposure, demonstrating the majority of all Pd^{2+}-ligated NO has desorbed. This observation is consistent with the in-situ DRUV-Vis studies that showed NO bound to Pd^{2+} mostly desorbed after treating in flowing air to 140 °C.

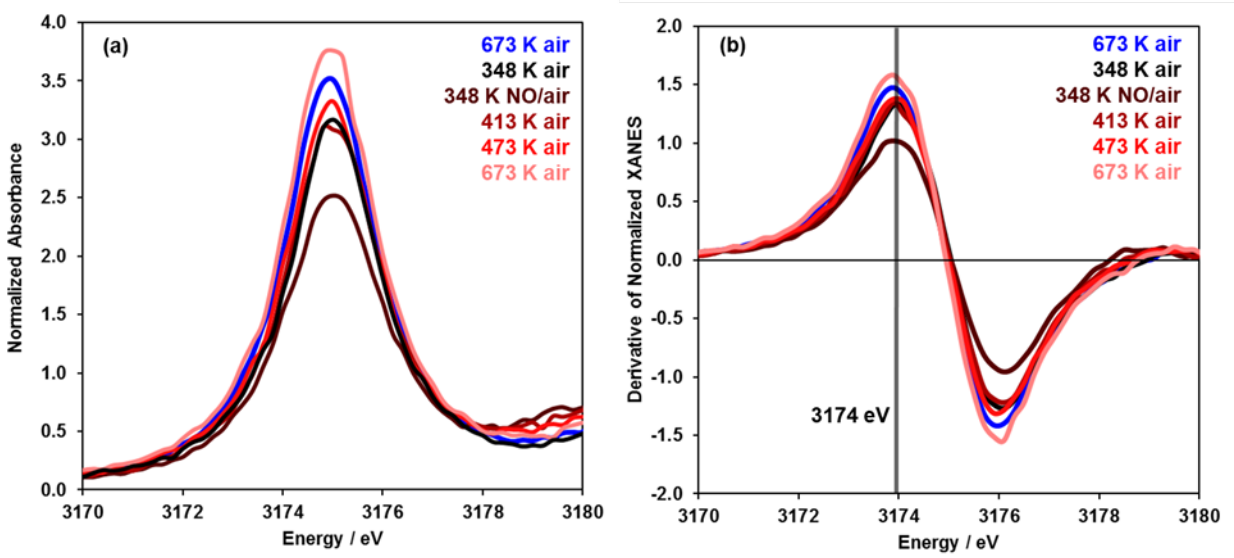

Figure C.8. (a) Pd L_3-edge XANES of a Pd-CHA (Si/Al = 4.5, 1.2 wt% Pd, predominantly ion-exchanged Pd^{2+}) material dehydrated in flowing air to 673 K (blue), then cooled to 348 K in flowing air (black), treated in flowing 500 ppm NO in balance air air at 348 K (dark red), then treated in flowing air to 413 K (red), 473 K (light red), and 673 K (pink). Air refers to 5 kPa O_2 in balance He. (b) The derivative of (a) to better show edge energies.

Similarly, the Pd-CHA sample was tested for NO adsorption/desorption in a wet stream (1–3 kPa H_2O) (Figure C.9). Results were similar to the dry case, in that exposure to wet NO caused a decrease in white line intensity and no shift in edge energy. However, after treating the material in flowing wet air to 473 K, the sample was never restored to a predominantly water-solvated Pd^{2+} cation. Unlike the dry NO storage case, wet NO storage appears to have formed some surface intermediate on Pd that cannot desorb by 473 K.

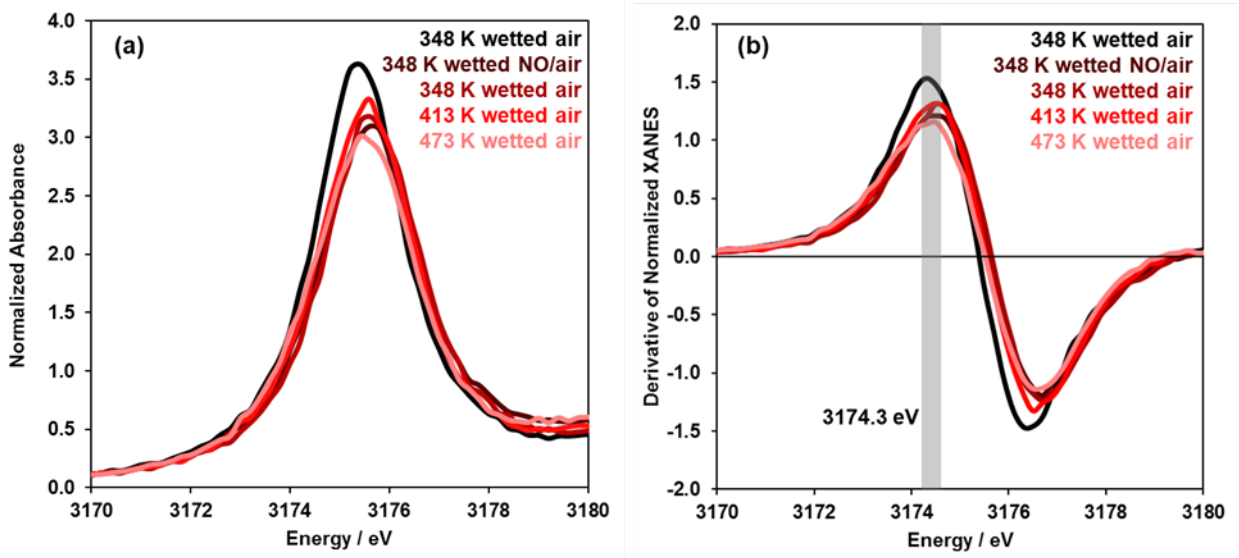

Figure C.9. (a) Pd L_3-edge XANES of a Pd-CHA (Si/Al = 4.5, 1.2 wt% Pd, predominantly ion-exchanged Pd^{2+}) material dehydrated in flowing air to 673 K, then cooled to 348 K in flowing air then rehydrated in wet (1–3 kPa H_2O) air (black), treated in flowing 500 ppm NO / wetted (1–3 kPa H_2O) air at 348 K (dark red), purged flowing wetted (1–3 kPa H_2O) air at 348 K (red), then treated to 413 K (light red) and 473 K (pink) in wetted (1–3 kPa H_2O) air. Air means 5 kPa O_2 in balance He. (b) The derivative of (a) to better show edge energies.

D. Δ-EXAFS: NON-DESTRUCTIVE QUANTIFICATIONS OF METAL STRUCTURES IN ZEOLITES

H_2 temperature programed reduction characterization of Pd-exchanged zeolites is currently the most accurate method to simultaneously quantify the number of mononuclear, ion-exchanged Pd^{2+} cations and agglomerated PdO domains. However, this technique converts all divalent Pd species into metallic Pd nanoparticles at the end of the measurement, effectively changing Pd structures and spatial distributions. In-situ X-ray absorption spectroscopy (XAS) has been used to qualitatively assess the amount of ion-exchanged Pd^{2+} without irreversibly changing the structure ofo the sample by comparing the magnitudes of second-shell scattering features in k^n-weighted (n = 2, 3) Fourier transform extended X-ray absorption fine structure (EXAFS) spetra of hydrated Pd-exchanged zeolites. Hydrated, ion-exchanged Pd^{2+} cations, such as $[Pd(OH_2)_4]^{2+}$ or $[Pd(OH)(OH_2)_3]^{+}$, do not show features for second-shell scattering with zeolite T-atoms (Si, Al) because they are coordinated to water and hydroxide ligands that contain H atoms in the second-shell that only weakly scatter X-rays; in contrast, PdO particles will show clear Pd-Pd second-shell scattering features. Hydrated samples with lower EXAFS second-shell magnitudes were proposed to contain more ion-exchanged Pd^{2+}, but this approach is non-quantitative and does not account for the effects of PdO particle size on second-shell scatter.

Here, we attempted a quantitative approach using a Δ-EXAFS method to quantify the difference in second-shell scatter between dehydrated and hydrated samples, which should apply to any Pd-exchanged zeolite of an arbitrary Pd speciation between ion-exchanged Pd^{2+} and PdO particles of sufficiently large size so as not to undergo significant changes in bulk structure in the presence of water. The differences in second-shell scatter between a hydrated ($[Pd(OH_2)_4]^{2+}$, $[Pd(OH)(OH_2)_3]^{+}$) and dehydrated ($[Pd(O_{zeo})_4]^{2+}$, $[Pd(OH)(O_{zeo})_3]^{+}$) complexes arise from differences in the scattering coefficients between hydrogen and framework silicon or aluminum atoms, respectively. Subtraction of the hydrated k^2-weigthed Fourier transform magnitude EXAFS spectrum from the dehydrated spectrum results in a Δ-EXAFS spectrum, wherein the second-shell scatter area was assumed to be proportional the fraction of ion-exchanged Pd^{2+} (Figure D.1). Assuming the PdO particles do not change size

or structure under water-containing conditions (1–2 kPa H_2O in balance air, ambient temperature), the Δ-EXAFS spectra will cancel any second-shell scattering contributions from PdO domains, and the residual second-shell area in a Δ-EXAFS spectrum should thus be proportional to the fraction of ion-exchanged Pd^{2+} species.

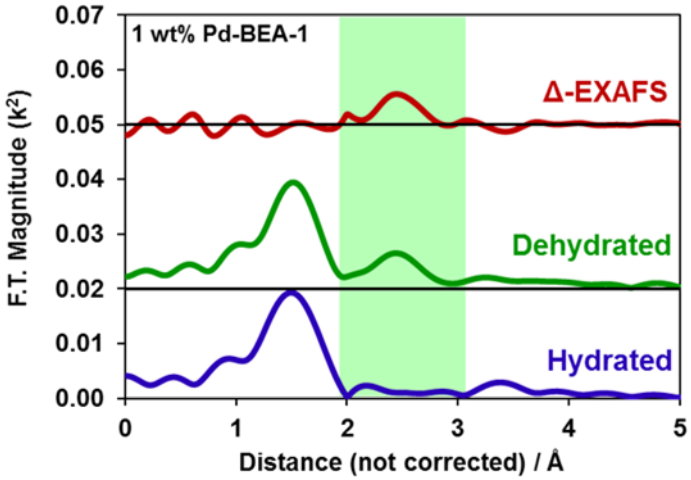

Figure D.1. A hydrated, dehydrated (773 K, air, 0.5 h, offset +0.02 units), and Δ-EXAFS (offset + 0.05 units) spectra of a predominantly mononuclear Pd^{2+} Beta material.

A series of Pd-exchanged CHA zeolites with varied Pd content (0.5 3.0 wt%) and framework Al densities (Si/Al = 4.5–∞) were characterized with this Δ-EXAFS method and H_2 TPR after treatment in flowing air to 1023 K for 0.5 h. The amount of ion-exchanged Pd^{2+} characterized with H_2 TPR is plotted as a function of the Δ-EXAFS second-shell area in Figure 2, and a positive (but non-linear) correlation was observed. For large PdO particles (particle sizes were not characterized, but their presence was assumed from large Pd-Pd second-shell scatter) supported on purely siliceous CHA frameworks, the Δ-EXAFS second-shell area was approximately zero, but samples containing smaller PdO particles (<5 nm) resulted in a negative Δ-EXAFS area. The negative Δ-EXAFS area could result from restructuring of small PdO nanoparticles in the presence of water. Another assumption that may not hold is that the integrated second-shell area is proportional the ion-exchanged Pd^{2+} content. Determining if this were true would require a rigorous understanding of the mathematical transformation of raw XAS spectrum to the Fourier transform magnitude k^2-

weighted space. Lastly, another potential contribution to the scatter in the data (Figure 2) could be from imperfect treatment with beamline equipment. For future experiments, it is recommended to pretreat materials in the same furnace (not at the photon source) in flowing air above 800 K, and then characterize the material with H_2 TPR and Δ-EXAFS with a dehydration treatment below 800 K.

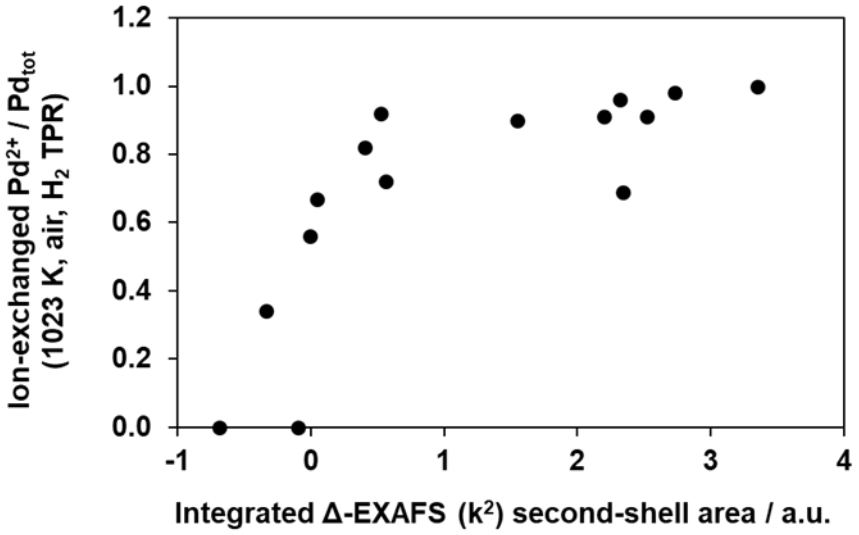

Figure D.2. A comparison of the integrated Δ-EXAFS (k^2-weighted) second-shell area to the amount of ion-exchanged Pd^{2+} (per total Pd) after treatment in flowing air to 1023 K for 0.5 h.

E. INFLUENCE OF ZEOLITE CRYSTALLITE SIZE ON THE REDISPERSION OF METALLIC PD NANOPARTICLES TO PD(II) SITES

Chapters 2 and 3 showed that the average particle size and spatial distribution of Pd influences the extent of redispersion of agglomerated Pd domains to mononuclear Pd^{2+} ion sites under high-temperature (>723 K) air treatments. The influence of Pd spatial distribution, in turn, suggests that the extent of redispersion should also depend on zeolite crystallite size, variations in which would change the average distance between Pd species and framework Al trapping sites (i.e., Brønsted acid sites). Varying the zeolite crystallite size, at constant Pd particle size, would also provide an avenue to probe non-mean field effects of Ostwald ripening proposed in the literature [45]. Here, a series of Pd-CHA zeolites was synthesized with varying crystallite size, but with constant Al and Pd densities, to study the influence of average crystallite size on the formation of mononuclear Pd^{2+} ion sites.

Following literature reported methods, three CHA zeolites were synthesized using various zeolite growth modifiers to yield materials of different average crystallite size (Figure E.1, Table E.1) [175], [176].

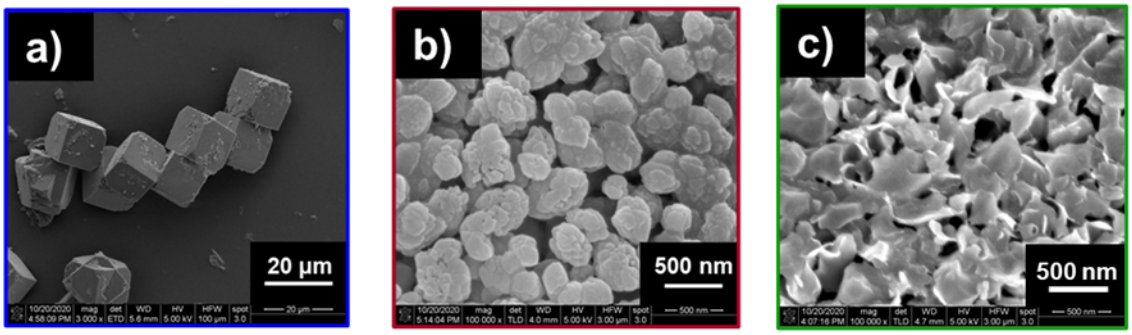

Figure E.1. Ex-situ scanning electron microscopy images of three CHA materials of different crystallite size: (a) 10 μm, (b) 500 nm, and (c) nanosheets (<10 nm). Table E.1 summarizes the material compositions.

Pd was deposited via incipient wetness impregnation using a $Pd(NH_3)_4(NO_3)_2$ precursor. The materials were left under ambient conditions overnight to dry, then characterized with H_2 temperature programmed reduction (TPR) experiments, where the samples were reversibly

Table E.1. A summary of the compositional space of CHA materials of varying average crystallite size. Co^{2+} titration values (normalized to total Al) were used to estimate the number of Al pairs in the 6-membered ring of CHA [22].

Estimated crystallite size via SEM	Si/Al	Co/Al	Pd_{tot}/Al (IWI balance)	Pd wt% (IWI balance)
10 μm	24	0.014	0.24	1.7
500 nm	22	0.006	0.24	1.8
nanosheets (<10 nm)	24	n.m.	0.29	2.1

cycled between H_2 TPR characterization (573 K, 5 kPa H_2) and progressively increasing air treatment temperatures (700–1000 K, increasing in 100 K increments). The resultant H_2 TPR profiles are in Figure E.2, and quantification of PdO and Pd^{2+} ion sites are plotted in Figure E.3.

The 10 μm and 500 nm crystallites showed increasing amounts of mononuclear Pd^{2+} formed with increasing temperature, consistent with previous literature observations that higher air temperature treatments result in greater amounts of mononuclear Pd^{2+} content. The nanosheet crystallites had similar amounts (within error) of mononuclear Pd^{2+} for all temperatures tested, which was contrary to initial expectations. It was initially hypothesized that decreasing the average crystallite size would minimize the average distance between Pd deposited at the crystallite surface and framework Al trapping sites and thus result in greater amounts of mononuclear Pd^{2+} formed at all treatment temperatures. Therefore, this result may suggest alternative hypotheses; however, the amounts of mononuclear Pd^{2+} content for the nanosheet material were low because the Si/Al of this material was 24, which may also suggest the data in Figure E.3 may be overinterpreted.

Another CHA nanosheet material was synthesized with a higher framework Al density to host more mononuclear Pd^{2+} ion sites during cycling experiments, and compared to other CHA zeolites (of unknown crystallite size) of similar bulk Al density (Figure E.4). From Figure E.4, the nanosheet material showed a slight increase in mononuclear Pd^{2+} content with air treatment temperature, but it was not as significant as the other materials (of presumably greater average crystallite size) of similar bulk Al density. Therefore, the results

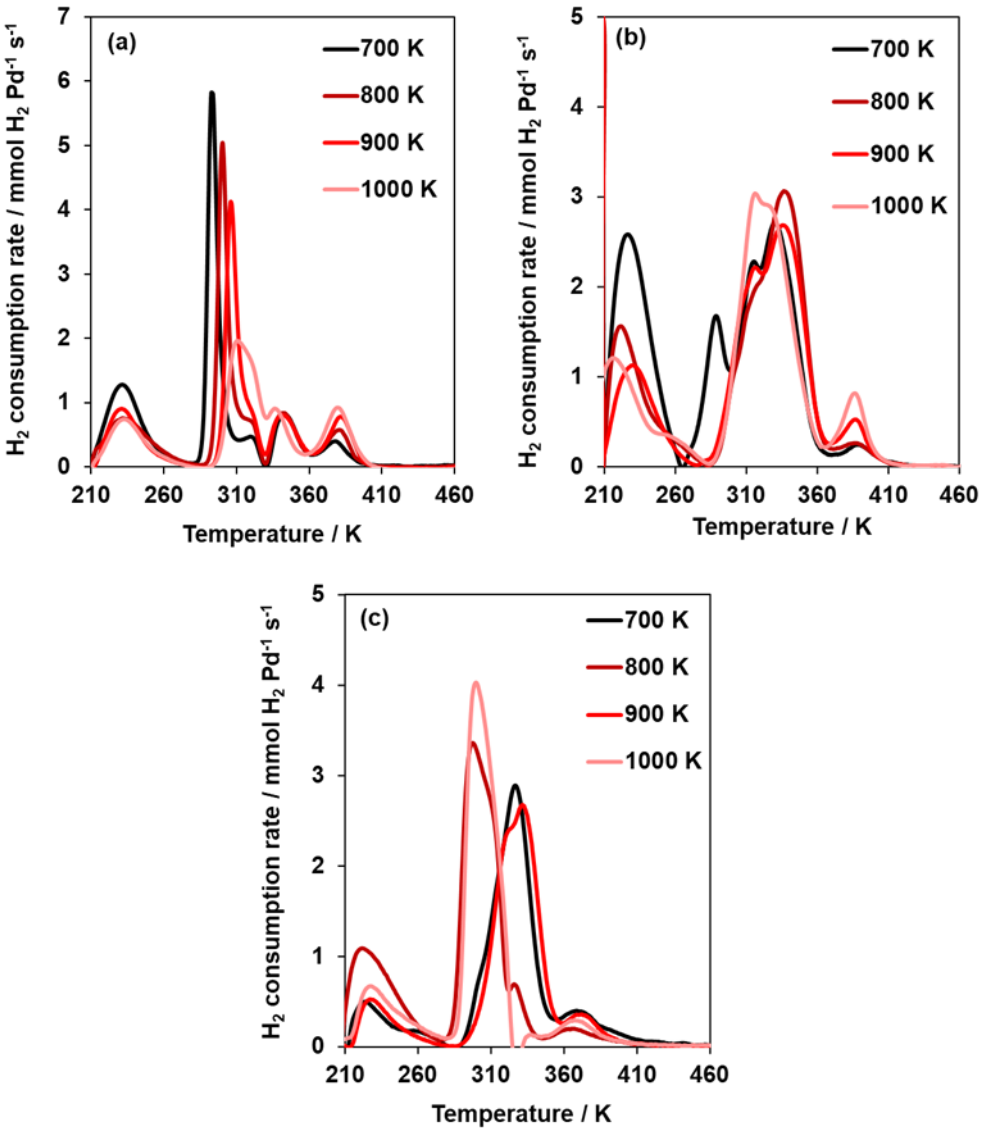

Figure E.2. H_2 TPR profiles of Pd-CHA materials of varied crystallite size: (a) 10 μm, (b) 500 nm, (c) nanosheets. Quantifications are plotted in Figure E.3.

from the Si/Al = 22–24 and 9–13 studies demonstrate these nanosheet materials do not form more mononuclear Pd^{2+} at higher air temperatures, in contrast to other CHA zeolite sample tested in this work.

The observations on the nanosheet materials lead to three new hypotheses. First, it is possible these nanosheet materials are intrinsically less stable, and the elevated air treatment temperatures lead to the structural deactivation of Brønsted acid sites. For these two

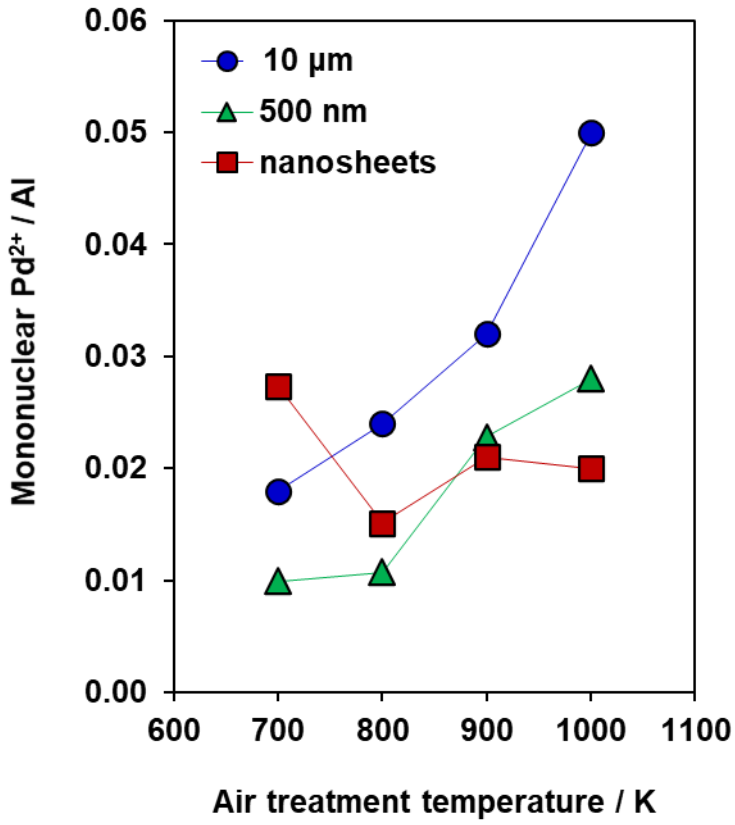

Figure E.3. Quantifications of mononuclear Pd^{2+} content (per framework Al) from Figure E.2. Average crystallite sizes listed in legend.

nanosheet materials, the deactivation of Brønsted acid sites may fortuitously cancel the increased Pd mobility with air temperature, resulting in no observable increase in mononuclear Pd^{2+} content as a function of air treatment temperature. To test this hypothesis, follow up NH_3 temperature programmed desorption studies are recommended to quantify the number of Brønsted acid sites on nanosheet materials as a function of air treatment temperature. Second, the materials were prepared via incipient wetness impregnation using $Pd(NH_3)_4(NO_3)_2$, which is known to convert to metallic Pd during air temperature treatments (>500 K) before redispersing to mononuclear Pd^{2+} cations. Additionally, Chapter 3 shows larger Pd particles contain greater kinetic and thermodynamic barriers for the conversion to mononuclear Pd^{2+}. Therefore, it is possible the nanosheet materials favor the formation of larger Pd agglomerates on the external surface using this synthesis method. It is recommended to perform follow up characterizations (O_2 chemisorption or STEM) to estimate initial Pd particle sizes.

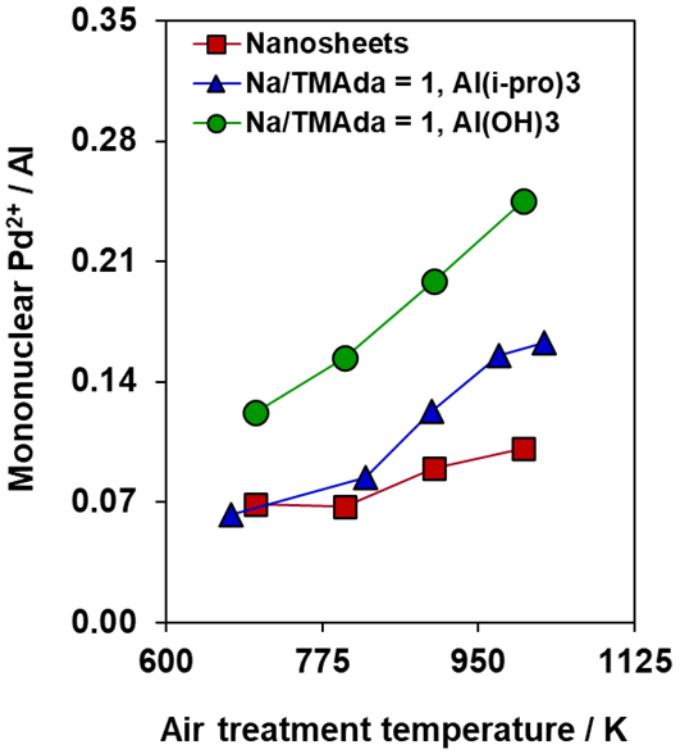

Figure E.4. A summary of H_2 TPR quantifications of mononuclear Pd^{2+} as a function of air treatment temperature for CHA zeolites of Si/Al = 9–14. The nanosheet materials were flake-like, evidenced SEM but not provided here. The other CHA materials were not characterized with SEM, but the Al precursors are given in legend following literature reported recipes.

Third, it is possible that more complex factors govern the relative importance between inter- and intracrystalline diffusion on Pd interconversion processes. Here, the nanosheet materials minimizes characteristic lengths scales for intracrystalline diffusion, which may favor the agglomeration of Pd in larger particles at external crystallite surfaces, rationalizing the trends observed on the nanocrystalline materials.

VITA

Trevor Michael Lardinois was raised in Pulaski, Wisconsin by Kandy and Jesse Lardinois. Their parental teachings of respect, discipline, and excellence promoted Trevor's academic successes, resulting in chemical engineering degrees from the University of Wisconsin - Madison (B.S.) and Purdue University (Ph.D.). Along the academic journey, he married Stephanie (Uhlig), and they had their first son, named Luca. Together, they will move to the Chicago suburbs after Trevor finishes his Ph.D. studies, never forgetting who helped pave their path to happiness.